



Terms and Conditions of Use of Digitised Theses from Trinity College Library Dublin

Copyright statement

All material supplied by Trinity College Library is protected by copyright (under the Copyright and Related Rights Act, 2000 as amended) and other relevant Intellectual Property Rights. By accessing and using a Digitised Thesis from Trinity College Library you acknowledge that all Intellectual Property Rights in any Works supplied are the sole and exclusive property of the copyright and/or other IPR holder. Specific copyright holders may not be explicitly identified. Use of materials from other sources within a thesis should not be construed as a claim over them.

A non-exclusive, non-transferable licence is hereby granted to those using or reproducing, in whole or in part, the material for valid purposes, providing the copyright owners are acknowledged using the normal conventions. Where specific permission to use material is required, this is identified and such permission must be sought from the copyright holder or agency cited.

Liability statement

By using a Digitised Thesis, I accept that Trinity College Dublin bears no legal responsibility for the accuracy, legality or comprehensiveness of materials contained within the thesis, and that Trinity College Dublin accepts no liability for indirect, consequential, or incidental, damages or losses arising from use of the thesis for whatever reason. Information located in a thesis may be subject to specific use constraints, details of which may not be explicitly described. It is the responsibility of potential and actual users to be aware of such constraints and to abide by them. By making use of material from a digitised thesis, you accept these copyright and disclaimer provisions. Where it is brought to the attention of Trinity College Library that there may be a breach of copyright or other restraint, it is the policy to withdraw or take down access to a thesis while the issue is being resolved.

Access Agreement

By using a Digitised Thesis from Trinity College Library you are bound by the following Terms & Conditions. Please read them carefully.

I have read and I understand the following statement: All material supplied via a Digitised Thesis from Trinity College Library is protected by copyright and other intellectual property rights, and duplication or sale of all or part of any of a thesis is not permitted, except that material may be duplicated by you for your research use or for educational purposes in electronic or print form providing the copyright owners are acknowledged using the normal conventions. You must obtain permission for any other use. Electronic or print copies may not be offered, whether for sale or otherwise to anyone. This copy has been supplied on the understanding that it is copyright material and that no quotation from the thesis may be published without proper acknowledgement.

Simulations of Hydrodynamics in the Paddle Dissolution Apparatus and Dissolution from Multi-layered Compacts

by

Leonard McCarthy, B.Sc. (Pharm.), M.P.S.I.

being a thesis submitted for the degree of
Doctor of Philosophy in Pharmaceutics

at

University of Dublin, Trinity College.



under the direction and supervision of

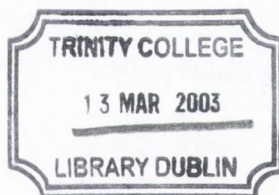
Dr. Anne Marie Healy, B.Sc. (Pharm.), Ph.D., M.P.S.I.

and

Professor Owen I. Corrigan,

B.Sc. (Pharm.) (N.U.I.), M.A., Ph.D. (N.U.I.), F.T.C.D., F.P.S.I.

August 2002

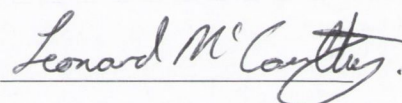


THESIS
7213

DECLARATION

This thesis is submitted by the undersigned to the University of Dublin, Trinity College, for examination for the degree of Doctor of Philosophy. It has not been submitted as an exercise for a degree at any other university. I myself carried out all the practical work except where duly acknowledged. This manuscript was completely written by me with the aid of editorial advice from Dr. Anne Marie Healy and Professor O.I. Corrigan.

I give permission for the Library to lend or copy this thesis upon request.

A handwritten signature in cursive script that reads "Leonard McCarthy". The signature is written in dark ink and is positioned above a horizontal line.

Leonard McCarthy

To my parents

In memory of Julie

TABLE OF CONTENTS

TABLE OF CONTENTS

Acknowledgements	i
Presentations and publications associated with this thesis	iii
Abbreviations and symbols	v
Summary	xi
Origin and Scope	xiii

Introduction

Chapter 1. Introduction

1.1	Dissolution	1
1.1.1	Introduction	1
1.1.2	Diffusion controlled dissolution of single component solids	1
1.1.3	Forced convection	5
1.1.4	Dissolution test	9
1.2	Fluid Dynamics	15
1.2.1	History of fluid dynamics	15
1.2.2	Computational fluid dynamics (CFD)	16
1.3	Inert non swellable matrix systems	27
1.3.1	Theoretical analysis of rate of release of solid drugs dispersed in solid matrices	27
1.3.2	Percolation theory	32
1.3.3	Ethylcellulose	38
1.4	Layered drug delivery systems	41
1.4.1	Zero order drug delivery	41
1.4.2	Controlled release from layered drug delivery systems	42
1.4.3	Simple layered drug delivery systems	43
1.4.4	Layered matrix drug delivery systems	45
1.5	DynoChem simulation program	46
1.5.1	Background	46
1.5.2	Implementation of DynoChem program	47
1.5.3	DynoChem mass transfer model	48

Experimental

Chapter 2. Materials and methods

2.1	Materials used in experiments	51
2.2	Instruments and accessories used in experiments	52
2.3	Computer software used	53
2.4	Preparation of theophylline monohydrate	53
2.5	Characterisation methods	53
2.5.1	Thermal analysis	53
2.5.2	Powder X-ray diffraction studies	54
2.5.3	Karl Fischer analysis	54
2.5.4	Scanning electron microscopy	54
2.5.5	Helium pycnometry	55
2.6	Grinding	55
2.7	Sieving	55
2.8	Blending	55
2.9	Production of single component compressed discs	55
2.9.1	Intrinsic dissolution rate compacts	56
2.10	Production of drug delivery systems	56
2.10.1	Simple layered compacts	56
2.10.2	Matrix compacts	56
2.10.3	Layered matrix compacts	57
2.11	Dissolution studies	57
2.11.1	Intrinsic dissolution rate studies	58
2.11.2	Analysis of samples from dissolution studies	58
2.12	Saturated solubility determinations	62
2.12.1	Acid excipients	62
2.12.2	Theophylline monohydrate	63
2.12.3	Analysis of samples from solubility determinations	63
2.13	Statistical Techniques used in experiments	63
2.13.1	Simple Comparative Experiments	64
2.13.2	Curve fitting	65
2.13.3	Regression analysis	66

2.14	Gambit/Fluent CFD methods to model fluid flow in USP paddle dissolution apparatus	67
2.14.1	Technical specifications of computational resources	67
2.14.2	Unstructured grid approach	68
2.14.3	Structured grid approach	77
2.14.4	Introduction of a cylindrical compact	91
2.15	DYNOCHEM – Application of mass transfer model	98

Results and Discussion

Chapter 3. Hydrodynamics and dissolution in the paddle dissolution apparatus

3.1	Dissolution rates from surfaces of single component compacts	99
3.1.1	Introduction	99
3.1.2	Dissolution from entire surface of compacts	99
3.1.3	Dissolution from curved surface of compacts only	102
3.1.4	Dissolution from planar surfaces of compacts only	104
3.1.5	Conclusion	106
3.2	CFD modelling of fluid dynamics in the USP paddle dissolution apparatus	107
3.2.1	Introduction	107
3.2.2	Unstructured Grid Approach	107
3.2.3	Structured Grid Approach	115
3.2.4	Introduction of a cylindrical compact	136
3.3	Conclusions	152

Chapter 4. Dissolution from simple multi-layered compacts

4.1	Introduction	154
4.2	Salicylic acid as model drug	154
4.2.1	Benzoic acid and salicylic acid (BA/SA/BA)	154
4.3	Theophylline monohydrate as model drug	155
4.3.1	Theophylline monohydrate and succinic acid (SuA/Thmh/SuA) in 0.01N HCl	156

4.3.2	Theophylline monohydrate and adipic acid (AA/Thmh/AA) in 0.01N HCl	157
4.4	Initial modelling of dissolution from Simple Layered Systems	158
4.4.1	Calculation of surface area changes in three-layered systems	158
4.4.2	Calculation of k Values	161
4.4.3	Initial modelling results of dissolution from layered systems	163
4.5	Dynochem simulations of dissolution from simple layered systems	166
4.5.1	Visual process scheme	166
4.5.2	Process calculations	168
4.5.3	Simulation of dissolution from benzoic acid/ salicylic acid compacts in 0.1N HCl	172
4.5.4	Simulation of dissolution from theophylline monohydrate/ succinic acid compacts in 0.01N HCl	175
4.5.5	Simulation of dissolution from theophylline monohydrate/ adipic acid compacts in 0.01N HCl	177
4.6	Conclusions	180

Chapter 5. Dissolution from layered matrix compacts

5.1	Introduction	182
5.2	Feasibility studies on layered matrix systems	182
5.2.1	Initial studies	182
5.2.2	Three layered ethylcellulose and theophylline monohydrate drug core with fumaric acid outer layers	183
5.3	Controlled polymer particle size	184
5.3.1	Experimental design	184
5.3.2	Single layer matrix compacts	186
5.3.3	Triple layer matrix compacts	190
5.4	Predicting drug release from layered matrix systems	198
5.4.1	Percolation studies	199
5.4.2	Dynochem simulations	205
5.5	Conclusions	231

Chapter 6. General Discussion

6.1	Introduction	234
6.2	Hydrodynamics and dissolution from single component compacts	235
6.2.1	Dissolution rates from different surfaces/ positions of compacts	235
6.2.2	Hydrodynamics in the paddle dissolution apparatus at 50 rpm	236
6.2.3	Effect of different paddle rotation speeds	239
6.2.4	Effect of the addition of a cylindrical compact	239
6.2.5	Mass transfer predictions from a single component compact	241
6.3	Simple layered drug Compacts	241
6.3.1	Initial modelling of dissolution from simple multi-layered compacts	242
6.3.2	Dynochem modelling of dissolution from simple layered compacts	243
6.4	Layered matrix compacts	245
6.4.1	Effect of outer layer solubility	247
6.4.2	Effect of particle size of polymer	249
6.4.3	Percolation studies	250
6.4.4	Simulation of dissolution from layered matrix compacts	251
6.5	Conclusions	254
6.6	Future work	255
6.6.1	CFD model of the dissolution apparatus	255
6.6.2	Model of drug dissolution from layered compacts	257
	References	259

Appendices

Appendix 1	Navier-Stokes equations in a cylindrical co-ordinate system	270
Appendix 2	Characterisation of theophylline monohydrate after formation from the anhydrous starting material	271
Appendix 3	Calibration curves used to determine the concentration of substances in solution.	273

Appendix 4	Intrinsic dissolution rate of theophylline monohydrate (\pm 5% PVP)	275
Appendix 5	Gambit Journal File 1	276
Appendix 6	Gambit Journal File 2	278
Appendix 7	Unix code 1	287
Appendix 8	Unix code 2	288
Appendix 9	Unix code 3	289
Appendix 10	Derivation of equation to determine mass transfer from curved surface of a cylinder	291
Appendix 11	Dynochem process sheet example 1	294
Appendix 12	Dynochem process sheet example 2	296
Appendix 13	Dynochem process sheet example 3	298

ACKNOWLEDGEMENTS

I would like to extend sincere gratitude to Dr. Anne Marie Healy for her guidance, support and commitment throughout the course of my studies. Her dedication to my research and the preparation of this thesis are greatly appreciated.

I am grateful to Professor Owen Corrigan for his direction and advice, particularly in the preparation of this thesis.

I wish to acknowledge Esprit, under the E.U. 4th Framework, for providing financial assistance through the PSUDO project, which provided a starting point for this research. I am grateful to Trinity College for providing me with travel funding. Thanks also to the International Society of Pharmaceutical Engineering, for awarding me the Bursary in Pharmaceutical Research, 1999.

I would like to thank Professor Jim Sexton of the Department of Mathematics in T.C.D. for providing access to the computational resources in the Trinity Centre for High Performance Computing. I am particularly grateful to Dr. Geoff Bradley for his guidance with the Fluent program and parallel processing and for developing the code to allow conversion of the resulting data into a useful format.

I am grateful to Carolin Kosiol for her in-depth introduction to the Fluent CFD program, for her introduction to the Unix operating system and for her codes to convert CFD data into graphical formats.

I would like to sincerely thank Professor Lawrence Crane, Dept. of Mathematics, for introducing me to the mathematics of diffusion and for developing a solution to mass transfer from a curved surface based on velocity shear rates in the surrounding fluid.

I am also grateful to Performance Fluid Dynamics (PFD) for providing me with the Dynochem simulation package. I would like to thank Eoin Casey for his introduction to the use of the package, its application to mass transfer and assistance with model development.

I would also like to thank the academic, secretarial and technical staff of the School of Pharmacy, in particular Brian, Pat, Nuala, Liesa and Derek Bell. I am grateful to Rhona and Ray in the Pharm. Chem. Dept. for their help with KFT. I would like to thank Lidia Tajber for carrying out helium pycnometry measurements and SEM of theophylline monohydrate.

Thanks to my fellow postgrads: Karl, Brendan, Shane, Bronagh, KOC, Karen G., Emma, Deirdre, Helena, Idris, Nicole, Stephen, Fiona, Mark, Rosario, Anthony, Fergal, Sally Ann. Thanks especially to Tina and Catriona for helping me laugh through many days in the lab.

Special thanks to Brendan, Richie, Deirdre, Emma and Karen for proof-reading this thesis. This is a true test of friendship!

Thanks to Colin, Soby, Paul, Greg, Brendan, Richie, Brian, Nicola, Nympha, Maebh, Kevin, Vernon, the Coen family and Mr Burgess for their friendship and encouragement (occasionally!), especially towards the end. Thanks to the Skillet Lickers for the 'beautiful, beautiful music'....

I am grateful to my brother, Ray, for keeping me in Dublin during my undergraduate years and for the use of his apartment in recent years.

Thanks to my bothers Kev and Ray and sister Jac for their love and friendship.

A very special thanks to Aideen, for putting up with me, through thick and thin, and for looking after me (and my belly), especially in recent months. This thesis would not have been possible without your love and support. I tried to fit in a chapter on you later on, but it just didn't quite gel with the rest....

Finally, I am forever indebted to my parents for their love and support, in every possible way, throughout my student years. I am eternally grateful.

PRESENTATIONS AND PUBLICATION ASSOCIATED WITH THIS THESIS

Oral Presentations

‘Modelling the effect of surface area changes on drug dissolution from multi-layer compacts’, in *Proceedings of the twenty-third TCD/QUB annual joint research seminar*, Trinity College Dublin, March 2000, L3 (abstract) [L.G. McCarthy, K.M. Gallagher, O.I. Corrigan and A.M. Healy].

‘The effect of changing surface area on drug dissolution from multi-layer compacts’, in *Proceedings of 19th Pharmaceutical Technology Conference*, Baveno-Stresa, Italy, April 2000, Volume 3, 90-102 [L.G. McCarthy, K.M. Gallagher, O.I. Corrigan and A.M. Healy].

Poster Presentations

‘Evaluation of the apparent diffusion boundary layer in the paddle dissolution apparatus’, in *Proceedings of the twenty-second TCD/QUB annual joint research seminar*, The Queen’s University of Belfast, March 1999, P17 [K.M. Gallagher, L.G. McCarthy, O.I. Corrigan, L. Crane, M. Crane and A.M. Healy]

‘Drug Dissolution in the Paddle Dissolution Apparatus’, in *Proceedings of the World Congress of Pharmacy and Pharmaceutical Sciences '99, 59th International Congress of FIP*, Barcelona, Spain, September 1999 P-015, 38 (abstract) [K.M. Gallagher, L.G. McCarthy, O.I. Corrigan, L. Crane, M. Crane, C. Pinto, N. Hurley and A.M. Healy].

Modelling drug delivery systems using finite element analysis, in *Proceedings of the 4th International Eurosim 2001 Congress*, Delft, June 2001, ISBN: 90-806441-1-0 [N. Hurley, L. Crane, M. Crane, A.M. Healy, O.I. Corrigan, K.M. Gallagher and L.G. McCarthy].

Simulating the hydrodynamic conditions in the USP paddle dissolution apparatus, in *Proceedings of International Symposium on Scientific and Regulatory Aspects of Dissolution and Bioequivalence, Athens, Greece, April 2002*, P302 [L.G. McCarthy, C. Kosiol, G. Bradley, A.M. Healy, J.C. Sexton and O.I. Corrigan].

Application of Computational Fluid Dynamics (CFD) with High Performance Computing (HPC) to Simulate Hydrodynamics in the Paddle Dissolution Apparatus, *2002 AAPS Annual Meeting and Exposition, Toronto, Canada, November 2002*, M2183 [L.G. McCarthy, C. Kosiol, A.M. Healy, G. Bradley, J.C. Sexton, O.I. Corrigan and A.M. Healy]. Abstract accepted for presentation.

Publications

Sensitivity of dissolution rate to location in the paddle dissolution apparatus, *Journal of Pharmacy and Pharmacology*, 54(3) (2002) 441-444 [A.M. Healy, L.G. McCarthy, K.M. Gallagher and O.I. Corrigan].

ABBREVIATIONS AND SYMBOLS

\pm	plus or minus
\leq	less than or equal to
\geq	greater than or equal to
\approx	approximately equal to
\sim	Approximately
\ll	much less than
\gg	much greater than
2θ	diffraction angle
α	shear rate of velocity in a boundary layer
a	radius of a cylinder dissolving from curved surface
a_d	Interfacial area of the disperse phase
A	surface area
$A(ax)$	total cross sectional area in axial direction
$A(ax_exp)$	axial surface area exposed to dissolution medium
$A(rad)$	total cross sectional area in radial direction
A'	total amount of drug present in the matrix per unit volume
AA	adipic acid
Abs.	Absorbance
AdA	adipic acid
A_{drug}	complete surface area of drug layer exposed
ANOVA	analysis of variance
AR	aspect ratio
b	width of a dissolving flat plate
β	tablet property
BA	benzoic acid
B.P.	British Pharmacopoeia
C or c	concentration
$^{\circ}C$	degree centigrade
C_c	concentration in the continuous phase
C_d	concentration in the disperse phase
CD	coefficient of determination
CFD	computational fluid dynamics
core	undissolved drug-containing region of a matrix compact
C_{liquid}	Concentration in liquid at time, t

cm	centimetre
C_o	intrinsic solubility
cpm	cycles per minute
C_s	saturated solubility
$C_{c,i}$	concentration of the continuous phase at the interface
$C_{d,i}$	concentration of the disperse phase at the interface
δ	(effective) diffusion boundary layer
δ_{ax}	thickness of moving boundary of the dissolved porous region in a matrix in the axial direction
δ_c	thickness of film from continuous phase to interface
δ_d	thickness of film from disperse phase to interface
δ_m	thickness of moving boundary of the dissolved porous region in a matrix
δ_{rad}	thickness of moving boundary of the dissolved porous region in a matrix in the radial direction
D	diffusion coefficient
D'	relative diffusivity
D_{app}	steady state (apparent) diffusion coefficient of drug through a matrix
D_{aq}	aqueous diffusion boundary layer
df	degrees of freedom
d_h	hydrodynamic boundary layer thickness
DSC	differential scanning calorimetry
ϵ	porosity
ϵ_o	initial porosity of a matrix
ϵ_d^a	accessible volume fraction of drug in a matrix
Excip	excipient
Etc	ethylcellulose
E_{pol}	erosion rate of polymer per exposed surface area from a matrix above the percolation threshold
E_{rate}	erosion rate of polymer from a matrix above the percolation threshold
F	F-statistic from an ANOVA table
FP	Fine particle grade
$f_{(ax)}$	fraction of the total surface area exposed in the axial direction
$f_{(rad)}$	fraction of the total surface area exposed in the radial direction
f_t	fraction of drug released at time, t
FuA	fumaric acid
G	intrinsic dissolution rate (mg/min/cm ²)
$\phi_{m,c}$	mass flow from the continuous phase to the interface

G_1, G_2, G_3	shape factors
GB	giga-byte
H	distance to where hydrodynamic boundary layer covers complete diameter of tube in a poiseuille flow
h	apparent diffusion layer thickness
$h_{(ax)}$	apparent diffusion layer thickness in the axial direction
$h_{(rad)}$	apparent diffusion layer thickness in the radial direction
h_{init}	initial height of a matrix compact
HCl	hydrochloric acid
HPC	high performance computing
HPLC	high performance liquid chromatography
k	dissolution rate constant
$K_{C(ax)}$	mass transfer coefficient into the continuous phase (liquid) from the interface in the axial direction
$K_{C(rad)}$	mass transfer coefficient into the continuous phase (liquid) from the interface in the radial direction
K_{CD}	overall mass transfer coefficient
$K_{CD(ax)}$	overall mass transfer coefficient in axial direction
$K_{CD(rad)}$	overall mass transfer coefficient in radial direction
k_0	zero order release rate constant
k_{drug}	rate of change of diameter of drug layer
k_{excip}	rate of change of diameter of drug layer
k_1	rate of decrease of diameter with time
k_2	rate of decrease of height with time
KFT	Karl Fischer titration
K_r	release-rate constant
l	length of a dissolving flat plate
l'	thickness of a slab
λ	Wavelength
log	log to the base 10
LSD	least significant difference
λ_{max}	maximum absorbance wavelength
M	molecular weight
MFLOPS	number of full operations (in millions) that can be performed per second
mg	milligram
mg%	milligrams per 100 ml
MHz	megahertz
min	minute

ml	millilitre
mm	millimetre
MRF	multiple (rotating) reference frame
MS	the adjusted mean squares
MSC	model selection criterion
MSE	the adjusted mean squares of error
M_t/M_∞	fractional drug release at time, t
M.W.	molecular weight
μ	universal scaling constant
μm	micrometer
n	exponent of best fit to the equation of Peppas (1985)
η	dynamic viscosity
η_{app}	apparent viscosity
nm	nanometre
p'	number of parameters estimated (in calculation of MSC)
P	pressure
ρ	density
ρ_{app}	apparent density after compaction
ρ'_{drug}	initial amount of drug present per initial unit volume of matrix layer
ρ'_{Etc}	initial amount of ethylcellulose present per initial unit volume of matrix layer
p	p-value associated with a student's t-test
p_c	percolation threshold
p_{c1}	lower percolation threshold
p_{c2}	upper percolation threshold
pH	$-\log_{10}(\text{hydrogen ion concentration})$
Ph. Eur.	European Pharmacopoeia
pol	polymer
PVP	polyvinylpyrrolidone
PXRD	X-ray diffraction measurements of powdered samples
Q	amount of drug released per unit exposed area
R	dissolution rate
r	radius
r_0	initial tablet radius
r^2	(squared) correlation coefficient
rad	radian
Re	Reynolds number
®	registered trade mark

rpm	revolutions per minute
s	second
SA	salicylic acid
Sc	Schmidt number
$S_{c_{drug}}$	curved surface area of drug layer
$S_{t_{drug}}$	area of transverse section of the drug layer
$S_{t_{excip}}$	area of transverse section of the excipient layer
S_{CD}	partitioning coefficient = C_d/C_c
S_D	estimated standard error of the mean difference between two samples
SD	standard deviation
SEM	scanning electron microscopy
SS	sequential sum of squares
SuA	succinic acid
S_x	standard errors of the samples of X in a regression analysis
S_y	standard errors of the samples of Y in a regression analysis
t	time
τ	tortuosity
t_0	lag time
t_r	retention time
$t_{0.025}$	two sided t-statistic with a significance level, $\alpha = 0.05$
TGA	thermogravimetric analysis
Thmh	theophylline monohydrate
TM	trade mark
TSA_{exp}	total surface area exposed to the dissolution medium
u	velocity in the radial direction
U_a	fluid velocity in the axial direction
u_b	velocity of the mainstream
U_r	fluid velocity in the radial direction
USP	United States Pharmacopoeia
U_t	fluid velocity in the tangential direction
UV	ultraviolet
UV-MCA	Multi-component ultraviolet analysis
U_x	fluid velocity in the tangential direction
V	volume
V_{tot}	apparent volume of matrix compact (including porosity)
V_t	true volume of matrix compact (including porosity)
v	kinematic viscosity

v or v_t	circumferential (rotational) velocity
v/v	volume per volume
vs.	versus
W	weight
W_{th}	weight of theophylline monohydrate in a matrix
W_{et}	weight of ethylcellulose in a matrix
ω	angular velocity of rotation
ω_f	angular velocity of rotation of a fluid
w/v	weight per volume
w_i	weight applied to each point (calculation of MSC)
x	diameter/distance
x_0	initial diameter
x_{drug}	diameter of drug layer
x_{excip}	diameter of excipient layer
\bar{X}	mean of sample X
y	Height/thickness
y_0	initial height
\bar{Y}_1	mean of sample 1
\bar{Y}_2	mean of sample 2
\bar{Y}	mean of sample Y
Y_{obs_i}	observed data points (calculation of MSC)
\bar{Y}_{obs}	predicted data points (calculation of MSC)
\bar{Y}_{cal_i}	weighted mean of the observed data (calculation of MSC)
z	distance in the z direction

SUMMARY

Studies involving the calculation of dissolution rates from individual surfaces of large single component compacts, to assist in the prediction of dissolution rates from simple layered compact systems, revealed that non-uniform hydrodynamics were present in the paddle dissolution apparatus. Dissolution fluxes varied depending on the location of the surface from where dissolution occurred and also on the position of the compact in the vessel, with highest dissolution rates occurring for compacts within a region of 3 mm from the base of the vessel. A virtual Computational Fluid Dynamics model of the paddle dissolution apparatus was developed and validated against previously measured fluid velocities in the apparatus. The method revealed that fluid flow behaviour below the level of the paddle was complicated, with large changes in velocity occurring over small distances. High fluid shear rates were noticeable towards the base of a large compact positioned at the bottom of the vessel, consistent with the observed increased dissolution rates in this region. Laminar flow was predicted for paddle rotation speeds of up to 150 rpm. Times to achieve complete mixing in the vessel were dependant on the paddle rotation speed. A mass transfer prediction made for the top surface, based on the angular rotation of the fluid in this region was in close agreement with the corresponding experimentally determined result. A semi analytical solution was developed to describe dissolution from the curved surface of a compact sitting at the base of the vessel based on the examination of fluid shear rates in the axial direction in the diffusion boundary layer immediately outside the curved surface. The predicted mass transfer rate was higher than the experimentally determined dissolution rate, the deviation being explained in terms of the shortcomings of the assumptions of the model. The validated CFD method could be used in future work to examine the effect of various parameters on the hydrodynamics or mixing properties within the apparatus and may ultimately prove a useful tool in the examination of the hydrodynamic relations in in-vitro in-vivo correlations (IVIVC).

Control of the surface area of drug layer exposed with time, dissolving by convective diffusion, provides a possible method to attain zero order release. Layered cylindrical compacts, consisting of alternate single component drug and soluble excipient layers, were studied to examine the possibility of controlling the surface area changes with

time from a central drug layer. Initial feasibility dissolution studies involving a benzoic acid/ salicylic acid three layered system showed that control of exposed drug surface area, and thus controlled dissolution from a simple layered cylindrical compact was achievable. Sigmoidal shaped release profiles were seen when theophylline monohydrate was used as the model drug, between two layers of soluble acid excipient, the dissolution rates being affected by the solubility of the outer layers. A dynamic simulation program was used to develop a model to predict dissolution rates with time from these simple layered compacts. The model, which was based on the physicochemical properties of the individual layers and the experimentally determined dissolution rates from individual surfaces, predicted dissolution profiles which were in good agreement with experimental results.

The effect of the addition of soluble acid excipient layers to a central theophylline monohydrate-containing inert matrix layer was also examined. The addition of the layers had the desired effect of shifting the kinetics of drug release from Fickian release towards zero order release. A dynamic model was developed to predict dissolution profiles from the layered matrix compacts, involving the evaluation of a moving boundary of the developing leached porous region within the matrix layer and the effect of increasing surface area due to dissolution of the acid excipient layers.

The final model for drug dissolution from a layered matrix compact including the effect of the addition of layers of soluble acid excipient onto the matrix core, produced simulated dissolution profiles, which showed good agreement with the experimental data for a series of polymer concentrations in the matrix core and for acid excipient layers of relative low and high solubilities. The final Dynochem model could be used as a pre-formulation tool to predict dissolution profiles from layered matrix systems, based on physicochemical properties, thus decreasing the time spent on initial dissolution feasibility studies.

ORIGIN AND SCOPE

Drug release rate from conventional dosage forms generally declines with time caused by a decrease in surface area and/or increase in diffusional pathway of the drug over time. Delivery of a drug at a constant rate is a major goal in pharmaceutical research and numerous methodologies have been devised to achieve such 'zero order' release kinetics (Yang and Fassihi, 1997a). Most cases of dissolution of solids in liquids are convective-diffusion controlled and the dissolution is proportional to the surface area available for dissolution (Nernst, 1904, Brunner, 1904). Therefore, control of the surface area of drug exposed with time from a simple diffusion based dissolution system provides a possible method to attain zero order release. The effect of increasing surface area of drug available for dissolution in two-component mixed compacts consisting of drug and excipient, caused by the dissolution of the soluble excipient and resulting in increased drug release rate, has prompted the need to further evaluate the effect of changing surface area with time in a drug delivery system, due to differing dissolution rates of drug and excipient (Healy and Corrigan, 1996). A simple layered compact, consisting of drug and soluble excipient in alternate single component cylindrical layers, provides a convenient device to examine the possibility of controlling the surface area of drug available for dissolution with time. Accurate predictions of the surface area changes with time from such a system, based on the physicochemical properties of the components may ultimately lead to a better model for dissolution from multi-component systems.

Layered matrix drug delivery systems (DDS) have been previously described (Deasy et al., 1993; Conte et al., 1993; 1994a; Yang and Fassihi, 1997b; Conte and Maggi 1998). However, little attention has been focused on the development of models to predict drug release from such systems, nor has there been an attempt to control dissolution rate from the central drug layer via a control of the surface area available during dissolution. Drug release has not, as yet, been examined from layered DDS consisting of a central, active-containing, insoluble non-swellable heterogeneous matrix core between layers of soluble acid excipient. The increase in surface area of the drug layer over time, as the excipient dissolves, may transform the kinetics of drug release from a layered matrix system to a more zero order type profile.

In-vitro dissolution in a forced convection apparatus (e.g. the paddle dissolution apparatus) is fundamentally controlled by hydrodynamics (Grijseels et al., 1981). Thus accurate modelling of in-vitro diffusion-controlled dissolution requires knowledge of the hydrodynamics of the system. Limited studies into the hydrodynamics of the paddle dissolution apparatus have revealed that complex hydrodynamics are present in the vessel (Bocanegra et al., 1990; Diebold, 2000). Furthermore, there have been reports in the literature describing high variability in results, unpredictability and randomness of observed results for dissolution apparatus calibrator tablets (Achanta et al. 1995; Qureshi and McGilveray, 1999). Variable fluid dynamics in the vessel have been proposed as a likely source of high variability in results from the paddle dissolution apparatus (Qureshi and Shabnam, 2001). The novel application of Computational Fluid Dynamics (CFD) to accurately simulate the hydrodynamics in the vessel of the paddle dissolution apparatus may help to explain such variability in the test. Predictions of fluid velocities adjacent to virtually modelled dissolving surfaces may also help to a-priori predict dissolution rates from single component systems and also from the proposed layered compact systems.

The primary objectives of this work were:

1. To examine the hydrodynamics in the paddle dissolution apparatus, through a virtual CFD model, and to validate the resulting hydrodynamics against measured fluid velocities in the apparatus.
2. To correlate the CFD velocities with actual dissolution rates and experimentally determined values for the apparent diffusion boundary layer thickness for various positions in the apparatus and to examine the possibility of a priori predicting mass transfer from the CFD generated velocities.
3. To examine the possibility of controlling the surface area changes from simple layered compacts consisting of alternating single component drug and soluble excipient layers to achieve controlled release of drug.
4. To examine the possibility of attaining zero order release through the application of soluble acid excipient layers to the planar surfaces of a central drug-containing non-swellable inert matrix layer.
5. To develop models to predict the surface area changes involved in dissolution from simple layered compacts and from layered matrix compacts of the individual layers and thus predict dissolution behaviour from these systems

based on the physicochemical properties of the components and dissolution behaviour from individual surfaces in the paddle dissolution apparatus.

Chapter 1

Introduction

1.1 DISSOLUTION

1.1.1 Introduction

Dissolution plays an important role in drug release from pharmaceutical preparations. After disintegration of a tablet, the individual drug particles must dissolve before absorption from the gastro-intestinal tract can occur. Dissolution involves two distinguishable processes: firstly the surface reaction that loosens individual molecules from the solid (solvation) and secondly the transport of these molecules from the surface into the solvent (Grijseels et al., 1981). Most cases of dissolution of solids in liquids are diffusion controlled as the surface reaction is so fast that the transport of dissolved molecules from the surface to bulk can be considered as the rate limiting step in the dissolution process (Carstensen, 1972).

1.1.2 Diffusion controlled dissolution of single component solids

1.1.2.1 Stagnant layer model

The classical model used in pharmacy to describe dissolution processes is the stagnant layer model. Based on the theories of Noyes and Whitney (1897) and Nernst and Brunner (1904), it is assumed that, under steady state conditions in a thin layer at the solid surface the liquid is static. The transport process through this layer is a diffusion process occurring due to a concentration gradient between the saturated concentration at the solid surface, C_s , and the concentration at the boundary between the film of thickness h and the bulk solution, C . The process is illustrated schematically in Figure 1.1

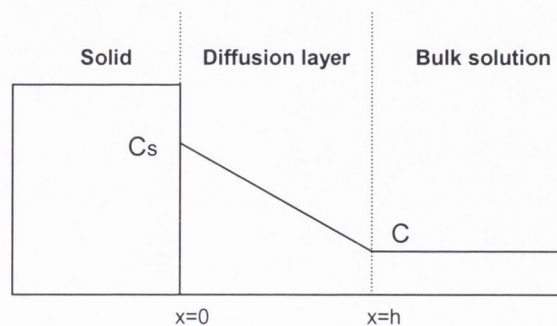


Figure 1.1 Schematic of the Nernst-Brunner model for the dissolution of a single-component solid dissolving in a pure solvent.

The model evolved from the application of Fick's first law, which states that:

$$J = -D \frac{\delta C}{\delta x} \quad \text{Equation 1.1}$$

where J (the diffusional flux) is the amount of substance passing perpendicularly through a unit surface area per unit time, D is the diffusion coefficient and $\delta C/\delta x$ is the concentration gradient. For a mass of substance dissolved in a given volume, V , of dissolution medium with a surface area A of dissolving material, Equation 1.1 can be written as:

$$\frac{V}{A} \frac{dC}{dt} = \frac{-D(C_s - C)}{h} \quad \text{Equation 1.2}$$

The weight of the solid dissolved, W , with respect to time can be given by:

$$\frac{dW}{dt} = kA(C_s - C) \quad \text{Equation 1.3}$$

where k is the dissolution rate constant (D/h).

In practice, dissolution studies are performed under sink conditions, which implies that the volume of medium is sufficiently large so that C never exceeds 10-15% of the saturated solubility, C_s . Under these conditions i.e. $C_s \gg C$, Equation 1.3 can be written as:

$$\frac{dW}{dt} = \frac{DAC_s}{h} \quad \text{Equation 1.4}$$

or

$$G = (dW/dt)/A = \frac{DC_s}{h} \quad \text{Equation 1.5}$$

where G is the dissolution rate per unit surface area or the intrinsic dissolution rate (Wells, 1988). The limitation of the model lies in the fact that it does not describe the actual situation, since in reality no stagnant layer exists. From stagnant layer theory it is not possible to predict the thickness h of the diffusion layer or the dependence of dissolution rate on fluid velocity.

1.1.2.2 Hydrodynamic approach to dissolution rate

In reality, convection rather than diffusion controls the transport process in a liquid even at relatively small Reynolds numbers ($Re \geq 10$) (Grijseels et al., 1981).

In a liquid undergoing convection, the entire zone of liquid motion can be divided into two regions (Levich, 1962); the bulk where transport of dissolved material mainly takes place by macroscopical fluid flow and a boundary layer region near the dissolving surface, where, due to the roughness of the solid and the viscosity of the liquid, the solvent velocity decreases gradually to zero. As compared with the bulk, there is a slower removal of dissolved matter by convection in the boundary zone, thus near the surface a higher concentration exists than in the bulk. This causes a net diffusion in the direction normal to the surface. Diffusion of dissolved molecules through the boundary layer into the bulk is a process of relatively short duration, since at a short distance from the solid surface the diffusional transport is overruled by convection that entrains the diffused molecules. The distance that has to be covered by pure diffusion then depends strongly on the hydrodynamics in the liquid.

1.1.2.2.1 Hydrodynamic boundary layer

When a liquid flows along a solid surface, the velocity of the fluid in the vicinity of the surface is reduced by friction. In a thin boundary layer the velocity of the fluid undergoes an abrupt change. The bulk velocity is reduced to zero at the solid surface. The zone in which this takes place is termed the 'hydrodynamic boundary layer'. The thickness of the hydrodynamic layer is often defined as the distance from the surface of the solid to the point where the tangential velocity u_x attains a value equal to 90% of the velocity u_b of the main stream (Levich, 1962). The thickness of the hydrodynamic boundary layer (d_h) along a semi-infinite plate can be calculated according to Levich (1962):

$$d_h = 5.2 \left(\frac{\nu x}{u_b} \right)^{1/2} \quad \text{Equation 1.6}$$

where ν is the kinematic viscosity and x is the distance along the surface.

1.1.2.2.2 Diffusion boundary layer

Only in the immediate vicinity of the surface, where liquid motion is almost absent, a region of rapidly changing concentration exists where molecular diffusion must be taken into account. This zone is termed the *effective* diffusion boundary layer δ , (Levich, 1962). The magnitude of δ can be calculated from hydrodynamic theory independent of dissolution rate data.

Levich (1962) derived the following relationship between the thickness of the effective diffusion boundary layer (δ) and the thickness of the hydrodynamic boundary layer (d_h):

$$\delta = K_1 \left(\frac{D}{\nu} \right)^{1/3} d_h \quad \text{Equation 1.7}$$

where D is the diffusion coefficient, ν is the kinematic viscosity, (ν/D) is the dimensionless Schmidt number (Sc) and $K_1 = 0.6$ for the case of solvent flow past a semi-infinite dissolving plate. Since in practice D is about a thousand times smaller than ν , δ will have a value of about ten times smaller than d_h .

Substituting d_h from Equation 1.6 in Equation 1.7 gives:

$$\delta = 3 \left(\frac{D}{\nu} \right)^{1/3} \left(\frac{\nu x}{u_b} \right)^{1/2} \quad \text{Equation 1.8}$$

which expresses δ in terms of viscosity, diffusion coefficient, liquid velocity and distance from the leading edge of the dissolving surface. As a first approximation, assuming a linear concentration gradient in the diffusion boundary layer leads to an expression for the diffusional flux:

$$J = \frac{D(C_s - C)}{\delta} \quad \text{Equation 1.9}$$

This is the same form of equation as that derived for the Nernst-Brunner theory. However, in this case δ is a known function of the physical properties of the liquid, of the velocity and the diffusion coefficient of the dissolving solid.

The main differences between the stagnant (Nernst-Brunner) and the convective diffusion theory are:

- 1) In the Nernst-Brunner theory, the liquid adjacent to the solid surface is assumed to be static and mass transfer occurs by diffusion only, while the convective diffusion model accounts for both the diffusion process and liquid motion, which lead to mass transfer by convection.
- 2) In the Nernst-Brunner model it is assumed that the thickness of the diffusion layer, h , is the same all over the surface of the solid and diffusion in tangential direction is discarded. According to Levich (1962), convective and molecular diffusion

both across and along the boundary layer must be considered and the thickness of the effective diffusion layer, δ , varies along the surface.

- 3) In the case of the Nernst-Brunner theory, the diffusion layer, h , is assumed to be constant for a given regime of motion. Equation 1.8 shows that δ depends not only on the physical properties and velocity of the solvent, but also on the diffusion coefficient of the dissolving substance.

1.1.3 Forced convection

Forced convection refers to liquid that is forced into convection by means of an external source (e.g. a pump or a stirrer). The dissolution rate in a liquid compelled to flow along a solid surface can be predicted from the boundary layer theory, provided knowledge of the hydrodynamic conditions is available. Dissolution in some specific hydrodynamic systems that have been mathematically analysed by previous workers are described in the following section.

1.1.3.1 Dissolution from a flat plate

From Equation 1.9 Levich (1962) derived an expression for the dissolution rate from a flat plate with length, l , and width, b , along which a fluid flows and a laminar boundary layer develops:

$$R = 0.68(\Delta C)D^{2/3}v^{-1/6}u_b^{1/2}bl^{1/2} \quad \text{Equation 1.10}$$

Under similar circumstances the dissolution rate of a circular surface with radius r is:

$$R = 1.58(\Delta C)D^{2/3}v^{-1/6}u_b^{1/2}r^{3/2} \quad \text{Equation 1.11}$$

1.1.3.2 Dissolution in a Poiseuille flow

Dissolution from a tube wall has also been modelled, as a peculiar flow pattern develops in this case. At a certain distance H from the tube inlet, the hydrodynamic boundary layer of which the thickness increases in the direction of flow, covers the whole diameter of the tube. From this point on no further increase of d_h occurs, but a fully laminar flow develops with a parabolic velocity profile. This is called a Poiseuille flow.

Levich (1962) developed an equation for the flux, J , from the dissolving tube wall in a fully developed Poiseuille flow:

$$J = 0.68D^{2/3}(\Delta C)v^{-1/6}\left(\frac{u}{r}\right)^{1/3}x^{1/3} \quad \text{Equation 1.12}$$

where r is the radius of the tube and x is the distance along the surface. The parabolic Poiseuille velocity profile is similar to that which develops in fluid flow between two flat plates, since near the solid wall velocity, u_x , is proportional to distance y from the surface. When a plate of length l and width b dissolves in such a flow, the flowing expression can be used (Nelson and Shah, 1975):

$$R = 0.808D^{2/3}\alpha^{1/3}(\Delta C)bl^{2/3} \quad \text{Equation 1.13}$$

where α is shear rate in the boundary layer:

$$\alpha = \left. \frac{du_x}{dy} \right|_{y=0}$$

Although this expression was derived assuming a linear velocity profile over the tablet surface, excellent agreement was obtained with experimentally determined dissolution rates of tablets in a dissolution cell, which was designed to promote Poiseuille flow (Shah and Nelson, 1975).

A more recent study involved the development of a model, which did account for the parabolic velocity profile and which could be solved numerically (Neervannan et al., 1993). The modified model predictions were slightly better at high flow rates, although the simplified assumption was found to predict the experimental results as closely as the numerical solution.

1.1.3.3 Dissolution from a rotating disc surface

The rotating disc apparatus is widely used for dissolution rate experiments, the greatest advantage of the method being that the equations for convective diffusion acquire their simplest form here. In this case, the hydrodynamic boundary layer does not depend on the radial position on the rotating disc's surface. Consequently, the diffusion layer thickness δ is constant over the whole surface.

For laminar flow past the disc ($Re \leq 10^4$), the diffusion boundary layer thickness, δ and dissolution rate, R , can be defined as:

$$\delta = 1.61 \left(\frac{D}{\nu} \right)^{1/3} \left(\frac{\nu}{\omega} \right)^{1/2} \quad \text{Equation 1.14}$$

$$R = 1.9D^{2/3} \nu^{-1/6} \omega^{1/2} (\Delta C) r^2 \quad \text{Equation 1.15}$$

where ω is the angular rotational velocity. The relationship between dissolution rate and the square root of the angular velocity has been experimentally verified by several authors (Bisaillon and Tawashi, 1971; Mooney et al., 1981).

1.1.3.4 Dissolution from a stationary disc-rotating fluid system

Although most of the contemporary dissolution testing devices are modifications of the beaker method, characteristics which influence the performance of these devices have not, until recently, been determined in the context of fluid mechanics models (Khoury et al., 1988). Advantages relating to a configuration of an apparatus using a stationary dissolving surface in a stirred dissolution medium include simplicity and ease of construction, as well as elimination of the concern for misalignment and wobble of a rotating shaft. Fluid flow in this type of system has been termed Bödewadt flow, owing to the initial studies carried out by Bödewadt into such a system (Bödewadt, 1940). The velocity profiles for this configuration were later examined by Schlichting (1975). Fluid flow behaviour in this case is similar in effect to the case of the rotating disc-stationary fluid, except the velocity components are reversed. The rotation of flow near a stationary disc-rotating fluid is illustrated in Figure 1.2.

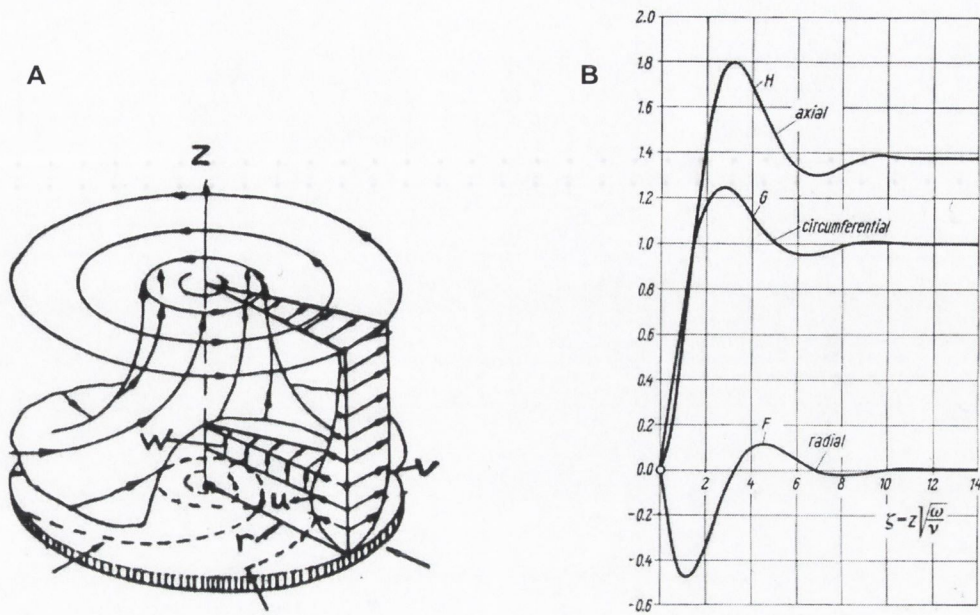


Figure 1.2 Flow near a stationary disc in a rotating fluid (Bödewadt flow) with angular rotation ω . (A) Velocity components ; u , radial, v , circumferential, w , axial. (B) Velocity distribution in the boundary layer (reproduced from Schlichting, 1975).

In an idealised case, the fluid motion at a large distance from the stationary disc is in solid body rotation. In this case the fluid has a constant angular rotation, ω for any radius, r , which results in increasing circumferential (i.e. tangential) velocities with increasing radii according to Equation 1.16.

$$v = \omega r$$

Equation 1.16

The fluid here is in equilibrium under the influence of centrifugal force, which is balanced by a radial pressure gradient. Near the wall of the disc however, the peripheral velocity of the fluid is reduced, thus decreasing the centrifugal force, whereas the radial pressure gradient directed towards the axis remains the same. This causes fluid near the disc surface to flow radially inwards, and for reasons of continuity that motion must be compensated by an axial flow upwards, as shown in Figure 1.2(A). Such a 'secondary flow' phenomenon has been likened to the settling of tea leaves in a heap near the centre at the bottom of a teacup after vigorous stirring. Velocity distributions for this configuration have been predicted by Bödewadt (1940) and later by Schlichting (1975) and are illustrated graphically in Figure 1.2(B).

Mass transfer from the stationary disc-rotating fluid system was first studied by Smith and Colton (1972a, 1972b). The first evaluation of this system using conditions applicable to pharmaceutical systems was performed by Khoury et al. (1988). An assessment of the hydrodynamic boundary layer for such a system led to the following expression:

$$d_h \propto (v/\omega)^{1/2} [f(r)] \quad \text{Equation 1.17}$$

Applying the relationship between the diffusion and the hydrodynamic boundary layer discussed by Levich (Equation 1.7) leads to an expression for the diffusion boundary layer:

$$\delta \propto (D/v)^{1/3} (v/\omega)^{1/2} [f(r)] \quad \text{Equation 1.18}$$

Applying this equation for the diffusion boundary layer to Equation 1.9 and fitting of the model to experimentally calculated dissolution rates (to determine the proportionality constant) yielded the following expression for the dissolution rate (R) from a stationary disc-rotating fluid set-up (Khoury et al., 1988).

$$R = 1.33D^{2/3} C_s (v)^{-1/6} (\omega)^{1/2} r^{3/2} \quad \text{Equation 1.19}$$

1.1.4 Dissolution test

Dissolution testing currently plays a pivotal role in designing, developing and testing new formulations/drug delivery systems (Banaker, 1992). Dissolution tests are required to provide evidence that the drug is actually released from the dosage form at an appropriate rate to ensure an adequate time for absorption of the drug into the body. Thus, in effect, the method is considered to simulate the release/dissolution environment, which the tablet/delivery system is likely to encounter on administration. The dissolution test is therefore a critical test in the design, evaluation, control, and therapeutic efficacy of solid dosage forms.

A meaningful and reliable dissolution test should meet at least six basic performance criteria (Dakkuri and Shah, 1982):

1. Reproducibility of the flow pattern. This may be achieved by rigidly specifying the dimensions and geometry of the apparatus so that inter-laboratory and intra-

laboratory variation are kept to a minimum. Also, the dosage form should be placed in the same position with respect to the fluid flow.

2. Sensitivity to detect the effect of small differences in formulation and manufacturing variables on the release of active ingredient from the dosage form.
3. Correlation of the observed differences of in-vitro to those of in-vivo bioavailability must be accomplished; i.e. the method must simulate the in-vivo environment to such a degree that the attainment of an in-vitro/in-vivo correlation is possible.
4. Flexibility of the test that will make it applicable to a wide range of drug products.
5. Simplicity. The test apparatus must be relatively easy to operate on a routine basis and must not require an extended amount of time to set up for operation.
6. Automation. The dissolution test consists of more than one procedure, any one of which may be manual or automatic. An automated method possesses many advantages including accuracy, time saving, versatility and ease of validation.

Although numerous methods have been reported in the literature (Dakkuri and Shah, 1982), few if any were designed with the objective of meeting all the above considerations. The great majority of dissolution devices that have been developed belong to the stirred-vessel type.

1.1.4.1 Paddle dissolution test apparatus

The dissolution test was introduced as a USP method in the 1970's (Cohen et al., 1990) with the introduction of a number of monographs, in particular the oral tablet and capsule products. The compendial dissolution test is provided to determine compliance with dissolution requirements for a dosage form. The minimum amount of drug substance (expressed as a percentage of the labelled content) that must be in solution at 37°C and at a given time interval (or intervals) under a specified set of conditions is specified in the appropriate monograph. The assay procedure is also specified.

The paddle dissolution test has been a success as a quality control tool, with some inference that it can also be used as a test to reflect the bioavailability of a drug product in humans. The USP dissolution test method 2 (paddle apparatus) has

become the workhorse instrument in the modern dissolution laboratory (Beckett et al., 1996). The basic components of the USP paddle dissolution apparatus are shown in Figure 1.3 (USP 24, 2000), the geometry and set-up of the system being identical to those of the British Pharmacopoeia (BP, 2002) and the European Pharmacopoeia (EP, 2002)

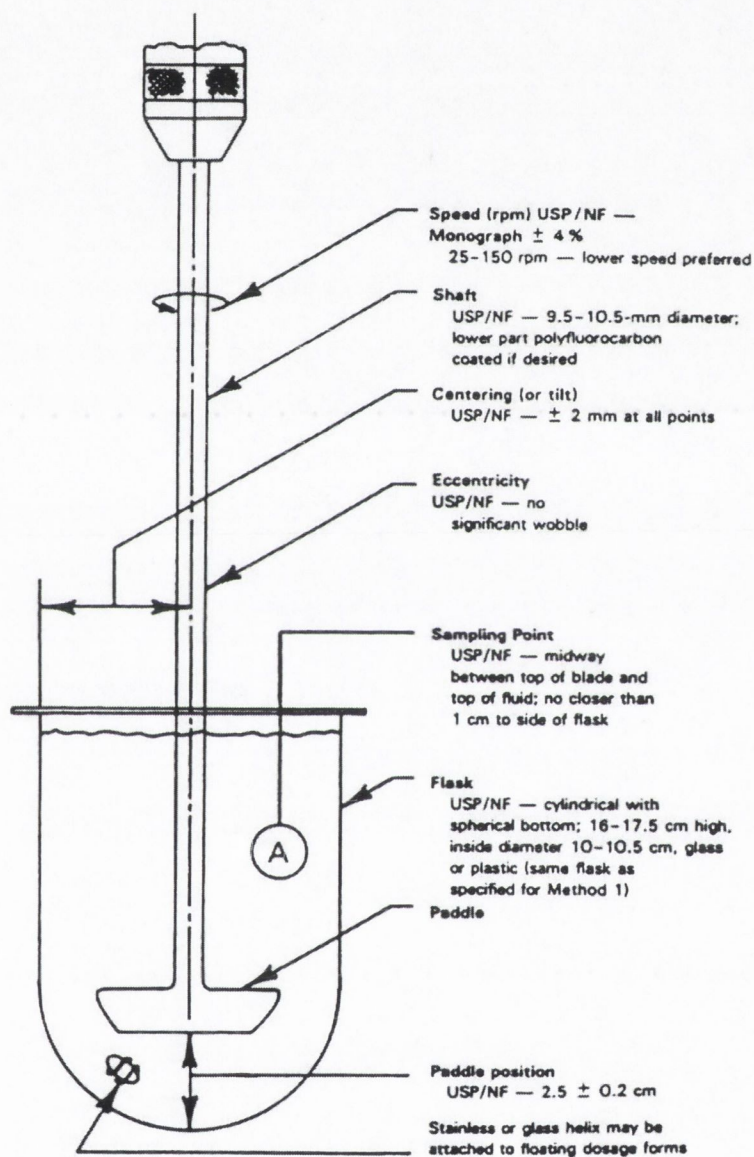


Figure 1.3 Schematic illustration of the USP dissolution test method 2 (reproduced from Banaker, 1992).

1.1.4.2 Variability in drug dissolution testing

Considering the popularity and usefulness of drug dissolution testing, regulatory agencies and pharmaceutical manufacturers are suggesting an enhanced role for such

testing for expeditious approval and economical availability of drug products on the market (Qureshi and McGilveray, 1999). That is, drug dissolution, though extensive (e.g. use of different media, drug release profiles rather than single point testing), could be sufficient in many cases without *in vivo* testing to establish safety and efficacy of a drug product following minor formulation and manufacturing changes. This has been the rationale for the development of SUPAC guidelines (Scale Up and Post Approval Changes, 1995).

The USP apparatus 2 is expected to provide rugged and reproducible results, on which decisions about product quality, bioavailability, bioequivalence etc. are based. So far, the success of dissolution testing has been mostly based on the experience gained where the major portion of drug content is released from a product in a relatively short time i.e. < 45 minutes (Qureshi and McGilveray, 1999). However there is no requirement for comparing within run/ between run variability. Meanwhile, success in relating *in vitro* (dissolution) results to *in vivo* (bioavailability) has remained elusive, but desirable and needed (Qureshi and Shabnam, 2001). Furthermore, there have been reports in the literature describing high variability in results, unpredictability and randomness of observed results for dissolution apparatus calibrator tablets (Cox et al., 1982; Achanta et al., 1995; Qureshi and McGilveray, 1999; Qureshi and Shabnam, 2001). In practice, the apparatus tends to be extremely sensitive to outside and inside variables, with large changes in dissolution profiles resulting from small changes in factors such as paddle rotation speed, vibration, de-aeration and insertion of sampling probes (Beckett et al., 1996).

In one international collaborative study, based on the test conducted using calibrator tablets and a commercially available glibenclamide tablet, it was confirmed that drug dissolution testing is a highly variable technique, such that 15 out of 28 participating laboratories were not able to produce results within acceptable ranges for USP calibrator tablets (Qureshi and McGilveray, 1999). Various explanations have been suggested concerning the causes of variability, ranging from quality of calibrator tablets, instrument problems to lack of operators' training (Achanta et al., 1995).

It is likely however that the round bottom of a dissolution vessel in combination with stirring devices (e.g. paddle) results in a varied flow dynamics within the vessel,

which appears to be the cause of the observed high variability in the testing (Cox et al., 1982). Considering a variable mixing/ stirring and flow pattern in a drug dissolution vessel as a likely source of high variability in results, Qureshi and Shabnam (2001) carried out experiments using the USP paddle apparatus by placing a metal strip in the dissolution vessel. The presence of the strip prevented the typical cone formation often seen with particulate systems during dissolution (Beckett et al., 1996). Significantly higher dissolution results were obtained from the studies containing the strip than those without the strip, suggesting that in many cases, products will provide lower than anticipated results, which may not be reflective of the product drug release characteristics. Test to test variability, within or between laboratories, can also be high depending on the settling position of the product once dropped in the vessel and/ or due to slight aberration in the walls of the vessel by altering the extent of spread of disintegrated material at the bottom of the vessel (Qureshi and Shabnam, 2001). It is suggested that some modification of the current dissolution system is needed to address this variability, if drug dissolution testing is to be used as a reliable technique. For improved test equipment, one would require mild turbulence, help in spreading the disintegrated material and an efficient solvent replenishing mechanism (Qureshi and Shabnam, 2001).

1.1.4.3 Fluid flow in the USP paddle dissolution apparatus

As part of the development of a standardised dissolution apparatus, Withey and Bowker (1972) carried out flow visualisation techniques to compare flow patterns in six different devices. Of the devices studied, the USP paddle apparatus was the most promising with regard to reproducibility of dissolution rate and uniformity of mixing. Little attention was paid, at the time, to properly defining the hydrodynamics in these systems, the main purpose being good reproducibility (Grijseels, 1981). The lack of experimental data concerning the complex flow fields produced by the USP paddle dissolution apparatus, coupled with the effect of possible variable hydrodynamics in the USP paddle dissolution apparatus on the reproducibility and sensitivity of the dissolution data, has prompted research into the fluid dynamic behaviour within the vessel of the apparatus. Bocanegra et al. (1990) carried out a detailed analysis of the flow behaviour in this apparatus using a one-component He-Ne fiber optics laser Doppler anemometer with conditional computer sampling acquisition. Three

dimensional fluid velocity measurements were carried out for a number of regions inside the vessel at 50 and 60 rpm. A representation of the flow field as determined from these studies is shown in Figure 1.4.

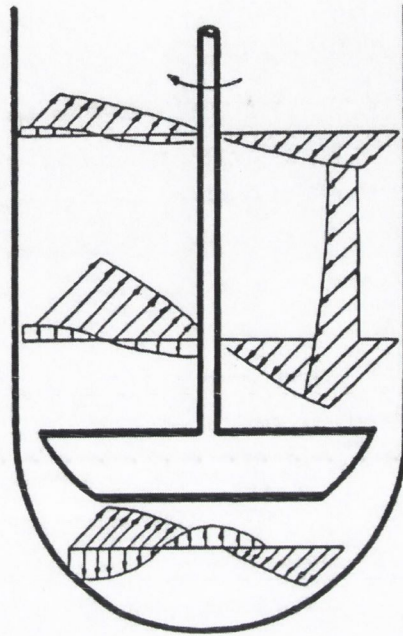


Figure 1.4 Postulated fluid flow field from a laser flow visualisation for the USP paddle dissolution apparatus (reproduced from Bocanegra et al., 1990).

Fluid flow is generated by the momentum transfer from the paddle via normal stresses. In the region above the paddle, a major component of flow is tangential, which leads to circular fluid motion (shown as vectors directed outward from the paper). In the axial direction a rotational secondary flow was observed. This component of the flow results in an oscillation in the axial component of the flow, which had not been previously reported and was suggested to be of potential importance in the sensitivity and reproducibility of the dissolution data (Figure 1.4).

1.2 FLUID DYNAMICS

1.2.1 History of fluid dynamics

Early scientific investigations into the behaviour of liquids were based on empirical methods and trial and error. The first major scientific insight into fluid behaviour came with the introduction of the perfect gas law by Clapeyron, which was a combination of Charles' Law and Boyle's Law:

$$PV = nRT \quad \text{Equation 1.20}$$

where V is the volume, P is the pressure and T is the temperature of a gas and n is the number of moles. While the perfect gas law describes the physical properties of a gas at rest, it does not describe the effects of incompressible fluids or the behaviour of fluids in motion (Fluid Dynamics).

The descriptive set of equations introduced by Claude-Luis Navier in 1822 and later verified by George Gabriel Stokes (1845) related the local pressures and velocities within a body of moving fluid and consist of the conservation of mass, momentum and energy (Navier-Stokes equations). The derivation of these expressions is beyond the scope of this thesis, however a full set of the equations for fluid flow in cylindrical co-ordinates is included in Appendix 1. Although these equations pre-date the perfect gas law, they remained obscure due to their great mathematical complexity and because the effect of viscosity was not considered. The first useful basis for fluid dynamic analysis came with the introduction of Prandtl's description of the 'boundary layer', which described the thin layer of fluid that passes over an object where frictional forces are significant. At the outer edge of the boundary layer the fluid does not feel frictional effect, but as it approaches the surface of the object, the fluid slows down quickly due to viscosity (no-slip). A diagram showing Prandtl's boundary layer is shown in Figure 1.5.

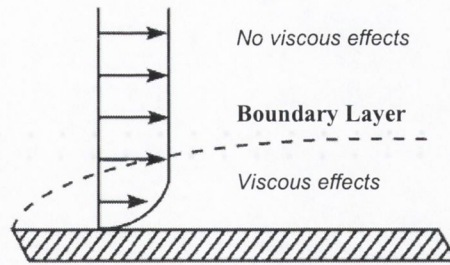


Figure 1.5 Diagram of fluid flow over a flat plate, showing the development of a boundary layer.

This boundary layer theory allowed Navier-Stokes equations to be simplified and solved more easily. The Navier-Stokes equations, the perfect gas law and boundary layer theory are today the basis of advanced fluid dynamic analysis. The equations are second-order nonlinear partial differential equations that have not been analytically solved in general, although analytical and numerical (computer) solutions have been obtained for certain specific situations (Franzini and Finnemore, 1997).

1.2.2 Computational fluid dynamics (CFD)

In order to completely describe fluid motion the following quantities must be known: density, pressure, temperature and velocity in the three dimensional directions. Because there are six unknown quantities, six equations in total are required to be solved in order to determine a solution for three dimensional flow (perfect gas law, conservation of mass and conservation of momentum in three dimensions). The Navier-Stokes equations are difficult to solve, firstly because they cannot be solved independently in a straightforward manner (coupled) and, secondly, the solution of these equations at each point is dependent on the solution at every other point in the flowfield. The steady improvement in the speed of computers and the available memory size since the 1950's has led to the emergence of Computational Fluid Dynamics (CFD). Recent developments in computer power shown in Figure 1.6 and concurrent progress in numerical methods, have promoted the acceptance of CFD as a reliable and generally applicable engineering tool (Bartels et al., 2002).

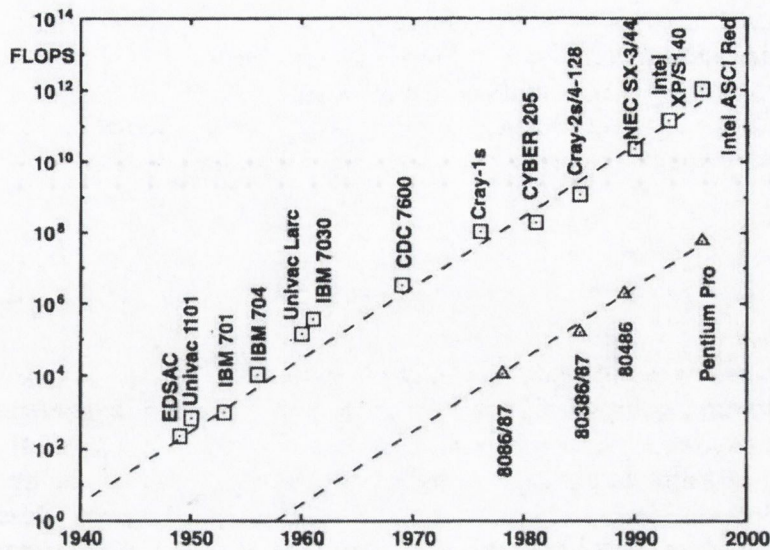


Figure 1.6 Development of the peak performance of supercomputers and PC processors from 1940 to 2000 (reproduced from Bartels et al., 2002).

One of the differences between a theoretical and a computational approach to solving problems is that a theoretical solution is valid at every point in the flowfield. On the other-hand, CFD attempts to solve the equations only at a finite number of specific points. Consequently, a computational solution does not give a continuous and well-behaved mathematical function as a solution. Rather, it provides a numerical answer at specific points where it has been decided to calculate it. In order for a computational solution to give as much detail as a theoretical solution, the equations need to be solved at enough points. The selection of the definition of these discrete points at which solutions are calculated is the science of ‘grid generation’ (also termed ‘mesh generation’).

1.2.2.1 Theory of grid generation

Computational techniques differ from analytical or theoretical solutions in that they only solve equations at specific points rather than for the entire flow field. Choosing these points may become quite difficult - especially for a complex geometry and may require hundreds of thousands or even millions of points. To assist in this first step towards finding computational solutions, the field of grid generation has arisen. Before the specific points can be generated, the size of the area to be computed must be assigned, which is called the ‘computational domain’. For internal flows, such as fluid flow in a vessel, the computational domain itself is defined by the geometry of

the walls of the vessel. Then, one of the many grid generation techniques must be chosen that will best generate the specific computational points. For complex geometries grid generation techniques usually involve the application of differential equations. There are several different techniques that are commonly used to develop computational grids for CFD. The quality of the grid is important and can strongly influence the solution, including whether or not a solution can, in fact, be found using fluid dynamic techniques. In general terms, a dense grid with many points will give a solution of great detail, but will require more computer memory and time to reach a solution. Since this trade-off in computer resources and solution quality is required, it is more efficient to use a dense grid in areas where the solution may change rapidly such as in a boundary layer of fluid motion but to use a coarser grid with fewer computational points in areas where the solution is expected to change more gradually. One method of grid generation, called 'unstructured' grids, involves a triangular layout of the computational points. Meshing of complex convoluted geometries is facilitated using this method, as a triangle is a more versatile shape than a rectangle. Another advantage is that the clustering of grid points in certain areas can be achieved more easily. The disadvantage of the unstructured grid is that it is sometimes not compatible with faster solution methods and so can take longer for a solution to be found. Unstructured grids are also not applicable to problems involving a large degree of 'swirl' or rotational velocity (e.g. impeller in a vessel). A 'structured' grid approach, which arranges the computational points in a roughly rectangular layout, is usually more beneficial in the solution of such complex flows. However, meshing of complex geometries can be arduous using the 'unstructured' grid approach (Gambit Modelling Guide, 1998).

1.2.2.2 Computational solution to the Navier-Stokes equations

Once the grid or 'computational domain' has been selected the partial derivatives of the appropriate equations can be approached by 'finite differences' at each grid point. Using this 'finite difference' approach, the continuous problem domain is 'discretised', so that the dependent variables are considered to exist only at discrete points. Derivatives are approximated by differences, resulting in an algebraic representation of the partial differential equation. Thus a problem involving calculus has been transformed into an algebraic problem. There are a number of techniques

available for solving the Navier-Stokes equations at these specific points. The most common is the 'time-marching' approach where a solution is found at one instant and then calculated again at another instant a short time in the future. In this manner, computational solutions can progress one step at a time. By stepping sequentially through time it is possible to arrive at the final solution more easily than if it was attempted to be calculated directly in one 'run'. Notwithstanding this, it is not normally possible to calculate the solution in one pass because of the complexity of the equations involved. Consequently, the solution is calculated at successive time-steps until the difference between successive calculated values has been found to be smaller than a pre-defined level. At this point the solution is said to have 'converged'. Once convergence has been attained, this means that a 'steady-state' or final solution has been found. Another reason to step through time is that sometimes there is no 'steady-state' solution to a fluid dynamic problem. There may be turbulent swirls or oscillating flow behaviours that are constantly present in the flow.

All differential equations require what are called 'boundary conditions' in order to find their solution. In the case of the Navier-Stokes equations, these conditions must be applied along all the edges of the grid that describes the computational domain. These boundary conditions give information about the fluid (e.g. fluid flow inlet or outlet) and about the individual surfaces in the computational domain (e.g. solid surfaces to prevent the passage of fluid). Without these boundary conditions, physical information about the flow such as pressure, flow direction, no-slip conditions on a hard surface, etc. cannot be incorporated into the solution. Once these boundary conditions have been applied, the solution can move to the next time-step.

Although there are many methods for calculating solutions at each time-step, most of them fall into two categories; 'implicit' and 'explicit' methods. Implicit methods involve solving the equations at the same time for a group or all of the points in the flowfield. This technique requires a large amount of computer memory to store the information for each grid point simultaneously while the solution is being found and also requires more complex programming. The advantage of implicit methods are that they allow a larger time-step to be taken between each solution so that the final solution can be reached in fewer steps. Explicit methods, on the other hand, involve finding the solution to the equations one grid point at a time. These methods are

easier to program, require less memory and are faster in computing the solution at each time-step. However, because each grid point is solved in isolation, some of the interdependence between points is lost. This requires that smaller time-steps be taken in advancing towards the final solution. In summary, the steps in determining a computational solution to the Navier-Stokes equations are (<http://www.cfd-online.com>):

1. Determine the boundaries of the flow field to be calculated.
2. Apply grid generation techniques to identify individual points at which the equations will be solved.
3. Solve the Navier-Stokes equations at that time-step in either an implicit or explicit manner.
4. Apply the boundary conditions on the edges of the grid.
5. Proceed to the next time-step and repeat steps 3 and 4 until the solution converges to a steady-state or until a time-dependant picture of the unsteady behaviour has been recorded.

1.2.2.3 Parallel processing

Parallel processing refers to the concept of speeding-up the execution of a computer program by dividing the program into multiple fragments that can execute simultaneously, each on its own processor. The overall goal of parallel processing is to reduce the total amount of time before achieving a solution. It is becoming increasingly more expensive to produce a single extremely fast processor, therefore it has become more cost effective to use more relatively inexpensive processors in parallel. Parallel processing in CFD involves partitioning of the computational domain into several sub-domains, each partition will then 'reside' on a different compute-node.

Each compute-node will perform the relevant calculations on the individual sub-domain (computation), while the values of such computations for cells at the interfaces between the sub-domains are updated via communication between the relevant processors for these points (communication). Latency is the set-up time required for communication between the processors, while the bandwidth is the rate at which data is transferred. In general, as the number of compute-nodes increases,

turnaround time for the solution will decrease (a program being executed across n processors might be expected to execute n times faster than it would using a single processor). However, parallel efficiency decreases as the ratio of communication to computation increases (Fluent5 User's Guide, 1998). Such behaviour can be described in terms of an efficiency curve as shown in Figure 1.7.

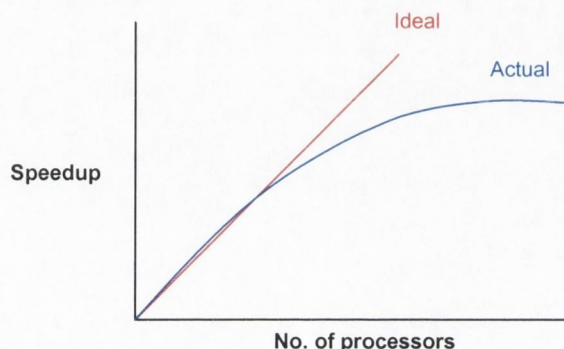


Figure 1.7 Efficiency curve of a parallel processor computing system. Ideally speedup is directly proportional to the number of processors, however eventually, communication overheads begin to dominate.

It is possible to partition the grid using a number of different partition approaches. The major goals of grid partitioning are to create partitions with equal numbers of cells, to minimize the number of partition interfaces (to decrease partition boundary surface area) and to minimize the number of partition neighbours (Fluent5 User's Guide, 1998).

1.2.2.3.1 Grid adaption

A very fine grid is essential for an accurate prediction of the velocity field in stirred tank reactors (Bartels et al., 2002). It is possible to refine a grid based on geometric and numerical solution data. By using solution-adaptive refinement, it is possible to add cells where they are needed in the mesh, thus enabling the features of the flow field to be better resolved. Consequently, the resulting mesh is optimal for the flow solution because the solution is used to determine where more cells are added. In this way, computational resources are not wasted by the inclusion of unnecessary cells.

Important fluid interactions often occur in the regions of boundary zones, such as the development of strong velocity gradients in the boundary layer near a wall.

1.2.2.4 Overview of FLUENT CFD package

Fluent is the general name used for a collection of computational fluid dynamics (CFD) programs sold by Fluent Inc. and is the CFD software, which was used in this work. Fluent is a state-of-the-art computer program for modelling fluid flow and heat transfer in complex geometries (Fluent5 User's Guide, 1998). Fluent provides complete mesh flexibility, solving flow problems with structured or unstructured meshes that can be generated about complex geometries. Supported mesh types include 2D triangular/quadrilateral, 3D tetrahedral/hexahedral/pyramid/wedge, and mixed (hybrid) meshes. It is also possible to refine or coarsen a grid based on the flow solution. The Fluent family contains a series of tools, the two core programs being Gambit and Fluent. The task of approaching a CFD problem is split into two main sections, grid formation and solver execution. Gambit is the preprocessor, which is used to generate the computational domain, for geometry modelling and to develop the initial grid or mesh. This produces a file called a 'mesh file', which is the connector file between Fluent and Gambit. Once the grid has been read into Fluent, all remaining operations are performed within the solver. These include setting boundary conditions, defining fluid properties, executing the solution, refining the grid, and viewing and postprocessing the results. Two types of files are used by the solver in Fluent in order to find a solution, these being a 'case' file and a 'data' file. The case file holds all information regarding the grid setup, boundary conditions, material properties etc., while the data file contains information relating to all gridpoints within the mesh. Figure 1.8 indicates the structure of the programs used from the Fluent suite and how these programs interact with each other.

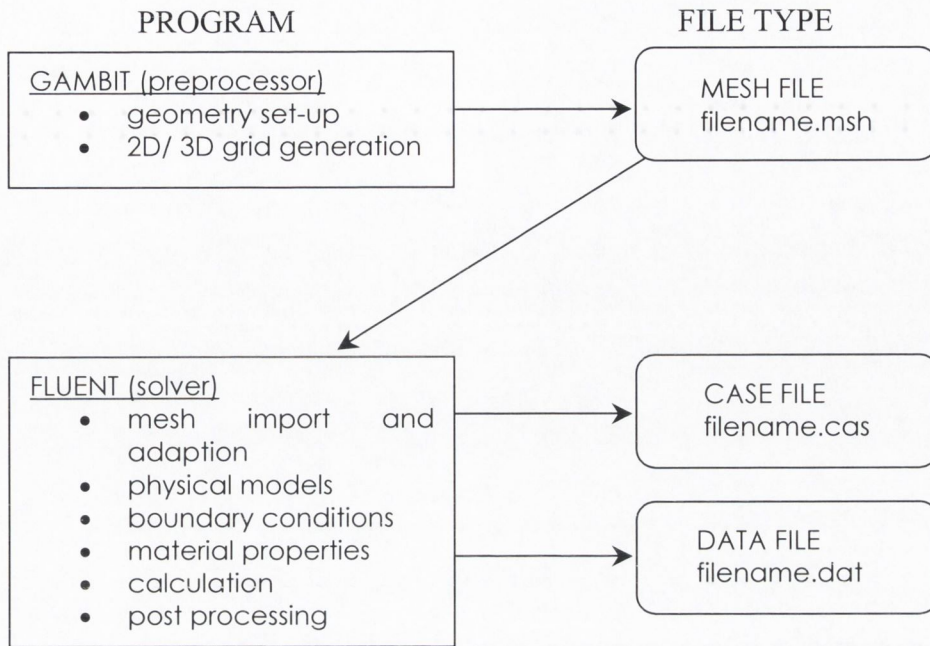


Figure 1.8 Structure of the Fluent system (Fluent5 User's guide, 1998).

In attempting to solve the governing integral equations for the conservation of mass and momentum, it is possible to use a number of different solver formulations in the Fluent program. The two numerical methods available to do so are, a) segregated solver and, b) coupled solver. Both approaches consist of:

- Division of the domain into discrete control volumes using a computational grid.
- Integration of the governing equations on the individual control volumes to construct algebraic equations for the discrete dependent variables such as velocities and pressure.
- Linearisation of the discretised equations and solution of the resultant linear equation system to yield updated values of the dependent variables.

The two numerical methods differ in the approach used to linearise and solve the discretised equations. Using the segregated approach, the governing equations are solved sequentially. Because the governing equations are non-linear (and coupled), several iterations of the solution loop must be performed before a converged solution is obtained. Each iteration consists of the steps summarised in Figure 1.9, the steps being continued until the convergence criteria are met.

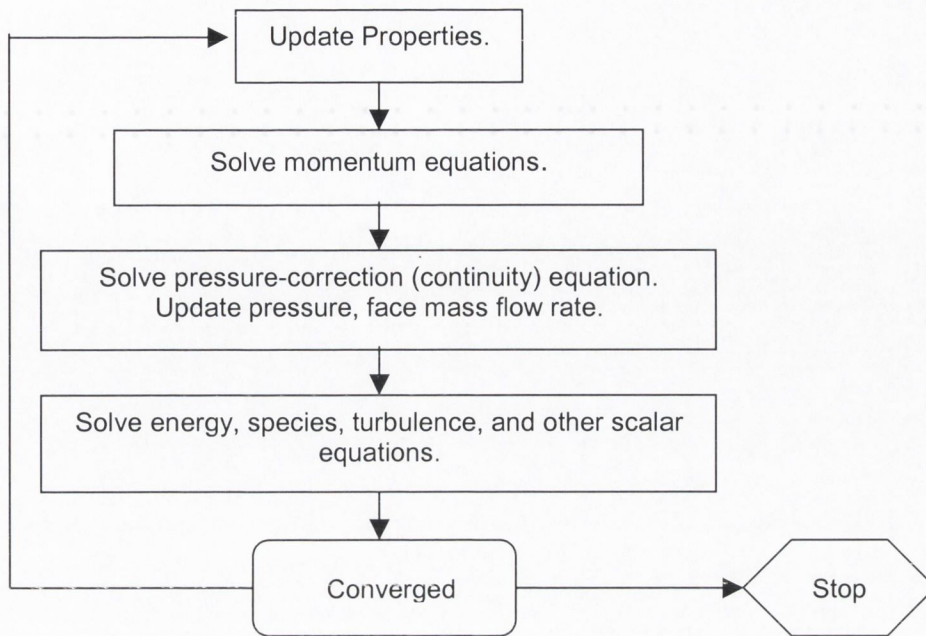


Figure 1.9 Overview of the segregated solution method (Fluent5 User's Guide, 1998).

In both the segregated and coupled solution methods the discrete, non-linear governing equations are linearised to produce a system of equations for the dependent variables in every computational cell. The resultant linear system is then solved to yield an updated flow-field solution. The manner in which the governing equations are linearised may take an 'implicit' or 'explicit' form with respect to the dependent variable of interest.

In the segregated solution method, each discrete governing equation is linearised implicitly with respect to that equation's dependent variable. This will result in a system of linear equations with one equation for each cell in the domain. In summary, the segregated approach solves for a single variable field (e.g., pressure) by considering all cells at the same time. It then solves for the next variable field by again considering all cells at the same time, and so on.

Fluent uses a control-volume-based technique to convert the governing equations to algebraic equations that can be solved numerically. This control volume technique consists of integrating the governing equations about each control volume, yielding discrete equations that conserve each quantity on a control-volume basis. Again, a

number of techniques are available for discretisation in the solver, including first order upwind, power law scheme and second-order upwind. One important factor involved in equation discretisation is the 'under relaxation factor', which reduces the change of the scalar quantity of interest produced during each iteration. This is a user-defined solver input, which can have a significant effect on the resulting solution. Another user defined solver input is the type of 'pressure interpolation scheme'. In the solution of the relevant momentum equations, it is necessary to know pressure field and face mass fluxes at each cell. However, the pressure field and face mass fluxes are not known *a priori* and must be obtained as part of the solution. Fluent uses a co-located scheme, whereby pressure and velocity are both stored at cell centres. However, the momentum equation requires the value of the pressure at the face between cells. Therefore, an interpolation scheme is required to compute the face values of pressure from the cell values. Apart from the standard default scheme, Fluent offers a number of other interpolation schemes, including, the linear scheme, the second-order scheme, the body-force-weighted scheme and the 'Presto' scheme (Fluent5 User's Guide, 1998).

Fluent also provides three pressure-velocity coupling algorithms to derive an equation for pressure from the discrete continuity equation, these being 'Simple', 'Simple C' and 'Piso' (Fluent5 User's Guide, 1998).

1.2.2.4.1 Rotating reference frame

In many situations, fluid flow is through a stationary system with flow inlets and outlets (e.g. flow through a pipe). In such situations, the reference frame which defines the position of grid points within the computational domain is an inertial reference frame (i.e. the co-ordinate system is static, e.g. the static dimensions of the pipe). However in the case of a paddle rotating in a vessel it is necessary to model a reference frame that is accelerating (i.e. circular motion). A flow of this type can only be modelled in a co-ordinate system that is moving with the rotating equipment and thus experiencing a constant acceleration in the radial direction, generally referred to as a 'rotating reference frame'. In this situation, the acceleration of the co-ordinate system is included in the equations of motion describing the flow.

The concept of a rotating reference frame in a mixing vessel is shown in Figure 1.10 (Fluent5 Users Guide, 1998), which illustrates the transformation from a stationary to a moving reference frame.

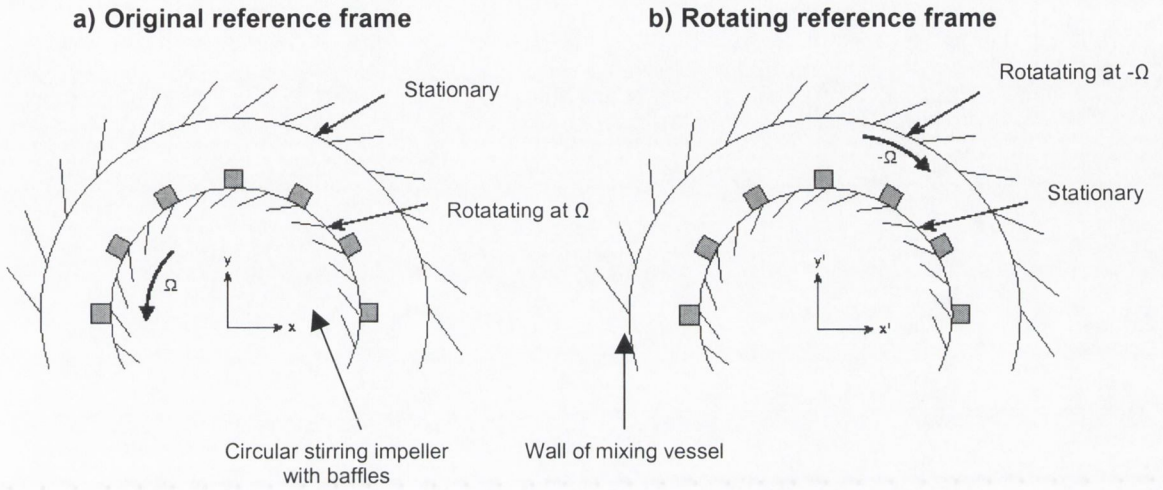


Figure 1.10 Diagram showing the concept of transformation of a coordinate to a 'rotating reference frame' in a mixing vessel with baffles (Fluent 5 Users Guide, 1998).

Steady state conditions are assumed at the interface between the two reference frames, which means that there is no friction between the two regions and that the velocities at the interface must be the same in absolute terms for each reference frame.

1.3 INERT NON SWELLABLE MATRIX SYSTEMS

1.3.1 Theoretical analysis of rate of release of solid drugs dispersed in solid matrices

1.3.1.1 Higuchi models

Two mechanisms of release of drug from solid matrices were theoretically analysed by Higuchi; dissolution of drugs distributed in a homogeneous matrix (1961) and later for drugs distributed in a granular insoluble matrix with connecting capillaries (1963). The two methods of drug release are illustrated schematically in Figure 1.11.

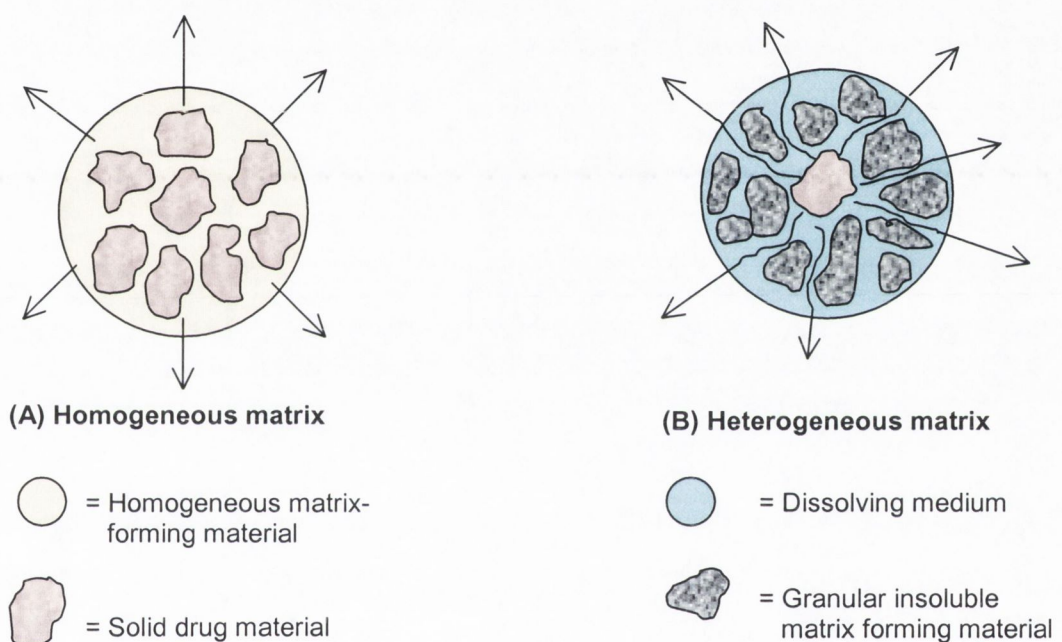


Figure 1.11 Two methods of drug release from matrix pellets. (A) Homogeneous matrix, where extraction of the drug occurs via a simple diffusional process through and from an enveloping, homogeneous matrix. The drug is presumed to go from the crystal surfaces into the uniform matrix and out into the bathing solvent, which in turn acts as a perfect sink. (B) Granular matrix with connecting capillaries, where leaching of the drug by the bathing fluid occurs, which is able to enter the drug-matrix phase through pores, cracks, and inter-granular spaces. The drug is presumed to dissolve slowly into the permeating fluid phase and to diffuse from the system along the capillary channels filled with the extracting solvent (Higuchi, 1963).

1.3.1.1.1 Release from a planar system having a homogeneous matrix

The Higuchi 'square root of time' equation was initially developed for release from an ointment base containing finely dispersed drugs, but is equally applicable for release from a sustained action homogeneous matrix (Higuchi, 1961). Using a derivation of

Fick's law, the amount of total drug released from such a system into a bathing medium acting essentially as a perfect sink would be determined by the relationship:

$$Q = \sqrt{Dt(2A' - C_s)C_s} \quad \text{Equation 1.21}$$

where Q = the amount of drug released after time t per unit exposed area, D = the diffusivity of the drug in the homogeneous matrix media, A' = the total amount of drug present in the matrix per unit volume, C_s = the solubility of the drug in the matrix substance.

1.3.1.1.2 Release from a planar system having a granular matrix

For the leaching type release mechanism occurring through diffusion movement utilizing inter-granular openings, the above relation must be modified for the effective volume where diffusion can occur and the effective diffusional path (Higuchi, 1963). Therefore, the derivation is essentially the same as that of Equation 1.21, except that the cross sectional area of the diffusional path must be reduced by the porosity factor, ϵ , and the apparent solubility of the drug in the total system per unit volume must also be decreased by the same factor. The tortuosity factor, τ , must also be introduced to correct for the lengthened diffusional path caused by the necessary lateral excursions of the drug through the porous network. Therefore, release from this system can be represented by:

$$Q = \sqrt{\frac{D\epsilon}{\tau}(2A' - \epsilon C_s)C_s t} \quad \text{Equation 1.22}$$

Since the porosity factor in Equation 1.22 refers to the porosity of the leached portion of the pellet, it differs from the initial porosity of the initially formed matrix, ϵ_0 . The difference would correspond directly to the volume of free space previously occupied by the extracted component. Thus

$$\epsilon = \epsilon_0 + A'(1/\rho) \quad \text{Equation 1.23}$$

where ρ is the true (skeletal density) of the drug substance (for systems where the drug is the only extractable component). Possible deviations from the model cited by Higuchi (1963) included; possible alterations of the matrix in the presence of moisture, possible weakening and/ or erosion of the matrix structure in pellets containing a relatively high proportion of drug and the possible influence of solvent

flow induced within pellets by external agitation, particularly with pellets of relatively high porosity. Desai et al. (1965, 1966a, 1966b) and Singh et al. (1967) have made extensive experimental and further theoretical studies of Equation 1.22. In their approach several different plastics and several drugs were involved. They independently determined the appropriate D (diffusion cell experiments), the solubility C_s , the appropriate ϵ (two ways), and τ by an independent experiment with the same matrix. Under the expected conditions (good penetration of the pores when $\epsilon C_s \ll 2A$), Equation 1.22 agreed quantitatively with the experimental data over a wide range of variables.

These investigators also showed (Desai et al., 1966a) that in some instances (polyethylene matrices without surfactant) wetting may be poor and therefore the effective values of τ may in the tens of thousands. These studies showed that, in these cases, the diffusion-controlled model probably fails, and the release rate is determined by the channel penetration rate of the solvent. In other instances (polyvinyl chloride matrices in water) wetting was efficient, but air removal from the matrix significantly altered the drug release pattern (Desai et al. 1966b).

Fessi et al. (1978) reported limitations of the Higuchi square root of time equation for insoluble matrices with a high content of soluble drug. An initial lag phase was evident, which was defined as being the result of a dissolution-rate limiting step. Drug release was then linear with respect to square root of time up to a critical time point, which was determined as being the time at which the dissolution medium had completely penetrated the matrix system. Beyond this time the loading of drug available for release no longer exceeded the maximum solubility (C_s) and so the release rate fell below that predicted by the Higuchi equation. A second linear phase of drug release versus square root of time was seen, suggesting that simple diffusion was operative.

1.3.1.2 Cobby model

Using similar principles as Higuchi, Cobby et al. (1974) presented equations describing the release of drugs from matrix tablets having either a spherical, a cylindrical, or a bi-convex shape.

In each case, the three dimensional equation had the cubic form:

$$f_t = G_1 K_r t^{1/2} - G_2 (K_r t^{1/2})^2 + G_3 (K_r t^{1/2})^3 \quad \text{Equation 1.24}$$

Where f_t = the fraction of drug released to time t , K_r = release-rate constant and G_1 to G_3 = shape factors. The fundamental parameters of the release-rate constant are described by:

$$K_r = \frac{1}{Ar_o} \sqrt{DC_s(2A - \varepsilon C_s) \frac{\varepsilon}{\tau}} \quad \text{Equation 1.25}$$

where r_o = initial tablet radius. The shape factors are dependant on measurable geometric parameters of the matrix tablet and are calculated accordingly for spherical, cylindrical or biconvex shaped tablets. However, the release constant K_r is independent of tablet shape, as demonstrated experimentally. The equation for a cylindrical tablet takes the following form:

$$f_t = (q + 2)K_r t' - (2q + 1)(K_r t')^2 + q(K_r t')^3 \quad \text{Equation 1.26}$$

where $t = t^{1/2} - t_o^{1/2}$ and t_o = lag time before release is first detected and q = initial tablet diameter/tablet height. Despite its simplicity, Equation 1.26 was shown to be applicable to many shapes of cylindrical tablets (Cobby, 1978).

1.3.1.3 Peppas equation

To simplify somewhat the analysis of controlled release data from polymeric devices of varying geometry, Peppas proposed a new empirical, exponential expression which relates the fractional release of drug, M_t/M_∞ to the release time, t (Peppas, 1985).

1.3.1.3.1 Semi empirical equation for drug release from thin polymer slabs

The short time Fickian diffusional release from a thin drug polymer film maintained at a constant uniform drug concentration and releasing into a perfect sink can be approximated by:

$$\frac{M_t}{M_\infty} = 4 \left[\frac{Dt}{\pi l'^2} \right]^{1/2} \quad \text{Equation 1.27}$$

where, l' , is the thickness of the slab.

Therefore, Fickian diffusional release from a thin film is characterised by an initial $t^{1/2}$ time dependence of the drug released, the 'short time' approximation being valid for the first 60% of the total released drug i.e. $M_t/M_\infty \leq 0.60$ (Ritger and Peppas, 1987). Therefore, the fractional release at any time can be characterised by a constant multiplied by the square root of time. A second limiting case is one where the drug release is independent of time, i.e., the kinetics is of zero-order. Such a situation is described by a general equation of the form.

$$\frac{M_t}{M_\infty} = k't \quad \text{Equation 1.28}$$

As many situations of drug release processes fall between these limiting cases, i.e. they can be represented by coupling of Fickian and a non-Fickian mechanism. Therefore a generalised expression accounting for the two previous cases can be written as:

$$\frac{M_t}{M_\infty} = kt^n \quad \text{Equation 1.29}$$

where k is a constant incorporating characteristics of the macromolecular network system and the drug, and n is the diffusional exponent, which is indicative of the transport mechanism (again valid for the first 60% of the fractional release). Fickian diffusion is defined by n equal to 0.50 and non-Fickian by n greater than 0.50.

1.3.1.3.2 Dependence of the diffusional exponent on geometry

The application of the empirical Equation 1.29 to the first 60% of the release process in either cylindrical or spherical systems cannot be correctly interpreted with reference to the diffusional limits of n as were defined from planar geometry. The solution employed by Ritger and Peppas (1987) to apply Equation 1.29 to non-planar geometries was to define new diffusional limits of n for each geometry based on the first 60% of the fractional release. Thus, for a cylinder, the diffusional exponent, n , for a Fickian drug release mechanism was found to be 0.43. Anomalous (non-Fickian) transport from a cylinder corresponded to a diffusional exponent between 0.45 and 1.00. Similarly, for a sphere the diffusional exponent, n , for a Fickian drug release mechanism was found to be 0.43, while anomalous (non-Fickian) transport from a sphere corresponded to a diffusional exponent between 0.43 and 1.00 (Ritger and Peppas, 1987).

1.3.1.4 Ford model

Ford et al. (1991) proposed an extended model of Equation 1.29 which corrects for a lag period. They attributed a lag period as being equivalent to the time required to hydrate the system and allow penetration of the dissolution medium. Fitting data to this adjusted model (Equation 1.30) allows the calculation of a lag time, where appropriate:

$$Q = k(t - t_0)^n \quad \text{Equation 1.30}$$

where Q is the amount of drug released per unit exposed surface area (g/cm^2), k is the release rate constant ($\text{g}/\text{cm}^2/\text{min}^n$), t is the time, t_0 the lag time and n is the diffusional exponent for drug release.

1.3.2 Percolation theory

1.3.2.1 Percolation thresholds

The percolation theory is a powerful tool that is applicable to a wide number of scientific disciplines. It was introduced in the pharmaceutical field by Leuenberger et al. (1987) to characterise solid dosage forms. This theory gives a better explanation of the mechanism of the formation of a tablet and biopharmaceutical properties of compacts (Caraballo et al., 1993). Using the concepts of percolation theory, it has been found that a tablet can be considered as a site/bond percolation phenomenon (Leuenberger et al., 1992; Leuenberger and Leu, 1992).

Bond and site percolation can be defined as follows: a pair of two particles may be described as a cluster of size two, because two neighbouring sites are occupied (site percolation). On the other hand, the same pair of particles can be described as a cluster of size one, because there is only one bond between them (bond percolation). Thus for each type of lattice there is a site and a bond percolation threshold (Stauffer and Aharony, 1992).

The concept of a cluster can be defined as a group of neighbouring sites occupied by the same component. The concentration at which there is the maximum probability that a cluster just starts to percolate a tablet is termed the percolation threshold.

In the case of binary mixtures of two different materials, site percolation is important. According to percolation theory, a binary mixture exhibits in three dimensions, two percolation thresholds (Leuenberger et al., 1992). For low concentrations of component A in a mixed compact of A and B, this component will form only isolated clusters in the compact and its concentration is said to be below the lower percolation threshold, p_{c1} . As the concentration of A in the system is increased, as soon as the particles form a connective network, i.e. a network of powder particles which reaches all sides of the compact, the lower percolation threshold is reached and component A is said to percolate the compact. The same situation will arise for component B as its concentration is changed within the mix. Thus a lower percolation threshold is defined, p_{c1} , where one of the components (A) just begins to percolate and a second, upper percolation threshold, p_{c2} , may be defined where the second component (B) ceases to have an infinite cluster. Between the two thresholds, the two components form two interpenetrating percolating networks and a bicoherent system is said to exist (Leuenberger et al., 1990). Below the lower and above the upper threshold, the clusters of A and B respectively are finite and isolated. Thus, in site percolation of a binary powder mixture, p_c corresponds to a critical concentration ratio of the two components.

At a percolation threshold some property of the system may change abruptly or may suddenly become evident. Such an effect starts to occur close to p_c and is usually called a critical phenomenon., e.g. compressibility/compactibility of a powder system, dissolution rate of active from a binary mixture etc. (Stauffer and Aharony, 1992, Leuenberger et al., 1987).

1.3.2.2 Percolation theory and dissolution kinetics

Harstedt and Wright (1990) applied percolation theory to the diffusion of water-soluble solutes in water-soaked porous media by following the release of benzoic acid from poly(vinyl stearate) matrices. If a porous material is subdivided into many small spaces (or sites) and one labels the occupant of each subdivision as conducting (water-filled pores within the polymeric matrix) or non conducting (solid particles of the polymer), it is then possible to use percolation theory to describe the important transport and geometrical properties of the material.

The dimensionless form for steady-state diffusion through a porous system is defined as the relative diffusivity, D' , and is shown as follows:

$$D' = \frac{D_{app}}{D_{aq}} \quad \text{Equation 1.31}$$

where D_{app} is the (apparent) steady-state bulk diffusion coefficient of the solute through the matrix, and D_{aq} is the aqueous diffusion coefficient of the drug. Solution of Fick's diffusion equation for the case of drug release from a heterogeneous matrix with modifications in terms of percolation concepts led to the following:

$$Q = \sqrt{D_{app} C_s [2\varepsilon_d^a \rho - (\varepsilon_d^a + \varepsilon_o) C_s] t} \quad \text{Equation 1.32}$$

where t is time, C_s is the saturated solubility of the water-soluble solute (drug), ρ is the solid state density of the drug, ε_o is the inherent porosity of the matrix (porosity before any dissolution) and ε_d^a is the accessible volume fraction of drug (determined from the plateau region of the Higuchi plot). The relative diffusivity of the drug, D' , was determined by fitting the release data to Equation 1.32, D_{aq} being an independently determined constant.

The percolation threshold was then determined using the scaling laws:

$$\frac{D_{app}}{D_{aq}} \propto (\varepsilon - \varepsilon_c)^\mu, \quad \varepsilon > \varepsilon_c \quad \text{Equation 1.33}$$

$$\text{and} \quad \frac{D_{app}}{D_{aq}} = 0, \quad \varepsilon \leq \varepsilon_c \quad \text{Equation 1.34}$$

where ε is the porosity (total porosity), ε_c is the porosity at the percolation threshold and μ is a universal scaling constant (assumed equal to 2 for three dimensional lattice) (Stauffer and Aharony, 1992). The percolation threshold could thus be determined using non-linear multiple regression analysis, by fitting the diffusivity data to the scaling law in Equation 1.33.

Two percolation thresholds were defined by Bonny and Leuenberger (1991) from a matrix system. At the lower percolation threshold, p_{cl} , the drug particles begin to form a connective network within the matrix and the diffusion will be anomalous just

at the threshold. At the upper percolation threshold, p_{c2} , the particles, which should form the matrix, start to get isolated within the drug particles and the tablet would disintegrate. The amount of drug $Q_{(t)}$ released after the time t is proportional to t^k and the exponent k depends on the percolation probability, p . When $p < p_{c1}$; only a few particles connected to the tablet surface can be dissolved and $Q_{(t)}$ reaches a constant value. When $p \approx p_{c1}$; anomalous diffusion occurs with $k' \approx 0.2$ in three dimensions (Stauffer and Aharony, 1992), valid for p within the range $p_{c1} \pm 0.1p_{c1}$ approximately. Close to the lower percolation threshold, the diffusion coefficient obeys the scaling law defined by Equation 1.33. When $p_{c1} < p < p_{c2}$; normal matrix controlled diffusion occurs with $k = 0.5$. When $p_{c2} < p$; zero order kinetics occur with $k = 1$.

Subsequently, Caraballo et al. (1993) applied percolation theory to evaluate the influence of particle size of drug and excipient on the release behaviour of solid matrices. The study was prompted by the description of the existence of zero-order release periods using ethylcellulose matrix tablets (Gurny et al., 1982), the presence of these periods being attributed to the saturation of drug into the water filled pores of the matrix. Under these conditions the dissolution rate becomes slower than the rate of diffusion and determines the release kinetics of the process. Later, Potter et al. (1990) observed that the drug and excipient sizes, as well as the drug loading of tablets exert a great influence on the release behaviour. Furthermore, these factors have a considerable effect on the time of onset and duration of the zero order release period. Caraballo et al. (1993) explained such behaviour in terms of percolation theory, avoiding the classical approach, which relates drug release rates to the tortuosity, i.e. a theoretical parameter, one which cannot be experimentally determined. Thus, a smaller particle size of soluble drug leads to faster dissolution as a result of the easier formation of an infinite cluster of this substance. Similarly, tablets prepared with the insoluble excipient of smaller particle size will contain a more consistent insoluble infinite cluster, which will determine a slow release rate of the soluble drug.

Percolation theory was also applied to explain the time to reach zero order release from matrices of differing particle sizes of soluble drug, by dividing the release process into two stages. For a large particle size drug, solvent access and the

diffusion process are facilitated by pores of high cross sectional area. In this manner, for the first phase, solvent inside the pores is far from the saturation state and will not result in a zero order release phase, but the release rate of drug will be faster than from a smaller particle size drug fraction. In the second phase, zero order kinetics are achieved as saturation conditions in the water-filled pores occurs. However, the time to reach this zero order release phase will be longer for a larger particle size drug fraction and the release rate in this second phase will be lower than a smaller particle size fraction of drug, since the finite clusters are already exhausted of drug. Similarly, applying percolation theory, a decreased drug loading would result in a longer time to establish conditions of saturation in the aqueous filled pores (Caraballo et al., 1993).

1.3.2.3 Effect of formulation factors on percolation thresholds

More recent applications of percolation theory to drug release from matrix compacts has examined the effect of formulation variables on the percolation threshold. As earlier studies on percolation theory were handicapped by the requirement of an underlying regular lattice, it is better to use a volume ratio in place of lattice sites for pharmaceutical systems containing substances with different particle sizes (Caraballo et al., 1996). A linear relationship was observed between the percolation threshold and the mean drug particle size employed (Caraballo et al., 1996). This observation was explained using a correlated percolation model, which considers that the distribution of components in the system is not completely random, as random percolation does not adequately explain the observation. Later, Caraballo et al. (1997) examined the influence of several formulation factors over the release behaviour of carteolol hydrochloride from inert matrix systems. The observed influence of the nature and percentage of the polymer and the nature of the filler substance were explained in terms of percolation theory. A later study revealed that the particle size of the excipient has an opposite effect to the drug size on the drug percolation threshold (Millán et al., 1998). Nevertheless, the influence of drug and excipient sizes on the drug percolation threshold are of the same magnitude. More recently, no significant differences were found on the drug percolation thresholds for two excipients having very different mechanical behaviour (Soriano et al., 1998). Therefore, it is possible that the percolation threshold of a drug may be valid for any

(or at least a large number) of excipients, although it must be taken into account that an important fragmentation can occur when very brittle substances are employed.

1.3.2.4 Calculation of percolation thresholds in inert matrices

The approach proposed by Bonny and Leuenberger (1991) in determination of the upper and lower percolation thresholds, p_{c1} and p_{c2} , involves fitting the dissolution data via simple linear regression to Equation 1.35 to clarify for which loadings the square root of time law is fulfilled.

$$Q_{(t)} = a + b\sqrt{t} \quad \text{Equation 1.35}$$

where $Q_{(t)}$ is the cumulative amount of drug release per unit area, t is time and a and b are constants of a simple linear regression analysis of a plot of $Q_{(t)}$ versus $t^{1/2}$.

To determine the diffusion mechanism, the data are also evaluated according to Equation 1.36 by a non-linear least square fit.

$$Q_{(t)} = a^1 + b^1 \cdot t^n \quad \text{Equation 1.36}$$

and a^1 and b^1 are constants of a non-linear least squares fit of a plot of $Q_{(t)}$ versus t .

1.3.2.4.1 Upper percolation threshold

The upper percolation threshold p_{c2} can be calculated by a change in the squared correlation coefficients of the $t^{1/2}$ evaluation (Equation 1.35) for various levels of drug and polymer (Bonny and Leuenberger, 1991). After the upper percolation threshold, matrix particles are not able to form a continuous network throughout the matrix, resulting in isolated pockets of matrix particles and ultimately in erosion of the matrix during dissolution. The resulting change in the length of the diffusional pathway results in a change in the kinetics of drug release. This effect will coincide with an increase in the parameter, n , following a non-linear least squares regression fit to Equation 1.36.

1.3.2.4.2 Lower percolation threshold

Evaluation of the lower percolation threshold p_{cl} involves calculation of the tablet property β , as described by (Bonny and Leuenberger, 1991):

$$\beta = \frac{b}{\sqrt{2.A' - \epsilon.C_s}} \quad \text{Equation 1.37}$$

where b is determined from the appropriate fit to Equation 1.35 or to Equation 1.36 as previously described, A' is the concentration of the dispersed drug in the compact, and C_s is the saturated solubility of the drug in the permeating fluid and ϵ is the total porosity of the matrix. The porosity factor, ϵ , represents the volume fraction of soluble drug in the system, plus any natural porosity present initially in the compact following compaction. Therefore, calculation of the porosity for each system requires knowledge of the true (skeletal) density of the soluble drug and the insoluble matrix-forming polymer, together with the dimensions of the compacted matrix.

Percolation theory predicts that the tablet property, β , is determined by a linear relationship of ϵ :

$$\beta = c(\epsilon - \epsilon_c) = -c\epsilon_c + c\epsilon \quad \text{Equation 1.38}$$

Where c is a constant and ϵ_c is the critical porosity ($= p_{cl}$). Thus, ϵ_c can be calculated using non-linear or even a linear regression analysis of a plot of β vs. ϵ (Bonny and Leuenberger, 1991).

1.3.3 Ethylcellulose

The matrix-forming polymer used in the current work was ethylcellulose, the properties of which are described in the following section.

1.3.3.1 Properties

The most widely used polymers in the pharmaceutical industry are the cellulose derivatives (Rekhi and Jambhekar, 1995). All are derived from, and hence possess the polymeric backbone of cellulose, which contains a basic repeating structure of β -anhydroglucose units, each having three replaceable hydroxyl groups.

The ethylcellulose derivative is a hydrophobic, inert polymer. The molecular structure of ethylcellulose is shown Figure 1.12.

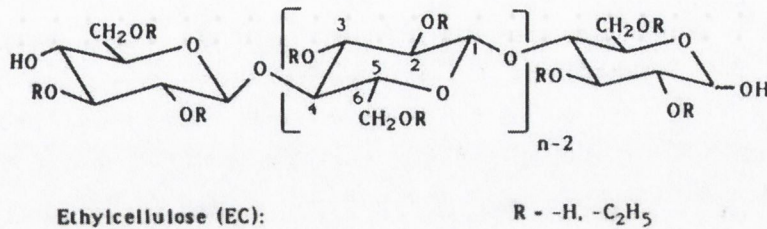


Figure 1.12 Molecular structure of ethylcellulose (reproduced from Kumar and Banker, 1993).

Ethylcellulose is the most stable of the cellulose derivatives. It takes up very little water from moist air or during immersion, and this evaporates readily leaving ethylcellulose unchanged. Light, visible or ultraviolet, has no discolouring action on ethylcellulose, and application of heat up to its softening point (140°C) has little effect on ethylcellulose (Rekhi and Jambhekar, 1995).

1.3.3.2 Application in pharmaceutical formulations

The properties of ethylcellulose, such as lack of toxicity (Pollock and Sheskey, 1997), stability during storage (Rekhi and Jambhekar, 1995) and good compressibility (Upadrashta et al. 1993) make it suitable for sustained release matrices. Ethylcellulose products are essentially tasteless, odourless, colourless, non-caloric, and very inert physiologically (Pollock and Sheskey, 1997). Ethylcellulose is widely used to control the dissolution rate of drugs from sustained-release products in, for example, film coated tablets (Porter, 1989; Narisawa et al., 1994), masking the taste of drugs, granulation, binders (Dow Chemical Brochure), and in microencapsulated dosage forms (Deasy et al., 1980). Its solubility in a wide variety of solvents facilitates its use when solution application is desirable (Rekhi and Jambhekar, 1995). In recent years, ethylcellulose has been evaluated as a matrix forming polymer in solid inert non-swelling non-erodible matrices (Dabbagh et al., 1996; Pollock and Sheskey, 2001).

1.3.3.3 Factors affecting drug release from ethylcellulose matrices

1.3.3.3.1 Polymer fraction

As the polymer fraction increases in insoluble matrix systems, the release rate of drug declines (Dabbagh et al., 1996). This observation has been attributed to a decrease in porosity and increase in tortuosity of the matrix systems containing increasing amounts of polymer.

1.3.3.3.2 Viscosity grade

Owing to its widespread use in film coating, ethylcellulose is available in a range of viscosity grades. As viscosity control is achieved by controlling the chain length, i.e. the degree of polymerisation or the number of anhydroglucose units during the production process, the apparent viscosity (η_{app}) can be regarded as an indirect measure of the molecular weight of the polymer. The relationship between the molecular weight (*M.W.*) and the apparent viscosity (η_{app} , measured in mPas) can be expressed in the form:

$$M.W. = k(\eta_{app})^n \quad \text{Equation 1.39}$$

where k and n are constants for each polymer determined by regression analysis and which depend on the method used to measure the molecular weight of the polymer. The ethylcellulose viscosity grade can have a significant effect on the mechanical properties of films when used in film coating applications. At low molecular weight increases, their strength also increases until some critical molecular weight when there is no further increase (Rekhi and Jambhekar, 1995). Conversely, polymer viscosity grade has been shown to have a minor effect on drug release from solid matrix formulations, because the ethylcellulose is not in a hydrated state during drug dissolution in such systems (Pollock and Sheskey, 1997). Pollock and Sheskey (2001) reported extended release profiles in matrix compacts containing the lower ethylcellulose of low viscosity grades. However, on further examination, it was noticed that these tablets were of differing hardnesses, as discussed later (Section 1.3.3.3.4).

1.3.3.3.3 *Particle size of polymer*

Ethylcellulose particle size has been shown to have a significant effect on drug release rates from solid matrix compacts, with faster dissolution rates seen with higher particle size range polymer fractions (Dabbagh et al., 1996; Potter et al., 1990; Pollock and Sheskey 2001). This observation has been attributed to the increased penetration of water into the matrices, when coarser particle size fractions of polymer were used (Dabbagh et al., 1996). Traditional modelling from such systems would ascribe this behaviour to a decrease in tortuosity exhibited by the matrix formed by the larger size fraction of polymer (Potter et al., 1990). The particle size of the polymer was also seen to affect the tablet crushing strength, with higher values reported with smaller particle size polymer fractions (Pollock and Sheskey, 1997; Pollock and Sheskey 2001).

1.3.3.3.4 *Tablet hardness*

Tablet hardness has been shown to significantly affect drug release rates. However, it has been demonstrated that when ethylcellulose polymers of similar particle size ranges but differing viscosities are used as the matrix formers, the viscosity grades have no effect on release rates if all compacts are compressed to constant hardness (Pollock and Sheskey, 2001).

1.4 LAYERED DRUG DELIVERY SYSTEMS

1.4.1 *Zero order drug delivery*

In the past two to three decades, numerous methodologies, devices and innovations have been utilised and investigated in order to achieve zero-order kinetics over a prolonged time period. The basic mechanism of drug liberation from such systems is governed by swelling/erosion, dissolution/diffusion, osmosis, ion-exchange, polymer coating/membrane barrier, specific geometries and surface modifications (Yang and Fassihi, 1997). Systems that exhibit zero order kinetics release drug at a constant rate that is independent of time or drug loading as described by:

$$M_t = k_o t$$

Equation 1.40

where M_t is the mass of drug released at time t and k_o is the zero order release rate constant. A plot of M_t versus time will be linear, with a slope of k_o . Zero order drug delivery is often desirable in therapeutics as constant delivery can allow constant absorption of drug by the body (assuming that dissolution is the rate-limiting step in the process), thereby attaining a constant level of drug available for therapeutic effect, while avoiding the undesirable side effects associated with high doses of drug.

1.4.2 Controlled release from layered drug delivery systems

The concept of drug delivery systems (DDS) consisting of more than one layer has been examined by previous investigators. Deasy et al. (1992) demonstrated the possibility of controlling the surface area exposed of active containing cylindrical compacts in a composite implant containing alternating active and inactive spacer devices (Deasy et al., 1992). A variety of controlled release rates of drug were attained depending on the drug loading of the active layers, the erosion rate of the inactive layers and the geometry of the layers.

Various geometrical and compositional modifications of monolithic matrices have also provided linear (zero order) and quasi linear release kinetics (Conte et al., 1993, Yang and Fassihi, 1997a). Simple monolithic matrix systems are incapable of attaining zero-order release due to the inherent limitations that the area of diffusing surface decreases and the diffusional pathlength increases as time progresses. GeomatrixTM delivery system design is an example of a commercially successful hydrophilic matrix, which is based on a symmetrical three-layered tablet geometry (Conte et al., 1993, 1994a, 1994b, Conte and Maggi, 1998). Initial work in this area involved the application, during tableting, of compressed barrier layers on one or both planar surfaces of a hydrophilic matrix containing the active ingredient. The release rate of the core was reduced and the kinetics of drug release was shifted towards zero order release as a result of the application of the barrier layers. Later, an expandable polymer was used to produce the barrier layers, resulting in a more homogeneous system in which both the barriers and the core swell at the same rate without any internal stress. Both swellable and erodible barrier layers were examined and, ultimately, the multi-layer design has allowed drug release properties such as delayed, pulsatile or biphasic release patterns (Conte and Maggi, 1998). Moreover, from a

technology viewpoint, application of such barriers, using currently available machinery such as multi-layer tablet presses with different feeding stations (Layerpress[®], Manesty[®], Hata[®]), has been shown to be more reliable than application by film coating.

Yang and Fassihi (1997a, 1997b) have attained controlled release from multi-layered drug delivery systems consisting of a controlled release monolithic layer between a barrier layer and an instant release layer. Disengagement of the controlled release layer (following the dissolution of the instant release layer) allowed the maintenance of approximately constant surface area zero-order release kinetics for up to 24 hours.

Chidambaram et al. (1998) have since examined release from layered matrices consisting of non-swellable, hydrophobic middle layers containing the active drug to which hydrophilic and/or hydrophobic layers are press coated. Linear release profiles were achievable using hydrophilic barrier layers on both faces of a hydrophobic matrix tablet, or by applying a hydrophobic layer on one face and a hydrophilic layer on the other face of the matrix tablet. More recently, Bettini et al. (2002) have shown that the relative position of a swellable, erodible or disintegrating layers in a triple layered monolithic matrix system can lead to different in-vitro and in-vivo release kinetics.

1.4.3 Simple layered drug delivery systems

According to the equation of Nernst and Brunner (1904, Equation 1.4), drug dissolution is directly proportional to the surface area of drug available for dissolution. Therefore, a zero-order type release profile is predicted, should the surface area of drug remain constant, for a simple diffusion based dissolution system. Initial studies in the present work in attempting to attain constant drug surface area during dissolution involved dissolution from simple cylindrical compacts of drug and soluble excipient, the drug and excipient comprising single component layers. If the excipient dissolved at a faster rate than the drug, this would result in an increase in the planar surface area of the drug exposed to the dissolution medium, at what was the original drug-excipient layer interface. Maximal control of drug layer surface area is attainable by positioning the drug layer between two excipient layers. The theory of the effect of the soluble excipient on surface area of the drug layer is illustrated graphically in Figure 1.13.

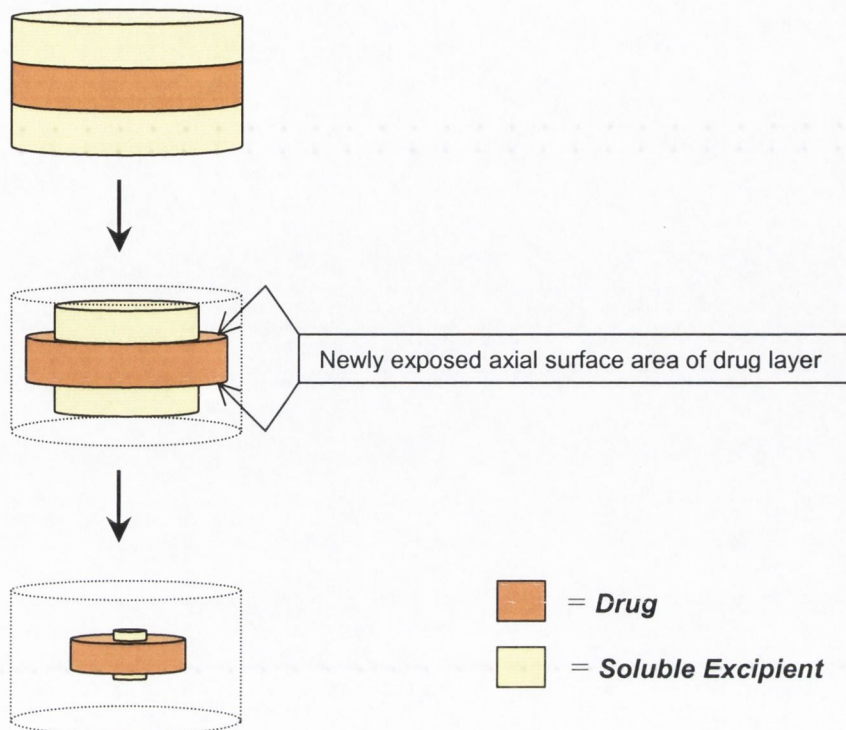


Figure 1.13 Schematic showing concept of a 'simple layered drug delivery system', illustrating the exposure of new surface area of drug layer in the axial direction due to dissolution of the soluble acid excipient layers. The increase in the axial surface area of the drug layer could compensate for the decrease in the radial surface area, with potential for constant release rate.

Drug release rate declines at a faster rate at early time points from an uncoated drug layer. Conversely, in the simple layered systems, simple geometrical analysis would predict that the increasing axial area of the drug layer exposed with time, is higher at earlier time points. Therefore, it should be theoretically possible to compensate for the decreasing release rate of drug from the central layer, with the increase in surface area exposed in the axial direction, at least for a period of time. In fact, various release profiles could be generated from this type of system, depending on the relative solubilities of the drug and excipient layers, on the geometry of the system, and on the amount of drug initially present in the drug layers as well as other factors. It is also desirable to predict the effect of such factors on the resulting dissolution kinetics from layered systems. Such systems are hereafter referred to as 'simple layered drug delivery systems'.

1.4.4 Layered matrix drug delivery systems

Previously studied layered drug delivery systems of various types have been discussed above. However, drug release has not, as yet, been examined from layered DDS consisting of a central, active-containing, insoluble non-swellable heterogeneous matrix core between two layers of soluble acid excipient. It was hoped that the inclusion of a layer of soluble acid excipient onto the planar surfaces of the matrix would transform the kinetics of drug release from the layered matrix systems to a more zero order type profile. The increase in the surface area of the matrix layer in the axial direction, caused by the dissolution of the soluble acid excipient layers with time, could compensate for the increase in diffusional path-length in the matrix layer with time. The drug release rate from an uncoated matrix system declines at a faster rate at early time points, while the increasing surface area effect of the layered matrix system is greater at earlier times. Therefore, the net effect of both increasing diffusional path-length and increasing surface area of the matrix layer could ultimately lead to a more zero order drug release profile. The concept is illustrated in Figure 1.14.

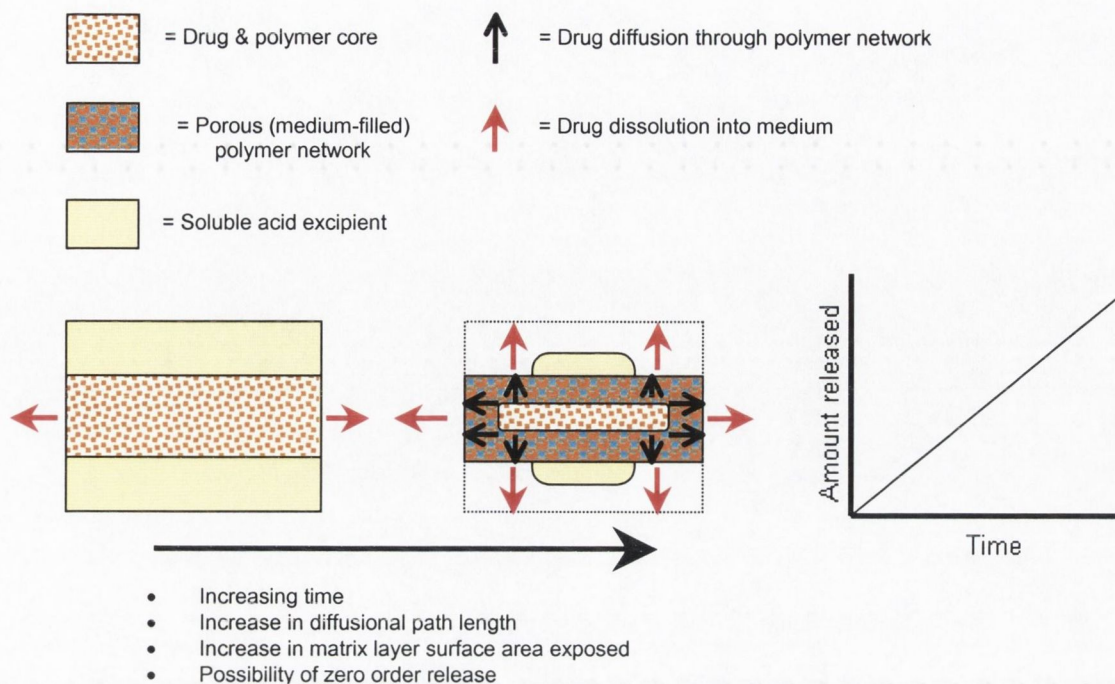


Figure 1.14 Graphical illustration of the process of drug release from a 'layered matrix drug delivery system', consisting of an insoluble non-swellable heterogeneous matrix layer, between two soluble acid excipient layers. The competing mechanisms of the increase in the matrix layer surface area exposed (caused by the dissolution of the acid layer) and the increase in diffusional path-length in the matrix layer with time have potential to allow zero order release of drug.

Similar to the 'simple layered drug delivery systems', it is desirable to predict the effect of formulation parameters factors on the resulting dissolution kinetics from these layered systems. Such systems are hereafter referred to as 'layered matrix drug delivery systems'.

1.5 DYNOCHEM™ SIMULATION PROGRAM

1.5.1 Background

Dynochem is PC based physico-chemical modelling tool provided by Performance Fluid Dynamics Ltd. (PFD) that enables users to examine the effect of scale-dependent physical phenomena (e.g. mixing, heat transfer, mass transfer, feed rate, etc.) on scale independent process chemistry. It is used as a predictive tool for scale-up, optimisation and trouble-shooting of synthesis reaction steps, workup and isolation stages in the pharmaceutical, fine chemical, agrochemical and biopharmaceutical industries.

DynoChem uses numerical integration to calculate the interactions between chemical and physical rate processes, including reactions, feeding, removal, mass transfer and heat transfer. Rather than dividing the process into several thousand zones (e.g. like CFD) with only one phase present, DynoChem uses the fact that in many multi-phase problems, the main resistance to physical transport is at the boundary between the phases, e.g. between gas bubbles and liquid. In many applications concentration (or thermal) gradients within each phase are insignificant compared to gradients near the phase boundary.

A phase is a fundamental concept in DynoChem. It represents material in a certain state (solid, liquid or gas) with an associated pressure, temperature, specific heat capacity, density and composition. From these parameters, the mass and volume of the phase can be calculated.

1.5.2 Implementation of DYNOCHEM™ program

Dynochem uses Excel based input files to define all parameters, variables and processes. The interaction between the input files is illustrated in Figure 2.1.

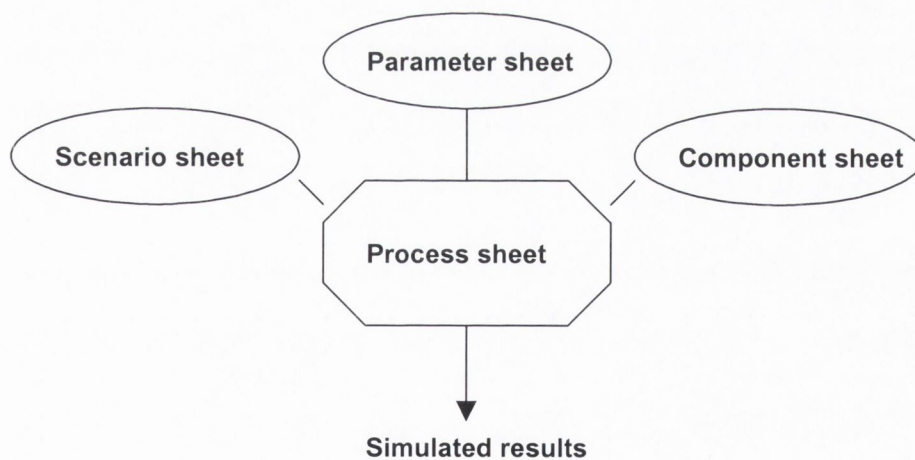


Figure 2.1 Schematic of interaction between DynoChem input files.

The Process Scheme is a novel concept, originally described in publications from Zeneca (Muller, 1996). It is a non-mathematical description of the key chemical and physical mechanisms in the process, in a single simple diagram. It is the first step towards building a dynamic process model and will visually include the various internal phases involved (solid, liquid, gas), the various internal rate processes (mass

or heat transfer), and any possible external interactions (heating or cooling). The various transfer processes included in the process scheme are then transferred to kinetic equations in the process sheet. Many rate equations are already included in the DynoChem database (including mass transfer rate equations). The scenario sheet contains any input variables of the relevant phases that were defined in the process sheet, while the component sheet contains fundamental physical information regarding the various phases (temperature, molecular weight etc.).

1.5.3 DYNOCHEM™ mass transfer model

The film theory, on which DynoChem's mass transfer model is based, assumes that the rate of transfer in both phases is proportional to the difference between the bulk and interfacial concentration and the interfacial area. Mass transfer is always between two phases, and usually one of those is dispersed in the other. The following diagram demonstrates the principle of the film model:

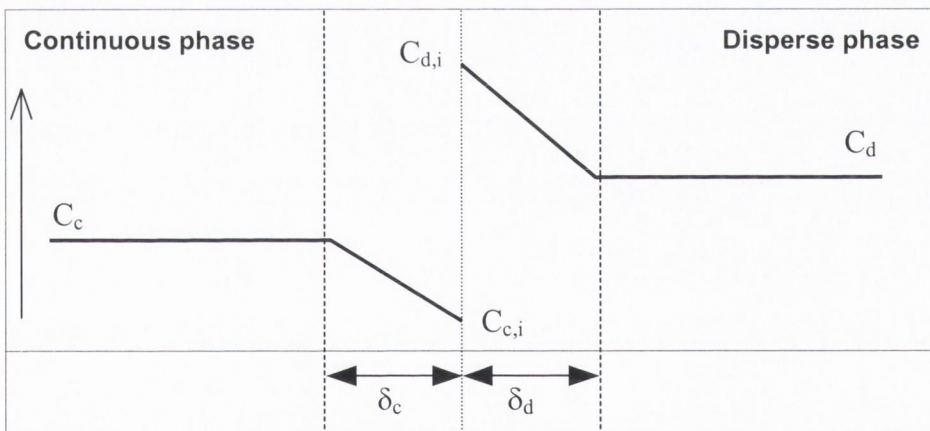


Figure 2.2 Schematic of the principle of Dynochem's film model of mass transfer between a disperse and a continuous phase. δ_c is thickness of film at from continuous phase to interface, δ_d thickness of film at from disperse phase to interface, $C_{c,i}$ is the concentration of the continuous phase at the interface and $C_{d,i}$ is the concentration of the disperse phase at the interface.

The main assumption of the film theory is that the concentrations at the interface are in equilibrium, and may be represented by a partitioning coefficient, S_{CD} :

$$S_{CD} = \frac{C_d}{C_c} \quad \text{Equation 1.41}$$

where C_d is the concentration in the disperse phase and C_c is the concentration in the continuous phase. The total mass transported through the interface φ_m then becomes:

$$\varphi_m = A \frac{-D_c}{\delta_c} (C_{c,i} - C_c) = -K_C A (C_{c,i} - C_c) \quad \text{Equation 1.42}$$

Introducing the partitioning coefficient in Equation 1.42, the mass flow from the continuous phase to the interface $\varphi_{m,c}$ becomes:

$$\varphi_{m,c} = -K_C A \left(\frac{C_{d,i}}{S_{CD}} - C_c \right) \quad \text{Equation 1.43}$$

and from the interface to the disperse phase:

$$\varphi_{m,d} = -K_D A (C_{d,i} - C_d) \quad \text{Equation 1.44}$$

The final assumption of the film theory is that the mass flow into the film equals the mass flow out of the film, which allows the elimination of the interfacial concentration, so the mass transfer rate becomes proportional to the bulk concentrations only:

$$\varphi_{m,d \rightarrow c} = K_{CD} A \left(\frac{C_d}{S_{CD}} - C_c \right) \quad \text{Equation 1.45}$$

where

$$K_{CD} = \frac{k_d k_c}{k_d + \frac{k_c}{S_{CD}}} \quad \text{Equation 1.46}$$

The parameter K_{CD} is the overall mass transfer coefficient and has the dimensions of m/s. The value of K_{CD} is dependent on the hydrodynamics along the interfacial surface. Little is known about the exact value of K_{CD} as function of location, especially not in complex geometries and mixtures where there is a wide range of hydrodynamic conditions. Both the amount of interfacial area and the value of K_{CD} are often difficult to estimate, particularly for particulate systems.

In the Dynochem film model, the mass transfer coefficient is defined as the average of $K_{CD}A$ over a unit volume of liquid, i.e. $K_{CD}a$ in which a is the interfacial area per unit volume.

The final model for mass transfer as used by DynoChem is therefore:

$$\varphi_{m,d \rightarrow c} = V_d K_{CD} a_d \left(\frac{C_d}{S_{CD}} - C_c \right) \quad \text{Equation 1.47}$$

where

$$K_{CD} a_d = \frac{k_d a_d \cdot k_c a_d}{k_d a_d + \frac{k_c a_d}{S_{CD}}} \quad \text{Equation 1.48}$$

where a_d is the interfacial area per unit volume of dispersion.

The Dynochem mass transfer model was used to predict drug release rates from various systems as outlined in the methods (section 2.15).

EXPERIMENTAL

Chapter 2

Materials and methods

2.1 MATERIALS USED IN EXPERIMENTS

MATERIAL	SUPPLIER/ MANUFACTURER
Adipic Acid	Sigma Chemical Company
Benzoic Acid	Riedel-de Haën
De-ionised water	---
Ethylcellulose 10 FP (fine particle size grade)	Dow Chemical Company
Ethylcellulose 10 Std Premium	Dow Chemical Company
Fumaric acid	Aldrich
Hydranal Composite 5	Riedel-de Haën
Hydranal Standard 5.00	Riedel-de Haën
Hydrochloric acid 37%w/w	Riedel-de Haën
Methanol (HPLC grade)	Scharlau Chemie S.A.
Ortho-Phosphoric acid 85%	Riedel-de Haën
Paraffin Wax, pastillated	BDH Laboratory Supplies
Plastipax 5ml syringes	Becton Dickinson
Polyvinyl-pyrrolidone (PVP) Av Mol Wt 40,000	Sigma Chemical Company
Reichart microscope hot-stage	Reichart
Salicylic Acid	BDH Laboratory Supplies
Standard buffer solution pH 4.00	Riedel-de Haën
Standard buffer solution pH 7.00	Riedel-de Haën
Sterican 1,20 x 40mm needles	Braun AG
Succinic acid	Aldrich
Supor-450TM membrane filters (0.45 μm)	Gelman Sciences Inc.
Syringe filter holders, 13mm, plastic	Gelman Sciences Inc.
Theophylline powder, anhydrous	Sigma Chemicals Ltd.
Whatman filter paper no.1 (qualitative)	Whatman

2.2 INSTRUMENTS AND ACCESSORIES USED IN EXPERIMENTS

INSTRUMENT	MANUFACTURER
13mm hydraulic punch and die set	Perkin-Elmer
Agate mortar and pestle	FSA apparatus
Beckman System Gold Programmable Solvent Module 126	Beckman Inc.
Beckman System Gold Programmable Detector Module 166	Beckman Inc.
Differential Scanning Calorimeter (Mettler DSC)	Mettler
Dissolution test apparatus 'DT6'	Erweka
Hitachi S3500N scanning electron microscope	Hitachi
Hydraulic press	Perkin-Elmer
HP 8452A UV/ visible spectrophotometer (and software)	Hewlett Packard
IBM RS/6000 F50 shared memory parallel processor system	IBM
IBM RS/6000 SP distributed memory parallel processor system	IBM
Mettler analytical balance	Mettler
Metler Toledo 820 Thermal Analysis System	Metler
Metrohm 701 KF Titrino	Metrohm
Metrohm 703 Ti stand	Metrohm
Micromeritics Accupyc 1330 pycnometer for 1cm ³ sample holder	Micromeritics
MM2 Mixer Mill accessories:	Retsch
2 x stainless steel jars (25ml volume)	
4 x 12 mm stainless steel grinding balls	
Shimadzu SIL-9A HPLC autosampler	Shimadzu
Sieve, hand held (106, 180, 250, 355 μ m aperture)	Retsch
Shaker waterbath	Gallenkamp
Siemens D500 X-ray diffractometer	Siemens
Sliding callipers	Inox Helios
Turbula shaker mixer	Glen Mills Inc.
X-Ray Diffractometer (D500)	Siemens

2.3 COMPUTER SOFTWARE USED

SOFTWARE	SUPPLIER
Scientist, version 2.0	Micromath Scientific Software
Microsoft Excel for Windows 97	Microsoft
Minitab, version 13	Minitab Inc.
Dynochem	Particular Fluid Dynamics (PFD)
Fluent, version 5.1.1	Fluent Inc.
Gambit, version 1.3	Fluent Inc.

2.4 PREPARATION OF THEOPHYLLINE MONOHYDRATE

Theophylline monohydrate was prepared from anhydrous theophylline using the method described by Ledwidge (1997). 15 g of anhydrous theophylline was dissolved with stirring in 200 ml water heated to 70°C, the resulting solution was cooled in ice, and the precipitated solid was filtered. The hydrate was exposed to ambient conditions for 48 hours or until constant weight was achieved. The resulting solid was lightly ground in an agate mortar and pestle, and screened through a 250 µm hand held sieve. Characterisation studies were carried out to confirm the presence of only the monohydrate form of theophylline as described in the following section. Results of characterisation studies are included in Appendix 2.

2.5 CHARACTERISATION METHODS

2.5.1 *Thermal analysis*

2.5.1.1 Differential Scanning Calorimetry

Differential Scanning Calorimetry (DSC) analysis was performed on theophylline monohydrate using a Mettler Toledo 821e Thermal Analysis system and associated software. Open (hermetically sealed with three vent holes) 40 µl aluminum analysis pans were used to analyse samples of approximately 5 to 10 mg weight. The heating rate was 10°C per minute over a range including the melting point of the drug. A blank open pan was used as the reference sample. A steady stream of nitrogen gas flowed over the sample and reference crucibles while the analysis was performed. The scanning range used in these studies was 25°C to 300°C.

2.5.1.2 Thermogravimetric analysis

Thermogravimetric analysis (TGA) was performed on theophylline monohydrate samples using a Mettler Toledo TG50 Thermogravimetric analysis system with a Mettler Toledo TA controller and associated software. Samples of weight 5 mg to 10 mg were placed on open 40 μ l aluminium lids on the weighing stage of the analysis system. The heating rate was 10°C per minute over a range including the melting point of the drug. A steady stream of nitrogen gas flowed over the sample and reference crucibles while the analysis was performed. The scanning range used in these studies was 30°C to 300°C.

2.5.2 Powder X-ray diffraction studies

X-ray diffraction measurements (PXRD) were performed on powdered samples in conventional cavity mounts with a Siemens D500 diffractometer using a DACO MP wide-range goniometer with a 1.00° dispersion slit, a 1.00° anti-scatter slit, and a 0.15° receiving slit. The Cu anode X-ray tube was operated at 40 kV and 30 mA. Samples were scanned over the range 5° 2 θ to 35° 2 θ with a step-size of 0.05° 2 θ .

2.5.3 Karl Fischer analysis

Karl Fischer titrations (KFT) were carried out on powdered samples using a Metrohm 701 KF Titrino linked to a Metrohm 703 Ti stand. The KF reagent (Hydranal Composite 5) was standardised using Hydranal Standard 5.00. Analyses were performed in triplicate.

2.5.4 Scanning electron microscopy

Theophylline monohydrate samples were viewed using scanning electron microscopy. Samples were mounted on aluminium slabs and sputter coated with gold prior to examination.

2.5.5 Helium pycnometry

Density measurements of powders was carried out using a Micromeritics Accucyc 1330 helium pycnometer for 1cm^3 samples. The volume of the chamber was calibrated against a standard sphere, the volume of which was known. Samples were placed in a silica-containing vacuum dessicator overnight prior to analysis. A purge pressure of 19.5 p.s.i.a was used in the pycnometer, volumes of samples being determined after the rolling average noise figure was less than 0.05cm^3 . Density figures are the average of 3 sample measurements.

2.6 GRINDING

Particle size reduction of appropriate powders was performed using either an agate mortar and pestle or a Retsch MM2 Mixer Mill. The stainless steel grinding jars, of volume 25ml, were filled to approximately one third volume. Two stainless steel grinding balls of 12mm diameter were placed in each grinding jar which were set to run at 90% of max agitation capacity for 10 minutes.

2.7 SIEVING

All sieving was done using Retsch hand held sieves (200 mm diameter, aperture sizes $106\ \mu\text{m}$, $180\ \mu\text{m}$, $250\ \mu\text{m}$ and $355\ \mu\text{m}$).

2.8 BLENDING

All blends were mixed in a TurbulaTM mixer for 10 minutes, before manually mixing with a micro-spatula in the container for 5 minutes.

2.9 PRODUCTION OF SINGLE COMPONENT COMPRESSED DISCS

Single component discs were prepared by compressing the appropriate amount of powder (250 mg, or 1500 mg) in a Perkin-Elmer hydraulic press for 10 minutes at 10,000 kg of pressure.

In some cases, the appropriate surfaces were coated with molten paraffin wax prior to dissolution using a micro-spatula, to leave the surface under investigation free for

dissolution. Where appropriate, compressed discs were affixed to the base of the dissolution vessel using molten paraffin wax.

2.9.1 Intrinsic dissolution rate compacts

Discs which were to release from the upper planar surfaces only (for the determination of intrinsic dissolution rates) were prepared as described by Corrigan and Timoney (1975). One planar surface was initially affixed to the centre of a 19 mm circular glass cover-slip using molten paraffin wax. A second glass cover-slip was positioned on top of the other planar surface and molten wax was carefully poured to fill the resulting space between the cover-slips and curved surface of the disc. The upper cover-slip was removed prior to dissolution, leaving the appropriate planar surface exposed to the dissolution medium. The compressed discs were affixed to the base of the dissolution vessel using molten paraffin wax.

2.10 PRODUCTION OF DRUG DELIVERY SYSTEMS

2.10.1 Simple layered compacts

'Simple' three-layered compacts were prepared by the following method: 500 mg of the bottom acid excipient layer powder was placed in the bottom of the die and compressed at approximately 1000 kg. The powder of the second (drug) layer was then added (500 mg) and recompressed at 1,000 kg. Finally the powder of the top layer was added and compressed at 10,000 kg for 10 minutes. 10,000 kg compression force was employed to minimize the height difference between layers, which was noticed at lower compression forces. Adipic acid/ theophylline monohydrate/ adipic acid compact surfaces (AA/Thmh/AA) did not bind together using the method described above. For this system, 5% PVP was incorporated into the theophylline monohydrate layer, by mixing appropriately in an agate mortar and pestle prior to loading into the die. Inclusion of 5% PVP was shown to not significantly affect the intrinsic dissolution rate of theophylline monohydrate (Appendix 4).

2.10.2 Matrix compacts

Appropriate quantities of theophylline monohydrate, ethylcellulose (and PVP, where appropriate) were weighed into 30 ml amber glass jars for each blend. Blends were

mixed as described in section 2.8. Matrix compacts were prepared by compressing 500 mg of the matrix blend in a Perkin-Elmer hydraulic press for 10 minutes at 10,000 kg of pressure. For percolation studies from matrix compacts, molten paraffin wax was applied to the surface of the compact, to allow dissolution from the top planar surface only. The percolation study compacts were then fixed to the base of the dissolution vessel using molten paraffin wax.

2.10.3 Layered matrix compacts

Blends for the central matrix layer were prepared as described in section 2.8, all matrix layer blends containing 5% PVP. Three-layer matrix drug delivery systems were prepared by the following method: 500 mg of the bottom acid excipient layer powder was placed in the bottom of the die and compressed at approximately 1000 kg. The matrix blend of the second layer was then added (500 mg) and recompressed at 1,000 kg. Finally the powder of the top acid excipient layer was added and compressed at 10,000 kg for 10 minutes.

2.11 DISSOLUTION STUDIES

All in-vitro release tests were performed using the USP dissolution method 2 (paddle dissolution apparatus, USP 24, 2000). The dissolution medium was 900 ml of freshly de-aerated 0.1N HCl or 0.01N HCl. The dissolution medium was maintained at 37°C in 1L dissolution vessels with a rotation speed of 50 rpm or 100 rpm as appropriate. A sample aliquot of 5.0 ml dissolution sample was withdrawn at appropriate intervals from a zone midway between the base of the vessel and the surface of the dissolution medium, at a distance of 2 cm from the vessel wall. All samples were replaced with an equal volume of fresh heated medium at 37°C. All samples were filtered through a 0.45 µm filter and analysed by UV spectroscopy, multi-component UV spectroscopy or HPLC, as appropriate. Cumulative amounts of drug (mg or % drug loading) were calculated and plotted as a function of time. The profiles shown are the average of either three or six determinations (hydrodynamic studies); error bars indicating standard deviation of these values.

2.11.1 Intrinsic dissolution rate studies

Compacts were prepared to release from the top planar surface only as described in section 2.9.1. Dissolution runs were carried out in triplicate. Samples were withdrawn at 5-minute intervals up to 30 minutes and at 10 minute intervals thereafter, as described above (section 2.11). The initial portion of each dissolution profile (0-15 min) was used to derive the intrinsic dissolution rate. The intrinsic dissolution was then used to determine the diffusion coefficient of the component by using Equation 1.5, the diffusion layer thickness, h , having been previously calculated from the experimentally determined dissolution rate of benzoic acid.

2.11.2 Analysis of samples from dissolution studies

2.11.2.1 Single component discs

All samples from dissolution studies on single component discs were analysed by UV spectroscopy using a Hewlett Packard HP8452A UV/visible spectroscopy, or by HPLC analysis as shown in Table 2.1.

Table 2.1 *Method of analysis of samples from dissolution runs of single component compressed discs.*

DISC COMPONENT	DISSOLUTION MEDIUM	ANALYTICAL METHOD
Benzoic acid	0.1N HCl	UV
Theophylline monohydrate	0.01N HCl	UV
Adipic acid	0.01N HCl	UV
Succinic acid	0.01N HCl	HPLC
Fumaric acid	0.01N HCl	HPLC

2.11.2.1.1 UV analysis

Where appropriate, dissolution samples were analysed by UV spectroscopy using a Hewlett Packard HP8452A UV/visible spectroscopy. Internal referencing was used for quantitation purposes for all UV samples. This technique was employed to improve the precision of UV spectroscopic results by minimising the effect of any minor changes that may cause a shift in the absorbance of the baseline (caused by, for example, changes in light intensity due to lamp instability). Internal referencing involves the subtraction of the absorbance at a reference wavelength absorbance from

the analytical wavelength absorbance (Owen, 1988). The reference wavelength is taken at a point along the baseline beyond the analytical wavelength. It is the difference between these absorbance readings which is used for quantitation purposes. The absorbance of dissolution samples, filtered and diluted appropriately, were read at the analytical wavelength of λ_{max} and at the reference wavelength range. The concentration of dissolution sample was then calculated, using the difference between these average absorbance values, with reference to an appropriate calibration curve, determined in the same medium at the same analytical and reference wavelengths. Details of UV quantitation specification methods are outlined in Table 2.2 below. Calibration curves were determined in all cases from at least three dilutions of three separate stock solutions. The relevant calibration curves are included in Appendix 3.

Table 2.2 *The analytical and reference wavelengths used in the determination of concentrations of samples from dissolution studies on single component discs in various media.*

DISC COMPONENT	DISSOLUTION MEDIUM	ANALYTICAL WAVELENGTH (nm)	REFERENCE WAVELENGTH (nm)
Benzoic acid	0.1N HCl	274	400
Theophylline monohydrate	0.01N HCl	272	400
Adipic acid	0.01N HCl	204-206	350-400

2.11.2.1.2 High performance liquid chromatography (HPLC) analysis

Samples from dissolution studies on single component discs of succinic acid or fumaric acid in 0.01N HCl were analysed by HPLC because the UV method was not precise at lower concentrations. HPLC analysis was performed using a Spherisorb S5 C8 5 μ m, 250 x 4.6 mm column. The other components of the HPLC system were: a Beckman System Gold Programmable Solvent Module 126 and a Beckman System Gold Programmable Detector Module 166, a Shimadzu SIL-9A autosampler. The software used to analyse data was Beckman System GOLDTM. The mobile phase used was methanol: 1% phosphoric acid, 50:50, run at ambient temperature with a flow rate of 0.8 ml/min. The detector wavelength was 202 nm for succinic acid and 208 nm for fumaric acid. This HPLC analysis method was adapted from the method outlined by Scharzenbach (1982).

Using this method, the retention times, t_r , of succinic acid and fumaric acid were approximately 8 minutes and 8.2 minutes, respectively. Peak areas were used for quantitation, with concentrations being determined by reference to a calibration curve constructed using at least three concentrations diluted from three stock solutions. A new calibration was performed for each analysis. An example of the calibration curve used is included in Appendix 3.

2.11.2.2 Simple layered compacts

Samples from multi-component dissolution studies were analysed by multi-component UV analysis or by HPLC analysis as summarised in Table 2.3. The methods used are outlined in below.

Table 2.3 *Method of analysis of samples from dissolution studies of simple layered compacts consisting of alternate single component layers. BA = benzoic acid, SA = salicylic acid, Thmh = theophylline monohydrate, UV-MCA = multi-component UV analysis. HPLC = high performance liquid chromatography.*

COMPONENT MEASURED	LAYER COMPONENTS OF SYSTEM	DISSOLUTION MEDIUM	ANALYSIS METHOD
BA	BA/SA/BA	0.1N HCl	UV-MCA
SA	BA/SA/BA	0.1N HCl	UV-MCA
Thmh	AA/Thmh/AA	0.01N HCl	HPLC
Thmh	SuA/Thmh/SuA	0.01N HCl	HPLC

2.11.2.2.1 Multi-component UV analysis

Where salicylic acid was used as the model drug in multi-layered compacts containing salicylic acid and benzoic acid a multi-component UV analytical technique was employed to analyse dissolution samples. The technique used allows quantitation of two components in a mixture solution, where there is only partial overlapping of the UV spectra of the two components. The method allows calculation of the concentration of one of the components from the absorbance at the wavelength at which there is no overlap from the second component. Assuming that the absorbances at any wavelength are additive, the concentration of the second component can be calculated from the residual absorbance at an overlapping wavelength. All salicylic acid/ benzoic acid mixture dissolution samples were

analysed for absorbances at 230 nm and 302 nm. The absorbance at 302 nm was used to calculate the concentration of salicylic acid alone, as benzoic acid showed no absorbance at 302 nm in the concentration range of up to 20 mg%. It was possible to calculate the absorbance at 230 nm due to salicylic acid alone using the mean ratio of the absorbance of salicylic acid at 230 nm to 302 nm (= 1.8) over the concentration range used. The benzoic acid concentration was then calculated from the residual absorbance at 230 nm. The assay method was verified using mixtures of benzoic acid and salicylic acid of known concentrations. Calibration curves were determined in all cases from at least three series of dilutions from three separate stock solutions. An example of the calibration curves are included in Appendix 3.

2.11.2.2.2 High performance liquid chromatography (HPLC) analysis of theophylline monohydrate

Where theophylline monohydrate was used as the model drug in multi-layered compacts containing theophylline monohydrate and other acid excipients in alternate layers, HPLC was used to quantify the concentration of theophylline monohydrate in dissolution samples. HPLC analysis was employed in this case because there was overlap in absorbances from acid excipients around the region of the λ_{max} of theophylline monohydrate. The column used for HPLC analysis of theophylline monohydrate samples was a Waters Spherisorb S5 ODS2 Analytical Column of the dimensions 4.6 x 125 mm. The other components of the HPLC system were: a Beckman System Gold Programmable Solvent Module 126, a Beckman System Gold Programmable Detector Module 166 and a Shimadzu SIL-9A autosampler. The software used to analyse data was Beckman System GOLDTM. The mobile phase used was 7% v/v acetonitrile in an aqueous buffer solution consisting of 0.136% w/v sodium acetate trihydrate and 0.5% v/v glacial acetic acid. The mobile phase was run at ambient temperature with a flow rate of 1.0 ml/min. using an absorbance wavelength of 280 nm. This HPLC analysis method was adapted from the method outlined by the United States Pharmacopoeia (USP 24, 2000). Acid excipients eluted from the column very quickly and did not interfere with theophylline monohydrate analysis. Using this method, the retention time for theophylline monohydrate was approximately 7 minutes - check. Peak areas were used for quantitation, with concentrations being determined by reference to a calibration curve constructed using

at least three concentrations diluted from three stock solutions. A new calibration was performed for each analysis. Calibration curves used are included in Appendix 3.

2.11.2.3 Single layer matrix drug delivery systems

Samples from dissolution studies on single layer matrix compacts containing theophylline monohydrate were analysed by UV spectroscopy as previously described in 2.11.2.1.1.

2.11.2.4 Layered matrix drug delivery systems

Samples from dissolution studies on layered matrix compacts containing theophylline monohydrate were analysed by HPLC as previously described in section 2.11.2.2.2.

2.12 SATURATED SOLUBILITY DETERMINATIONS

2.12.1 Acid excipients

Saturated solubility was determined for acid excipients in various media using the sealed ampoule method (Mooney et al., 1981). Excess solid (approximately 2 to 3 times the estimated solubility) was placed in 9 ml of solvent in a glass ampoule (10 ml nominal volume), which was then heat-sealed. The ampoules were placed in a shaker waterbath at 37°C, 100 cpm for 24 hours and 48 hours. A 5 ml sample was withdrawn after 24 hours and filtered through a 0.45 µm membrane filter. The concentration of acid excipient was determined by UV spectroscopy of a suitable dilution of the filtered sample, with reference to the appropriate calibration curve. All pipettes, pipette pumps, membrane filters and holders, glassware and beakers used in the process were pre-heated to 37°C in an oven, and removed from the oven immediately prior to sample withdrawal. The process was repeated for samples at 48hrs, using another vial. Solubility was determined in triplicate for each time point. Results quoted are the average of both time point results, as the concentrations in solution were not seen to change significantly between 24 hours and 48 hours. The media used in the solubility studies were 0.01N HCl (prepared by a 1:10 dilution of 0.1N HCl).

2.12.2 Theophylline monohydrate

Saturated solubility was also carried out on theophylline monohydrate in 0.01 N HCl at 37°C. Solubility was determined in the same manner as described above for solubility determinations of acid excipients (section 2.12.1). Results quoted are the average of both time point results, as the concentrations in solution were not seen to change significantly between 24 hours and 48 hours.

2.12.3 Analysis of samples from solubility determinations

2.12.3.1 Acid excipients

2.12.3.1.1 UV analysis

Saturated solubility samples of adipic acid were analysed by UV spectroscopy using a Hewlett Packard HP8452A UV/ visible spectrophotometer as previously described in 2.11.2.1.1. An example of the calibration curve used is included in Appendix 3.

2.12.3.1.2 HPLC analysis

Saturated solubility samples of fumaric acid and succinic acid were analysed by HPLC as previously outlined in section 2.11.2.1.2. Examples of the calibration curves used are included in Appendix 3.

2.12.3.2 Theophylline monohydrate

Samples of saturated solutions of theophylline monohydrate in 0.01N HCl or buffer pH 6.8 were analysed by UV spectroscopy using a Hewlett Packard HP8452A UV/ visible spectrophotometer as previously described in 2.11.2.1.1. Examples of the calibration curves used are included in Appendix 3.

2.13 STATISTICAL TECHNIQUES USED IN EXPERIMENTS

All statistical analyses were performed with the aid of Microsoft Excel 97 for Windows on a PC.

2.13.1 Simple Comparative Experiments

2.13.1.1 *t*-test

Simple comparative *t*-tests were applied in situations where two independent samples were involved. The standard error was calculated using a pooled estimate of the sample variance. The null hypothesis was tested using a *t*-ratio complying with a student's *t*-distribution having $n-1$ degrees of freedom, where n is equal to the sample number for each sample group. All tests were conducted at the 0.05 level of significance. The *t*-ratio for two sample means is given as:

$$t = \frac{\bar{Y}_2 - \bar{Y}_1}{S_D} \quad \text{Equation 2.1}$$

where t is the *t*-ratio, \bar{Y}_1 is the mean of sample 1, \bar{Y}_2 is the mean of sample 2 and S_D is the estimated standard error of the mean difference.

2.13.1.2 ANOVA

The generalisation of the *t*-test to permit comparisons between more than two sample means is called analysis of variance (ANOVA). In essence, ANOVA involves the statistical separation of the total sum of squares and the total degrees of freedom into a) random variation within experiments and b) variation between experiments. An ANOVA table is divided into the following columns:

<i>Source</i>	is the source of variation
<i>df</i>	is the degrees of freedom
<i>SS</i>	is the sequential sum of squares
<i>MS</i>	is the adjusted mean squares
<i>F</i>	is the <i>F</i> statistic (see below)
<i>p</i>	is the <i>p</i> -value which is the probability associated with the <i>F</i> -statistic

where:

$$MS = \frac{SS}{df} \quad \text{Equation 2.2}$$

The *F*-statistic in the ANOVA table is calculated by dividing the adjusted mean square value for the experimental parameter (between experiments) by the mean

square value for residual error (within experiments, i.e. error). A high F -statistic associated with a low p -value (<0.05) is considered statistically significant.

The least significant difference (LSD) to statistically distinguish between the means of any two of the experiments at a significance level $\alpha = 0.05$ is calculated as follows:

$$LSD = t_{0.025} \sqrt{\frac{MSE}{n}} \quad \text{Equation 2.3}$$

where MSE is the adjusted mean squares of error (within experiments) and $t_{0.025}$ is the two sided t -statistic with a significance level, $\alpha = 0.05$.

2.13.2 Curve fitting

Goodness-of-fit statistics for various models was provided by using Scientist (Ver. 2.0) (Micromath Scientific Software), which is a non-linear curve fitting package. Two statistical outputs were used to evaluate this goodness-of-fit; the coefficient of determination and the model selection criterion (MSC) (Scientist Handbook, 1995). The MSC value is a modification of the Akaike Information Criterion (AIC), that is normalised such that it is independent of the scaling of the data points. It is calculated in accordance with the following equation:

$$MSC = \ln \left[\frac{\sum_{i=1}^n w_i (Y_{obs_i} - \bar{Y}_{obs})^2}{\sum_{i=1}^n w_i (Y_{obs_i} - \bar{Y}_{cal_i})^2} \right] - \frac{2p'}{n} \quad \text{Equation 2.4}$$

where n is the number of data points, w_i are the weight applied to each point, Y_{obs_i} , are the observed data points, \bar{Y}_{obs} the predicted data points, \bar{Y}_{cal_i} the weighted mean of the observed data and p' is the number of parameters estimated. The MSC value is affected by the number of parameters being estimated and will place a higher burden on models with a greater number of parameters, such that, models fitted with different numbers of parameters can be compared (Scientist User Handbook, 1995). Equal weighting was used for all data sets during data fitting.

The coefficient of determination (CD) is defined by the formula:

$$r^2 = \frac{\left| \sum_{i=1}^n w_i (Y_{obs_i} - \bar{Y}_{obs})^2 - \sum_{i=1}^n w_i (Y_{obs_i} - Y_{cal_i})^2 \right|}{\sum_{i=1}^n w_i (Y_{obs_i} - \bar{Y}_{obs})^2} \quad \text{Equation 2.5}$$

The coefficient of determination is a measure of the fraction of the total variance accounted for by the model.

2.13.3 Regression analysis

Regression analysis was performed to produce a linear or quadratic function to predict the value of one of the variables, given a new value for the other. Regression equations are accompanied by an r^2 value, which gives an estimate of the level of variation of the experimental data attributed to the regression equation. The remainder of the variation may be attributable to random effects. Given n pairs of variables $(X_1, Y_1), (X_2, Y_2), \dots, (X_n, Y_n)$ of variables X and Y , the correlation coefficient, r , is defined as:

$$r = \frac{\frac{1}{n} \sum (X_i - \bar{X})(Y_i - \bar{Y})}{S_x S_y} \quad \text{Equation 2.6}$$

where S_x and S_y are the standard errors of the samples of X and of Y , \bar{X} is the mean of samples X , \bar{Y} is the mean of samples Y , r^2 is coefficient of determination. A high value of r^2 , approaching 1, would give an indication of a strong relationship between the variables involved in the regression model. r^2 was used in this thesis to describe the goodness-of-fit of the data with respect to the regression model.

2.14 GAMBIT/FLUENT CFD METHODS TO MODEL FLUID FLOW IN USP PADDLE DISSOLUTION APPARATUS

2.14.1 Technical specifications of computational resources

This work was performed on two different multiprocessor systems, the F50 and the SP. The F50, containing 4 processors, is available as a development system to perform front-end, preprocessing or debugging work before submitting large jobs to the SP, which contains 48 single processor IBM SP2 nodes. The F50 is a shared memory parallel processor, while the SP is a distributed memory parallel processor. Therefore, the 4 processors of the F50 can be shared simultaneously by different users, while a user defined number of processors can be individually assigned to perform parallel jobs according to a queue system on the SP system. The technical specifications of the systems are outlined in Table 2.4 and Table 2.5

Table 2.4 *Technical specifications of the F50 shared memory parallel processor system.*

GENERAL	
MAKE	IBM
MODEL	RS/6000 F50
OPERATING SYSTEM	UNIX (AIX 4.3.2)
NUMBER OF PROCESSORS	4
PROCESSORS	
ARCHITECTURE	Power2
CLOCK SPEED	166 MHz
PEAK PERFORMANCE	332 MFLOPS

Table 2.5 *Technical specifications of the SP distributed memory parallel processor system.*

GENERAL	
MAKE	IBM
MODEL	RS/6000 SP
OPERATING SYSTEM	UNIX (AIX 4.3.2)
NUMBER OF PROCESSORS	48
PEAK PERFORMANCE	30 GFLOPS
PROCESSORS	
ARCHITECTURE	Power2
CLOCK SPEED	160 MHz
PEAK PERFORMANCE	640 MFLOPS

2.14.2 Unstructured grid approach

2.14.2.1 Creation of stirrer

The geometry of the stirrer was built up using a series of Boolean operations involving 3-dimensional cylinders and bricks. The paddle wings are composed of a basic cylindrical shape of radius 41.5 mm which is truncated by two parallel chords which are 19 mm apart as shown by cylinder A in Figure 2.1.

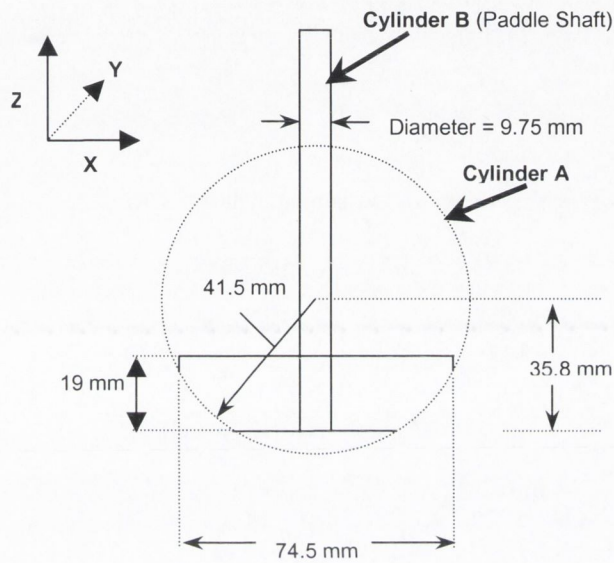


Figure 2.1 Two-dimensional diagram of the geometry of the USP dissolution paddle illustrating its basic composition as two intersecting cylinders.

The first geometry introduced was that of the paddle wings by introducing a cylinder with a radius of 41.5 mm in the X and Z planes and a depth of 4 mm in the Y plane. A temporary brick was then created to act as a tool to modify the cylinder as shown in Figure 2.2(a). This brick was moved to intersect with the cylinder, to allow formation of the bottom edge of the paddle (Figure 2.2(a)). To allow formation of the top edge of the paddle wings, the temporary brick was moved +19mm in the Z direction as shown in Figure 2.2(b). The brick was subtracted from the modified cylinder, retaining only the intersection volume, which formed the wings of the paddle.

An examination of Figure 2.1 shows that it was necessary to remove the sharp tips of the cusps of the paddle wings. This was achieved by forming another temporary brick as described above and translating it by the appropriate distance in the X direction to intersect with the paddle wing at the cusp, as shown in Figure 2.2(c). Again, the brick

was subtracted from the modified cylinder, retaining the brick. Similarly, this was repeated after moving the brick to the other paddle cusp, as shown in Figure 2.2(d). The shaft of the cylinder was then created with a height of 80 mm and a radius of 4.875 mm in the positive Z direction as shown in Figure 2.3(a). The shaft of paddle and paddle wings were then united as shown in Figure 2.3(b).

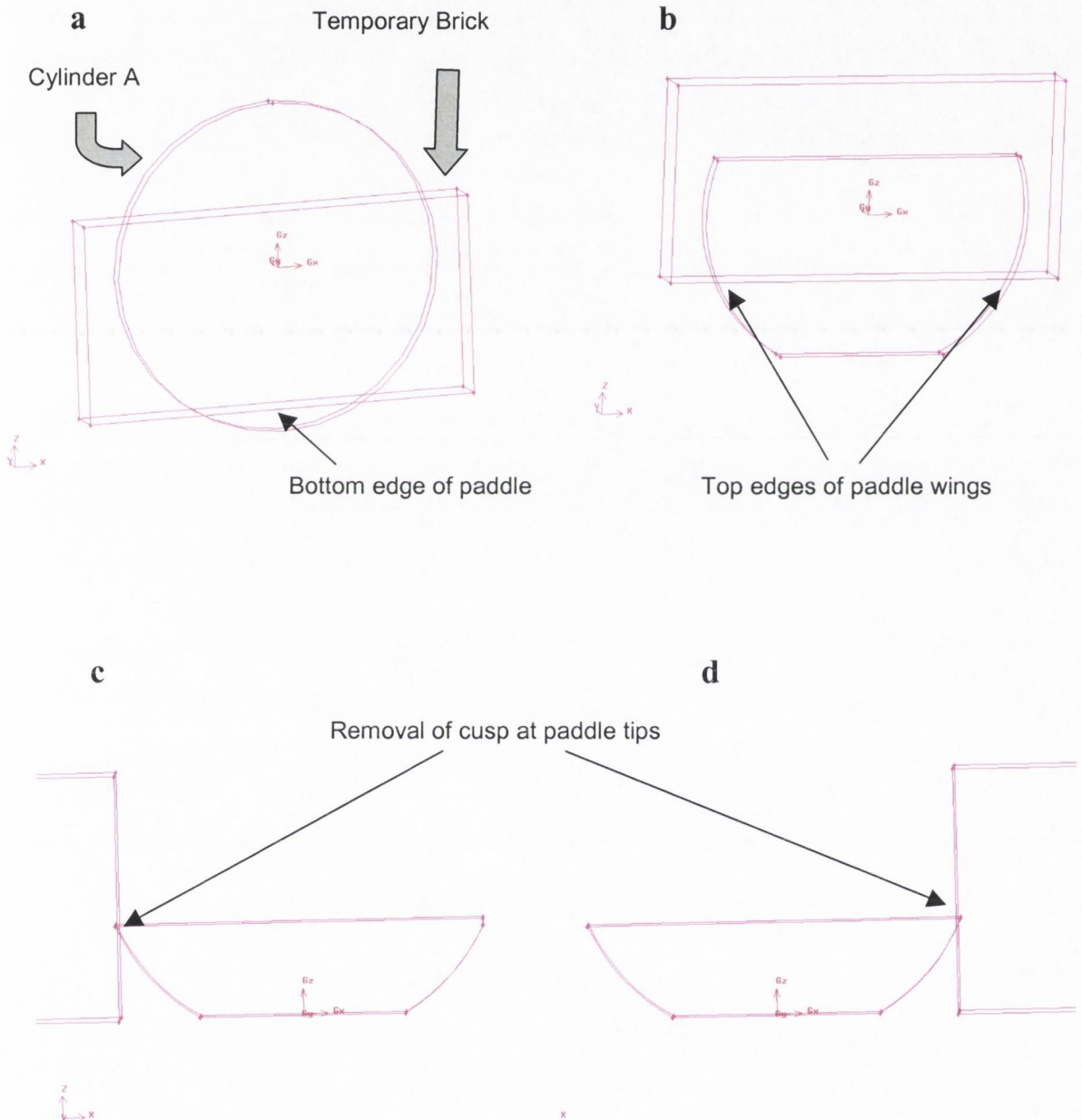


Figure 2.2 GAMBIT graphical interface diagram illustrating the use of a cylinder and a temporary brick in the build up of the paddle wings; (a) formation of the bottom edge of the paddle wings, (b) formation of the top edges of the paddle wings, (c) and (d) removal of cusp at each tip of paddle wings.

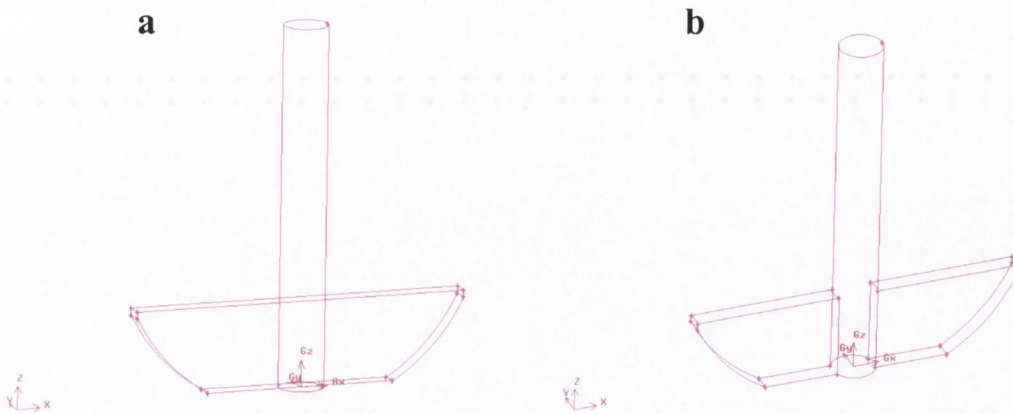


Figure 2.3 GAMBIT graphical interface diagram illustrating; (a) addition of second cylinder as shaft of paddle, before uniting the volumes and (b) final paddle geometry after intersection of shaft with paddle wings.

2.14.2.2 Creation of vessel

The vessel is composed of a cylindrical shape united with a hemispherical bottom. A cylinder of height 75.5 mm and radius 51 mm was created and then moved 51 mm in the Z direction. A sphere was created at the origin with a radius of 51 mm and also moved 51 mm in the Z direction. The vessel and sphere were then united as shown in Figure 2.4(a).

2.14.2.3 Creation of multiple rotating reference frame (MRF)

The paddle base was raised by 25mm to its final position relative to the vessel. A virtual cylinder and sphere were then created within the volume of the vessel to allow formation of the multiple rotating reference frame (MRF), which was necessary to allow the impeller to rotate with an angular velocity within the vessel (see section 1.2.2.4.1). The multiple reference frame was created in a similar manner as described above for the vessel. The cylinder height and radius were 60 mm and 45.1 mm respectively, while the radius of the sphere was 45.1 mm. The cylinder and the sphere were also united to create the multiple reference frame volume, which was moved in the Z direction to its final position, relative to the paddle and the vessel volumes, as shown in Figure 2.4(b).

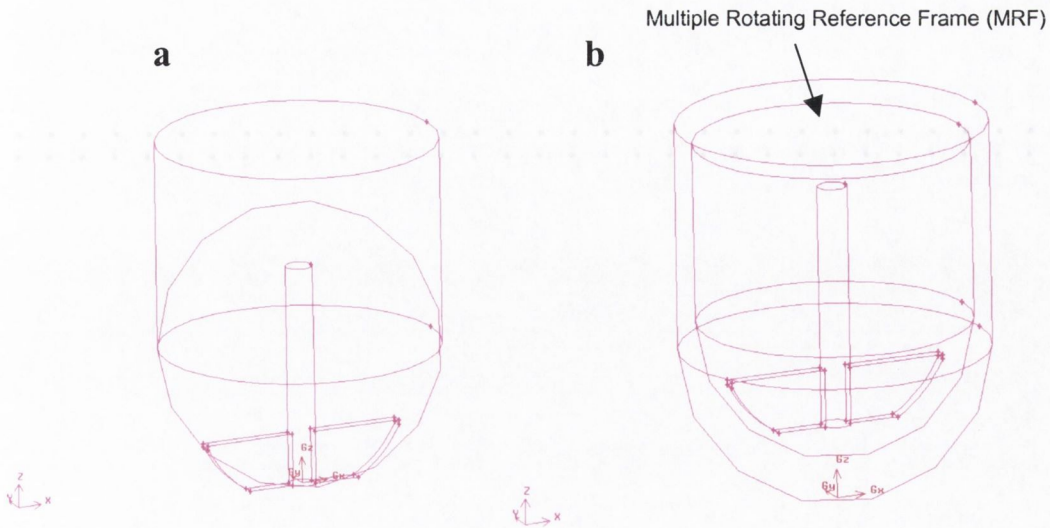


Figure 2.4 GAMBIT graphical interface diagram illustrating; (a) addition of cylinder and sphere of vessel, before intersection and (b) addition of multiple reference frame after completion of vessel and final positioning of paddle.

2.14.2.4 Boundary and continuum specifications

Firstly, it was necessary to define the volumes of the computational domain. The MRF volume was subtracted from the vessel volume to define a new ‘vessel’ volume, which was the volume between the vessel wall and the MRF volume. It was then necessary to re-define the MRF volume using the ‘stitch faces’ command and selecting the relevant faces. Similarly, it was necessary to subtract the paddle volume from the MRF volume. Again, it was necessary to stitch the faces of the paddle to re-define its volume after this operation.

The relevant boundary conditions were then required to be assigned to each face in the computational domain. The 3 faces of the vessel wall were changed to the ‘wall’ entity type. Similarly, the 3 faces of the MRF volume and the 13 faces of the paddle volume were changed to the ‘wall’ entity type. Continuum types were also applied on the relevant volumes. The vessel and MRF volumes were defined as fluids, while the stirrer was defined as a solid.

2.14.2.5 Mesh generation

The stirrer volume was meshed using the ‘tet/hybrid’ scheme, at the limit of refinement for this set-up, which was found to be 20 (GAMBIT will then mesh the smallest edge of the chosen volume at an interval count of 20 and attempt to apply this level of refinement to all other edges, and faces in the volume) as shown in Figure 2.5(a). Similarly, the MRF volume and vessel volumes were meshed using the ‘tet/hybrid’ scheme, at an interval count of 120 as shown in Figure 2.5(b) and Figure 2.5(c). The complete journal file, generated during the build-up of the grid is included in Appendix 5.

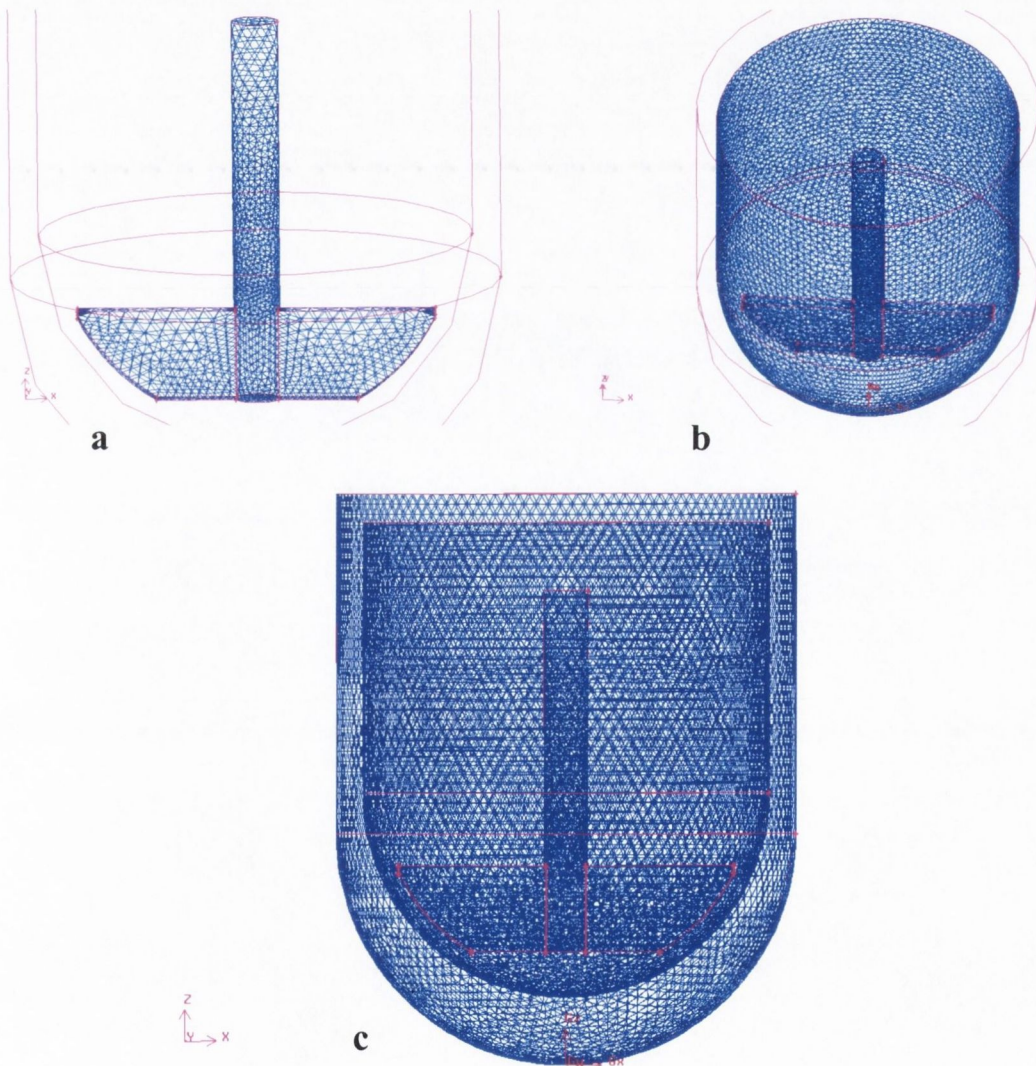


Figure 2.5 GAMBIT graphical interface diagram illustrating; (a) paddle after meshing using tetrahedral cells, (b) multiple rotating reference frame after meshing using tetrahedral cells and (c) vessel volume after meshing using tetrahedral cells.

2.14.2.6 Set up in Fluent

The GAMBIT file was saved as a 'mesh' file and exported to run on the solver program Fluent. Fluent contains a database of material properties, the default material being air. It was necessary to import 'water-liquid' as a material.

2.14.2.6.1 *Boundary conditions definition*

Numerical values are entered through Fluent onto the specifications previously defined in GAMBIT. In this initial set-up, the multiple reference frame is defined as a moving wall with an angular velocity of 5.236 rad/s (50 rpm), while the stirrer is stationary in the absolute reference frame. Water-liquid with the pre-defined viscosity (room temperature) was chosen as the material for the MRF and vessel volumes (laser Doppler measurements were carried out at room temperature, Bocanegra et al. 1990). (Later, mass transfer predictions from the surface of compacts, to compare with experimental mass transfer rates, were modelled with a viscosity of 37°C).

2.14.2.6.2 *Parallelisation (grid partitioning)*

Parallel processing on a multiprocessor system with Fluent involves two steps, as the parallel version of the program is a different version to the serial version:

1. Partitioning of the grid into a number of parts using the serial solver.
2. Initiation of the parallel solver, reading of the partitioned case file and calculation of the solution.

A performance analysis was carried out by Kosiol (2000) to determine the duration of execution for the same calculation problem using various numbers of processors. It was determined that the execution on eight processors was the most efficient use of the system for this type of problem, after balancing the compromise associated with the latency and the bandwidth of the system. Eight processors were therefore used for the present work for processing on the SP, while all developmental work used 4 processors on the F50 system. The bisection method used was 'Cylindrical Z Axis', which bisects the volume through the X and Y planes at various levels of the Z plane.

2.14.2.6.3 Solver set-up/ solution controls

The solver formulation used in this initial approach was that used by Kosiol (2000) and is outlined in Table 2.6, while the solution controls are outlined in Table 2.7.

Table 2.6 *Solver set-up used in the unstructured grid approach (without the inclusion of a compact).*

SOLVER FORMULATION INPUT	SETTING
SOLVER FORMULATION	Segregated Implicit
SPACE	3D
TIME	Steady
VELOCITY FORMULATION	Absolute

Table 2.7 *Solution controls used in the unstructured grid approach (without the inclusion of a compact).*

SOLUTION CONTROL FACTOR	INPUT	SETTING
UNDER-RELAXATION	Pressure	0.3
	Momentum	0.7
	Density	1
	Body Forces	1
DISCRETIZATION	Pressure	Standard
	Momentum	First Order Upwind
	Pressure-Velocity Coupling	SIMPLE

2.14.2.6.4 Solution initialisation and iteration

The residual monitor option was activated to 'plot' and the problem was initialised by setting all velocities in the domain to zero (a necessary step required before iterating). Because the case and data file for this problem had been partitioned (initially 4 processors on the developmental F50 system), it was possible to run the parallel Fluent solver in background mode, as solutions involving enormous numbers of calculations like this generally require several hours to converge. Firstly, a journal file (text file) was created, which contained the relevant commands to allow Fluent to read, iterate and save the relevant files, while running in background mode. An example of one such journal file is included in Appendix 7 (filename 'run.jou'). The parallel version of Fluent was then initiated to run according to the instructions

contained in the relevant journal file by entering a command similar to the following on the F50 shell:

```
FLUENT 3ddp -t4 -p -g < run.jou > & log_output &
```

This command line informs the F50 to run the 3Dimensional Fluent solver using double precision (3ddp, a more precise version of the solver), to run this version in parallel (-p), using 4 processors (-t4) and to not display a graphical user interface (-g). The commands are contained in a journal file called 'run.jou' (in the current working directory) and Fluent will save all outputs from the run including residuals of error in the file 'log_output'.

2.14.2.6.5 Convergence

Fluent solves the governing integral equations for the conservation of mass and momentum numerically. As there are three momentum equations involved in a 3D problem, there are four residuals of error (momentum in the x, y, z directions and the continuity equation) to be monitored for convergence, the point at which the solution is deemed to be complete. There are no universal metrics for judging convergence, however, the default convergence criterion in Fluent of $1e^{-3}$ is sufficient for most problems (Fluent5 User's Guide, 1998). In fact, it can be difficult to attain this level of residuals with rotating fluids containing a high degree of swirl, such as the problem being considered. Fluent offers a number of tools to accelerate convergence, most of which involve adaption of the grid in regions of high gradients of pressure or velocity. The residuals of error for the initial approach used are shown in Figure 2.6. The residuals rise initially, but then gradually decline until a plateau is reached. Therefore, the grid was adapted at 1614 iterations, which allowed the residuals to further decline, eventually reaching convergence after a total of 2619 iterations.

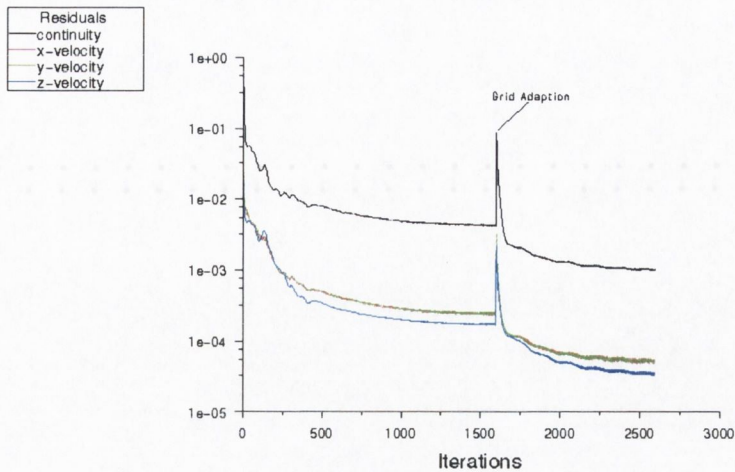


Figure 2.6 Residual error graph showing scaled residuals of error of momentum equations (x, y, and z components) and of the continuity equation versus number of iterations for the unstructured grid approach (without the presence of a compact). Note – units of y-axis are arbitrary.

2.14.2.6.6 Grid adaption

An examination of velocity magnitudes in the computational domain before adaption confirmed that there was a high velocity gradient in the region of fluid surrounding the paddle wings. The adaption technique used in the unstructured grid method was ‘boundary adaption’ using a ‘hanging node’ adaption approach. Each cell within a distance of four cells from the paddle surface was isotropically divided from a tetrahedron into 8 tetrahedra as shown in Figure 2.7. The subdivision consists of trimming each edge of the tetrahedron, and then subdividing the enclosed octahedron by introducing the shortest diagonal. Although the hanging node scheme provides significant grid flexibility, it does require additional memory to maintain the grid hierarchy, which is used by the rendering and grid adaption operations (hanging node).

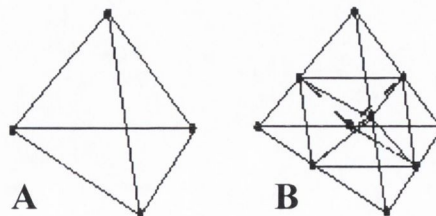


Figure 2.7 Principle of hanging node adaption of a 3D tetrahedral Cell: (A) before adaption and (B) after adaption.

Following grid adaption, the computational domain was again partitioned to run on the F50 (4 processors) as outlined in section 2.14.2.6.2 to assign each processor an equal workload. A graphical illustration of a cut through the mid-plane (in line with the paddle) of the final grid, after grid adaption, is shown in Figure 2.8. Further iterations were executed until the scaled residuals of error had decreased below the convergence limit, as shown in Figure 2.6. The results of the unstructured grid approach are discussed in Chapter 3.2.2.

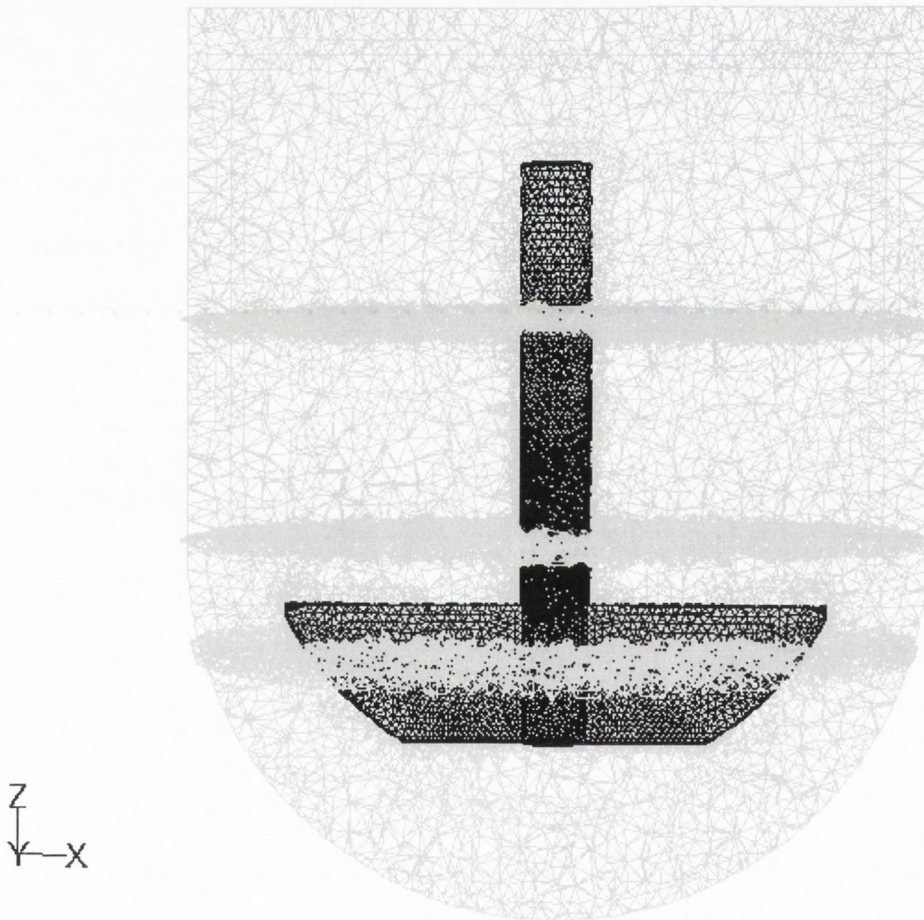


Figure 2.8 Initial mesh network following grid adaption, illustrating a 2D cut through the mid-plane of the vessel, the mesh on the surface of the stirrer and the interfaces between the four computational domains of the partitioned vessel.

2.14.3 Structured grid approach

The structured grid method involved a completely different approach. Firstly, a structured hexahedral mesh was built up in the pre-processor, which requires a considerably more tedious geometry production system. This entails a 2-dimensional to a 3-dimensional approach involving the evolution of vertices to edges, edges to

faces and faces to volumes. The eventual wireframe consists of a large number of individual volumes, which could be meshed individually into hexahedral cell units.

2.14.3.1 Creation of vessel hemisphere and lower section of paddle

The wireframe geometry of the USP vessel was built up initially from 2-dimensional sections, which were manipulated into 3-dimensional sections that would eventually comprise the overall volume of the USP paddle dissolution apparatus. The hemispherical bottom of the vessel consisted of four quarter-hemispheres, which were formed by reflection from an initial quarter. This initial quarter was built from a bottom up approach of vertex to edge to face to volume progression.

The important vertices of a plane, midway through the paddle wings, were individually defined using 3-dimensional co-ordinates, based on the compendial specifications. Individual edges of the paddle and vessel geometry, both straight and curved, were formed using the relevant vertices as shown in Figure 2.9(a). The individual edges were then merged to define faces A, B and C as shown in Figure 2.9(b). Face A, B and C were rotated 90° about an axis defined as the centre of the paddle shaft, producing a quarter hemispherical volume, which contained the main geometrical features of the paddle and vessel hemisphere (Figure 2.9(c)). Three volumes were defined at this stage, by merging the relevant faces. At this stage, most of the salient geometrical features of the volume were included, however, it was necessary to define some further volumes to include the paddle wings and also to subsequently facilitate trouble-free meshing of the vessel volumes. A temporary brick was introduced to define a new volume where the brick intersected with the inner volume (Figure 2.9(d)). Another temporary brick was then introduced to allow creation of the main body of the paddle wings (Figure 2.10(a)). This brick was also used to create the top volume of the paddle wings at the level of the cusp as shown in Figure 2.10(b). A plane of reflection was set up which allowed production of half of the hemispherical section of the apparatus, via reflection in this plane (Figure 2.10(c)). Introduction of another plane of reflection at this stage completed the full geometry of the lower hemisphere of the apparatus, including the paddle and wings as shown in Figure 2.10(d).

2.14.3.2 Creation of cylindrical volume of vessel

Another vertex was introduced corresponding to the centre point of the paddle shaft at the level of the top of the dissolution medium volume. A virtual 'sweep edge' was then introduced by connecting this vertex with the centre point of the vessel hemispherical bottom (Figure 2.11(a)). The sixteen faces of the top surface of the hemispherical bottom were selected and 'swept' in the direction of the virtual edge. This extrusion of faces produced sixteen new volumes corresponding to the upper cylindrical volume of the apparatus and the upper portion of the paddle shaft as shown in Figure 2.11(b).

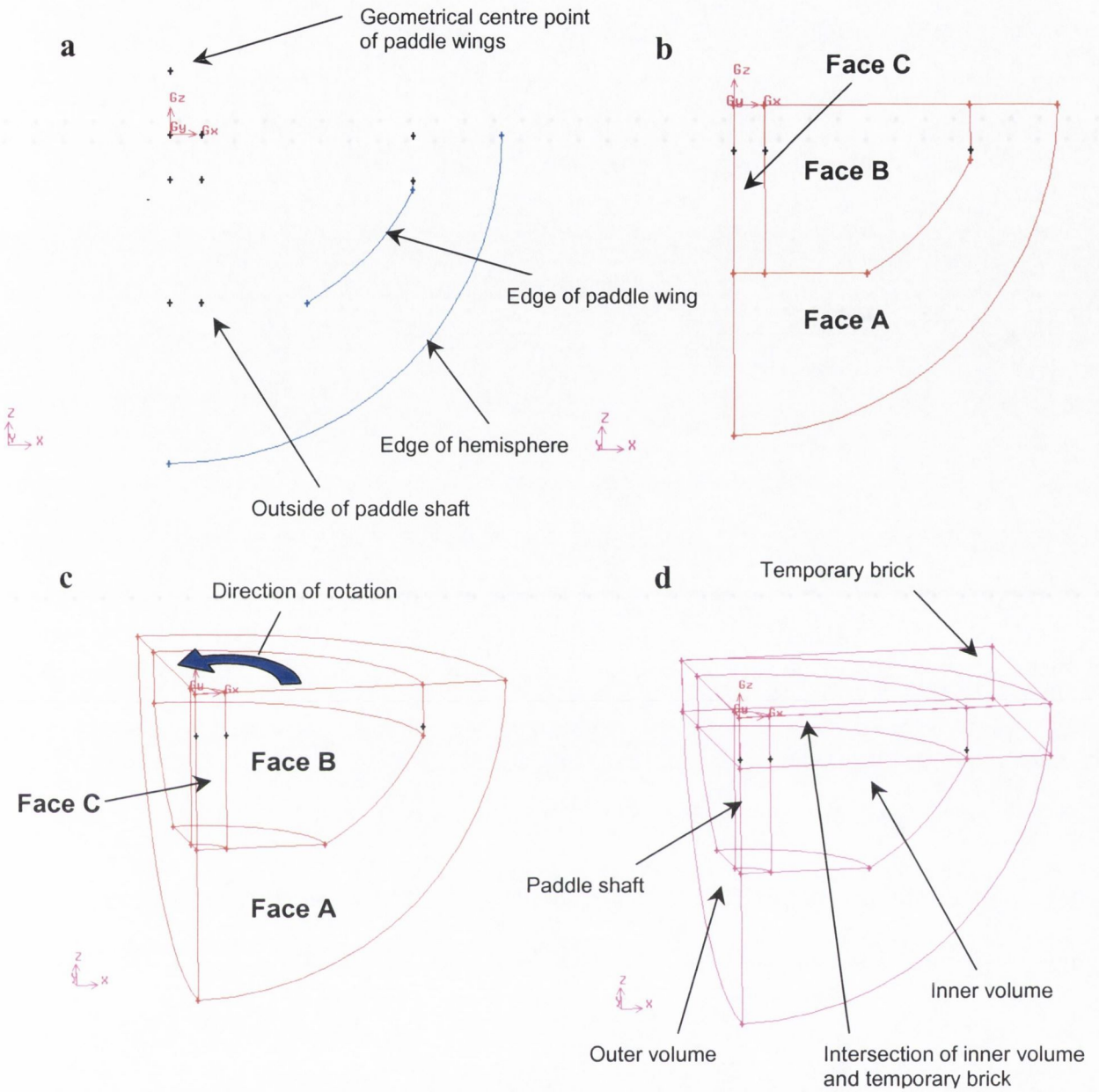


Figure 2.9 GAMBIT graphical interface diagram illustrating some of the steps involved in the generation of quarter of the vessel hemisphere and the lower section of the paddle: (a) creation of vertices and curved edges of stirrer wing and hemisphere, (b) creation of 2D edges of stirrer and hemisphere, (c) formation of quarter hemispherical volume after rotation of 2D edges and (d) generation of individual volumes from relevant faces and use of temporary brick to define a new upper volume.

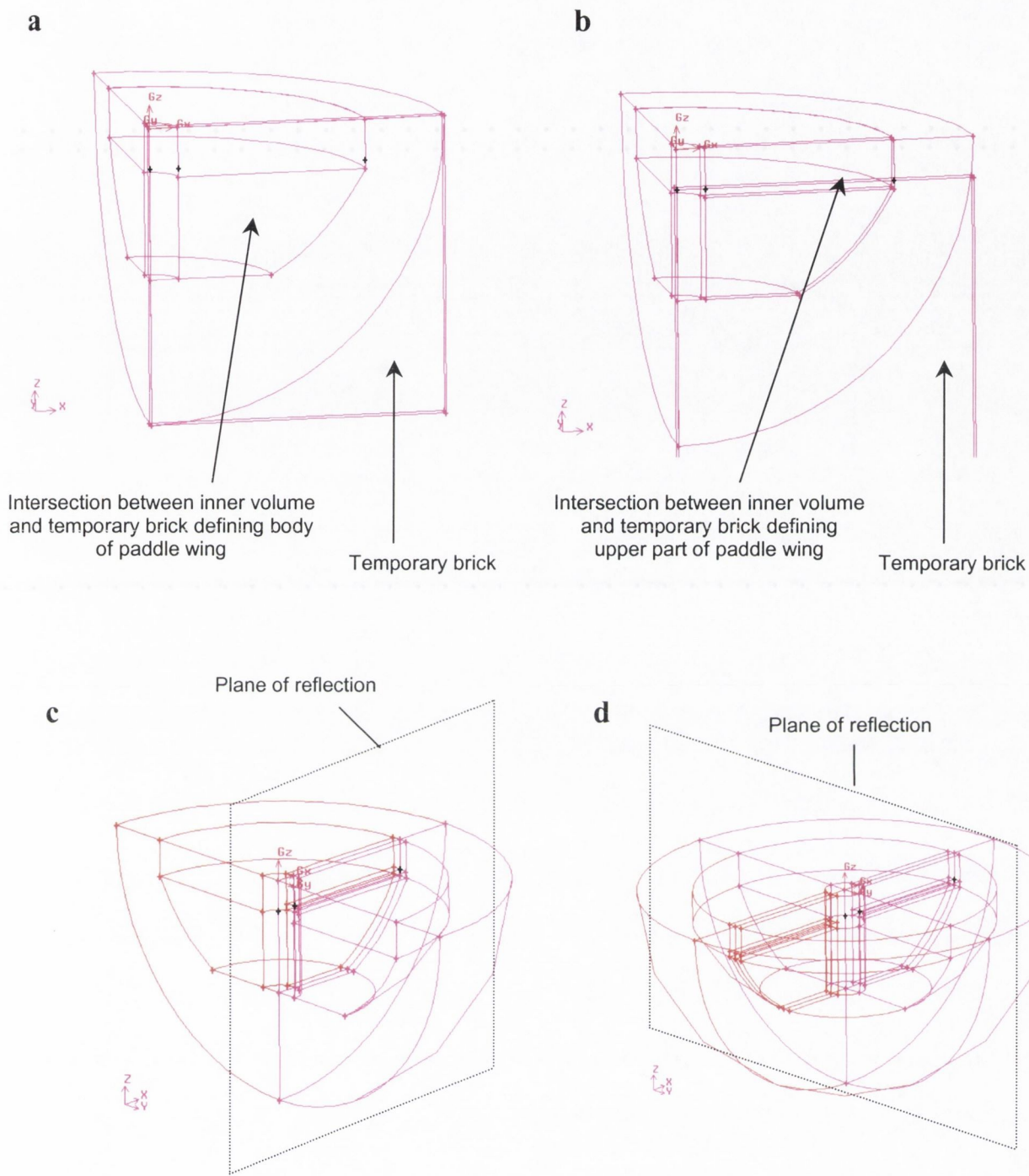


Figure 2.10 GAMBIT graphical interface diagram illustrating some of the steps involved in the generation of the hemispherical bottom from an individual quarter: (a) use of temporary brick to form the body of the paddle wing, (b) use of temporary brick to form upper part of paddle wing, (c) use of reflection plane to produce half of hemispherical bottom and (d) use of reflection plane to produce full hemispherical bottom.

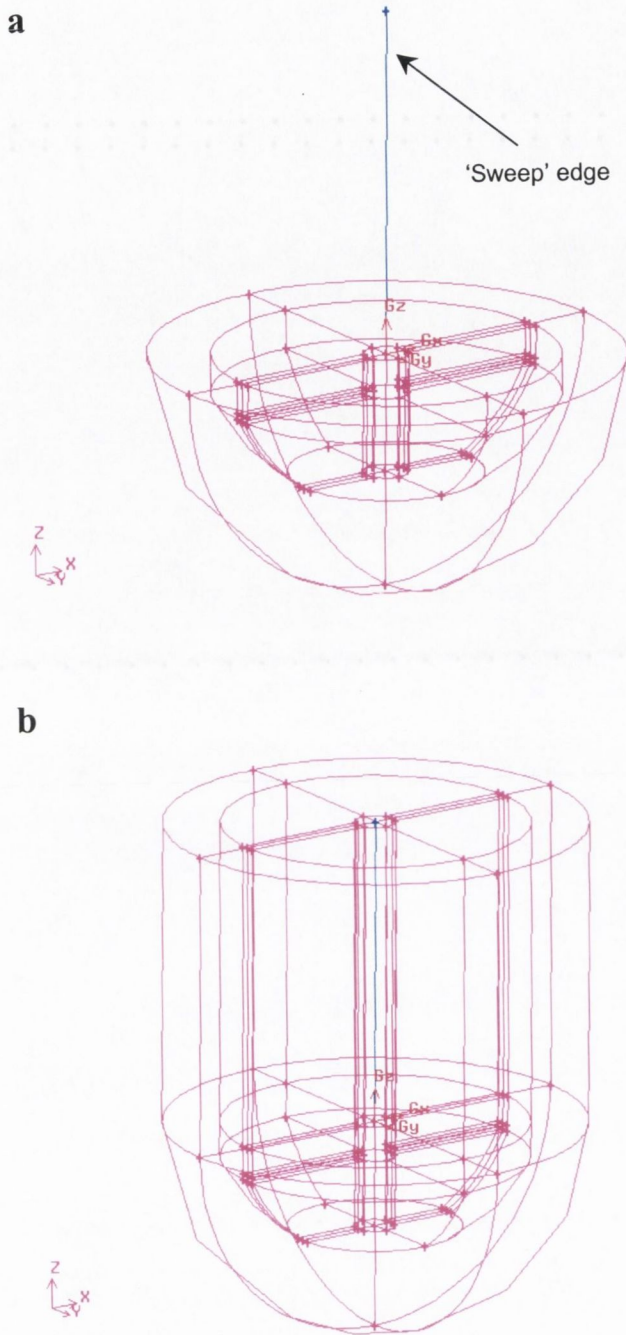


Figure 2.11 GAMBIT graphical interface diagram illustrating: (a) creation of 'sweep' edge prior to extrusion of cylindrical volume, and (b) final GAMBIT wireframe of USP paddle dissolution apparatus prior to meshing.

2.14.3.3 Introduction of Boundary Layers

In addition to the set-up constraints previously described, Fluent5 User's Guide (1998) recommends the need for sufficient resolution in the grid when solving flows that include swirl or rotation. The steep gradients in velocity and pressure involved in the regions of interface between fluid and solid components can complicate solution convergence. One tool to combat this problem is the ability to introduce 'boundary layers' in the fluid at any fluid-solid interface. This feature allows the user to define the thickness of the first layer of grid cells at the interface, the ratio of the thickness of subsequent layers and the total number of boundary layers at the interface. This tool was used to apply boundary layers at all interfaces between solid and fluid on the vessel volume. The criteria used for the formation of the boundary layers used are shown in Table 2.8, while the result of the application of boundary layers on the curved surface of the hemispherical volume is shown in Figure 2.12. Similarly, boundary layers were applied to all curved surfaces of the vessel volume at the interface between the vessel and the fluid as shown in Figure 2.13.

Table 2.8 *Criteria used for the formation of the boundary layers for structured grid approach (without the inclusion of a compact).*

SOLVER FORMULATION INPUT	SETTING
FIRST LAYER	200 μm
GROWTH FACTOR	1.5
TOTAL DEPTH	1.63 mm
NUMBER OF ROWS	4
INTERNAL CONTINUITY	No
CORNER SHAPE	Block
TRANSITION PATTERN	1:1
TRANSITION ROWS	0

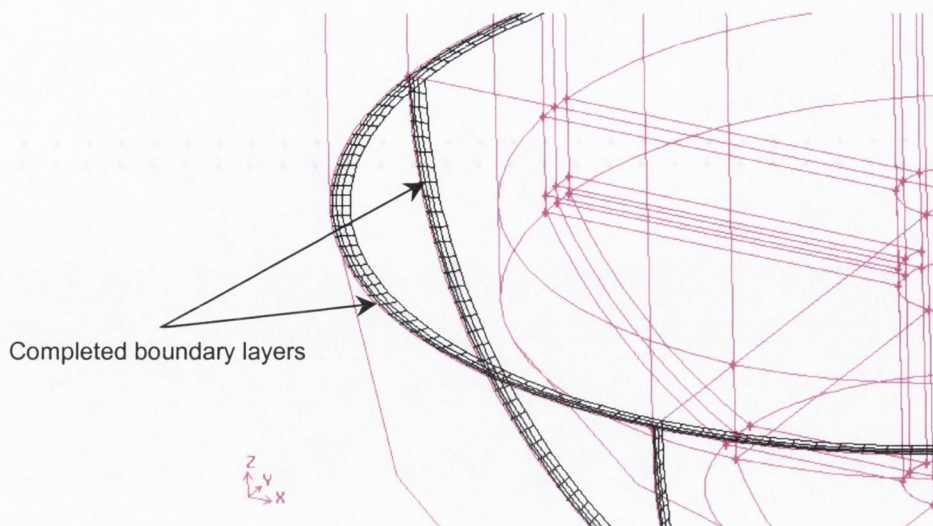


Figure 2.12 GAMBIT graphical interface diagram illustrating: the creation of boundary layers on the curved surfaces of the lower hemispherical volume.

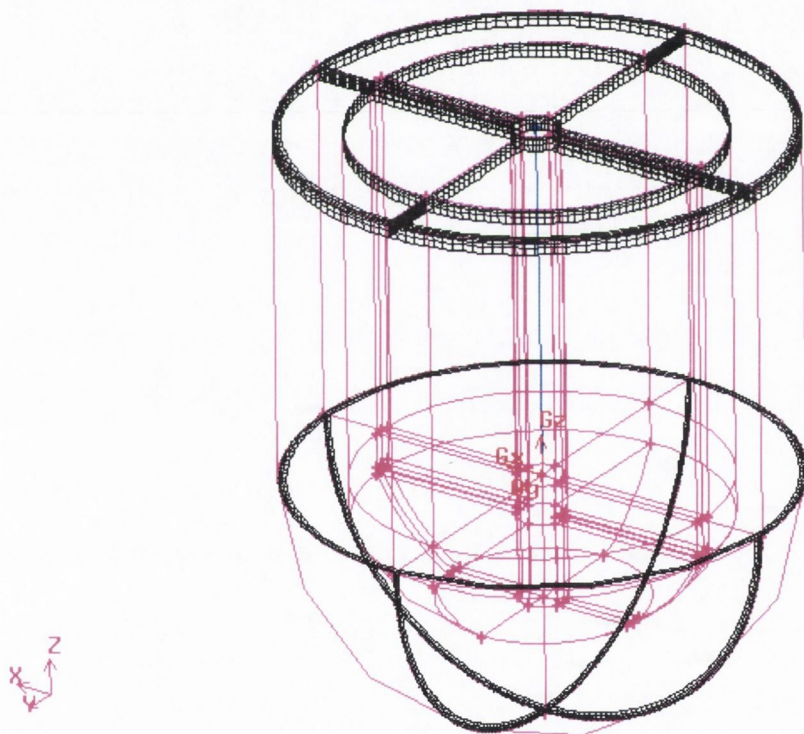


Figure 2.13 GAMBIT graphical interface diagram illustrating: the addition of boundary layers to all relevant edges at interface between the vessel geometry and fluid.

2.14.3.4 Mesh generation

The requirement of the application of the 'Presto' pressure discretisation scheme for the improved approach (see section 3.2.2.1) necessitated the use of a hexahedral or a quadrilateral basic mesh unit. Therefore, the choice of meshing tools for the

computational domain was limited to the cooper scheme. The cooper scheme is based on the principle of a volume consisting of a series of source faces, which may be projected on to each-other, in the direction of the remaining faces of the volume. Therefore, it is necessary to mesh individual edges, followed by individual faces of the relevant volume, to apply this meshing scheme. An example of the steps involved in the meshing of one volume of the computational domain is outlined in Figure 2.14, with the final mesh of this volume being shown in Figure 2.15. This procedure was repeated for all 54 volumes of the complete domain, the volumes of the hemispherical base of the vessel presenting particular difficulty for this approach. The final mesh setup was developed by refinement of individual sections of the grid in regions of high velocity gradient, by a gradual development process of successive grids to arrive at the final setup. The various grids examined contained between 500,000 and 2,000,000 individual cells. An illustration of the final geometry, after complete meshing, is seen in Figure 2.16.

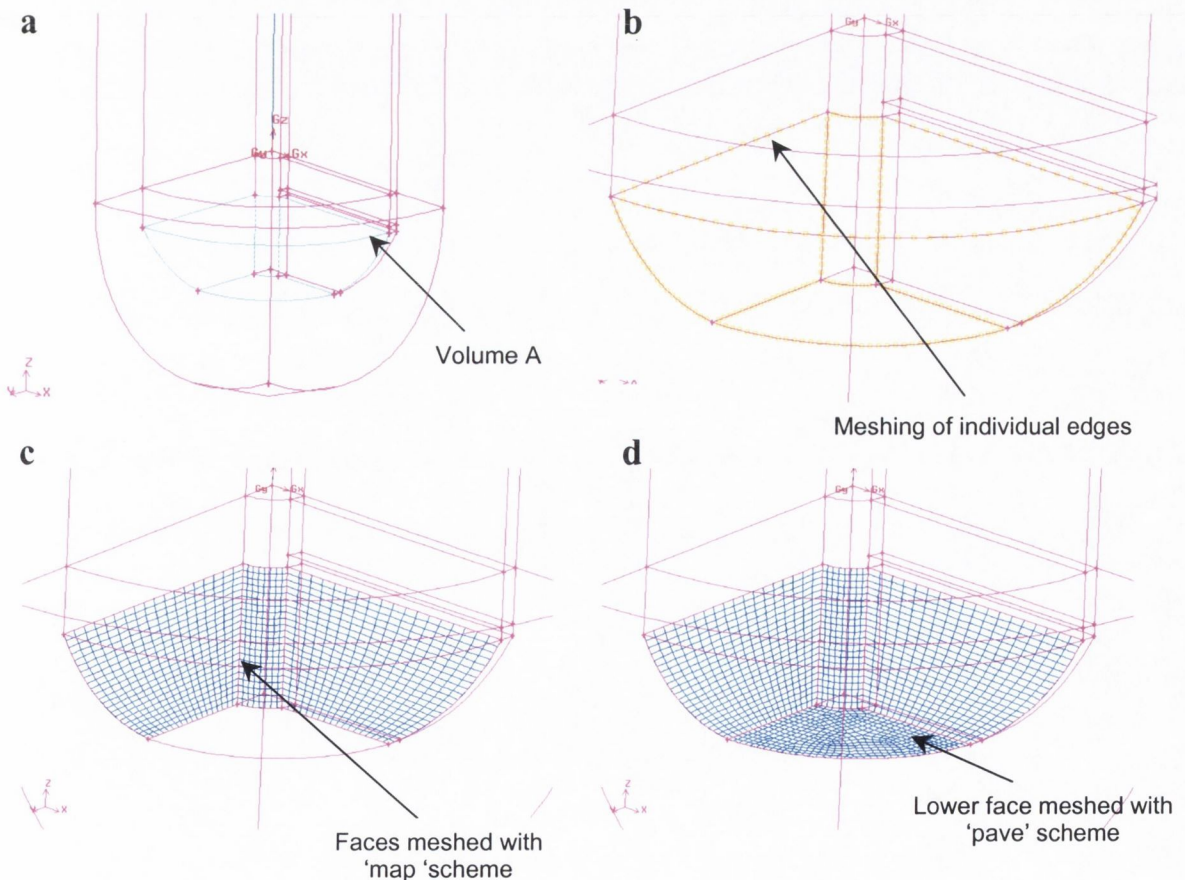


Figure 2.14 GAMBIT graphical interface diagram illustrating some steps involved in the meshing of a single volume: (a) position of current volume in the domain, (b) meshing of individual edges of current volume, (c) meshing of three faces of volume using the 'map' scheme and (d) meshing of lower face of volume using the 'pave' scheme.

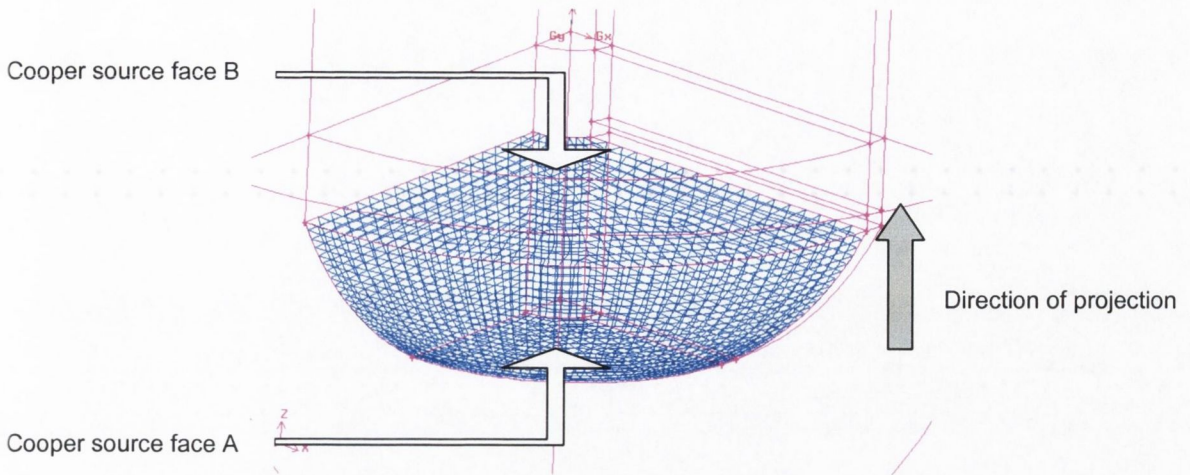


Figure 2.15 GAMBIT graphical interface illustrating the grid of the single volume after meshing using the ‘Cooper’ scheme, where face A was extruded through the volume to face B to produce the final grid.



Figure 2.16 GAMBIT graphical interface illustrating the grid of the complete volume after meshing using the ‘Cooper’ scheme.

A complete journal file, generated during the build-up of the complete grid using this structured grid approach is included in Appendix 6.

2.14.3.5 Boundary and continuum specification

Boundary and continuum specification using this newer approach required more meticulous selection of the relevant components, due to the increased number of faces and volumes that were generated. The details of the relevant components that were selected for the boundary specification are detailed in Table 2.9, while the details of the relevant components that were selected for the continuum specification are shown in Table 2.10.

Table 2.9 *Boundary specification details for structured grid approach (without the inclusion of a compact).*

BOUNDARY NAME	NUMBER OF FACES
VESSEL WALL	20
STIRRER WALL	52

Table 2.10 *Continuum specification details for structured grid approach (without the inclusion of a compact).*

BOUNDARY NAME	NUMBER OF VOLUMES
STIRRER	16
VESSEL FLUID	28

2.14.3.6 Set-up in FLUENT

The setup in Fluent did not differ significantly from that previously described for the initial setup in section 2.14.2.6. However, the modified approach did not include a multiple reference frame. It became apparent that the inclusion of a multiple reference frame was only necessary in situations where the vessel contained ‘baffles’. In cases of mixing vessels without baffles, a single rotating reference frame consisting of the fluid volume alone would be sufficient. The absence of a ‘multiple rotating reference frame’ would significantly simplify the problem in terms of computational calculation time (see introduction section 1.2.2.4.1).

2.14.3.6.1 Boundary conditions definition

In this modified set-up, the vessel fluid volume was defined as a rotating reference frame with angular rotation of 5.236 rad/s (50 rpm), while the stirrer wall was

stationary in the absolute reference frame. The vessel wall was defined as a rotating wall with an angular rotation of 0 rad/s (stationary in the absolute frame). As before, ‘water-liquid’ with the pre-defined viscosity (room temperature) was chosen as the material for the vessel volume.

2.14.3.6.2 Grid adaption

In the modified version of the set-up, it was desirable to have an area of high mesh refinement in the region of the stirrer wings. The grid in this area was produced to a high degree of refinement by the process previously described. However, a region of very high refinement was produced in the cells immediately beside the paddle by using the ‘hanging node’ adaption process. Each cell within a distance of four cells from the paddle surface was divided isotropically from a hexahedron into 8 hexahedra as shown in figure Figure 2.17, with a graphical illustration of a cut through the mid-plane (in line with the paddle) of the final grid after grid adaption being shown in Figure 2.18.

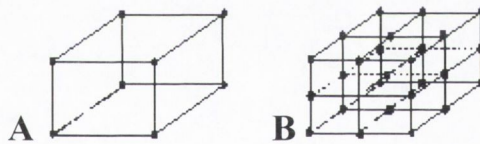


Figure 2.17 Principle of hanging node adaption of a 3D hexahedral Cell: (A) before adaption and (B) after adaption.

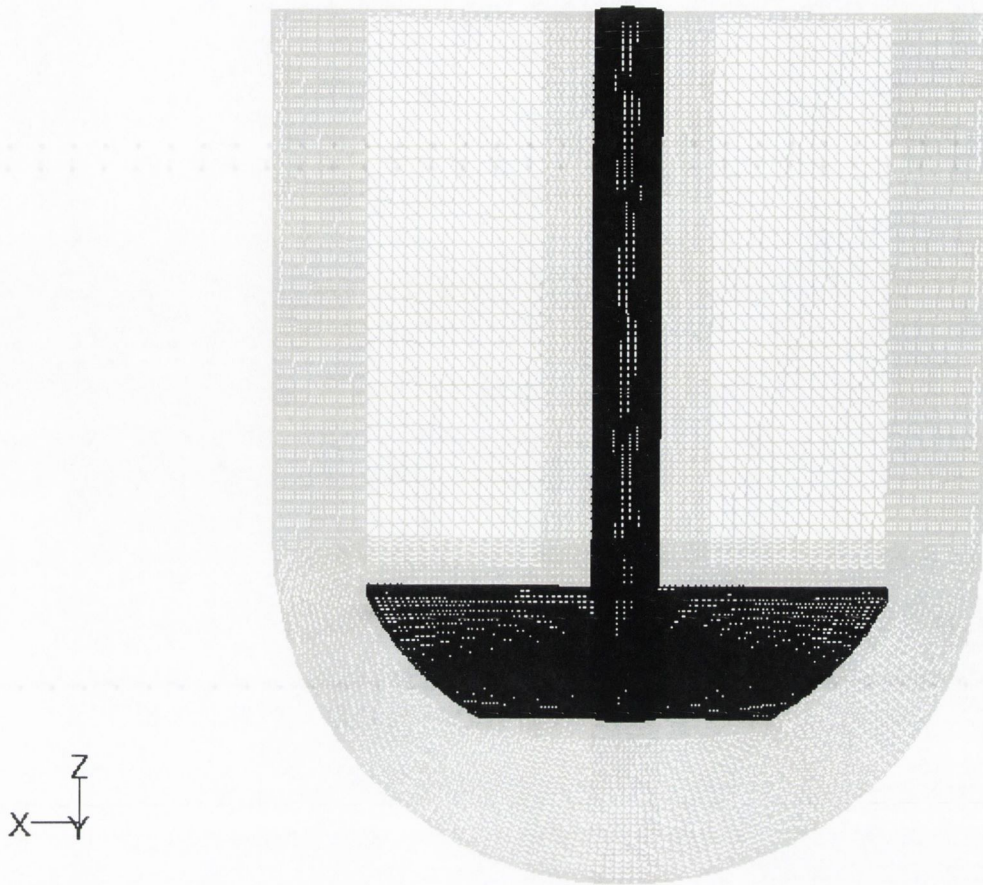


Figure 2.18 Final mesh network following grid adaption, illustrating a 2-dimensional cut through the mid-plane of the vessel and the mesh on the surface of the stirrer.

2.14.3.6.3 Parallelisation (grid partitioning)

Parallelisation was performed as previously described in section 2.14.2.6.2. All calculations were now performed on the SP processor, using 8 processors. Therefore, the complete domain was divided into 8 sub-domains, using ‘cylindrical Z axis’ as the bisection method.

2.14.3.6.4 Solver set-up

Fluent offers a large number of user defined solver formulation and solution control inputs. It was desirable, in the modified approach, to obtain fluid velocity measurements, which were in quantitative agreement with the experimental results of Bocanegra et al. (1990). Therefore, a considerable number of calculation runs were performed on the final version of the grid with modifications of each of the definable inputs, to obtain a solution, which was in agreement with the experimental data.

Following this approach, no alteration was made to the solver formulation; however, a number of changes were made to the solution control inputs, as summarised in Table 2.11. The changes were needed due to the complex nature of fluid flow containing a high degree of swirl (Fluent5 User's Guide, 1998). The Presto pressure discretisation scheme is recommended in such situations, while the other changes were attained through a gradual progression by comparison of successive result sets with the experimentally determined value, until there was close quantitative agreement.

Table 2.11 *Solution controls used in the structured grid approach.*

SOLUTION CONTROL FACTOR	INPUT	SETTING
UNDER-RELAXATION	Pressure	0.4
	Momentum	0.7
	Density	1
	Body Forces	1
DISCRETISATION	Pressure	Presto
	Momentum	First Order Upwind
	Pressure-Velocity Coupling	Simple C

2.14.3.6.5 Solution initialisation and iteration (Distributed memory SP system)

Solution initialisation was similar to that described in section 2.14.2.6.4. except that all calculations were performed on the SP after the 'case' and 'data' file for this problem were copied to this system. A journal file was again created, which contained the relevant commands to allow Fluent to read, iterate and save the relevant files, while running in background mode, similar to that shown in Appendix 7 (filename 'run.jou').

The IBM batch system (queue system), 'Loadleveler' is employed to run and schedule serial and parallel jobs on the SP system, as each node of the cluster is distributed to a defined user. This system setup requires the user to enter a queue system based on the type of job being submitted. Jobs are submitted through a command file, an example of which is included in appendix 8 (no_compact.cmd). An example of a command line on the SP shell, used to initiate the specified command file is as follows:

```
llsubmit no_compact.cmd
```

The command file, when initiated, enters the current job into the ‘Loadleveler’ queue system, until the defined number of compute nodes becomes available. Once initiated, the command file informs the system about the relevant information needed to run the job in parallel, including; the number of processors needed, the class of the job (length of time needed), the directory to be used to store the results, any output and error file names, the arguments needed to run the particular program (as previously described in section 2.14.2.6.4) and the journal file that contains the job commands (read file, iterate file, write file etc.).

2.14.3.6.6 Convergence

The default convergence criteria of $1e^{-3}$ were again used for the modified approach. The residuals of error for the modified approach are shown in Figure 2.19. The modified version reached the convergence criteria after 859 iterations without any further grid adaption, considerably faster than the original convergence iteration number of 2619. Results are discussed in Chapter 3 (section 3.2.3)

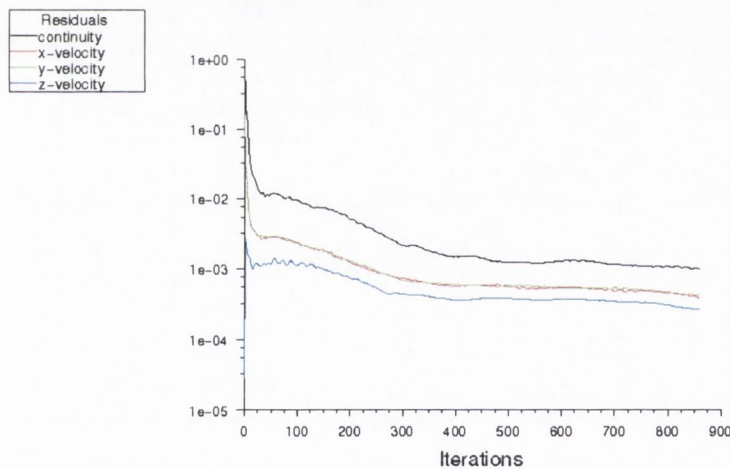


Figure 2.19 Residual error graph of the modified approach showing scaled residuals of error of momentum equations (x, y, and z components) and of the continuity equation versus number of iterations for the structured grid approach (without the inclusion of a compact). Note – units of y-axis are arbitrary.

2.14.4 Introduction of a cylindrical compact

2.14.4.1 Set-up in GAMBIT

A cylinder of 13mm diameter with a height of 11.5mm (3mm wax base plus 8.5mm compact height) was set up at the base of the vessel. This cylindrical volume was

then ‘intersected’ with the four quarters of the hemi-spherical base to define the new fluid volume of the vessel. This necessitated the formation of a new base of the compact and definition of the volume of the compact using the ‘stitch faces’ tool after selection of the relevant faces. The resulting wire-frame after addition of the compact is shown in Figure 2.20.

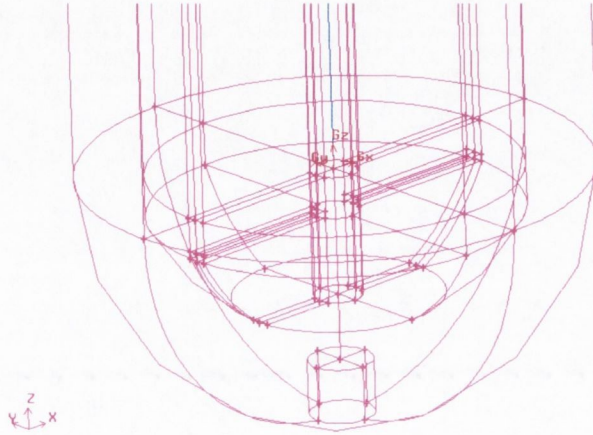


Figure 2.20 GAMBIT generated wire-frame of the USP dissolution apparatus after addition of a cylindrical compact.

Following the introduction of the compact, the set-up in GAMBIT was the same as that previously described, with regard to boundary layer inclusion, mesh generation using the hexahedral approach and the boundary and continuum set-up. However, the inclusion of the compact complicated the meshing process in the hemispherical region of the vessel. Meshing was facilitated by ensuring that individual edges of the top circular face quarters of the compact were meshed in exactly the same manner as the bottom circular face quarters of the paddle (as these faces were part of the projection faces in the volume-mesh operation). The addition of the compact at the base of the vessel also necessitated the definition of the compact as a wall in the boundary set-up and as a solid in the continuum set-up. Results are discussed in Chapter 3 (section 3.2.4).

2.14.4.2 Set-up in Fluent

2.14.4.2.1 Boundary conditions

The set-up in Fluent was exactly as described for the structured grid approach (section 2.14.3.6), with the compact surface being defined as stationary in the absolute reference frame.

2.14.4.2.2 Grid adaption

Similar to the solution with no compact, each cell within a distance of four cells from the paddle surface was refined using the hanging node adaption technique. Similarly, all cells within a region of three cells from the compact were also refined using hanging node adaption.

2.14.4.2.3 Parallelisation

Parallelisation was performed as previously described in 2.14.3.7. All calculations were performed on the SP processor, using 8 processors. Therefore, the complete domain was divided into 8 sub-domains, using the 'cylindrical Z axis' as the bisection method as described in section 2.14.3.6.3

2.14.4.2.4 Solver set-up

The solver set-up was as previously described in 2.14.3.6.4.

2.14.4.2.5 Solution initiation and iteration

These were as described in section 2.14.3.6.5.

2.14.4.2.6 Convergence

The convergence criteria were again set to $1e^{-3}$.

Results are discussed in section 3.2.4.

2.14.4.3 Increased grid resolution immediately outside compact

In order to examine fluid shear rates on the various surfaces of a compact, it was necessary to include a second cylinder (envelope cylinder) with a height and diameter

of 1mm greater than the cylindrical compact to allow the formation of a region of high refinement around the cylindrical compact. Again, this envelope cylinder was intersected with and later subtracted from the four quarters of the hemispherical volume at the base of the vessel to define four new regions of thickness, 1mm, between the compact and the envelope cylinder, as shown in Figure 2.21.

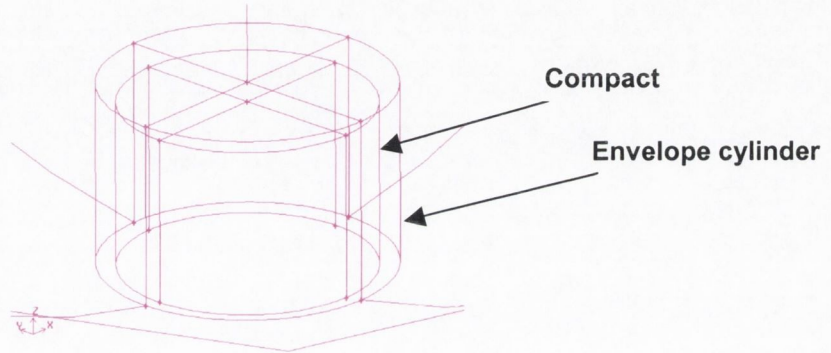


Figure 2.21 GAMBIT generated wireframe of a compact at the base of the vessel (diameter 13 mm, height 8.55 mm) surrounded by a cylinder with height and diameter 1mm greater than the compact cylinder (envelope cylinder).

The most efficient method of increasing grid resolution in the region of a surface is to include the formation of a boundary layer from the surface. In the interest of retaining the same degree of refinement outside the curved surface and the top planar surface, it was necessary to create four new curved surfaces at the intersection between each quarter section above the planar surface and outside the curved surface. To this end, four new edges were created in these regions by connecting the relevant vertices as shown in Figure 2.22.

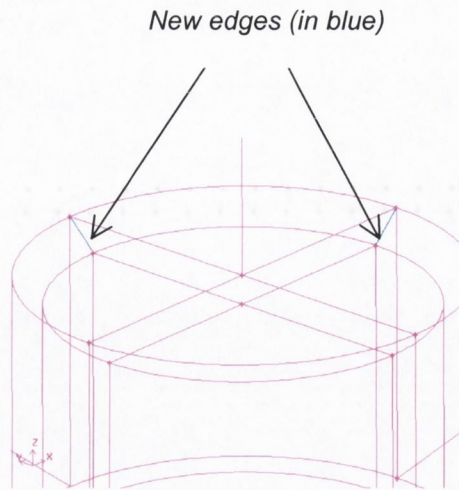


Figure 2.22 Formation of new edges at a 45° plane between the quarter sections above the planar surface and outside the curved surface of the compact. Four new edges were created in total.

After all the relevant new edges were formed, the new surfaces were defined at the intersection between each quarter section above the planar surface and outside the curved surface using the ‘stitch edges’ tool to define the new faces. This allowed the formation of eight new volumes outside the compact (four above the planar surface and four outside the curved surface) using the ‘stitch faces’ tool to define the new volumes from existing faces.

2.14.4.3.1 Boundary layer addition in the region outside the compact

After the volumes outside the compact had been defined, it was possible to add boundary layers extending from the newly defined faces between the quarter sections above the planar surface and outside the curved surface of the compact. The criteria used for the formation of the boundary layers used are shown in Table 2.12, while the result of the application of boundary layers on the various individual faces outside the compact is shown in Figure 2.23(a-c). Boundary layers were applied to all other curved surfaces of the vessel volume at the interface between the vessel and the fluid as previously described in section 2.14.3.3 and shown in Figure 2.23.

Table 2.12 Criteria used in the formation of boundary layers immediately outside the compact for set-up with compact surrounded by a refined 'envelope' volume.

SOLVER FORMULATION INPUT	SETTING
FIRST LAYER	20 μm
GROWTH FACTOR	1.5
TOTAL DEPTH	0.42 mm
NUMBER OF ROWS	6
INTERNAL CONTINUITY	No
CORNER SHAPE	Block
TRANSITION PATTERN	1:1
TRANSITION ROWS	0

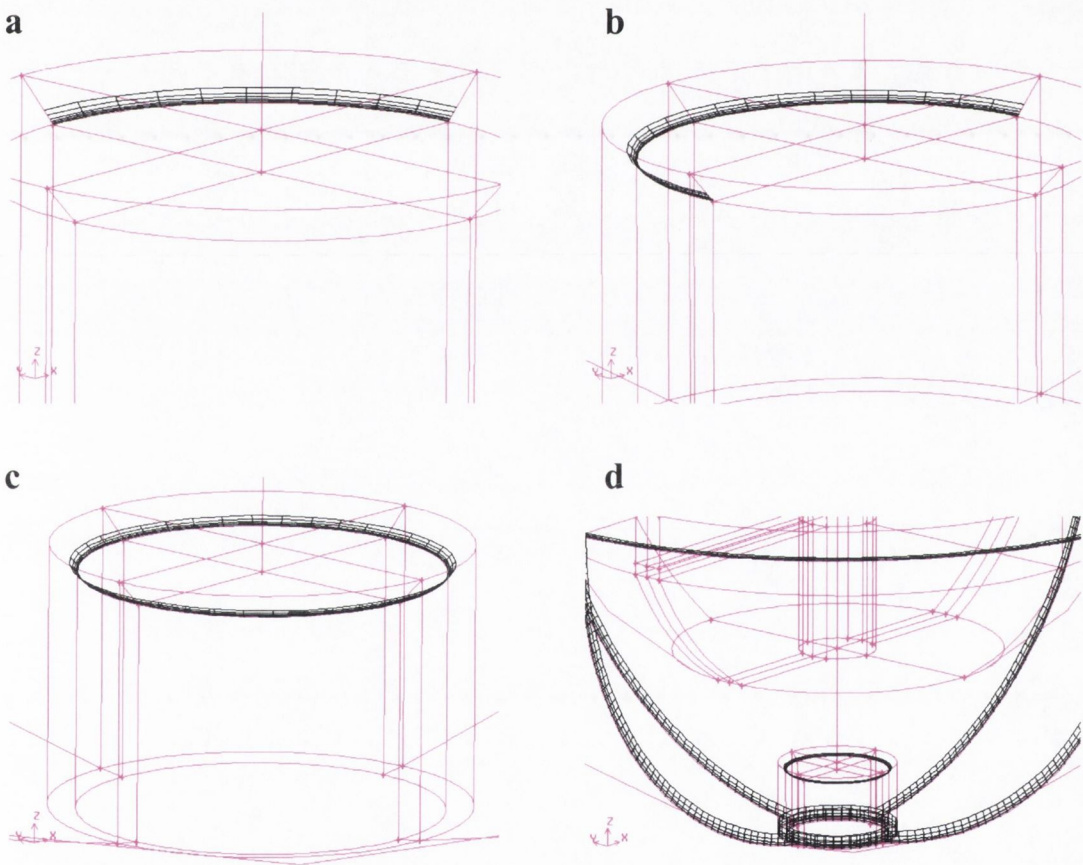


Figure 2.23 GAMBIT graphical interface diagram illustrating: the creation of boundary layers on the newly defined faces on the intersection between the quarter sections above the planar surface and the sections outside the curved surface of the compact (a, b and c) and the addition of further boundary layers to the lower curved surfaces of the compact (d).

2.14.4.3.2 Mesh generation

The volumes immediately surrounding the compact were meshed with a hexahedral mesh set-up using the cooper mesh tool, sweeping the boundary layers parallel to the compact surface to produce uniform refinement outside all surfaces of the compact. In order that the boundary layers were not ‘washed out’ during the projection operations, it was necessary to turn off the auto smoothing of the mesh options in the meshing defaults panel. For the remainder of the domain, all meshing was carried out as previously described in section 2.15.3.4.

2.14.4.3.3 Boundary and Continuum specification

The details of the relevant components that were selected for the boundary specification are detailed in Table 2.13, while the details of the relevant components that were selected for the continuum specification are shown in Table 2.14.

Table 2.13 *Boundary specification details for set-up with compact surrounded by a refined ‘envelope’ volume.*

BOUNDARY NAME	NUMBER OF FACES
VESSEL WALL	24
STIRRER WALL	52
COMPACT WALL	9

Table 2.14 *Continuum specification details for set-up with compact surrounded by a refined ‘envelope’ volume.*

BOUNDARY NAME	NUMBER OF VOLUMES
STIRRER	16
VESSEL FLUID	36
COMPACT	1

2.14.4.4 Set-up in Fluent

The grid containing the refined region immediately surrounding the compact was set up to run in FLUENT as previously described in section 2.14.4.2. Results are discussed in section 3.2.4.2.

2.15 DYNOCHEM™ – APPLICATION OF MASS TRANSFER MODEL

Using the film theory as outlined in the introduction (section 1.5), mass transfer was modelled from simple layered drug delivery systems (section 4.5), inert non-swellable non-erodible matrix compacts (section 5.4.2.4) and layered matrix drug delivery systems (section 5.4.2.5). The development of the individual mass transfer models are outlined in the relevant results section, while the completed models are included in Appendices 11-13.

RESULTS AND DISCUSSION

Chapter 3

Hydrodynamics and dissolution in the paddle dissolution apparatus

3.1 DISSOLUTION RATES FROM SURFACES OF SINGLE COMPONENT COMPACTS

3.1.1 *Introduction*

Traditionally, when modelling dissolution according to the Nernst-Brunner equation, it has been assumed that the apparent diffusion boundary layer thickness is constant on all surfaces of the dosage form for a particular paddle rotation speed. In this section, cylindrical compacts (of similar dimensions to the layered systems studied in later chapters) were coated with paraffin wax to allow release from certain surfaces only. Calculation of the apparent diffusion boundary layer thickness and the corresponding dissolution rate constant from the various surfaces, should facilitate a-priori modelling of dissolution rates from layered drug delivery systems. The initial objective of the present work was to experimentally estimate the apparent diffusion boundary layer thickness and dissolution rate constant, parameters reflective of the hydrodynamics of the systems, for single component compacts, at different surfaces and positions in the paddle dissolution apparatus.

3.1.2 *Dissolution from entire surface of compacts*

Dissolution was initially studied from the complete surface of compacts containing 1500mg of benzoic acid prepared as outlined in section 2.9, compacts having similar dimensions to the layered compacts later studied. Dissolution was performed in 0.1N HCl as described in section 2.11. Dissolution profiles from these systems, at 50 rpm and 100 rpm, can be seen in Figure 3.1.

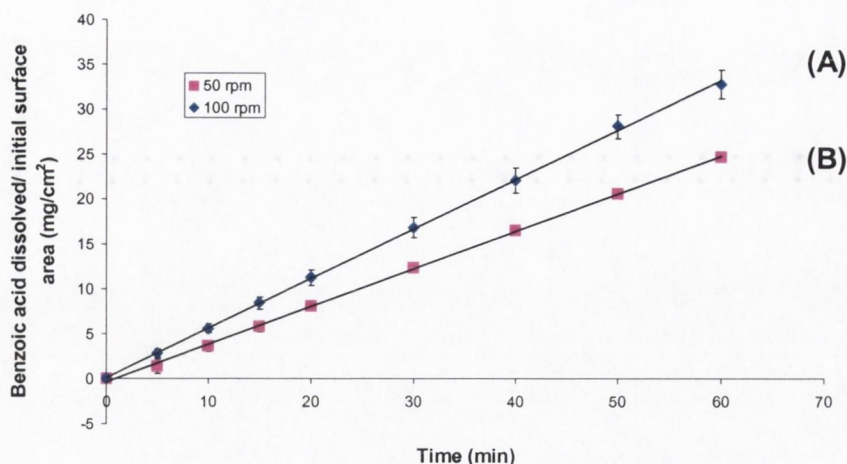


Figure 3.1 Comparison of dissolution profiles from uncoated benzoic acid compacts in the USP paddle dissolution apparatus with paddle rotation of 50 and 100 rpm. Error bars indicate standard deviations. Compacts are designated as A (100rpm) and B (50rpm) for later comparisons.

Although the surface area of the compacts was decreasing with time, the dissolution profiles are practically linear over the time period studied, as the decrease in surface area did not exceed 10% of the initial surface area exposed. Therefore values of r^2 of the least squares linear regression of the dissolution profiles were equal to 0.9993 and 0.9996 for 50rpm and 100rpm respectively. Because of the high r^2 values, the initial surface area values of these compacts were used in the calculation of h , the thickness of the apparent diffusion boundary layer and k , the dissolution rate constant. Estimates of k and h for these systems were calculated from the Nernst-Brunner equation (Equation 1.5), where dW/dT was the slope of a plot of amount release versus time, and $k = D/h$, can be seen in Table 3.1. As expected, there was a statistically significant difference between the dissolution rates at 50rpm and 100 rpm ($p < 0.05$).

Table 3.1 Values for initial surface area of compacts, with estimates of h and $k \pm$ standard deviations at 50 and 100 rpm ($n=6$).

SYSTEM STUDIED	A (cm ²)	h (x 10 ⁴ cm)	k (x 10 ⁴ cm/ sec)
A (100 rpm)	6.17	61.4 ± 2.9	20.2 ± 0.9
B (50 rpm)	6.15	80.9 ± 6.1	15.4 ± 1.2

A value of h for the complete surface of a compact of similar diameter, but smaller height has been previously calculated to 60×10^{-4} cm at 50 rpm (Healy, 1995).

Furthermore, it has been shown previously that dissolution rate in the USP paddle dissolution apparatus (into un-buffered solution) is proportional to $(rpm)^n$, where n takes a value of between 0.5 and 0.66 (Ramtoola, 1988). In the present case, however, n was calculated to be 0.39. The physical dimension and weights of the present compacts prevented their movement during the dissolution test and were therefore static, centrally at the base of the vessel during the test. It is possible that non-uniform hydrodynamic conditions on the various surfaces of the static compacts could be the cause of such abnormal dissolution behaviour. Further indication of this assumption was the observation of a groove or indent effect at the base of these compacts following dissolution, in the region below $\sim 3\text{mm}$ from the base of the compacts, as indicated in Figure 3.2.

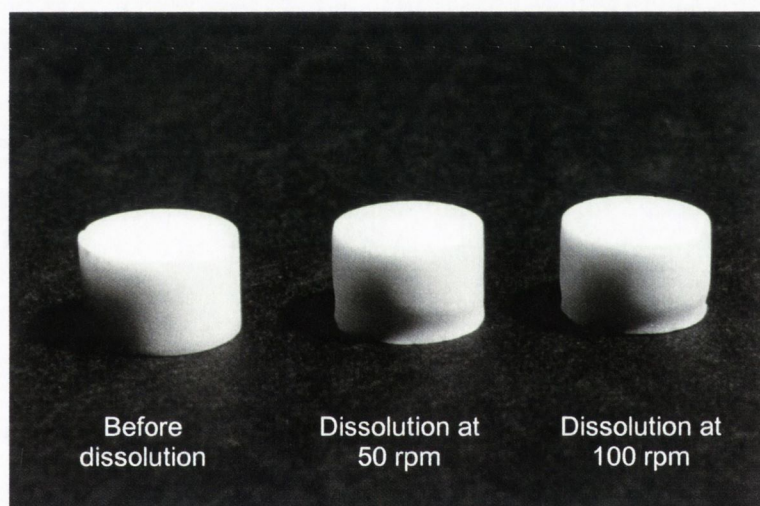


Figure 3.2 Photograph of the compact before dissolution and after dissolution for 1 hour, at 50 and 100 rpm.

It was postulated that the fluid flow patterns at the base of the USP paddle dissolution vessel may account for the observed grooving effect. This change in hydrodynamics may be caused by a change in fluid velocity from an inward radial velocity to an axial velocity component in this region of the vessel. All further dissolution work was carried out at 50 rpm only, as this pitting effect was not as noticeable at the lower rpm. In a further effort to overcome this pitting effect, dissolution studies were also carried out on compacts, which were raised up above this region on a pedestal of paraffin wax (approximately 3mm high). The effect of raising the compacts above

this region can be seen in the postulated fluid flow patterns of the USP paddle, shown in Figure 3.3.

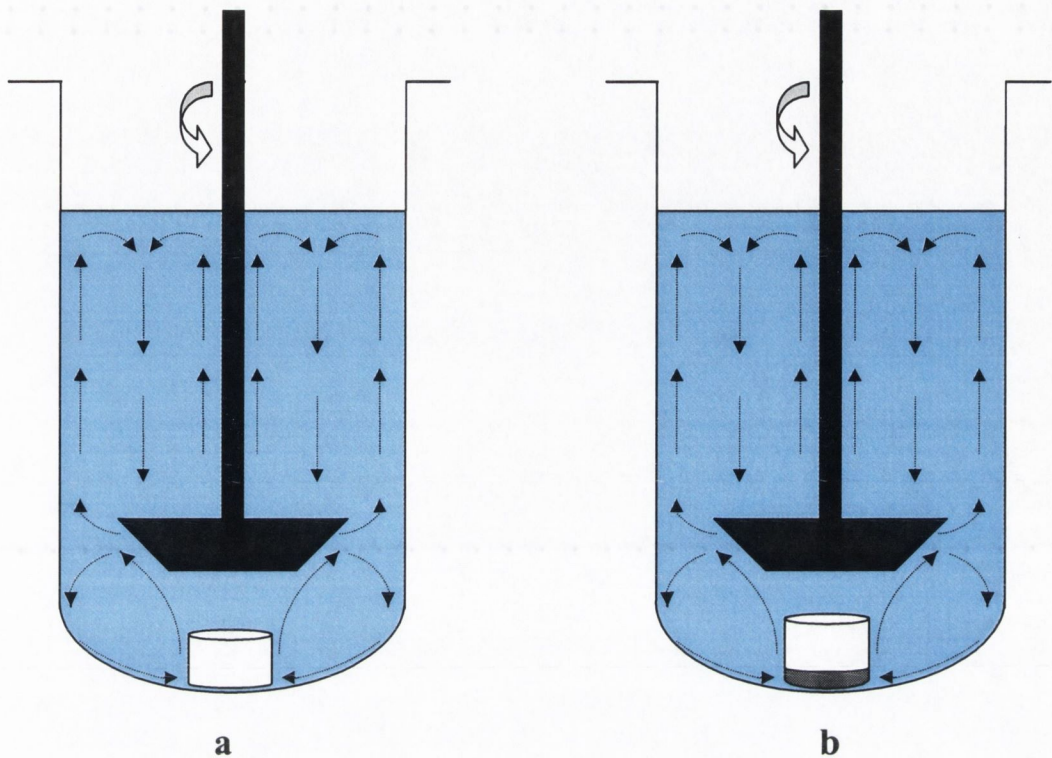


Figure 3.3 Diagram of postulated fluid flow patterns surrounding compacts which are located at the base (a) and raised up from the base (b) of the USP paddle dissolution apparatus vessel (modified from Beckett et al., 1996 and Diebold, 2000).

3.1.3 Dissolution from curved surface of compacts only

Compacts were then coated on both planar surfaces with paraffin wax which, when hardened, formed a coating impervious to the dissolution medium. This allowed drug dissolution to occur from the curved surfaces only. Dissolution was studied from the curved surfaces of the following types of compacts; compacts of 250 mg weight and 1.5 mm height (system C), compacts of full height (8.5 mm) at the base of the vessel (system D) and compacts of full height raised above the bottom of the vessel by 3 mm (system E). It was thought that raising the compacts above the bottom of the vessel would overcome the pitting effect, which had been previously seen. The method used involved moulding a portion of paraffin wax onto the base of the compact using a stainless steel disc holder. The resulting portion of wax had the same diameter as the compact and a mean height of 3mm. Dissolution profiles from these systems can be

seen in Figure 3.4. No indentation was observed on the compacts that were raised above the bottom of the vessel.

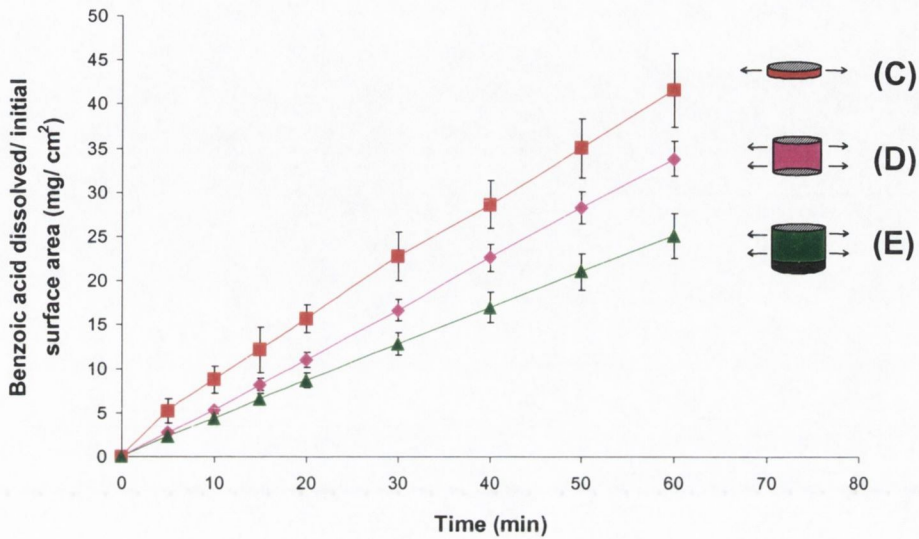


Figure 3.4 Comparison of dissolution profiles from the curved surface of compacts at different heights at the base of the USP paddle dissolution vessel at 50 rpm. Error bars indicate standard deviations.

There was a statistical difference between the slopes of these dissolution profiles ($p < 0.05$). The grooving towards the base of the curved surface was again evident with the compacts, which were coated top and bottom (system D), while this phenomenon was not apparent with the compacts that were raised on a wax pedestal. The estimates of k and h for these systems, calculated as outlined above, can be seen in Table 3.2 (surface area taken to be the initial surface area as r^2 of the least squares linear regression fit ≥ 0.997 for all systems).

Table 3.2 Values for initial surface area of compacts releasing from curved surface area at different heights at the base of vessel, at 50 rpm, with estimates of h and $k \pm$ standard deviations ($n=6$).

SYSTEM STUDIED	A (cm ²)	h (x 10 ⁴ cm)	k (x 10 ⁴ cm/ sec)
C	0.61	50.4 ± 5.3	24.7 ± 2.5
D	3.48	59.7 ± 4.2	20.8 ± 1.4
E	3.51	81.6 ± 7.8	15.3 ± 1.5

3.1.4 Dissolution from planar surfaces of compacts only

Compacts were also coated on one planar surface and on the curved surfaces with molten paraffin wax, which, when hardened, formed a coating impervious to the dissolution medium. This allowed drug dissolution to occur from one planar surface only. Dissolution was studied from the planar surfaces of the following types of compacts; from the top surface of a compact with height 1.5 mm (system F), from the top surface of a compact of full height 8.5 mm which had been raised by 3 mm from the bottom of the vessel by a wax pedestal (system G), from top surface of compacts of full height (H) and from the bottom surface of compacts of full height (system I). Dissolution profiles of amount released per initial surface area from these systems can be seen in Figure 3.5. The estimates of k and h for these systems can be seen in Table 3.3.

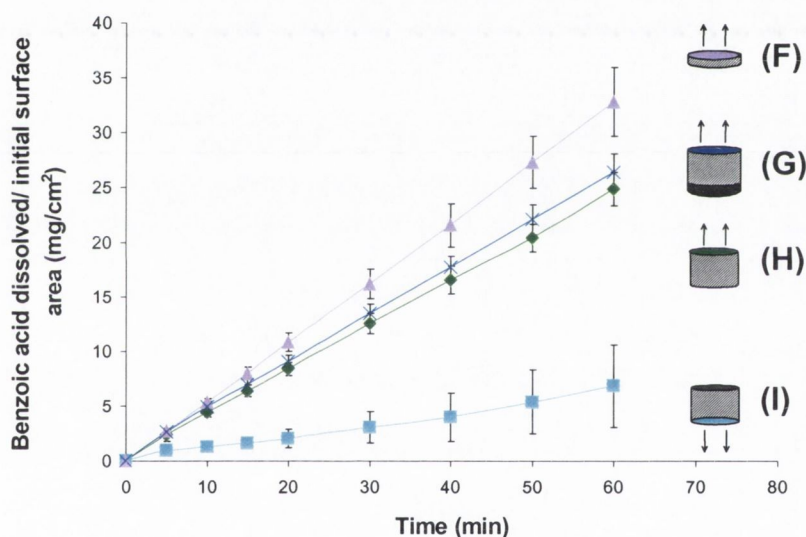


Figure 3.5 Comparison of dissolution profiles from the planar surface of compacts at different heights at the base of the USP paddle dissolution vessel at 50 rpm. Error bars indicate standard deviations.

Table 3.3 Values for initial surface area of compacts releasing from planar surface area, with estimates of h and $k \pm$ standard deviations ($n=6$).

SYSTEM STUDIED (rpm)	A (cm ²)	h (cm x 10 ⁴)	k (x 10 ⁴ cm/ sec)
F	1.33	62.5 ± 5.5	19.9 ± 1.8
G	1.33	78.2 ± 5.2	16.2 ± 1.1
H	1.33	83.0 ± 4.4	14.9 ± 0.8
I	1.33	595.8 ± 573.0	3.9 ± 2.7

The calculated dissolution rate constants of individual compacts of all systems (A-J) were then examined to allow comparison of variation between systems with variation within systems (error) in a one-way analysis of variance test (ANOVA). The results of the analysis of variance test are shown in Table 3.4. The low p value associated with the analysis of variance ($p < 0.001$) indicates that there is a highly significant difference in the dissolution rate constant, depending on the surface studied. To investigate which systems were significantly different, the least significant difference (LSD) was calculated using the pooled estimate of the variance based on all data. The LSD for a significance level, α , of 0.05 was calculated to be $1.6 \times 10^{-4} \text{ cm s}^{-1}$. There were four separate groups of statistically different dissolution rate constants, ranked in increasing order as follows:

a) System I; b) systems H, E, B and G; c) systems F and D; and d) system C.

Table 3.4 *The analysis of variance of k (cm s^{-1}) for the systems studied.*

SOURCE OF VARIATION	SUM OF SQUARES ($\times 10^6$)	DEGREES OF FREEDOM	MEAN SQUARES ($\times 10^6$)	F	P value
Between Systems	15.8	7	2.3	76.04	0.000
Error	1.1	40	0.0		
Total	16.9	47			

3.1.4.1 Dissolution rate differences from various surfaces

The dissolution rate constant for the curved surface (system D) was statistically significantly greater than that for either the upper (system H) or lower (system I) planar surfaces. There was a five-fold difference in k between the curved surface and the lower planar surface and a 1.4-fold difference between the curved surface and the upper planar surface.

3.1.4.2 Dissolution differences from various locations

The dissolution rate constant for the curved surface was statistically significantly greater when the compact was sitting on the base of the vessel (1.4-fold greater for system D compared to system E), while there was no significant change in k for the top planar surface when the compact was sitting on the base of the vessel (system H) compared to when it was raised (system G). The dissolution rate constants were also

statistically significantly greater for the small compacts than the large compacts raised from the base of the vessel, with a 1.6-fold difference in k when dissolution was from the curved surface (system C compared to system E) and a 1.2-fold difference in k when dissolution was from the top surface (system F compared to system G).

3.1.5 Conclusion

Statistically different dissolution rates were observed from various surfaces of compacts of benzoic acid which were static in a position centrally below the paddle during the dissolution test. Dissolution rates varied depending upon the surface and the location of the dissolving surface. Assuming that variable fluid dynamics in this region of the dissolution vessel were responsible for such observations, it was desirable to study such hydrodynamic behaviour in greater detail. Computational Fluid Dynamics (CFD) provided a most applicable tool to examine the fluid flow behaviour in this region and the fluid shear rates on the various surfaces of compacts studied.

3.2 CFD MODELLING OF FLUID DYNAMICS IN THE USP PADDLE DISSOLUTION APPARATUS

3.2.1 Introduction

The shortfall of the application of Computational Fluid Dynamics (CFD) to most real life situations is the lack of experimentally determined fluid flow rates in such situations to act as a validation tool for the predictions. Owing to the lack of information regarding the fluid flow behaviour in the USP paddle dissolution apparatus, and considering variability of fluid dynamics in the vessel as a contributory factor to observed variability in dissolution results, Bocanegra (1988) experimentally measured fluid velocity components at various planes in the USP dissolution apparatus using laser Doppler velocimetry techniques. These measurements provide an ideal opportunity to compare virtually determined CFD fluid dynamics in the USP apparatus with real data for fluid flow in the vessel. Kosiol (2000) used CFD to virtually determine fluid flow behaviour in the USP paddle dissolution apparatus at 50 rpm, using an unstructured grid approach. Qualitatively, the resulting CFD generated data compared well with the Bocanegra measurements, although there was quite a quantitative discrepancy. The aim of the present work was to improve on the CFD approach to attain CFD predicted data which agrees quantitatively with the laser Doppler measurements and to attain solutions at higher than the previous limit of 60 rpm. Ultimately, it was desired to use CFD to predict dissolution rates from virtual compacts in vessel.

3.2.2 Unstructured Grid Approach

The initial CFD approach involved repeating the unstructured grid method used by Kosiol (2000). The methods used are detailed in section 2.14.2. The viscosity value used for water in this initial model was that of 20°C, as the laser Doppler measurements of fluid flow in the USP paddle apparatus were performed at room temperature (Bocanegra, 1988).

3.2.2.1 Comparison with laser Doppler measurements

Bocanegra et al. (1990) produced laser Doppler measured velocity profiles from a series of planes at various heights and radii within the USP paddle apparatus, with outputs of axial radial, and tangential velocities as illustrated by Figure 3.6.

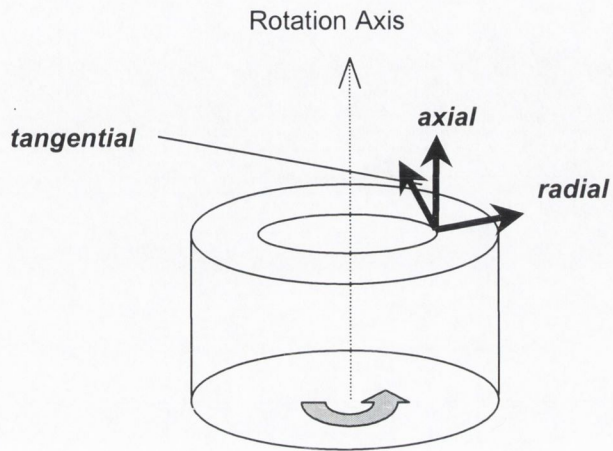


Figure 3.6 Cylindrical velocity components used in all velocity measurements. Positive axial indicates motion towards the surface; positive radial indicates motion towards the wall, while positive tangential indicates motion in the direction of paddle rotation.

The velocity profiles produced consisted of normalized velocity components for different radii at a certain plane height versus 'paddle relative position in degrees' (i.e. the angle made between the point in the vessel being analysed and the position of the paddle). All of the velocity data were normalized to the paddle tip speed (= 0.196 m/s at 50 rpm). Geometrical parameters are also normalised. The height of the fluid level (75.5 mm) measured from the plane where the hemispherical bottom develops and the radius of the hemispherical bottom (51 mm), respectively, are used in the normalization process. The normalised co-ordinate system adopted by Bocanegra et al. is indicated in Figure 3.7.

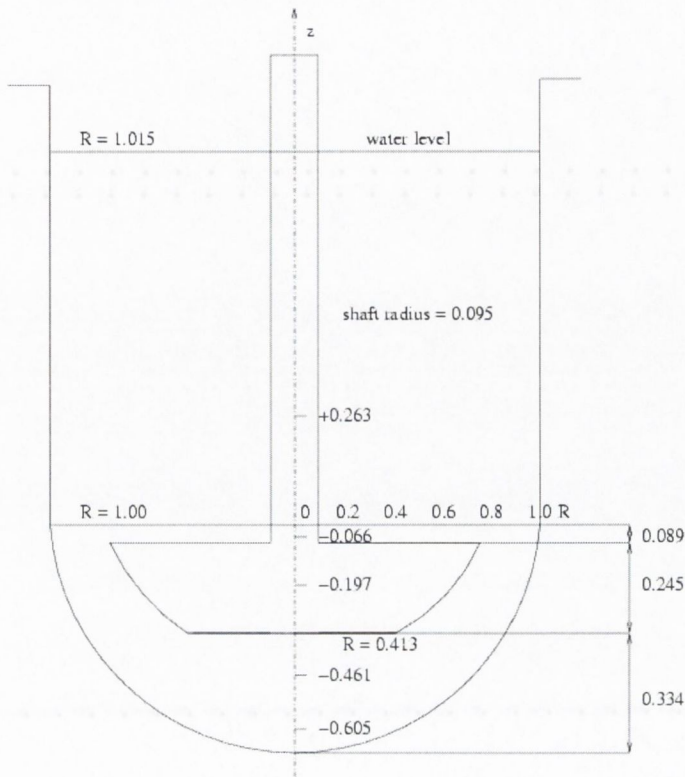


Figure 3.7 Normalised co-ordinate system used by Bocanegra et al. (1990) for the USP dissolution apparatus, where $R=r/r_w$ ($r_w = 50.8$ mm, the radius of the vessel above the hemispherical base) and $Z = z/z_1$ ($z_1 = 75.5$ mm, the height of the dissolution medium from the centre of the hemispherical base). The horizontal planes, $Z=+0.263$, $Z=-0.066$, $Z=-0.197$, $Z=-0.461$ and $Z=-0.605$ represent the horizontal heights of virtual planes in the vessel, where fluid velocity measurements were made.

Comparisons with the Bocanegra data are presented for three planes in the initial approach. In all contour plots, the paddle is positioned in line with the x-axis.

3.2.2.1.1 Tangential velocities 5.3 mm from base of vessel

Contours of predicted tangential velocities at a plane 5.3mm from the base of the vessel are shown in Figure 3.8(a), while the corresponding normalised (relative to paddle tip) predicted and measured tangential velocities (at the appropriate Bocanegra radii) are shown in Figure 3.8(b) and (c) respectively. Comparison reveals that the CFD predicted velocities are of a similar magnitude to the experimentally determined values. However, it is obvious that the curvature predicted between 0° and 180° and repeated again (periodicity) between 180° and 360° by the CFD results is not exhibited by the experimental values. The measured velocities predict an increase in tangential velocities at increasing radii, which Bocanegra referred to as 'solid body

rotation'. However, there is no graded increase in tangential velocities at increasing radii in the CFD predicted results, in fact radii $R=0.177$, 0.262 and 0.344 are in reverse graded order to the experimentally determined values.

3.2.2.1.2 Radial velocities 16.2 mm from the base of the vessel

Contours of predicted radial velocities at a plane 16.2 mm from the base of the vessel are shown in Figure 3.9(a), while the corresponding normalised (relative to paddle tip) predicted and measured radial velocities (at the appropriate Bocanegra et al. radii) are shown in Figure 3.9(b) and (c) respectively. The laser Doppler measurements indicated that the radial velocities fluctuate by only a small amount from zero on this plane as the paddle rotates. Again, this observation is not captured by the CFD simulated data, particularly for the radii 0.262 and 0.427 .

3.2.2.1.3 Tangential velocities 26.6 mm from the top of the paddle wings

Contours of predicted tangential velocities at a plane 26.6 mm from the base of the vessel are shown in Figure 3.10(a), while the corresponding normalised (relative to paddle tip) predicted and measured tangential velocities (at the appropriate Bocanegra radii) are shown in Figure 3.10(b) and Figure 3.10(c) respectively. The CFD results agreed qualitatively with the experimental, as there is little fluctuation of normalised tangential velocities with paddle position in both the experimental and CFD predicted results. An estimate of the discrepancy between the simulated results for this position, calculated on a visual approximation of the mean velocity, was calculated to be in the region of 35-40%, although the discrepancy for some of the other profiles would appear to be considerably higher.

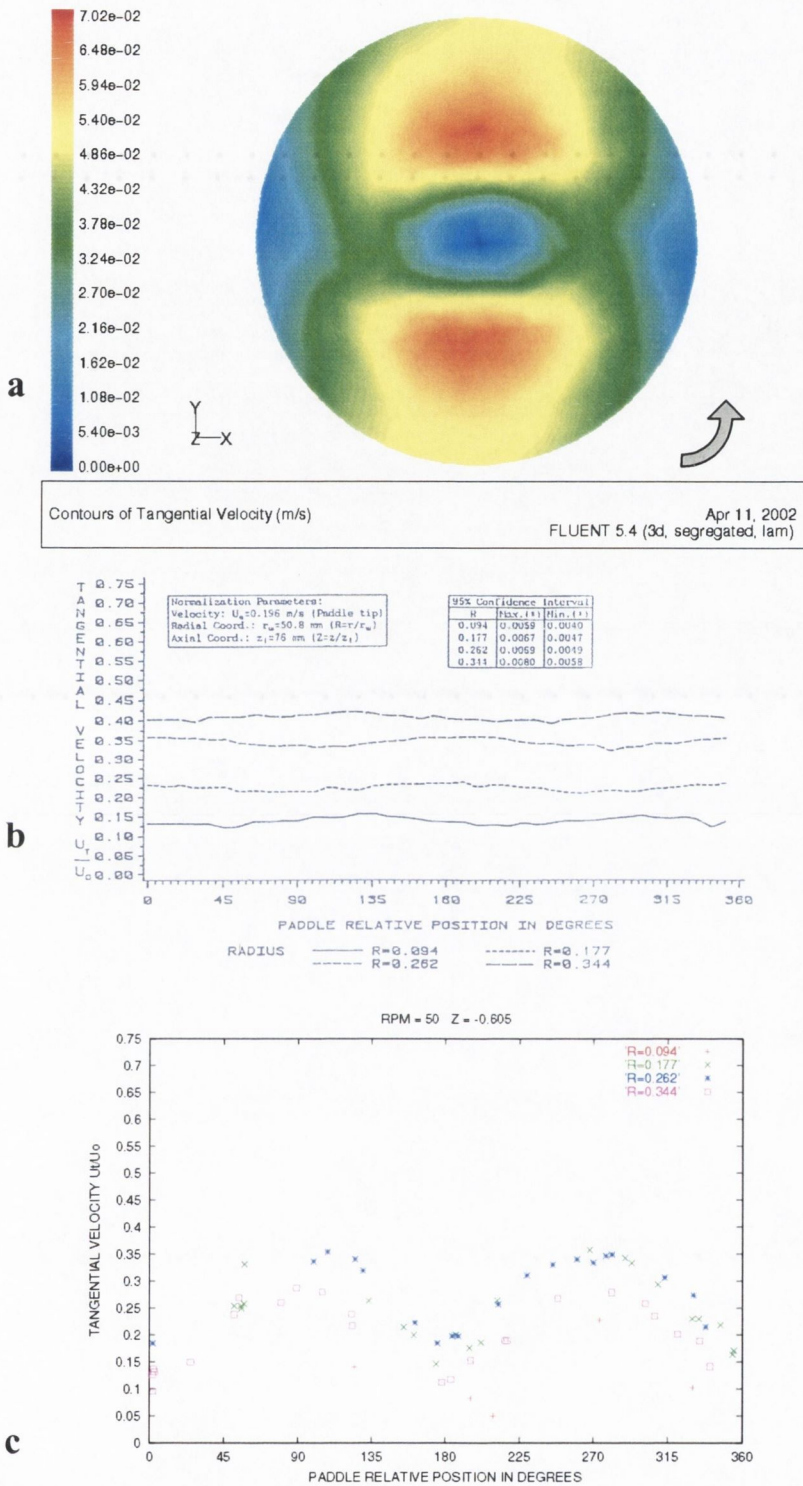


Figure 3.8 Comparison of CFD predicted and experimentally determined tangential velocities for four radii on a plane 5.3 mm from the base of the USP paddle dissolution apparatus; (A) CFD predicted contours of tangential velocity, (B) Laser Doppler measured normalized tangential velocities (Bocanegra et al., 1990), (C) Corresponding CFD predicted normalized tangential velocities.

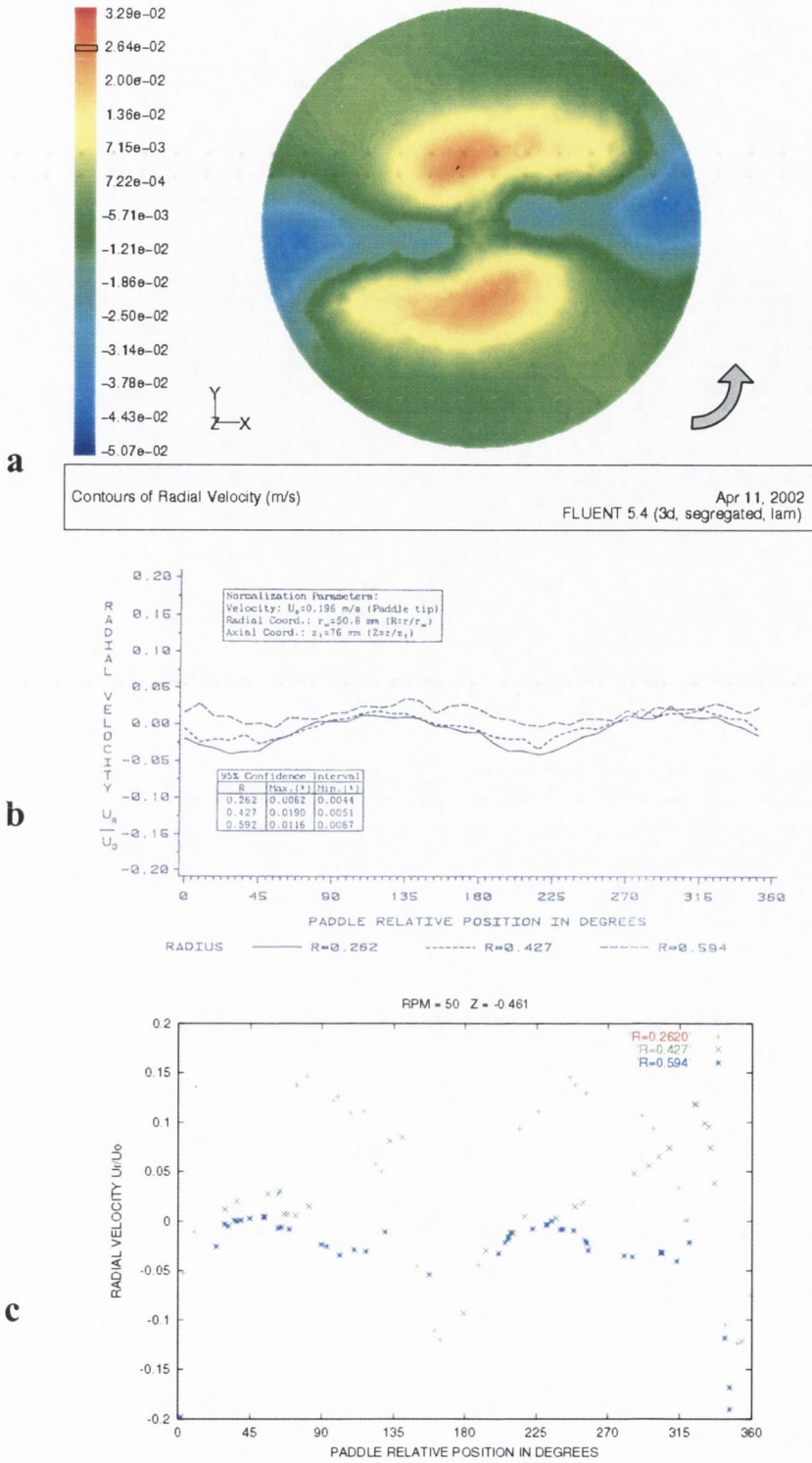


Figure 3.9 Comparison of CFD predicted and experimentally determined radial velocities for three radii at a plane 16.2 mm from the base of the USP paddle dissolution apparatus; (A) CFD predicted contours of radial velocity, (B) Laser Doppler measured normalized radial velocities (Bocanegra et al., 1990), (C) Corresponding CFD predicted normalised tangential velocities.

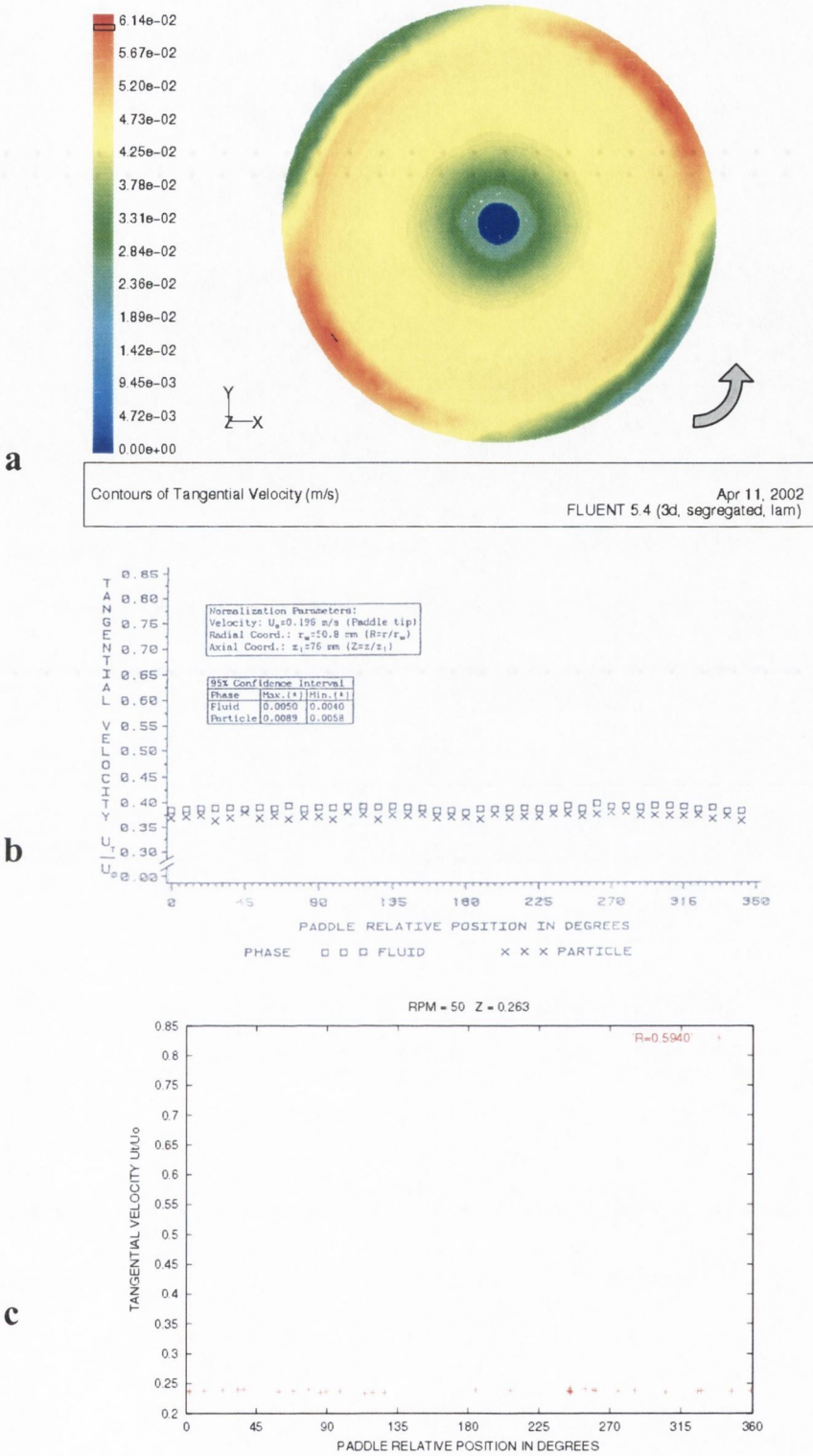


Figure 3.10 Comparison of CFD predicted and experimentally determined tangential velocities for one radius at a plane 26.6 mm from the top of the paddle wings of the USP paddle dissolution apparatus; (A) CFD predicted contours of tangential velocity, (B) Laser Doppler measured normalized tangential velocities (Bocanegra et al., 1990), (C) Corresponding CFD predicted normalised tangential velocities.

Overall, the unstructured grid approach to modelling fluid dynamics in the USP paddle dissolution apparatus produced results, which were in reasonable qualitative agreement with laser Doppler measured velocities. However, there was a substantial quantitative discrepancy between the predicted and measured fluid velocities, using the unstructured mesh approach of Kosiol (2000). The approach was at its limit of refinement, making it impossible to generate results for a paddle rotation speed at higher than 60 rpm. Another artefact of this approach was the observation that the presence of the multiple reference frame (MRF) volume had not reached equilibrium with the fluid outside the MRF (noticeable as a distinct hurdle in the contour plot of Figure 3.10a, in the border between these two regions). In fact, the complete volume of the vessel can be used a single rotating frame as there are no baffles in the USP apparatus to necessitate the need for a multiple reference frame (Fluent5 User's Guide, 1998). Also, it became obvious, on further investigation, that the modeling of rotating fluids with CFD requires a more precise handling of both the pre-processor program and the solver program. In flows that are driven by wall rotation (impeller rotation), the motion of the wall tends to impart a forced vortex motion to the fluid, an important resulting characteristic of such flows being the tendency of fluid with high angular momentum (the flow near the impeller) to be flung radially outward. This phenomenon is referred to as 'radial pumping', since the rotating wall is pumping the fluid radially outward (Fluent5 User's Guide, 1998). As the distribution of angular momentum in swirling flows evolves, the radial pressure gradient also changes, driving radial and axial flows in response to the highly non-uniform pressures that result. Thus, the changes in the static pressure distribution produces corresponding changes in the axial and radial flow velocities. This high degree of coupling between the swirl and the pressure field complicates the modeling of rotating flows.

Consequently, there is a need for sufficient resolution in the grid when solving flows that include swirl or rotation (Fluent5 User's Guide, 1998; Pedrosa and Nunhez, 2000) Also, the Fluent User's Guide recommends the use of the 'PRESTO' pressure discretization scheme, which is well-suited for the steep pressure gradients involved in swirling flows. However, it is only possible to apply this discretisation technique to grids consisting of hexahedral cells. Therefore, the current unstructured tetrahedral grid was not applicable to this pressure discretisation technique. Finally, a more specific solution control set-up was necessary in the solver, Fluent.

3.2.3 Structured Grid Approach

The methods used in the structured grid approach are detailed in section 2.14.3.

3.2.3.1 Comparison with laser Doppler measurements

3.2.3.1.1 Tangential velocities 5.3 mm from the base of the vessel

Contours of predicted tangential velocities below the paddle at a plane 5.3mm from the base of the vessel are shown in Figure 3.11(a), while the corresponding normalized (relative to paddle tip) predicted and measured tangential velocities (at the appropriate Bocanegra radii) are shown in Figure 3.11(b) and (c) respectively. Initial visual comparison would indicate there is a considerable improvement in correlation between experimental and simulated velocities, in contrast to the Kosiol approach (Figure 3.8). Qualitatively, simulated and experimental results for the modified approach compare favourably. A flat profile over all angles is exhibited for both results, indicating that there is no periodicity with regard to tangential velocities towards the base of the vessel (except for some minor curvature with the lowest radius for the simulated results). Quantitatively, the results also compare well. The lowest radius simulated results vary between 0.1 and 0.2, while the experimental values centre around 0.15. The next radius ranges from 0.2 to 0.3, with an experimental mean of approximately 0.25. Similarly, tangential velocities at the third and fourth radii are in the region of around 0.35 and 0.4 respectively, comparing very well with the experimental values. The flat profile indicated that there was no periodicity with regard to the position of the paddle for tangential velocities in this region of the vessel. It is possible to convert angular rotation of the paddle to tangential velocities at various radii of the paddle, using Equation 3.1,

$$v_t = wr \quad \text{Equation 3.1}$$

where v_t is the tangential velocity of the paddle at a particular radius, w is the angular (rotational) velocity of the paddle and r is the distance from the centre point of the paddle (radius). Conversion of the rotational velocity of the paddle to tangential velocities, at the same radii as examined in Figure 3.11 reveals that, close to the bottom of the vessel ($Z=-0.605$), tangential velocities were approximately equal to that of the paddle (for the corresponding radius). For example, for the paddle at

radius $R=0.344$, tangential velocity = $5.236 \times (0.344 \times 0.051) = 0.091 \text{ m/s} = 0.46$ relative tangential velocity, which is in close agreement with the corresponding simulated value for $R=0.344$ at $Z=-0.605$).

This graded increase in tangential velocity with increasing radius is plainly evident on examination of the figure of contours of velocity (Figure 3.11(a)), a feature originally speculated by Bocanegra et al. (1990) and further confirmed by the simulated data. Maximum tangential velocities on this plane were in the region of 9 cm/s.

3.2.3.1.2 Radial velocities 16.2 mm from the base of the vessel

Contours of predicted radial velocities below the paddle at a plane 16.2 mm from the base of the vessel are shown in Figure 3.12(a), while the corresponding normalized (relative to paddle tip) predicted and measured radial velocities (at the appropriate Bocanegra radii) are shown in Figure 3.12(b) and (c) respectively. Again, there is good qualitative visual correlation between the experimental and simulated velocities. All results fluctuate between -0.05 and $+0.05$, results not varying significantly between the three radii, for both the experimental and simulated velocities. The 180° periodicity shown for the laser Doppler measurements is also exhibited by the simulated data for the second and third radii, with a little fluctuation in the data of the lowest radius. Radial velocities on this plane ranged from -0.5 to $+0.5$ cm/s.

3.2.3.1.3 Tangential velocities 15.4 mm above the paddle wings

Contours of predicted tangential velocities at a plane 15.4 mm above the paddle wings are shown in Figure 3.13(a), while the corresponding normalized (relative to paddle tip) predicted and measured tangential velocities (at the appropriate Bocanegra radius) are shown in Figure 3.13(b) and (c) respectively. Quantitatively, the simulated results capture the flat velocity profile exhibited by the experimental values over all angles (no periodicity with regard to paddle position). This flat profile facilitates the estimation of the discrepancy between the experimental and simulated results, which was calculated to be in the region of 15%. This represents a significant improvement on the value of 35% to 40% estimated for the initial approach. Maximum tangential velocities on this plane were in the region of 10 cm/s.

3.2.3.1.4 *Axial velocities 2.0 mm above the paddle wings*

Contours of predicted axial velocities at a plane 2.0 mm above the paddle are shown in Figure 3.14(a), while the corresponding normalized (relative to paddle tip) predicted and measured axial velocities (at the appropriate Bocanegra radii) are shown in Figure 3.14(b) and (c) respectively. Examination of this data set indicate that the 180° periodicity exhibited by the experimental data is also evident in the simulated data. Quantitatively, there is little difference between the two data sets for all radii examined, although the peaks for $R=0.762$ are slightly more extreme for the simulated data and the troughs for the lowest radius are slightly lower for the simulated than the experimental measurements, as the paddle approaches the measuring volume at 0° and 180° paddle relative position. The contour plot shows that the axial flow in the region immediately above the paddle is quite complex. The volume immediately above the region swept out by the paddle wings is dominated by negative axial velocity (towards the base of the vessel), except for the region immediately in front of the paddle wings, which has a positive axial component. Outside of this area (between the paddle wings and wall) the fluid velocity has a high positive axial component. Axial velocities on this plane ranged from -4.5 to +5.2 cm/s.

3.2.3.1.5 *Tangential velocities 2.0 mm above the paddle wings*

Contours of predicted tangential velocities at a plane 2.0 mm above the paddle are shown in Figure 3.15(a), while the corresponding normalized (relative to paddle tip) predicted and measured tangential velocities (at the appropriate Bocanegra radii) are shown in Figure 3.15(b) and (c) respectively. It is seen that the a 180° periodic tangential velocity produced by the two bladed paddle exists and velocities decreased as the paddle approaches the measuring volume (paddle relative position of 0° and 180°) and increases as it leaves the measuring volume, for both data sets. Quantitatively, both data sets are very similar for all radii, except for $R=0.762$, which predicted higher fluid velocities for the CFD results. The magnitude of tangential velocity components above the stirrer were much higher than the corresponding axial velocities at this plane. Maximum tangential velocities on this plane were in the region of 12.5 cm/s.

3.2.3.1.6 Tangential velocities between the top and bottom of paddle wings

Contours of predicted tangential velocities at a plane 36.1mm above the bottom of the vessel (between the top and bottom of the paddle wings) are shown in Figure 3.16(a), while the corresponding normalized (relative to paddle tip) predicted and measured tangential velocities (at the appropriate Bocanegra radii) are shown in Figure 3.16(b) and (c) respectively. The 180° periodicity exhibited of the experimental data is also evident in the simulated data. Again, the two data sets are quantitatively very similar. As expected, the tangential velocity is maximal immediately before and after the paddle wings (paddle relative position of 0° and 180°), with lowest tangential velocities at 90° to the paddle wings. This result is clearly obvious from the contour plot. The magnitudes of the tangential velocities in this area are the highest velocities throughout the vessel (tangential velocities are the predominant component of velocity throughout the vessel). Maximum tangential velocities on this plane were in the region of 19 cm/s (the speed at the paddle tip).

3.2.3.2 Contrast between unstructured and structured grid approach

The initial unstructured grid approach provided results, which were, for the most part, qualitatively similar to the laser Doppler measurements. However, on a quantitative level, there was substantial difference between the simulated and laser Doppler measurements. An estimate of this error was calculated to be in the region of 35-40%. Conversely, although the structured grid approach demanded a more tedious wireframe and boundary/continuum set-up, results from this approach were more satisfactory. In this case, results were both qualitatively and quantitatively in close agreement with the laser Doppler measurements of Bocanegra et al. (1990). The final set-up for the structured grid approach, which closest matched the laser Doppler measurements, was adopted for all future simulation work.

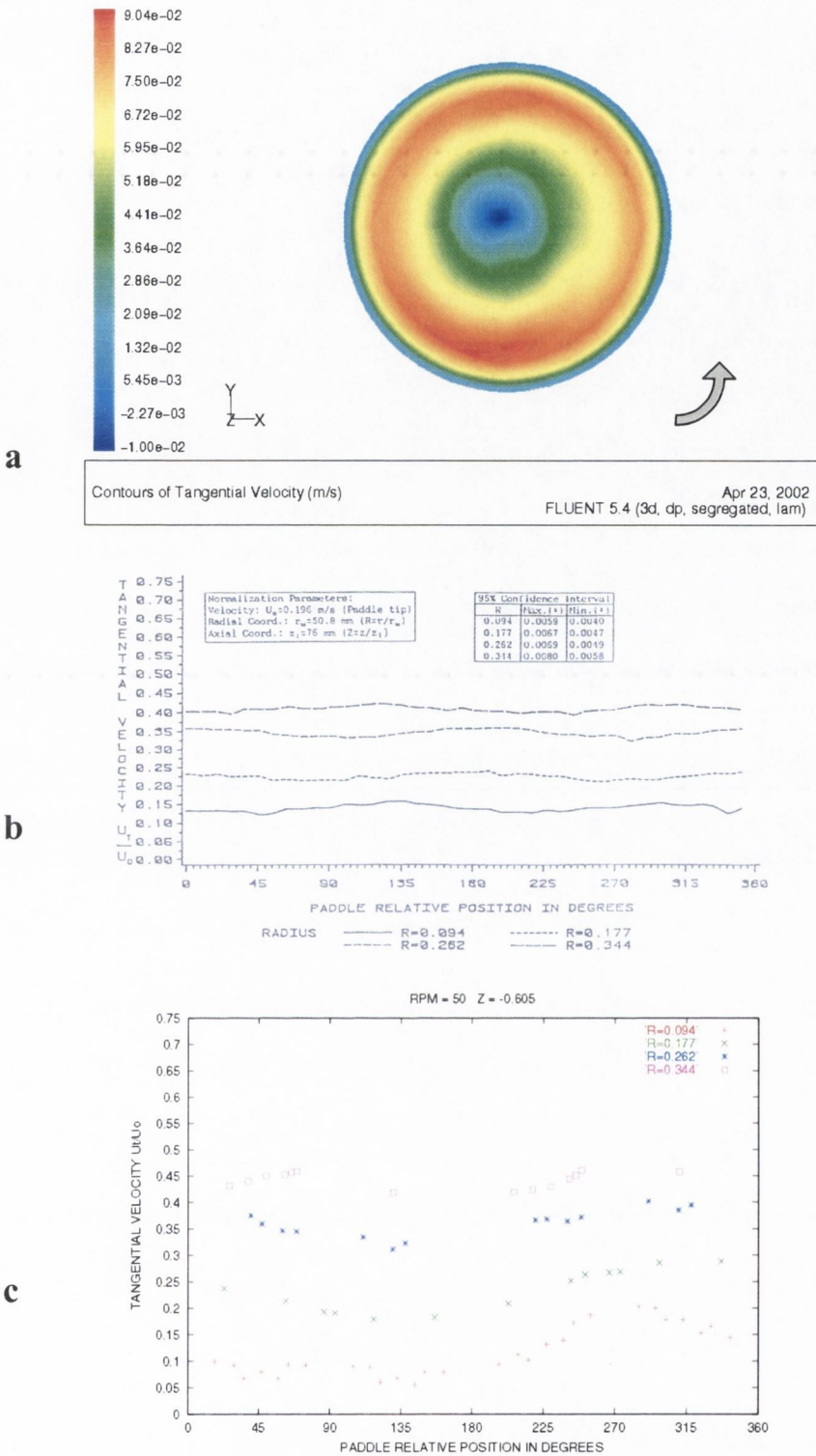


Figure 3.11 Comparison of CFD predicted and experimentally determined tangential velocities for four radii at a plane 5.3 mm from the base of the USP paddle dissolution apparatus, ($Z=-0.605$); (a) CFD predicted contours of tangential velocity, (b) laser Doppler measured normalized tangential velocities (Bocanegra et al., 1990), (c) corresponding CFD predicted normalized tangential velocities.

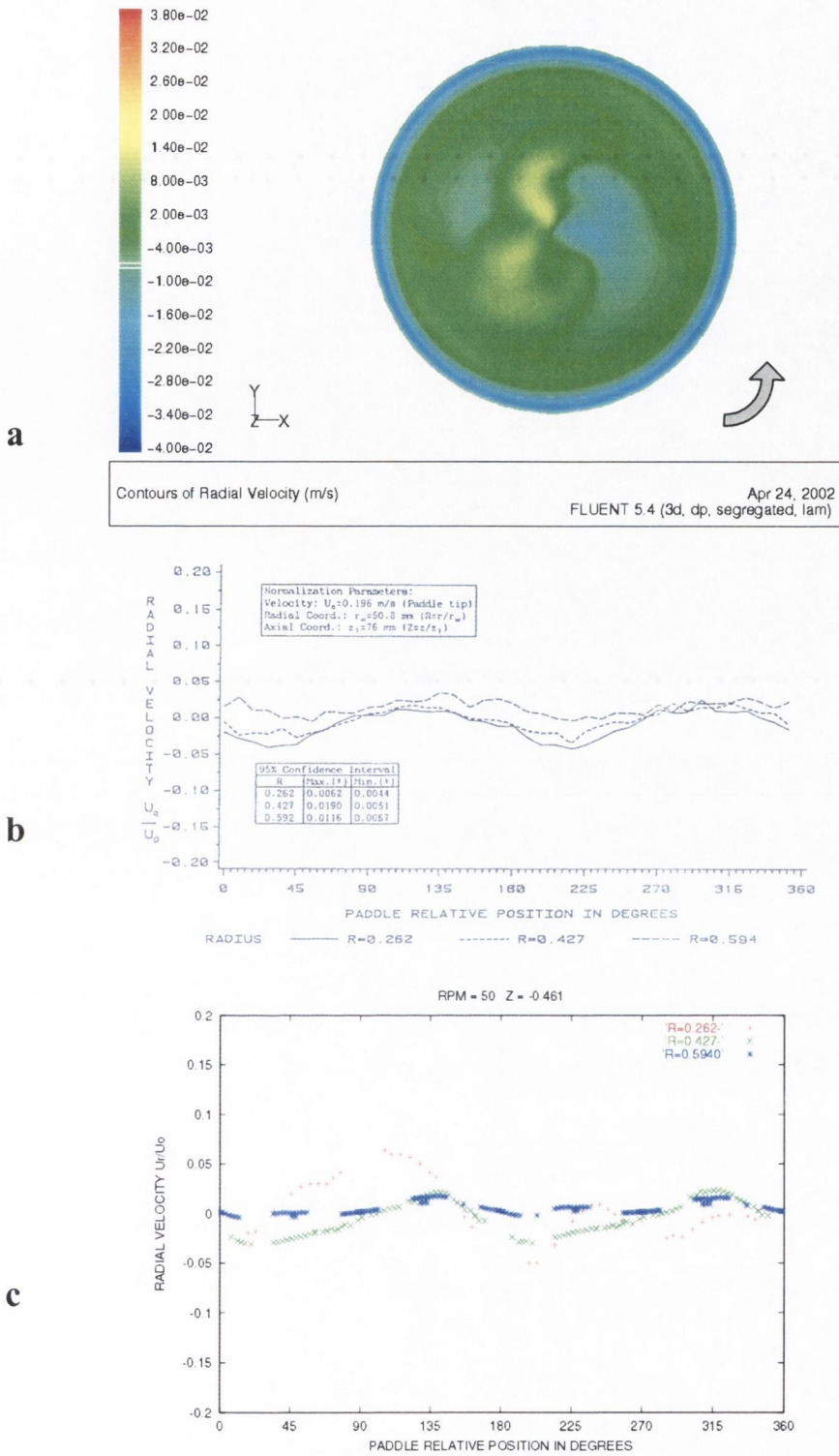


Figure 3.12 Comparison of CFD predicted and experimentally determined radial velocities for three radii at a plane 16.2 mm from the base of the USP paddle dissolution apparatus, ($Z=-0.461$); (a) CFD predicted contours of radial velocity, (b) laser Doppler measured normalized radial velocities (Bocanegra et al., 1990), (c) corresponding CFD predicted normalized radial velocities.

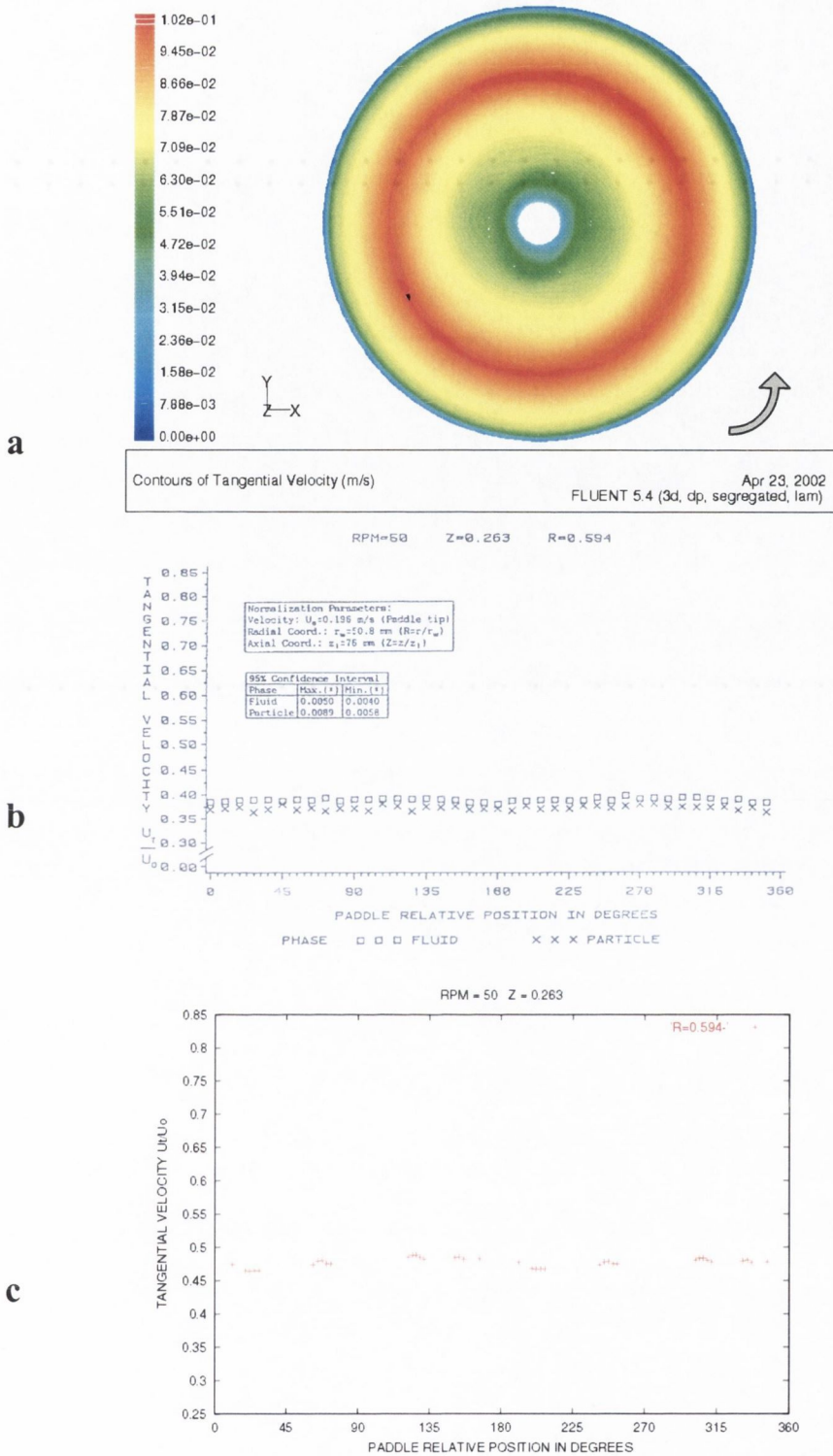


Figure 3.13 Comparison of CFD predicted and experimentally determined tangential velocities for one radius at a plane 15.4 mm from the top of the paddle wings of the USP paddle dissolution apparatus, ($Z=0.263$); (a) CFD predicted contours of tangential velocity, (b) laser Doppler measured normalized tangential velocities (Bocanegra et al., 1990), (c) corresponding CFD predicted normalized tangential velocities.

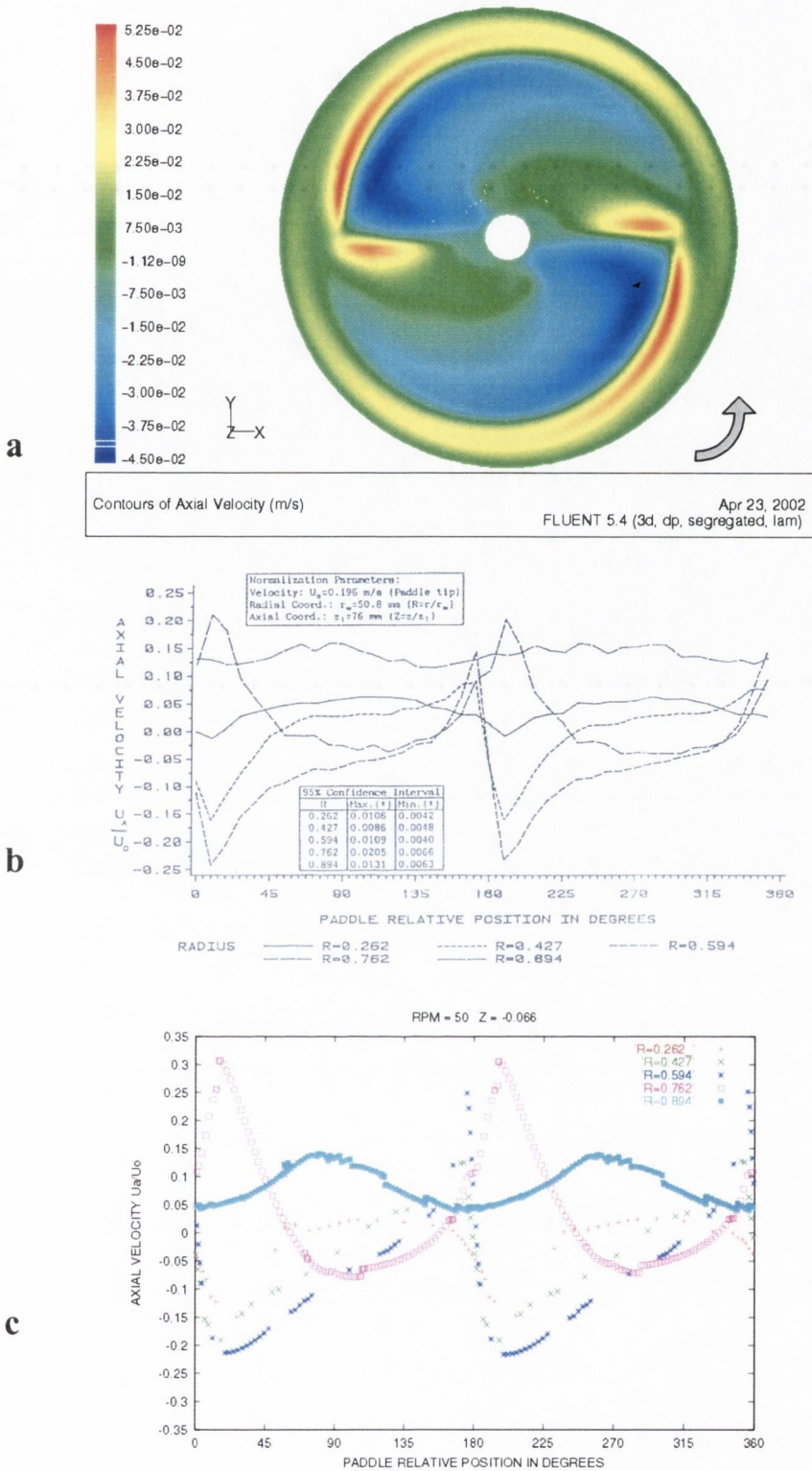


Figure 3.14 Comparison of CFD predicted and experimentally determined axial velocities for four radii at a plane 2.0 mm above the top of paddle wings, ($Z=-0.066$); (a) CFD predicted contours of axial velocity, (b) laser Doppler measured normalized axial velocities (Bocanegra et al., 1990), (c) corresponding CFD predicted normalized axial velocities.

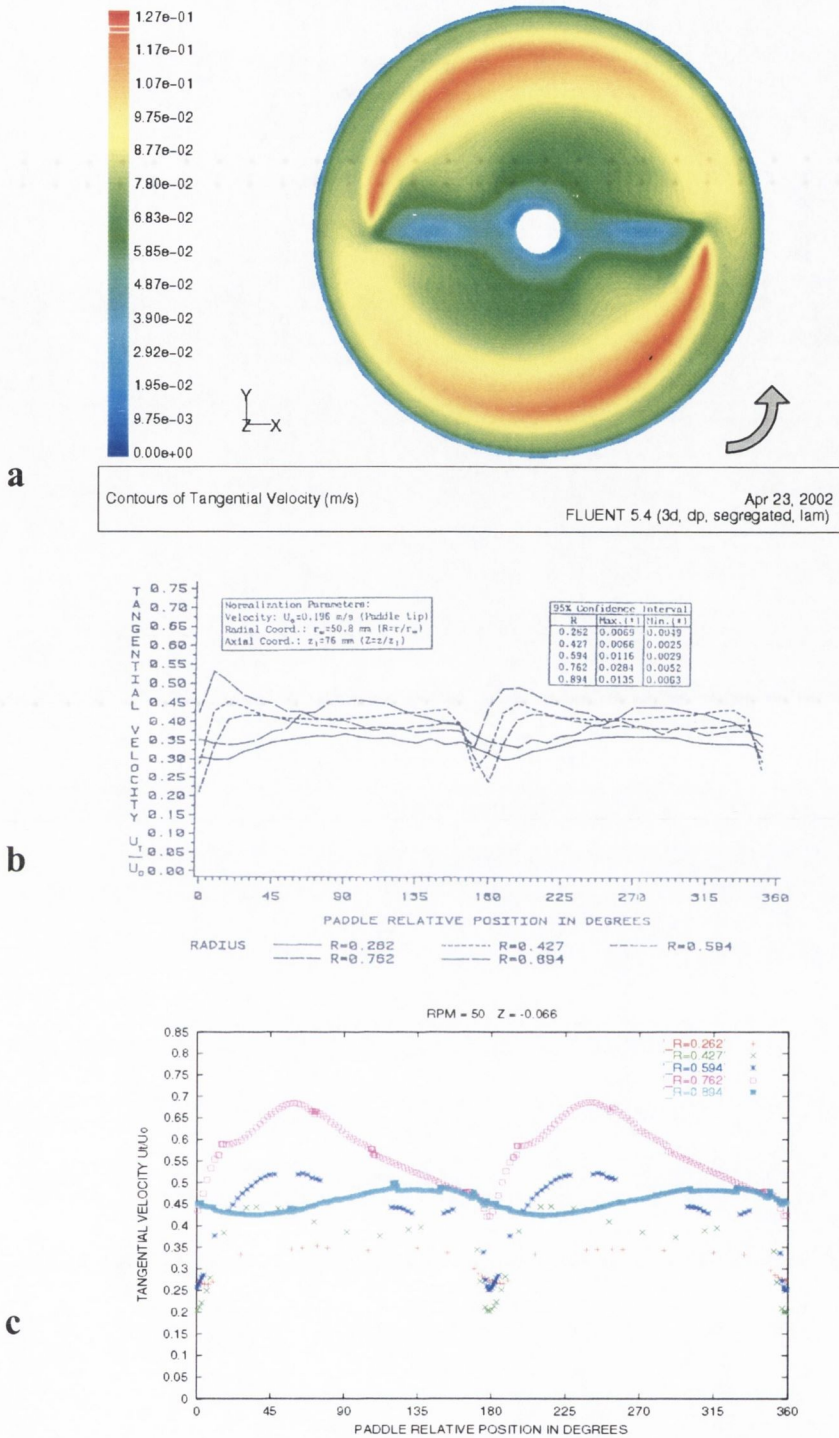


Figure 3.15 Comparison of CFD predicted and experimentally determined tangential velocities for five radii at a plane 2.0 mm above the top of paddle wings of the USP paddle dissolution apparatus, ($Z=-0.066$); (a) CFD predicted contours of tangential velocity, (b) laser Doppler measured normalized tangential velocities (Bocanegra et al., 1990), (c) corresponding CFD predicted normalized tangential velocities.

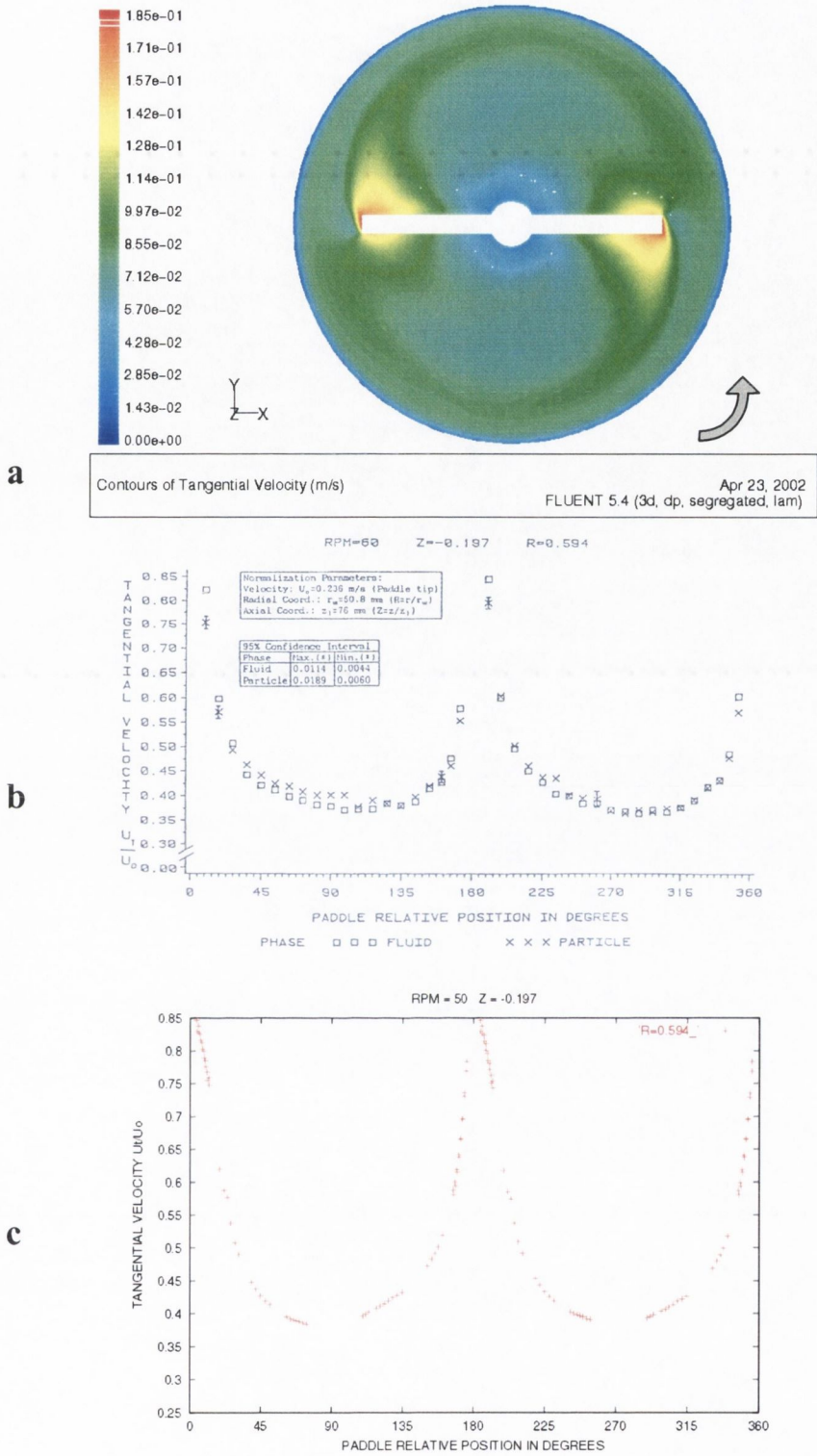


Figure 3.16 Comparison of CFD predicted and experimentally determined tangential velocities for one radius at a plane 36.1 mm from the base of the USP paddle dissolution apparatus (between the top and bottom of the paddle wings, $Z=-0.197$); (a) CFD predicted contours of tangential velocity, (b) laser Doppler measured normalized tangential velocities (Bocanegra et al., 1990), (c) corresponding CFD predicted normalized tangential velocities.

3.2.3.3 Comparison with other measurements of fluid flow in the paddle dissolution apparatus

The hydrodynamics of the paddle dissolution test have recently been studied using an ultra-sound pulse echo method (Diebold and Dressman, 2001). Maximum tangential velocities were measured at a lateral distance of 26 mm from the centre of the vessel for a series of heights within the vessel (S1-S4) and axial fluid velocities were measured at two radii from the top of the fluid into the bulk (O1 and O2). Fluid velocities were measured at different distances from the ultra-sound probe to find the maximum fluid velocity at a particular paddle rpm. Simulated velocities were determined for the corresponding positions in the CFD vessel. A comparison of the results at 50 rpm is shown in Table 3.5.

Table 3.5 Comparison between CFD predicted and ultrasound measurements of fluid flow for axial and tangential velocities in the paddle dissolution apparatus for various positions in the vessel, at 50 rpm (Diebold, 2000).

POSITION NAME	VELOCITY TYPE	DISTANCE FROM BASE (mm)	DISTANCE FROM CENTRE (mm)	ULTRASOUND MEASUREMENT (cm/s)	CFD PREDICTION (cm/s)
S1	Tangential (U_t)	16	27.7	8.67	6.21
S2	Tangential (U_t)	72	28.7	7.54	5.44
S3	Tangential (U_t)	105	25.7	8.36	5.86
O1	Axial (U_a)	29.1	25.5	1.09	3.09
O2	Axial (U_a)	29.1	43.3	-1.41	-2.90

Although there was qualitative agreement, there was a quantitative discrepancy between the CFD generated velocities and the ultrasound measured velocities of fluid dynamics in the vessel. A possible reason for the discrepancy is that CFD is better able to predict bulk fluid flow at steady state, rather than predicting the behaviour of fluids at local maxima such as those generated by the ultrasound method.

3.2.3.4 Analysis of fluid dynamics on a mid-plane through the vessel (50rpm)

While Laser Doppler measurements can only provide a single point in space measurement of one component of fluid velocity for each experimental determination, the advantage of CFD is that it can predict velocity measurements, simultaneously, for each node in the computational domain (effectively for hundreds of thousands to

millions of points in the vessel). Since the CFD results of the structured grid approach were both qualitatively and quantitatively in close agreement with the laser Doppler measured values, for a series of positions in the vessel, it was then possible to critically examine the fluid flow throughout the USP vessel in more detail.

3.2.3.4.1 Simulated velocities on a mid-plane aligned with the paddle

Simulated velocities on a plane aligned with the paddle wings are shown in Figure 3.17.

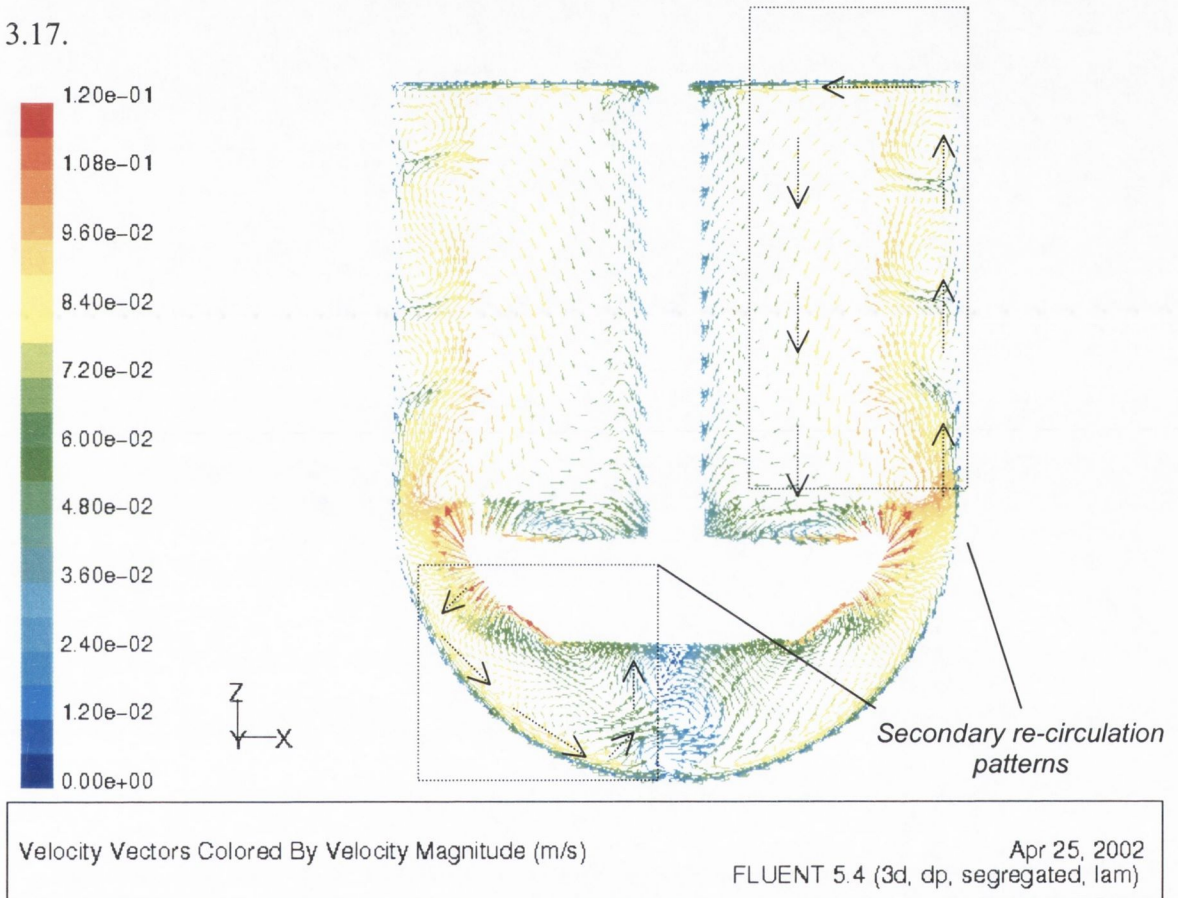


Figure 3.17 Simulated velocity vectors on a mid-plane in line with the paddle wings in the USP dissolution apparatus at 50rpm, coloured by velocity magnitude (only 1/6th of cell values included for clarity).

Initial examination of Figure 3.17 indicated that fluid velocities varied extensively with position throughout the vessel. As has been previously noted, the major component of fluid motion throughout the vessel was the tangential component. This is not surprising, as fluid flow is generated by the momentum transfer from the paddle via normal stresses, and the paddle rotation is in the tangential direction. However, the paddle rotation will necessarily induce secondary flows in the axial and radial

direction. The nature of such secondary flows in the USP paddle dissolution apparatus has been a matter of considerable speculation (Bocanegra, 1988; Beckett et al., 1996; Diebold 2000). Figure 3.17 provides an insight into the nature of the secondary flow in the axial direction at the mid-plane directly above and below the paddle. Bocanegra (1988) identified that the axial secondary flow resulted in an oscillation of the flow and speculated that this observation was of potential importance to the sensitivity and reproducibility of resulting dissolution data. However, this observation was based on a number of single point laser Doppler measurements for specific points in the vessel, the flow between these points being speculated flow. Examination of Figure 3.17 substantiates the speculated fluid flow field of Bocanegra et al. for the mid-plane in the USP dissolution apparatus. Another interesting observation is a number of small regions of eddy flow immediately inside the vessel wall between the paddle and the surface of the liquid.

Above the paddle, the secondary axial flow is positive (upwards) in the region near the vessel wall, while a negative (downwards) axial flow is predicted in the region near the stirrer shaft, resulting in a secondary re-circulation pattern. Examination of the radial flow from Figure 3.12 indicates that there is little radial flow in the cylindrical volume of the vessel, apart from the region immediately above the paddle wings and at the very top of the vessel volume, the points where re-circulation is facilitated. The radial component of velocity is at its highest at the level of the paddle (radial pumping). It was speculated the high radial component results in the formation of two distinct regions of mixing, i.e. the cylindrical volume above the paddle (the sample acquisition region) and the hemispherical volume below the level of the paddle (the drug dissolution region), as this radial component is later dissipated into an upward and a downward axial component at the vessel wall (Bocanegra et al, 1988). This assumption is tested later (section 3.2.3.5).

Velocities below the paddle were more complicated than those above the paddle. Axial components were negative near the wall, gradually changing to positive axial flow towards the centre. Radial velocities below the paddle have a high inward component in the region near the lower hemispherical wall and converge centrally below the paddle. Fluid velocities centrally below the paddle at this convergence point appear to be involved in a local 'vortex' flow, which will be examined in further

detail later, as it is in this region that dissolution from a solid (or particulate) drug delivery system is likely to occur. Recalling that the axial velocity component varied significantly with regard to paddle relative position (Figure 3.14(a)), it is imperative to examine the velocities on another mid-plane, apart from that directly in line with the paddle.

3.2.3.4.2 Simulated velocities on a mid-plane at 90° to paddle

Simulated velocities on a plane at 90° to the paddle wings are shown in Figure 3.18.

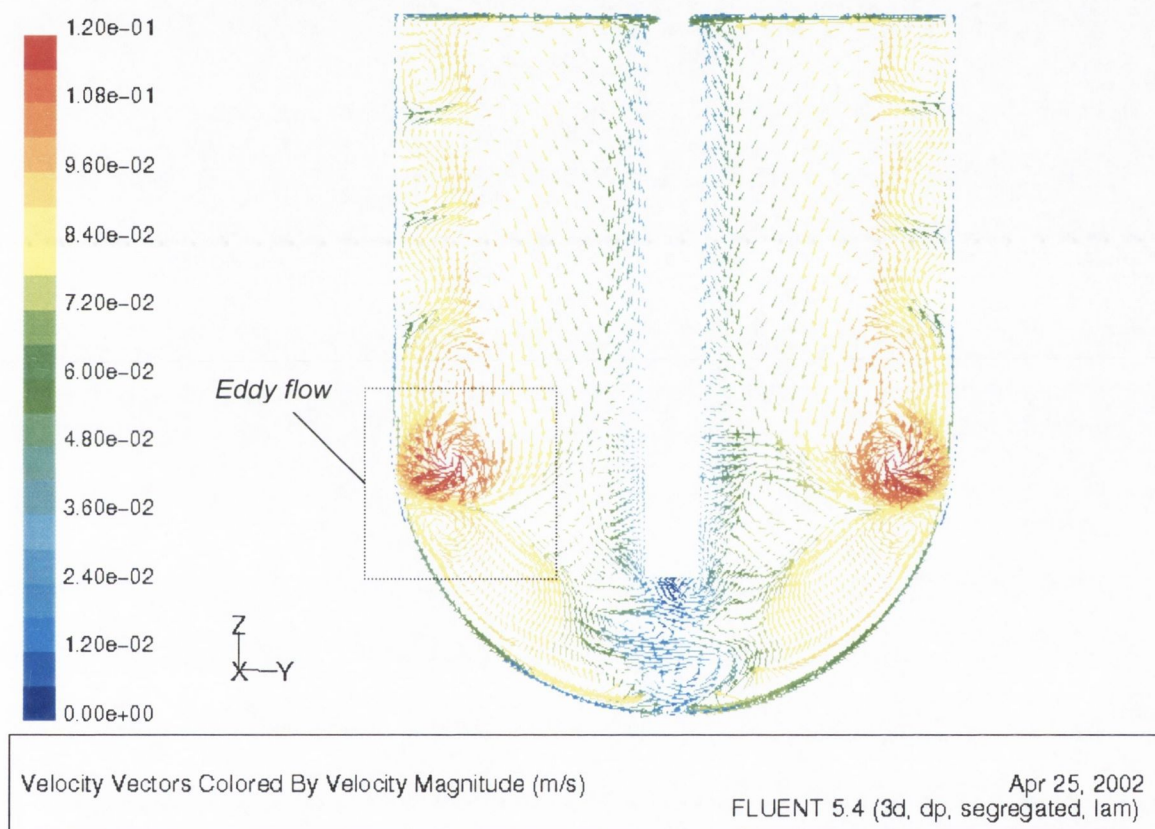


Figure 3.18 Simulated velocity vectors on a mid-plane at 90° to the paddle wings in the USP dissolution apparatus at 50rpm, coloured by velocity magnitude (only 1/6th of cell values included for clarity).

Fluid velocities in the region above and below the paddle at 90° to the paddle wings (Figure 3.18) do not appear to quantitatively differ significantly from those where the paddle was in line with the plane (Figure 3.17). However, this plane provides further insight into the nature of the mixing at the level of the paddle tip, between the two regions above and below this point. It appears that flow in this region is complicated by a region of eddy flow characterised by large changes in velocity components

within a small region. This region of eddy flow results in a small area of local recirculation. As this is the main mixing route between the regions above and below this point, it appears that this region is a further hindrance to adequate mixing between these two areas. The region of complex flow towards the base of the vessel is also evident in this fluid plane. Again, small regions of eddy flow are predicted immediately inside the vessel wall between the paddle and the surface of the liquid.

3.2.3.4.3 Velocity contours centrally below the paddle

As drug dissolution will occur in the region centrally below the paddle, fluid dynamics in this region are of particular interest. Contours of velocity magnitude on the mid-plane in line with the paddle wings, centrally below the paddle, are shown in Figure 3.19.

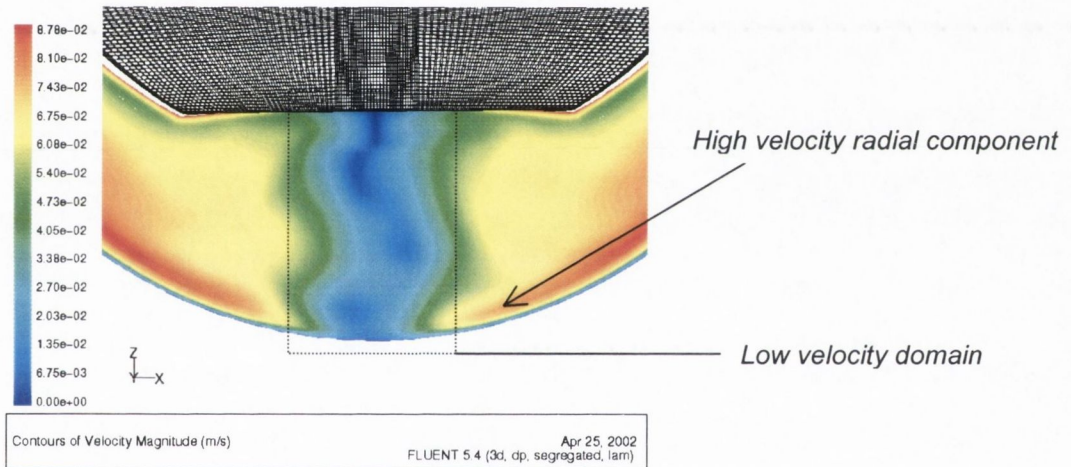
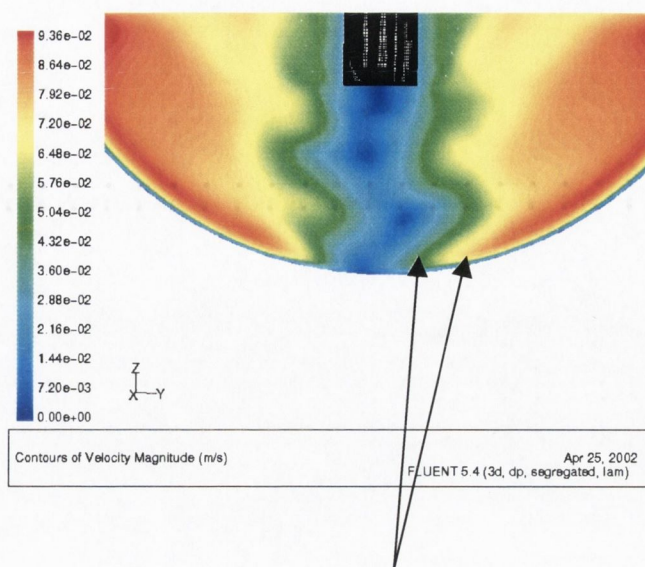


Figure 3.19 Contours of velocity magnitude on mid-plane in line with paddle wings, centrally below the paddle.

Although the fluid dynamics at the base of the USP dissolution are complex, it was evident that there is a large radial component towards the lower wall of the vessel. This region of high radial flow terminates centrally below the paddle at a region of low velocity. This domain of low velocity extends from the bottom of the vessel to the central lower part of the paddle. This low velocity domain, itself, is surrounded by a region of higher velocity. The diameter of this zone of low velocity was of a similar magnitude to the diameter of the compacts studied earlier (13mm). In order to determine if this observation was a localized phenomenon, contours of velocity magnitude on the mid-plane at 90° to the paddle wings, centrally below the paddle, are shown in Figure 3.20.



3 to 4 fold difference in velocity magnitude

Figure 3.20 Contours of velocity magnitude on mid-plane at 90° to the paddle wings, centrally below the paddle.

It is obvious from Figure 3.20 that this observation was not simply a localised phenomenon. In fact, at the very base of the vessel (the point where the delivery system is likely to be situated) there is a three to four fold difference in fluid velocity rates between two regions approximately only 8-10 mm apart, as indicated in Figure 3.20. It is postulated that this large variation in fluid velocity over a very short area, centrally below the paddle, is likely to be one reason for the variable dissolution rates in the USP dissolution, which have been previously demonstrated (section 3.1). It is possible that such erratic fluid dynamics would have a higher impact on a formulation that is situated within this region, compared to a buoyant system where random movements throughout the base of the vessel would diminish the effect of such hydrodynamics on the dissolution rates. At the base of this region of central low velocity exists a region of negligible fluid velocity. A region of ‘dead volume’ has been previously speculated to be responsible for the appearance of a ‘cone’ formation of particulate material during the dissolution test, owing to the decreased medium agitation and decreased surface area approaching the very bottom of the hemispherical part of the vessel (Qureshi et al., 2001). The same authors speculate that the round bottom of a dissolution vessel in combination with stirring devices (e.g. paddle) results in varied flow dynamics within the vessel which appears to be the cause of the observed high variability in the testing (Cox et al., 1983; PhRMA, 1997). The CFD predicted fluid velocities above provide substantial support for such speculation.

3.2.3.5 Mixing pathlines in the USP paddle apparatus at 50rpm

It is possible to track the flow of 'massless particles' throughout the solution domain with the Fluent software package. Effectively, the resulting output is a pathline, tracking the flow of fluid with time from an initial starting point or starting plane. On definition of a starting plane, the package will track imaginary massless particles from all gridpoints which are intersected with the computational domain by this plane. An imaginary plane was introduced to the hemisphere of the vessel of the 50rpm solution at 0.5mm from the base of the vessel, and the pathlines, which developed from this initial position, were tracked with time. The resulting pathline tracks, from 0.5 seconds to 60 seconds, from a plane 0.5mm from the very base of the vessel are illustrated in Figure 3.21. The resulting pathlines provide a novel insight into the three-dimensional mixing route throughout the USP paddle dissolution apparatus, a feature which has not been possible to deduce from previous velocimetry measurements. Initial mixing from the bottom of the vessel wall is facilitated by axial and tangential velocity components, resulting in an upward helical type flow pattern towards the base of the paddle impeller (0 to 1 second). Convergence with the fluid immediately beside the impeller (5 seconds) imparts significant tangential and radial velocity on the fluid, which results in the movement of the fluid towards the wall of the cylindrical part of the vessel (5 to 10 seconds). Flow from this point onwards is predominantly tangential in nature, with a varying degree of positive and negative axial movement, which results in the complete mixing of fluid throughout the vessel (20 to 40 seconds). Mixing appears also to be sub-optimal in the regions immediately inside the vessel walls, in the upper half of the cylindrical volume of the vessel. It would appear, therefore, that accurate positioning and repositioning of the sample acquisition point could have an impact on the resulting dissolution results. This factor could have a more sizeable influence on the efficiency of mixing throughout the vessel than the previously speculated problem of poor mixing between the hemispherical and cylindrical volumes, as the path-lines do not predict a dead-zone of mixing between these two regions (at the level of the paddle).

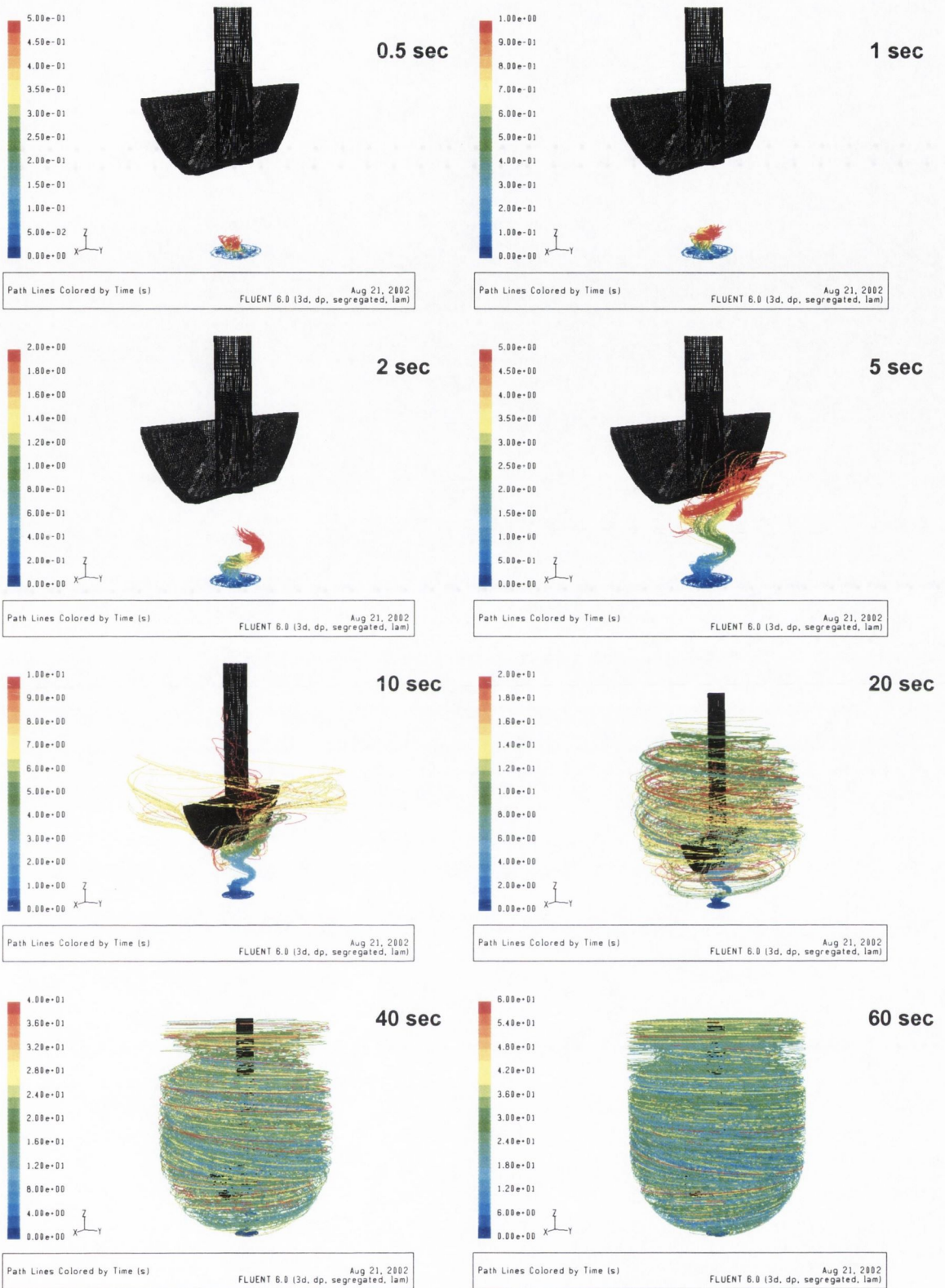


Figure 3.21 Pathlines of ‘massless particles’ tracked with time over 60 seconds from an initial plane 0.5 mm from the base of the USP paddle dissolution vessel at 50 rpm. Axes are in seconds.

3.2.3.6 Other impeller speeds

While the unstructured grid approach reached a limit of solution for the USP paddle apparatus at 60 rpm (Kosiol, 2000), the structured grid approach provided a more flexible set-up, which allowed significant refinement in user defined areas. The structured grid solution for 50 rpm was adapted in specific regions throughout the domain according to regions of high gradients of velocity magnitude. This hanging node adaption technique allowed the set-up to be examined at higher (and lower) impeller speeds than 50 rpm. Following grid adaption in this manner, Fluent was set up to examine flow for 25, 50, 100 and 150 rpm. Results of simulated velocities (not normalised to the paddle tip speed, i.e. m/s) are compared at the various rpm for similar positions in the vessel as those previously analysed by Bocanegra et al. (1990) at 50 rpm. Axial and tangential velocities are compared, as radial velocities were of a low magnitude in the body of the vessel. Axial velocities on a plane 2 mm above the paddle wings ($Z=-0.066$) at $R=0.594$ are presented at various rpm in Figure 3.22 and tangential velocities on a plane 36.1 mm from the base of the vessel ($Z=-0.197$) at $R=0.594$ are presented at various rpm in Figure 3.23.

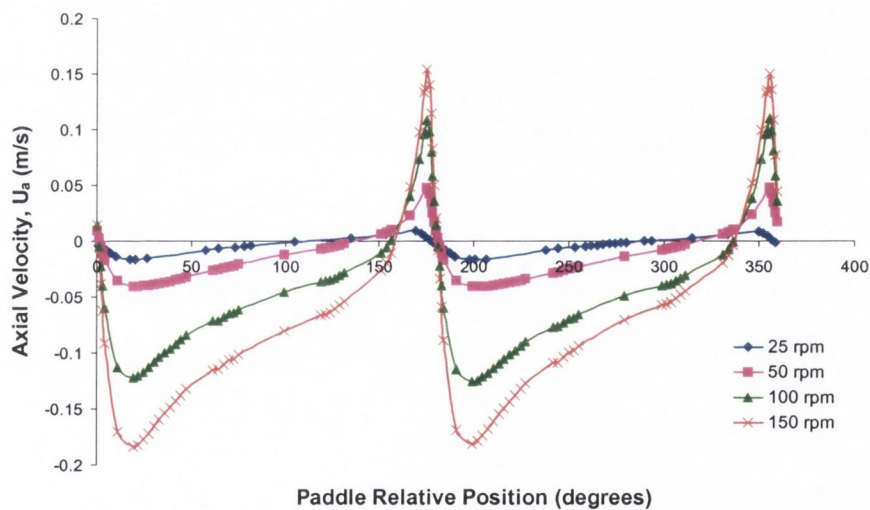


Figure 3.22 CFD simulated axial velocities (U_a , m/s) at $Z=-0.066$, $R=0.594$ (2 mm above the paddle wings) in the paddle dissolution apparatus versus paddle relative position for paddle rotation speeds of 25, 50, 100 and 150 rpm.

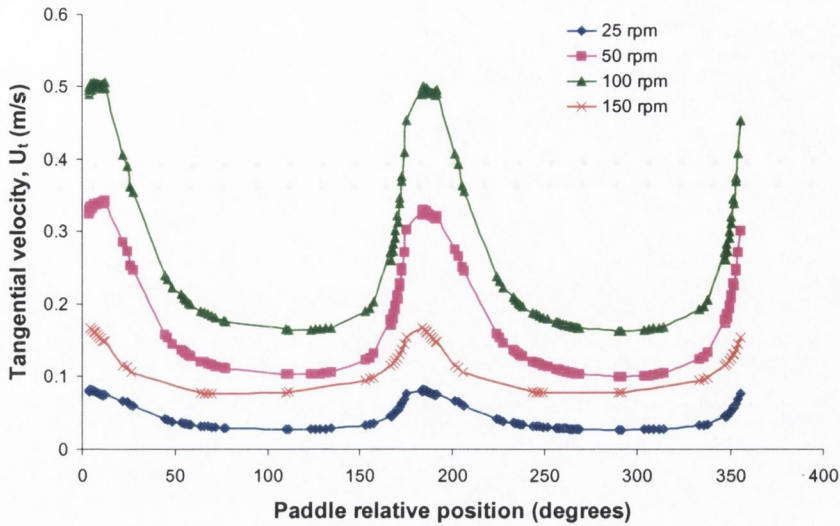


Figure 3.23 CFD simulated tangential velocities (U_t , m/s) at $Z=-0.197$, $R=0.594$ (36.1 mm from the base of the vessel) in the paddle dissolution apparatus versus paddle relative position for paddle rotation speeds of 25, 50, 100 and 150 rpm.

Therefore, it appears that a linear increase in magnitude of both the tangential and axial components is predicted by the model for paddle rotation speeds between 25 and 150 rpm. To examine the effect of the increase in rpm, the peak values at each rpm for the above velocity predictions were examined. The resulting plots of maximum velocity magnitude at each rpm for both planes are included in Figure 3.24.

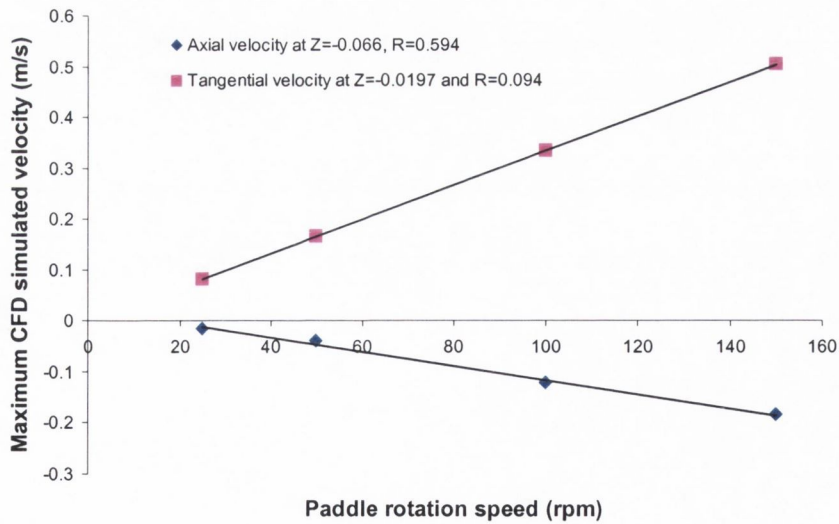


Figure 3.24 CFD predicted maximum axial and tangential velocities for two positions in the paddle dissolution apparatus for rotation speeds between 25 and 150 rpm. A) Axial velocities at $Z=-0.066$, $R=0.594$. B) Tangential velocities at $Z=-0.197$, $R=0.094$.

Therefore, a linear increase in the magnitude of the axial or tangential velocity is predicted by the CFD model for various paddle rotation speeds ($r^2 \geq 0.995$). This would indicate that laminar fluid behaviour occurs in the paddle dissolution apparatus for paddle rotation speeds of up to 150 rpm. Similar behaviour was predicted for axial and tangential velocities for various positions in the vessel and is consistent with laser Doppler measurements carried out in the vessel at various rpm (Diebold et al., 2001).

3.2.3.7 Effect of paddle rotation speed on mixing in the paddle dissolution apparatus

The effect of different paddle speeds on mixing pathlines in the apparatus was examined. Varying the impeller rotation speed had a marked effect on the time required to achieve complete mixing in the apparatus. The predicted fluid mixing path-lines in the vessel, at various rpm after 5 seconds, from a plane at 0.5 mm from the base of the vessel are shown in Figure 3.25.

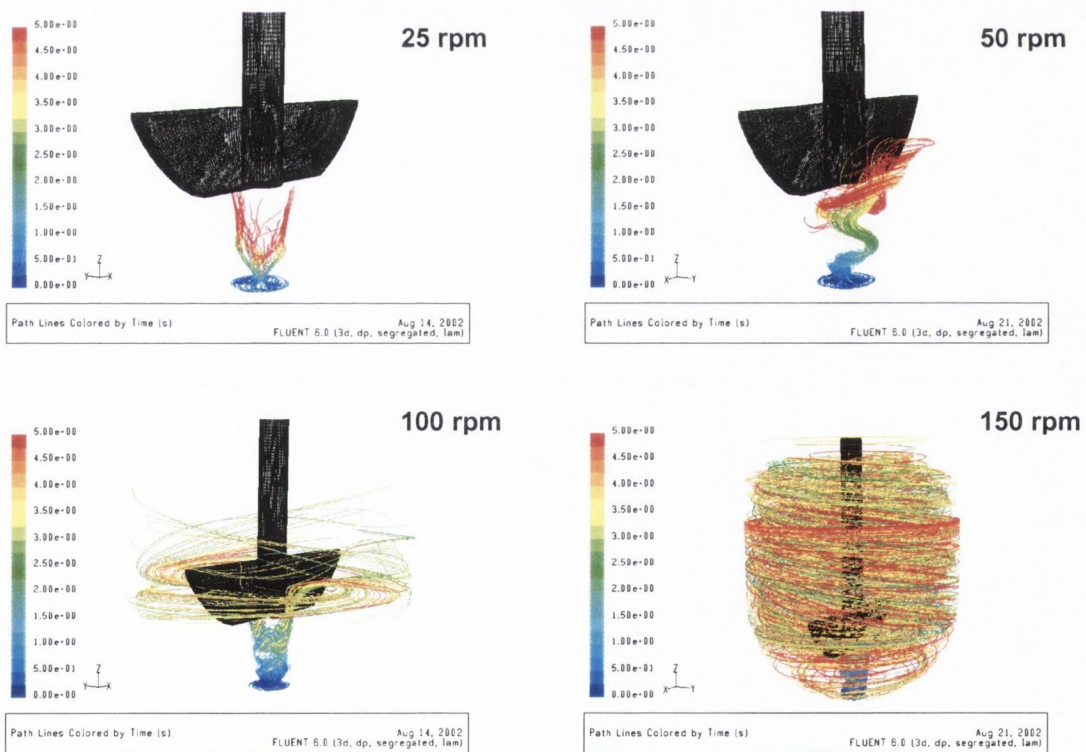


Figure 3.25 Pathlines of ‘massless particles’ tracked with time for 5 seconds from an initial plane 0.5 mm from the base of the USP paddle dissolution vessel at 25 rpm, 50 rpm, 100 rpm and 150 rpm. Axes are in seconds (max. 5 seconds in all plots).

Quite different flow patterns were predicted for the various rpm (in spite of the use of the same grid and solver formulation), particularly with regard to the time to allow complete mixing in the vessel. The approximate time required to attain complete mixing from the plane at 0.5 mm from the base of the vessel at the various rpm is summarised in Table 3.6.

Therefore, although complete mixing is predicted by the model, the time to achieve this intimate mixing is quite high at the common operating speeds of 50 and 100 rpm (although this model does not include diffusion caused by concentration differences).

Table 3.6 *Approximate time predicted by CFD model of the USP paddle dissolution apparatus required to achieve complete mixing in the vessel at various paddle rotation speeds (based on path-line tracks from 'massless particles')*

PADDLE ROTATION SPEED (rpm)	APPROXIMATE TIME TO ACHIEVE COMPLETE MIXING (s)
25	40-60
50	20-40
100	5-10
150	2-5

3.2.4 Introduction of a cylindrical compact

It was of interest to examine the effect of the addition of a cylindrical compact to the base of the dissolution vessel. Studying the resulting fluid dynamics near the compact surface was of relevance as a possible cause of alteration in dissolution rates from various surfaces of cylindrical compacts, which had been previously demonstrated (section 3.1.3). A detailed study of fluid dynamics in the region of such a cylindrical compact was also suggested as necessary future work following a previous study to simulate drug dissolution from drug compacts in the USP paddle dissolution apparatus (Public final report of Esprit HPCN PST activity, PSUDO, 2001). All simulated dissolution rates from the finite numerical approach of the PSUDO project were based on the assumption that the predominant component of fluid velocity outside the curved surface of such a compact was axial in nature. The actual value assigned to this component was postulated from the data of Bocanegra et al., where there was no cylindrical compact at the base of the vessel. This postulated value was used throughout the project. It was noted on completion of the project that precise

measurement of this fluid component was a necessary step in correctly predicting the dissolution rate from such systems. For the above reasons, the effect of the addition of a cylindrical compact to the base of the USP paddle dissolution apparatus was examined. The initial compact studied was of similar dimensions to system (E), section 3.1.3.

3.2.4.1 Flow vectors at the mid-plane

Simulated velocities on a plane aligned with the paddle wings in the USP dissolution apparatus at 50rpm, after inclusion of the compact, are shown in Figure 3.26.

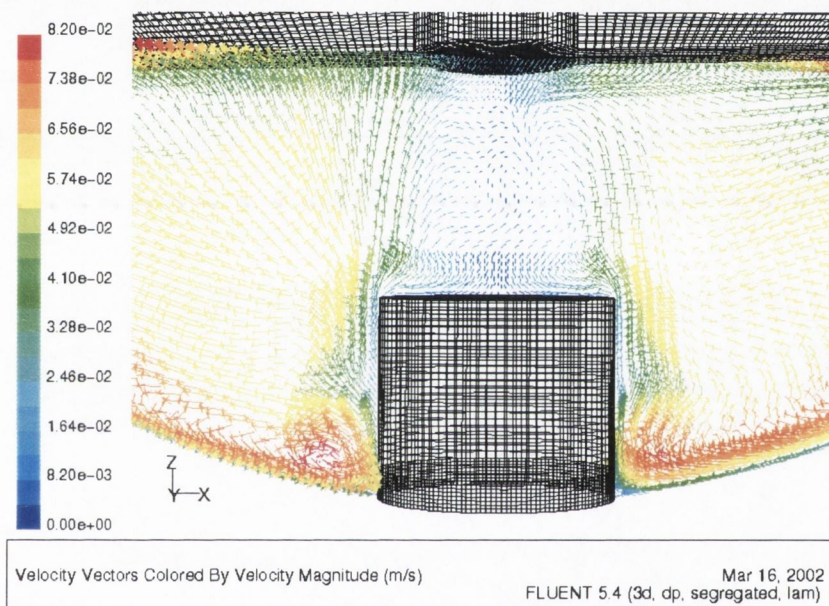


Figure 3.26 Simulated velocity vectors on a mid-plane in line with the paddle wings in the USP dissolution apparatus at 50 rpm with a compact of 8.5 mm height (sitting on a wax pedestal of 3 mm height).

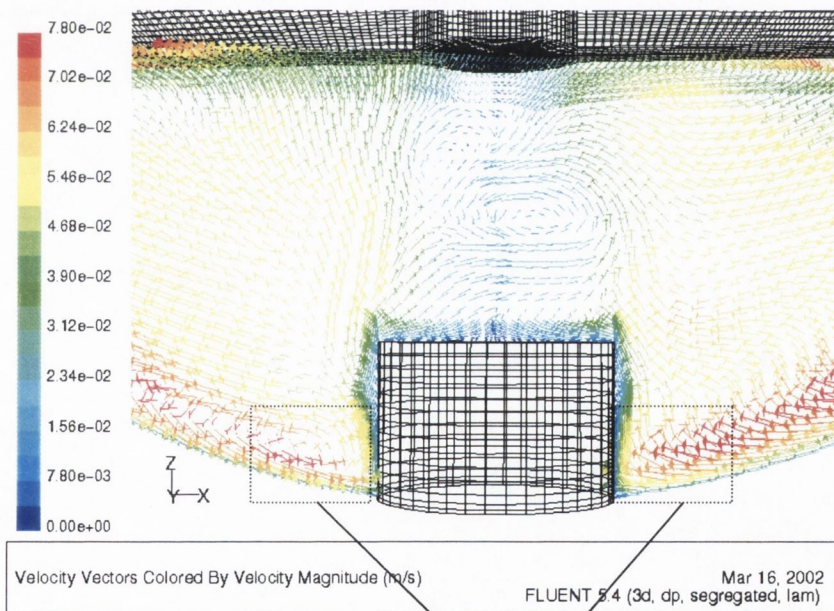
It is clear from Figure 3.26 that the presence of the compact has complicated the fluid flow at the base of the vessel. Visual inspection indicates that fluid shear rates vary depending on the compact surface and with the location on the surface. A region of high fluid shear rate with a large inward radial component is clearly evident towards the base of the compact. It would appear that this region of high fluid shear rate is located within the height defined by the wax pedestal of system E (section 3.1.3) i.e. the lower 3mm of cylindrical geometry above) and that the presence of the pedestal has had the desired effect of raising the actual compact above this region of complicated flow. A similar fluid flow pattern was observed at 90° to the paddle impeller.

3.2.4.2 Examination of velocity boundary layer

Although the grid region surrounding the compact had been adapted, it was clear the region immediately surrounding the compact was not of sufficient refinement to allow demonstration of the development of a velocity boundary layer in this region. In an effort to quantify the magnitude of the fluid velocity boundary layer on the various surfaces of a compact, a region of very high mesh refinement is needed in the region of the velocity boundary layer. For this section, it was decided to examine the compact, which was resting at the base of vessel (system B, section 3.1), as actual dissolution rates had been calculated for various surfaces from geometrically similar compacts (section 3.1).

3.2.4.3 Flow vectors at the mid-plane

Simulated velocities on a plane aligned with the paddle wings in the USP dissolution apparatus at 50rpm after inclusion of the compact with a high degree of refinement at the surface interface are shown in Figure 3.27.



High fluid shear rate with large inward radial component

Figure 3.27 Simulated velocity vectors on a mid-plane in line with the paddle wings in the USP dissolution apparatus at 50rpm with a compact of 8.5 mm height situated at the base of the vessel. Not all grid points are included (for clarity).

Similar to that shown in Figure 3.26, fluid shear rates vary depending on the compact surface and with the location on the surface, with a region of large inward radial component towards the base of the compact. This region of high fluid shear rate is consistent with the preferential erosion towards the base of compacts of benzoic acid, following dissolution in the USP paddle dissolution apparatus (section 3.1.2). The simulated compact was of the same dimensions as the compact which had been photographed with this preferential erosion (Figure 3.2).

3.2.4.4 Visual examination of velocity boundary layer

Closer inspection of the fluid velocities at the surface of the compact in Figure 3.27 reveals that the fluid immediately outside the surface of the compact undergoes a gradual increase from zero velocity to a plateau bulk value over a very small distance. To visually examine the development of this 'velocity boundary layer' (hydrodynamic boundary layer, d_h) in this region, a number of two-dimensional lines were introduced extending from the compact surface into the bulk fluid. The fluid vectors resulting at the intersection between these lines and the individual grid points were examined in closer detail and the graphical outputs included in Figure 3.28. The development of a velocity boundary layer from the surface of the compact into the fluid is obvious from the lines of selected velocity vectors in Figure 3.28, both outside the curved surface and on the upper planar surface. It appears, even on visual inspection, that the thickness of this velocity boundary layer differs depending on the surface and location investigated.

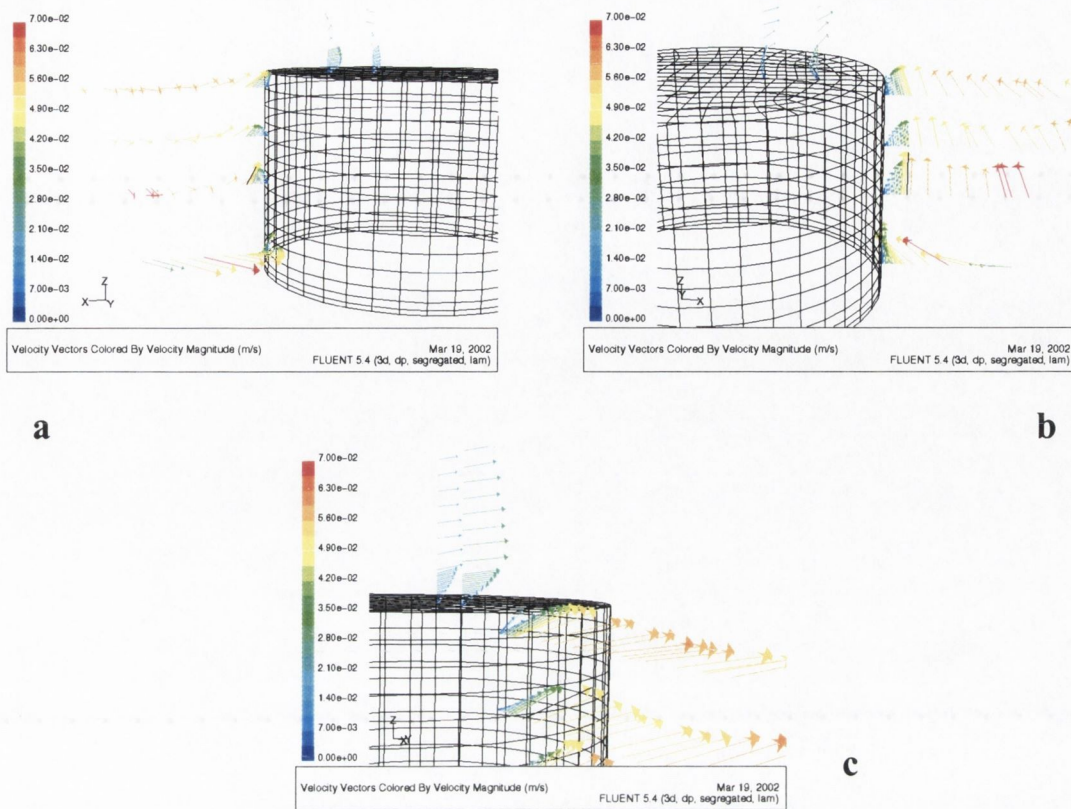


Figure 3.28 Vectors of velocity magnitude on various lines extending from the compact surface into the fluid, visually indicating the development of a velocity boundary layer in the fluid at the compact surface interface.

3.2.4.5 Quantitative analysis of velocity boundary layer

In the interest of correlating experimentally determined dissolution rates from the various surfaces of a compact with the simulated fluid velocities, it was necessary to examine the fluid velocity rates in the region immediately outside the fluid velocity boundary layer surrounding the compact surface. This objective necessitated the quantitation of the magnitude of this velocity boundary layer for the various surfaces of the solution of the simulated compact.

3.2.4.5.1 Top planar surface

The initial study focused on the fluid velocities above the top planar surface. The method of analysing the magnitude of velocity boundary layer from this surface consisted of definition of a series of planes in close proximity to the surface of the compact and examination of the tangential component of velocity (parallel to the surface) for such planes, in the region directly above the compact. A graphical

illustration of the changes in velocity over the first 2mm of the fluid interface above the top planar surface of the compact is shown in Figure 3.29.

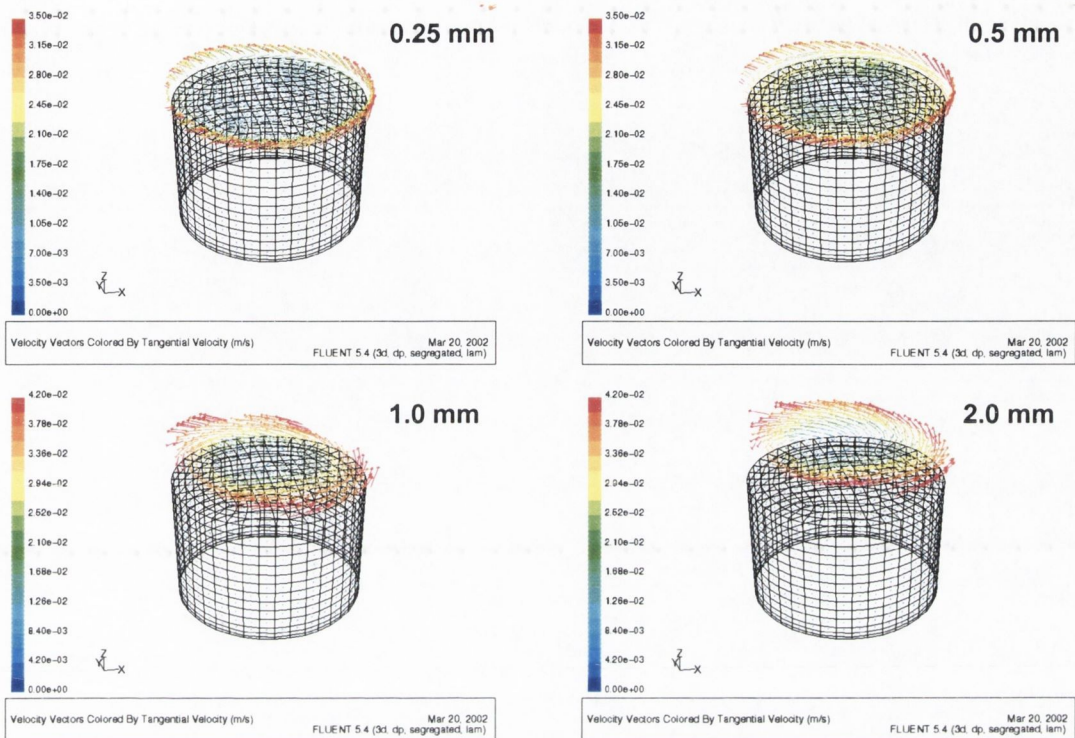


Figure 3.29 Vectors of tangential velocity at planes 0.25 mm, 0.5 mm, 1.0 mm and 2.0 mm from the top planar surface of the compact.

It is evident from Figure 3.29 that the tangential velocity above the top planar surface of the compact increases with increasing radius. It was postulated by Bocanegra et al. (1990) and Khoury et al. (1988) that this feature could be attributable to the fluid undergoing solid body rotation above the compact surface, induced by the solid body rotation of the impeller. If this was the case, then the fluid in this region would have a constant angular rotation, ω_f , which would be independent of the radius in this region, as described by Equation 3.1. If the fluid in this region is, in fact undergoing solid body rotation, then the tangential velocity components above the compact could be represented by a single value, ω_f .

To determine if ω_f was, in fact, independent of the radius, the tangential components of velocity were examined for a series of planes at increasing distance from the top circular surface (over the first 2 mm). Each file contained velocity data for all grid points in the region. To convert these data series into average tangential velocity

(over all angles) for a series of radii required the use of the C program, COMPARE (as outlined in Appendix 9). The resulting average tangential velocity at each radius was converted to a series of rotational velocities (ω_f), for each radius (40%, 60% 80% and 100% of the compact radius, for each plane). The average tangential velocity components for each radius examined at 1mm above the compact are shown in Figure 3.30, while the corresponding average rotational velocities for each radius examined are shown in Figure 3.31. The tangential velocity graph shows a graded increase in velocity with increasing radius, while the angular velocity plot overlaps for all radii examined (with some fluctuation for the lowest radius). Both plots are indicative of solid body rotation and this behaviour was displayed by the data for the other planes studied also. In order for all the tangential components of flow over the entire plane (compact diameter) to be represented by a single value, the individual values of angular velocity in Figure 3.31 were averaged for all radii and angles studies. The resulting value, ω_f , for each plane, would allow direct comparison of angular velocities between the planes at various heights.

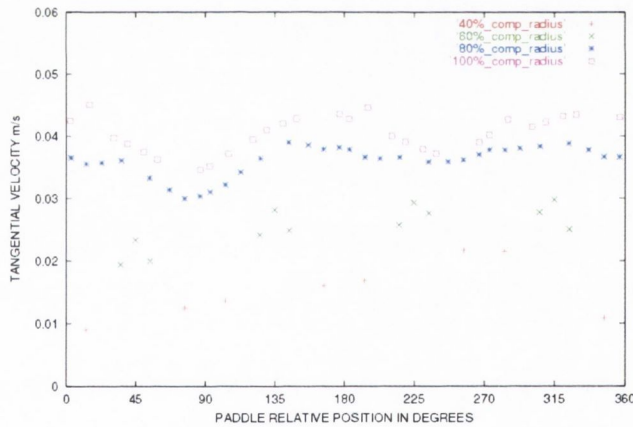


Figure 3.30 Graph of tangential velocities, v_t , over all angles on a plane 1 mm above the top planar surface of the compact, for four radii within this region.

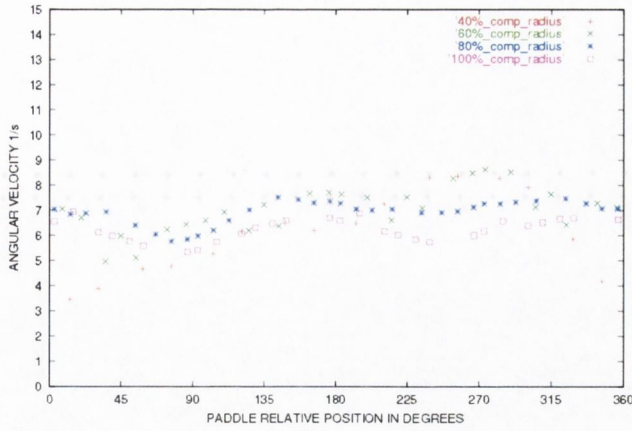


Figure 3.31 Graph of angular velocities (ω_f) over all angles on a plane 1 mm above the top planar surface of the compact, for four radii within this region.

The above process of calculating the average angular velocity was repeated for a series of planes within the region of high grid refinement at the fluid-compact surface interface. The resulting angular velocities for the various planes were plotted versus distance from the surface, as shown in Figure 3.32.

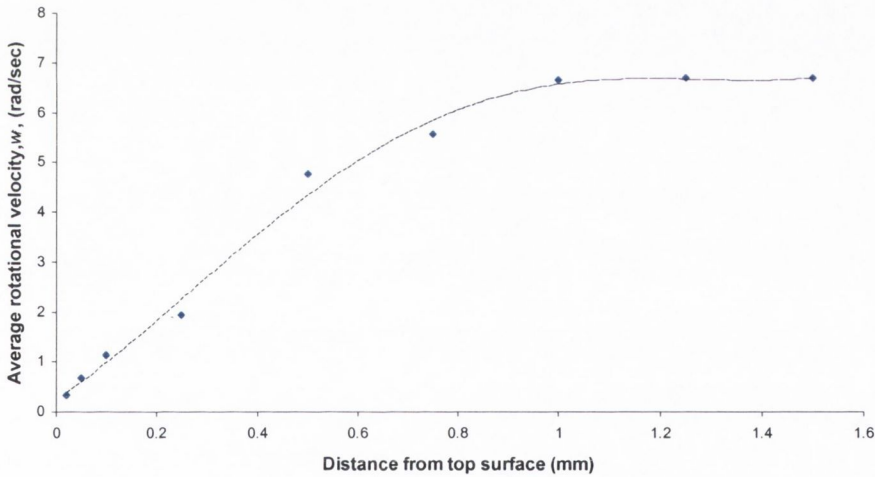


Figure 3.32 Graph of rotational velocities (ω_f) averaged over all angles for a series of planes (with radius of compact) within 1.5mm from the top planar surface of the compact at 50rpm

The parabolic shape of the profile in Figure 3.32 is representative of the development of a velocity boundary layer. The profile reaches a plateau after approximately 1mm, where the average angular velocity remains constant. Therefore, the thickness of the velocity boundary layer for this top planar surface can be said to be in the region of 1 mm.

3.2.4.5.2 Side (curved) surface- Average velocity components

In order to examine velocities outside the curved surface, cylinders of velocity data at various distances from the curved surface were exported. A new C program called CYLINDERS was used to calculate average values of the relevant velocity component between specified heights within these cylindrical velocity component data files (see appendix 9). The rotational velocities (ω_f) averaged over all angles between the base and top of the curved surface of the compact for a series of cylinders within 2 mm of the side curved surface of the compact at 50rpm are shown in Figure 3.33.

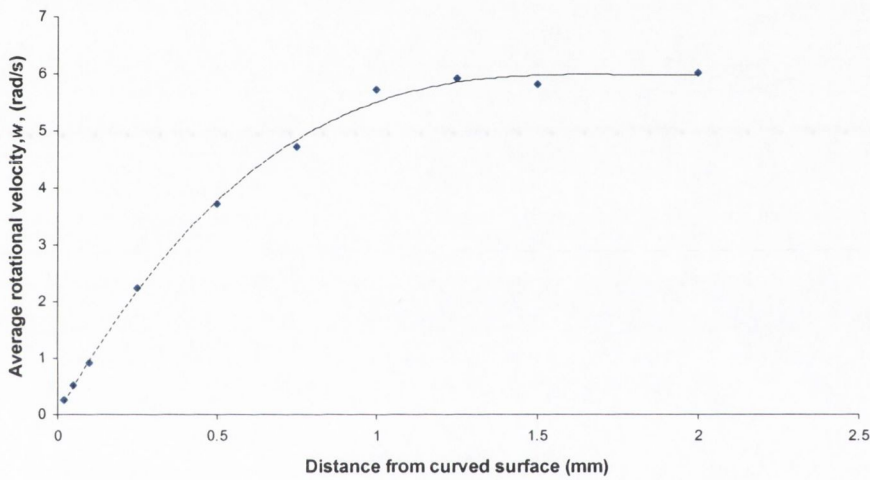


Figure 3.33 Graph of rotational velocities, ω_f , averaged over all angles from the base of the compact to the top of the curved surface for a series of cylinders within 2 mm from the side curved surface of the compact at 50rpm.

The velocity boundary layer thickness for the rotational component of velocity can be calculated in this case to approximately 1.25 mm. A similar evaluation was performed on the average axial component of velocity outside the curved surface of the compact, with the resulting profiles being shown in Figure 3.34.

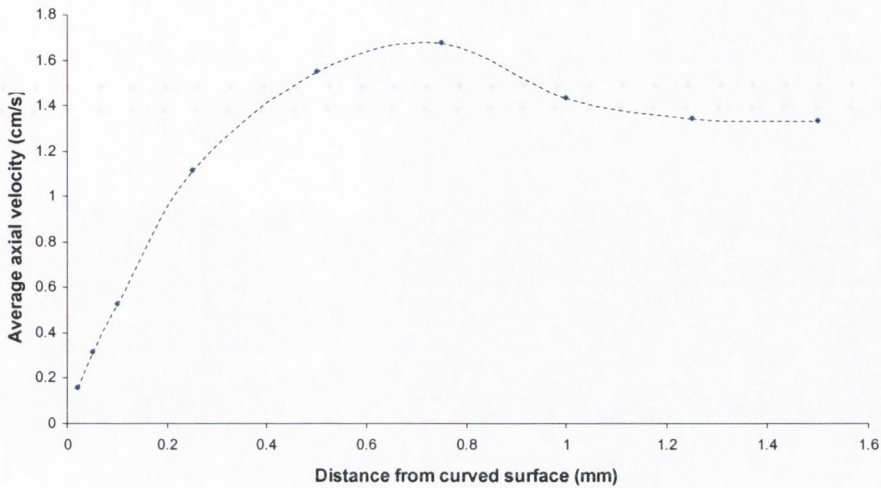


Figure 3.34 Graph of axial velocities averaged over all angles from the base of the compact to the top of the curved surface for a series of cylinders within 2 mm from the side curved surface of the compact at 50rpm.

Again, the average axial component of velocity outside the curved surface of the compact can be seen to attain a value of the bulk also at approximately 1.25 mm. The bulk axial velocity in this region can be calculated to be approximately 1.35 cm/s. Although the peak seen before the plateau in Figure 3.34 seems unusual, such behaviour has been mathematically predicted in flow where the surface is stationary with a rotating fluid, generally referred to as Bödewadt flow (Bödewadt, 1940) as described in section 1.1.3.4

3.2.4.5.3 Side (curved) surface- sub-divisions of velocity components

The velocity components in the hydrodynamic boundary layer outside the curved surface of the compact were of particular interest due to the variable dissolution rates which had been noted for this surface (section 3.1.3). Therefore, this region was separated into sub-divisions and the resulting fluid velocity components were examined in each subdivision. The cylindrical data in the region outside the curved surface was divided into six sub-divisions and the velocity components in each region treated as outlined in the previous section.

The tangential velocities averaged over all angles for six divisions between the base and top of the compact for a series of cylinders within 1.5 mm of the side curved

surface of the compact at 50rpm are shown in a three-dimensional graph in Figure 3.35. As the fluid in this region underwent solid body rotation, a more precise output of the shear rates in the velocity boundary layer is the examination of the rotational velocity. The rotational (angular) velocities averaged over all angles for six divisions between the base and top of the compact for a series of cylinders within 1.5 mm of the side curved surface of the compact at 50rpm are shown in a three-dimensional output in Figure 3.36. The bulk rotational velocity was higher for the lower 3 mm of the compact and the thickness of the velocity boundary layer is approximately 1 mm for all areas outside the curved surface.

The axial velocities, averaged over all angles for six divisions between the base and top of the compact for a series of cylinders within 1.5 mm of the side curved surface of the compact at 50rpm are shown in a three-dimensional output in Figure 3.37. Again, a high velocity region towards the lower base of the compact was evident from the axial velocity profile. The axial velocity component is not as large in magnitude as the tangential component outside the curved surface.

The radial velocities, averaged over all angles for six divisions between the base and top of the compact for a series of cylinders within 1.5 mm of the side curved surface of the compact at 50rpm are shown in a three-dimensional output in Figure 3.38. A region of high inward radial velocity is evident within the lower 1.5 mm outside the curved surface, consistent with the observed preferential erosion of the curved surface towards the base of actual compacts, following dissolution (section 3.1.2)

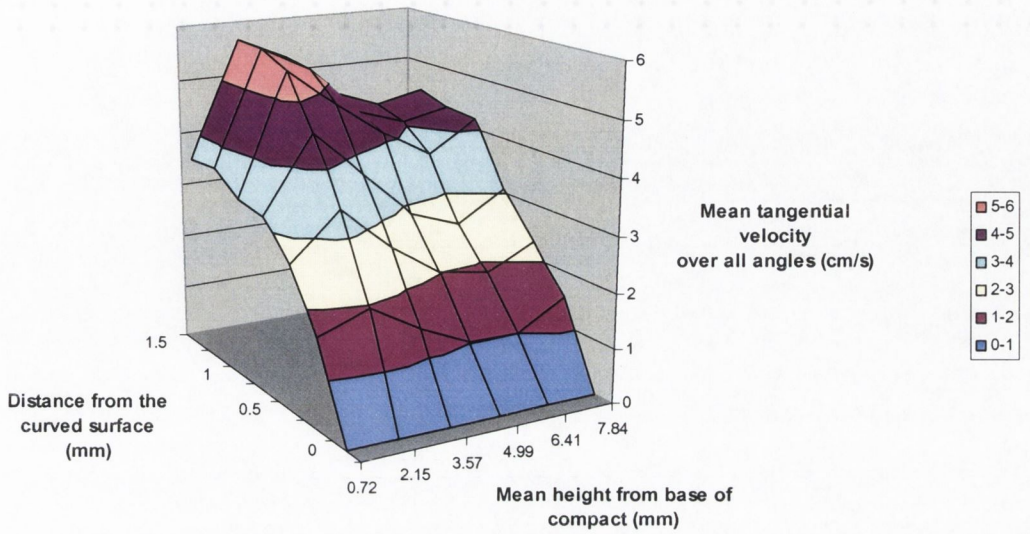


Figure 3.35 Graph of tangential velocities, averaged over six divisions from the base of the compact to the top of the curved surface, over all angles for a series of cylinders within 1.5 mm from the side curved surface of the compact at 50 rpm.

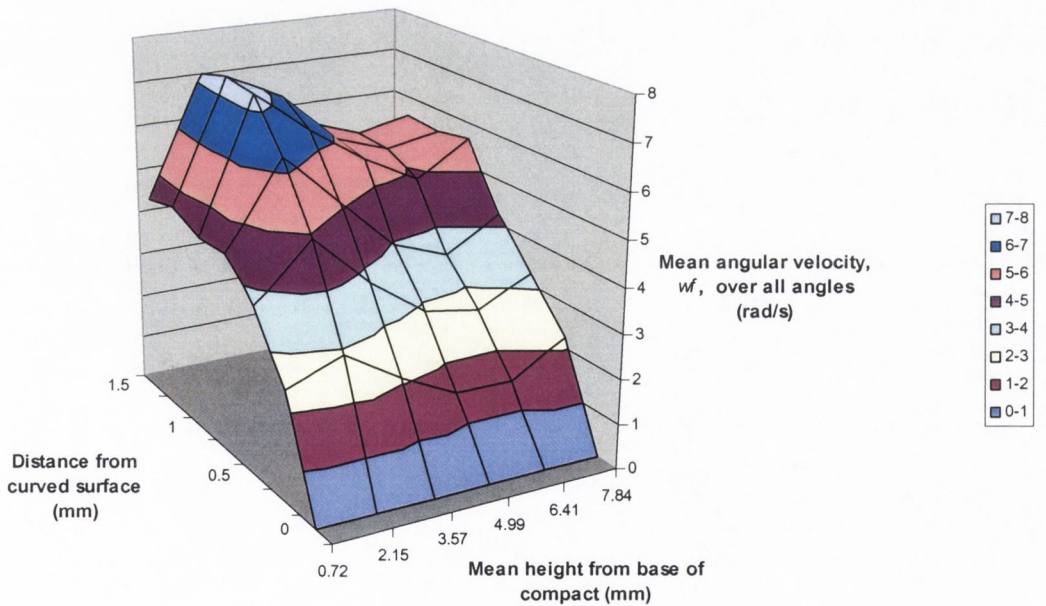


Figure 3.36 Graph of angular (rotational) velocities, w_f , averaged over six divisions from the base of the compact to the top of the curved surface over all angles for a series of cylinders within 1.5 mm from the side curved surface of the compact at 50 rpm.

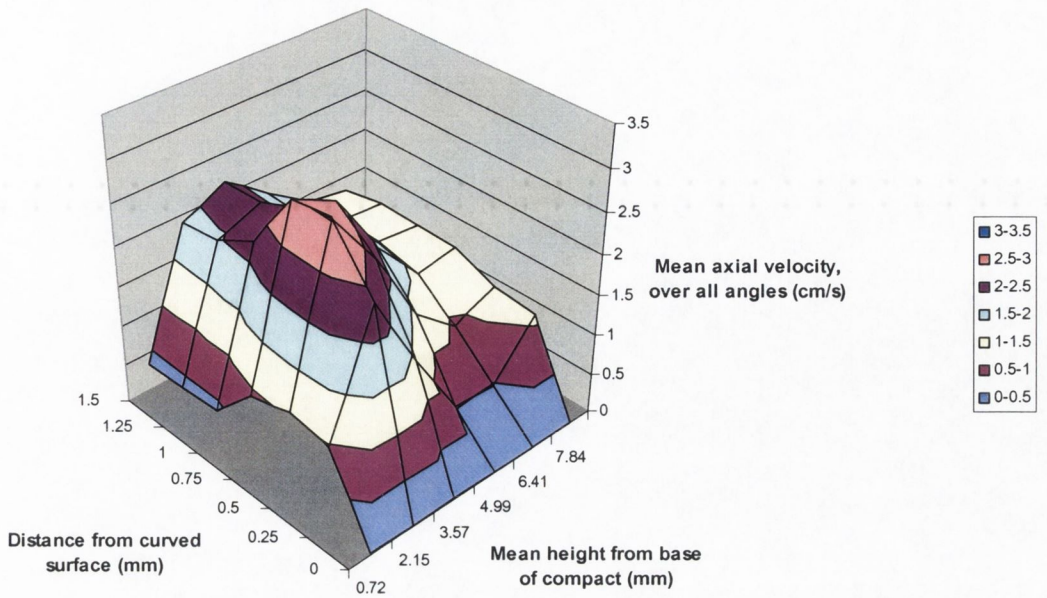


Figure 3.37 Graph of axial velocity, averaged over six divisions from the base of the compact to the top of the curved surface over all angles for a series of cylinders within 1.5 mm from the side curved surface of the compact at 50 rpm.

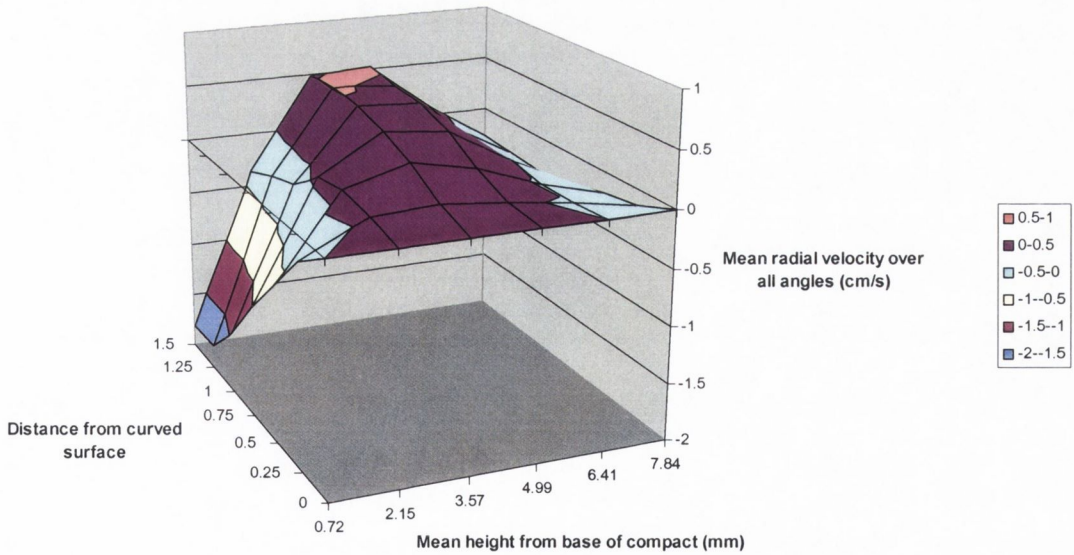


Figure 3.38 Graph of radial velocity, averaged over six divisions from the base of the compact to the top of the curved surface over all angles for a series of cylinders within 1.5 mm from the side curved surface of the compact at 50 rpm.

3.2.4.6 Mass transfer calculations

3.2.4.6.1 Mass transfer from top planar surface

Colton and Smith (1972) have discussed a mass transport model for a fluid undergoing solid body rotation above a stationary non-disintegrating disk. More recently, Khoury et al. (1988) have demonstrated the utility of a similar model applied to mass transfer systems of pharmaceutical interest (see section 1.1.3.4) described by the following equation,

$$R = 1.33D^{2/3}C_s(\nu)^{-1/6}(\omega)^{1/2}r^{3/2} \quad \text{Equation 3.2}$$

where R is the dissolution rate (g/sec), D is the diffusion coefficient (cm²/sec), C_s is the saturated solubility of the drug (g/cm³), ν is the kinematic viscosity of the dissolution medium (cm²/sec), ω is the angular velocity of the fluid (rad/sec) and r is the radius of the circular area exposed for dissolution (cm). The corresponding values for the top surface of a compact of benzoic acid of height 8.5 mm dissolving in the USP dissolution apparatus are included in Table 3.7, where ω was calculated from the bulk rotational velocity outside the velocity boundary layer above the top planar surface of the compact, as shown in Figure 3.31. Although the actual dissolution medium employed was 0.01N HCl, the viscosity value is that of water at 37°C. The predicted mass transfer rate using this approach for benzoic acid was calculated to be 0.60 mg/min, which compares favourably with an experimentally determined rate of 0.54 mg/min (system I, section 3.1.4).

Table 3.7 Summary of factors used to calculate mass transfer from the top planar surface of a compact, based on fluid velocities predicted by CFD

EQUATION FACTOR	Symbol	Units	Value
DIFFUSION COEFFICIENT	D ⁺	cm ² /sec (x 10 ⁶)	12.36
SATURATED SOLUBILITY	C_s ⁺	g/cm ³ (x 10 ³)	4.55
FLUID ANGULAR VELOCITY	ω	rad/s	6.67
KINEMATIC VISCOSITY	ν ^x	cm ² /sec (x 10 ³)	6.95
RADIUS OF CIRCULAR AREA	r	cm	0.65

⁺ (Ramtoola, 1988.), ^x (Visawanth and Natarajan, 1989)

3.2.4.6.2 Mass transfer from side (curved) surface

An analytical solution to predict mass transfer from the curved surface of a compact in a rotating fluid has not been previously examined. In this case, the tangential velocity does not contribute to mass transfer, as this velocity component is axis-symmetrical with the axis of the dissolving compact. In fact, the component of velocity which contributes to mass transfer from this surface is the secondary axial fluid velocity component. A semi-analytical model was developed to allow mass transfer predictions from the curved surface, based on knowledge of the axial fluid velocity component in the diffusion boundary layer outside the compact. The geometrical co-ordinates and velocity component of this model are outlined in Figure 3.39.

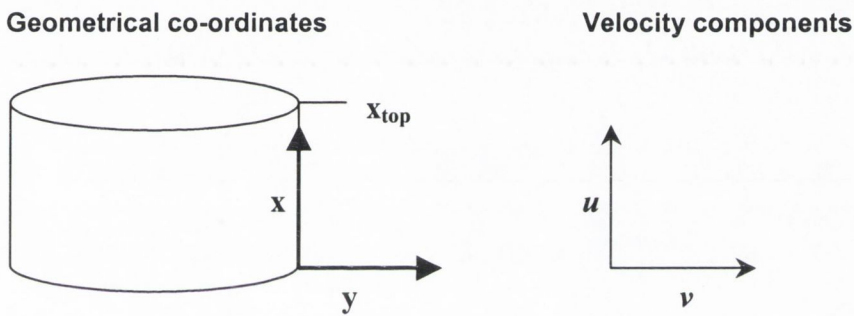


Figure 3.39 Geometrical co-ordinates and velocity components used in the derivation of the model of mass transfer from the curved surface of a stationary cylindrical compact in a rotating fluid.

The approach involves the determination of shear rates of axial velocity, α , in the diffusion boundary layer, at various heights of the compact, x . where:

$$\alpha = \frac{u}{y}$$

i.e. the slope of the axial fluid velocity profile immediately outside the compact in the diffusion boundary layer. The net dissolution rate of drug from the curved surface, R , can then be defined as:

$$R = 2\pi a C_o \left(\frac{3}{2} DF_o \right)^{2/3} \quad \text{Equation 3.3}$$

where

$$F_o = \int_0^{x_{top}} \alpha^{1/2} dx \quad \text{Equation 3.4}$$

and x_{top} is the height of the dissolving compact and a is the radius of the compact. A complete derivation of the equation can be found in Appendix 10. For this approach, α was calculated from the slopes of the axial velocity distributions in the diffusion boundary layer (i.e. slopes of axial velocity within 0.2mm outside the compact, for the six cylindrical sub-divisions as shown in Figure 3.37). The resulting slopes α , for each of the subdivisions are then converted to $\alpha^{1/2}$, and plotted versus the x-axis, as shown in Figure 3.40.

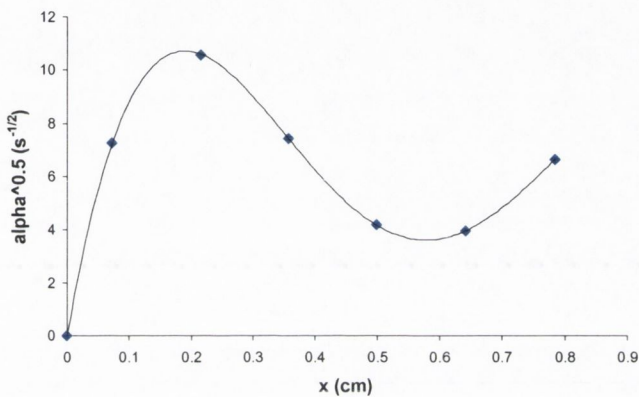


Figure 3.40 Plot of $\alpha^{1/2}$ versus distance in the x direction up the curved surface of the cylinder, where α is the fluid shear rate at the surface of the compact in the axial direction of flow.

The resulting polynomial fit to the curve in Figure 3.40 was integrated from 0 to x_{top} to yield a value for $F_o = 5.58 \text{ cm sec}^{-1/2}$. Applying this value to Equation 3.3 with the parameters previously defined in Table 3.7 yielded a value of $R = 2.46 \text{ mg/min}$. The corresponding experimental dissolution for this system was 1.97 mg/min (system D, section 3.1).

Possible reasons for the 25 % deviation include:

- It is assumed that fluid flow is parallel to the surface only. However, large radial velocity components have been shown to be present in the diffusion boundary layer (Figure 3.38), particularly in the region of the lower 3 mm of the compact.
- The semi-analytical model is based on the assumption that the cylinder is infinitely long, clearly not the case as the ratio of the height/width of the cylinder ≈ 1 .

3.3 CONCLUSIONS

Initial studies involving dissolution from the complete surface of single component compacts revealed that uniform hydrodynamic conditions were not present on all parts of the curved surface. Further studies revealed that dissolution fluxes varied depending on the location of the surface from where dissolution occurred and also on the position of the compact in the vessel. Highest dissolution rates per unit surface area were seen from the surfaces of compacts sitting within 3 mm from the base of the vessel. Dissolution studies were carried out on compacts sitting on a wax pedestal of approximately 3 mm height, in an effort to raise the compacts from this region.

A computational fluid dynamics model of the paddle dissolution apparatus was built up using a structured grid approach and a rigorous treatment of the post-processor set-up. The resulting simulated velocities were in close agreement with published laser velocimetry measurements in the apparatus (Bocanegra et al., 1990).

Predicted secondary flow patterns on mid-planes in the vessel agreed with those previously speculated for the apparatus (Bocanegra et al., 1990; Beckett et al., 1996). Fluid flow behaviour below the level of the paddle was complicated and large changes in velocity were evident over small distances. Such complicated hydrodynamic behaviour was speculated to be a contributing factor to the variable dissolution results previously reported (Qureshi et al. 1999, Achanta et al., 1995).

Path-lines of fluid mixing, examined from this central region at the base of the vessel for the duration of 1 minute at 50 rpm, did not reveal a region of poor mixing between the upper cylindrical and lower hemi-spherical volumes. However, mixing appeared to be sub-optimal towards the top of the vessel. Examination of different impeller rotation speeds revealed large differences in the time required to achieve complete mixing. Linear increases in velocity magnitudes were predicted for various positions in the vessel, thus indicating that the flow in the vessel was laminar up to at least 150 rpm.

The effect of the addition of a compact at the base of the vessel complicated the fluid flow at the base of the vessel. A region of high fluid shear was noticeable towards the

base of the compact. It appeared that the positioning of the experimental compacts on a wax pedestal of 3 mm height would have the desired effect of raising the compacts above this region of complicated fluid flow.

An examination of the velocities in a refined region immediately outside the surface of the compact revealed that the fluid above the planar surface was undergoing solid body rotation. Fluid flow behaviour outside the curved surface was more complex than fluid flow above the upper surface. Close examination of the velocity boundary layers outside the curved surface of the compact revealed that there were large peaks in the shear rates for a region within approximately 3 mm from the base of the compact, consistent with the grooving effect, which had been previously seen on the surface of compacts following dissolution.

A mass transfer prediction was made for the top surface, based on the angular rotation of the fluid in this region. The resulting dissolution rate was in close agreement with the corresponding experimentally determined result. A semi analytical solution was developed to describe diffusion from the curved surface of a compact sitting at the base of the vessel. This approach was based on the examination of fluid shear rates in the axial direction in the diffusion boundary layer immediately outside the curved surface. The predicted mass transfer rate using this equation was 25% higher than the experimentally calculated dissolution rate. The deviation was explained in terms of the shortcomings of the assumptions of the model.

4.1 INTRODUCTION

Initial simple layered compact studies examined the dissolution behaviour, in 0.1N HCl, of three layer compacts containing salicylic acid (SA) and benzoic acid (BA) as the model drug and excipient respectively. Studies concentrated on three-layered systems because three-layered tablets have been produced commercially (e.g. Geomatrix[®], Skyepharma U.K.) using commercially available technology (Layerpress, Manesty, Hata). In vitro dissolution studies were carried out in a medium of de-aerated 0.1N HCl as described in section 2.11. Dissolution samples were analysed for salicylic acid (model drug) as described in section 2.11.2.2.1.

4.2 SALICYLIC ACID AS MODEL DRUG

4.2.1 Benzoic acid and salicylic acid (BA/SA/BA)

Each layer consisted of 500mg and was prepared as outlined in section 2.10.1. Salicylic acid was the model drug in these systems. Dissolution of salicylic acid from the three-layered compact benzoic acid/salicylic acid/benzoic acid is shown in Figure 4.1, results shown being the average of three determinations.

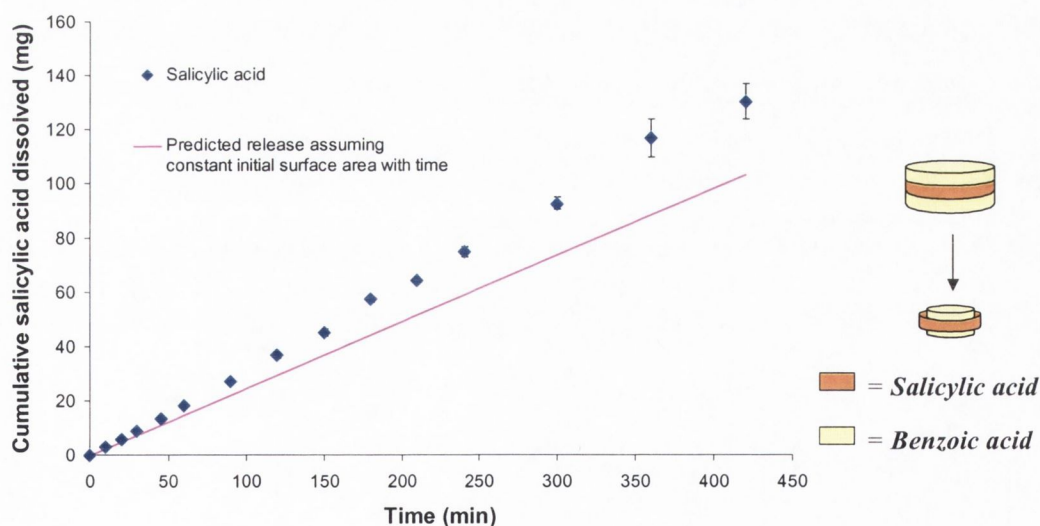


Figure 4.1 Cumulative salicylic acid dissolved from benzoic acid/salicylic acid three-layered system (BA/SA/BA), 500mg per layer, in 0.1N HCl. Error bars indicate standard deviations. The straight line is the predicted dissolution rate of the drug layer, should the surface area remain constant during dissolution. Schematic illustrates layered compact undergoing dissolution.

The predicted linear release profile in Figure 4.1 was generated by inserting the initial surface area of salicylic acid available into the equation of Nernst and Brunner (Equation 1.5) to allow calculation of a predicted initial release rate (dW/dt). This value was then extrapolated over time to yield a predicted linear release profile assuming that the surface area of salicylic acid available for dissolution remained constant with time.

As can be seen from the dissolution profile, the salicylic acid release remained linear ($r^2 = 0.998$) over the course of the dissolution test (420 min). The dissolution rate actually increased above the release for constant surface area. Thus the newly exposed surface area of the salicylic acid layer, due to dissolution of the more rapidly dissolving benzoic acid layers, has a compensatory effect on the decreasing surface area of the curved surface of the central salicylic layer.

4.3 THEOPHYLLINE MONOHYDRATE AS MODEL DRUG

Theophylline was chosen as the model drug for further layered systems, as its solubility was higher than salicylic acid, which had only partially dissolved after 7 hours dissolution. Theophylline exists in two physical forms, as the anhydrous form and as the monohydrate form. In order to avoid quantitation of the kinetics involved in the conversion of the anhydrous form to the monohydrate on dissolution (and thus further complicating the modeling of the effect of changes in surface area), it was decided to use the monohydrate form of theophylline as the model drug. Theophylline monohydrate was formed from the anhydrous starting material as described in section 2.4.

As theophylline monohydrate is more soluble than benzoic acid or salicylic acid, more soluble acid excipients were chosen for use as the excipient layers for these systems. PVP was included at the level of 5% in the theophylline monohydrate layer of compacts containing adipic acid, as the layers of these compacts separated when a binder was absent. PVP was shown to not have a significant effect on the slopes of the intrinsic dissolution rates (Appendix 4).

It has been reported that theophylline has a pK_a near pH 0.5 (Cohen, 1990). To prevent partial ionisation of the drug, the medium used in these experiments was de-aerated 0.01N HCl, adjusted to $pH 2 \pm 0.05$ with 0.1N HCl. Dissolution studies were carried out as described in section 2.11. Samples were analysed for theophylline monohydrate content by HPLC analysis as described in section 2.11.2.2.2.

4.3.1 Theophylline monohydrate and succinic acid (SuA/Thmh/SuA) in 0.01N HCl

Dissolution of theophylline monohydrate from the three-layered compact succinic acid/theophylline monohydrate/succinic acid (SuA/Thmh/SuA), 500mg per layer, into 0.01N HCl is shown in Figure 4.2, results shown being the average of three determinations.

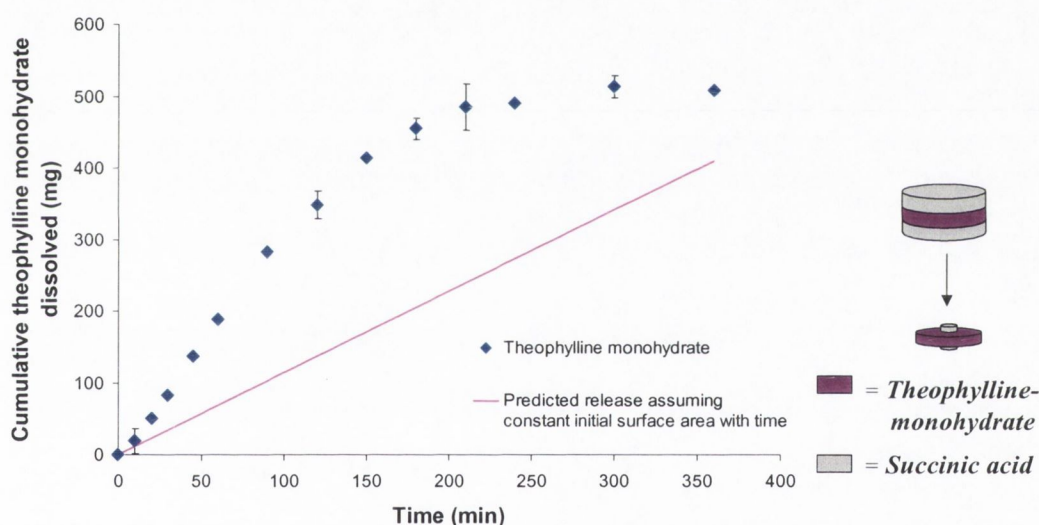


Figure 4.2 Cumulative theophylline monohydrate dissolved from theophylline monohydrate/succinic acid three-layered system (SuA/Thmh/SuA), 500mg per layer, in 0.01N HCl. Error bars indicate standard deviations. The straight line is the predicted dissolution rate of the drug layer, should the surface area remain constant during dissolution. Schematic illustrates layered compact undergoing dissolution.

As can be seen from Figure 4.2, the dissolution of theophylline monohydrate from this system was much greater than that predicted should the initial surface area available for dissolution remain constant over this period. This was caused by the rapid dissolution of the more soluble succinic acid layers (all had dissolved within 30 minutes). Thus the succinic acid layers did not have an appreciably large effect on the

theophylline monohydrate release dissolution release profile. However, the presence of the succinic acid layers has resulted in a dissolution profile, which is sigmoidal shape. Dissolution rates are increasing for the first 30 minutes, resulting in an upward curvature in the profile. Following complete dissolution of the succinic acid layers, the dissolution profile curved downwards.

4.3.2 Theophylline monohydrate and adipic acid (AA/Thmh/AA) in 0.01N HCl

Dissolution of theophylline monohydrate from the three-layered compact adipic acid/theophylline monohydrate/adipic acid (SuA/Thmh/SuA), 500mg per layer, into 0.01N HCl is shown in Figure 4.3, results shown being the average of three determinations.

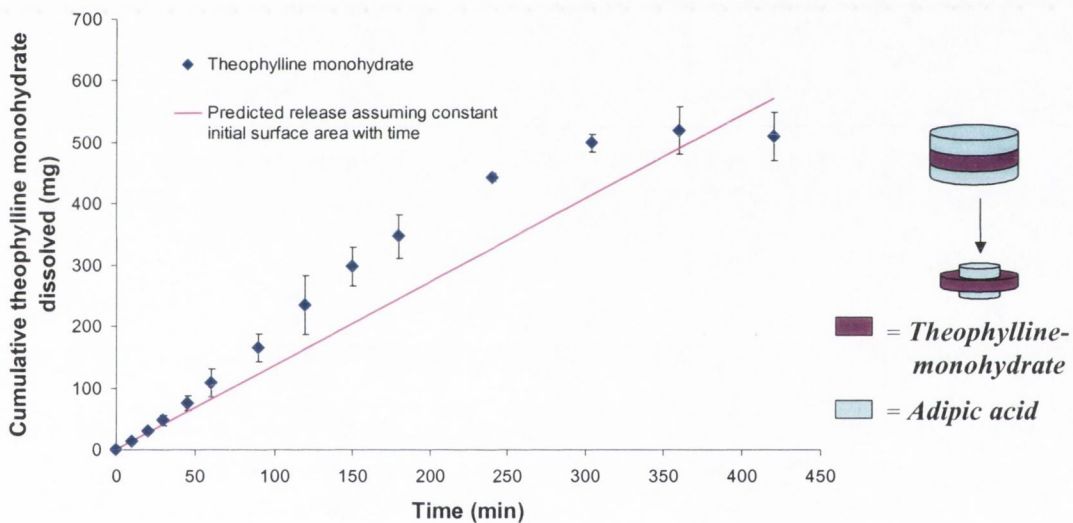


Figure 4.3 Cumulative theophylline monohydrate dissolved from theophylline monohydrate/adipic acid three-layered system (AA/Thmh/AA), 500mg per layer, into 0.01N HCl. Error bars indicate standard deviations. The straight line is the predicted dissolution rate of the drug layer, should the surface area remain constant during dissolution. Schematic illustrates layered compact undergoing dissolution.

As can be seen from Figure 4.3, the theophylline monohydrate dissolution profile initially curved upwards. However, as the adipic acid layers dissolved in the first 2 to 3 hours, the theophylline-monohydrate profile subsequently curved downwards, as the theophylline content became depleted. Again the profile is sigmoidal in shape. The theophylline release was also increased above that which was predicted, should the exposed surface area of theophylline remain constant for this period.

Chapter 4

Dissolution from simple multi-layered compacts

4.4 INITIAL MODELLING OF DISSOLUTION FROM SIMPLE LAYERED SYSTEMS

4.4.1 Calculation of surface area changes in three-layered systems

A relatively simple model was developed to determine the surface area changes over time of the central-drug layer, due to regression of the more soluble outer layers, and exposure of new surface area for dissolution at what was the original drug/excipient layer interface. This method requires a number of assumptions to be made. If it can be assumed that dissolution of drug and excipient layers from the curved surface occurs in a direction perpendicular to this curved surface only, and that the dissolution rate is independent of height within each layer, and assuming that the thickness of the drug layer does not change with time, then we can mathematically predict the surface area changes of the drug layer, over time.

For a cylinder such as a compressed disc, its weight (W) is given by

$$W = \rho \frac{\pi x^2 y}{4} \quad \text{Equation 4.1}$$

where x is the diameter and y is the thickness (i.e. height) and ρ is the density of the material. If the diameter and height decrease uniformly with time (at different rates, k_1 and k_2 respectively, Healy, 1995) then;

$$\frac{dx}{dt} = -k_1 \quad \text{Equation 4.2}$$

and

$$\frac{dy}{dt} = -k_2 \quad \text{Equation 4.3}$$

Integration of Figure 4.2 and Figure 4.3 leads to the following:

$$x = x_o - k_1 t \quad \text{Equation 4.4}$$

and

$$y = y_o - k_2 t \quad \text{Equation 4.5}$$

where x_o is the initial diameter and y_o is the initial thickness.

Introducing Equation 4.4 and Equation 4.5 into Equation 4.1 leads to the following equation:

$$W = \frac{\pi\rho}{4}(x^o - k_1t)^2(y^o - k_2t) \quad \text{Equation 4.6}$$

If the diameter of the drug layer decreases uniformly with time, with a rate constant, k_{drug} and the diameter of the excipient layer also decreases uniformly with time, with a rate constant, k_{excip} , then:

$$\text{and} \quad x_{\text{drug}} = x_o - k_{\text{drug}}t \quad \text{Equation 4.7}$$

$$x_{\text{excip}} = x_o - k_{\text{excip}}t \quad \text{Equation 4.8}$$

Where x_o is the initial diameter of the drug layer and of the excipient layer, x_{drug} is the diameter of the drug layer at time t , and x_{excip} is the diameter of the excipient layer at time t . These assumptions are illustrated in Figure 4.4.

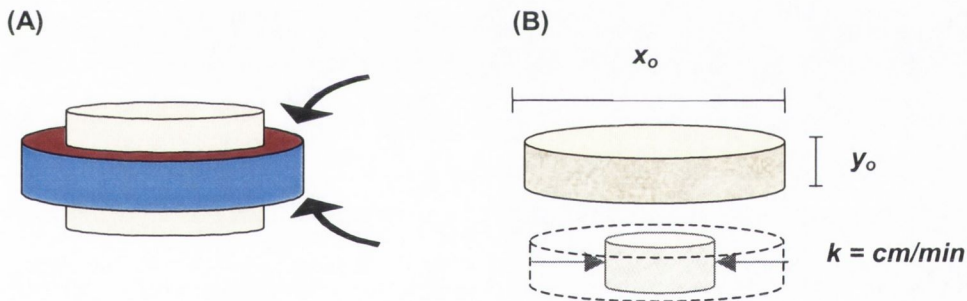


Figure 4.4 Illustration showing surface area changes of three layered compact undergoing dissolution (A) showing exposure of new surface area of drug layer (red). The model assumes that each layer consists of a cylinder throughout dissolution (B) and that the diameter changes uniformly with time at a rate k_i .

Thus, if k_{drug} and k_{excip} from Equation 4.7 and Equation 4.8 can be determined, then the surface area changes over time can be predicted mathematically.

If the curved surface area of the drug layer is SC_{drug} , the complete area of a transverse section of the drug layer is St_{drug} , and the complete area of a transverse section of the excipient layer is St_{excip} , then:

$$SC_{\text{drug}} = \pi(x_o - k_{\text{drug}}t)y_o \quad \text{Equation 4.9}$$

and

$$St_{\text{drug}} = \frac{\pi}{2} \left(\frac{x_o^2}{2} - k_{\text{drug}}.x_o.t + \frac{k_{\text{drug}}^2 t^2}{2} \right) \quad \text{Equation 4.10}$$

Similarly,

$$St_{\text{excip}} = \frac{\pi}{2} \left(\frac{x_o^2}{2} - k_{\text{excip}}.x_o.t + \frac{k_{\text{excip}}^2 t^2}{2} \right) \quad \text{Equation 4.11}$$

In the case of three-layered systems, the total newly exposed surface area of the drug layer due to regression of the more soluble excipient layers is equal to twice the difference between St_{drug} and St_{excip} , as there are 2 drug/ excipient-interfaces in this case shown in Figure 4.4(A). Therefore, the total exposed surface area of the drug layer in the three-layered systems, with respect to time, (A_{drug}) can be defined as follows:

$$A_{\text{drug}} = SC_{\text{drug}} + [2(St_{\text{drug}} - St_{\text{excip}})] \quad \text{Equation 4.12}$$

thus:

$$A_{\text{drug}} = \pi(x_o - k_{\text{drug}}t)y_o + \pi \left[\begin{array}{l} \left(\frac{x_o^2}{2} - k_{\text{drug}}.x_o.t + \frac{k_{\text{drug}}^2 t^2}{2} \right) \\ - \left(\frac{x_o^2}{2} - k_{\text{excip}}.x_o.t + \frac{k_{\text{excip}}^2 t^2}{2} \right) \end{array} \right] \quad \text{Equation 4.13}$$

Equation 4.13 allows calculation of release rates from the three-layered systems by insertion into Equation 4.14, and thus by integration over time, the cumulative amount of drug release with time can be predicted.

$$\frac{dW}{dt} = \frac{A_{\text{drug}}DCs}{h} \quad \text{Equation 4.14}$$

4.4.2 Calculation of k Values

Two methods were employed in the calculation of the relevant k values employed in the predicted release equations, method 1 and method 2 as described below.

4.4.2.1 Method 1 (Experimental determination of k values)

For the model drug layers, k_{drug} values were determined from the dissolution profiles of compacts coated with wax on the top and bottom planar surfaces. The resulting dissolution profiles were fitted to Equation 4.6 using Scientist™ with $k_2 = 0$, which allowed calculation of $k_1 = k_{\text{drug}}$.

For the excipient layers, k values were determined from the dissolution profiles of uncoated compacts for the first 60 minutes of dissolution. The resulting dissolution profiles were fitted to Equation 4.6 (k_1 and k_2 both allowed to float in this case), which allowed calculation of $k_1 = k_{\text{excip}}$. Results of the experimentally calculated k values are summarized in Table 4.1.

Table 4.1 Experimentally calculated k values from the best fit to Equation 4.6 (Method 1). MSC is the model selection criterion, CD is the coefficient of determination

COMPONENT INVESTIGATED	RATE TYPE	EXPERIMENTALLY CALCULATED k VALUE ($\times 10^4$ cm/min)	CD	MSC
Salicylic acid in 0.1 N HCl	k_{drug}	3.40	1.000	6.47
Benzoic acid in 0.1 N HCl	k_{excip}	6.40	0.999	5.90
Theophylline.monohydrate in 0.01N HCl	k_{drug}	26.2	0.999	7.58
Adipic Acid in 0.01N HCl	k_{excip}	45.9	0.998	4.93
Succinic Acid in 0.01N HCl	k_{excip}	150.4	0.997	4.52

4.4.2.2 Method 2 (Prediction of k values using intrinsic properties of drug/excipient)

A separate model was developed to predict the k values for these systems, using only intrinsic properties of the drug/excipient. Derivation of this method involves the use of the method used by Ballard and Nelson (1962), focusing on compacts which are coated with wax on the upper and lower surfaces.

The curved surface area of such a compact, A_{curv} , can be defined as:

$$A_{curv} = \pi x_o y_o \quad \text{Equation 4.15}$$

therefore, the curved surface area at time t for such a compact is:

$$A_{curv} = \pi(x_o - kt)y_o \quad \text{Equation 4.16}$$

Insertion of Equation 4.16 into the Nernst-Brunner equation (Equation 4.14) leads to:

$$\frac{dW}{dt} = \frac{-DC_s}{h} [\pi(x_o - kt)y_o] \quad \text{Equation 4.17}$$

Integration of Equation 4.17 with respect to time provides an expression for the weight of the compact remaining with respect to time (W_t). At $t=0$, $W = W_o$, which is the constant of integration, leading to the following expression:

$$W_t = W_o - \frac{DC_s \pi y_o}{h} \left(x_o t - \frac{kt^2}{2} \right) \quad \text{Equation 4.18}$$

Using the method of Healy (1995) for a cylinder decreasing in weight from the curved surface only, Equation 4.6 can be modified for release from a compact capped on the upper and lower surfaces to yield an expression for the weight remaining of the compact with respect to time.

$$W_t = \rho \frac{\pi(x_o - kt)^2 y_o}{4} \quad \text{Equation 4.19}$$

Letting Equation 4.18 = Equation 4.19 and insertion of Equation 4.1 for W_o in Equation 4.18 leads to the following equation:

$$t^2(k^2) + \left[-2tx_o - \frac{2DC_s t^2}{\rho h} \right] (k) + \frac{4DC_s x_o t}{\rho h} = 0 \quad \text{Equation 4.20}$$

Equation 4.20 is in the form of a quadratic equation, which can be solved for k . Solving for k in this manner yields a value, which is independent of time.

To determine the k value by this method requires knowledge of the saturated solubility C_s , the diffusion coefficient D , and the density of the drug/excipient. Solubility studies were carried out as described in section 2.12.1. Diffusion coefficients were determined from intrinsic dissolution rate experiments as described

in section 2.9.1. Density measurements were calculated from the weights, and dimension of the compacts. A summary of these values is shown in Table 4.2 and the corresponding k value for the systems studied is shown in Table 4.3. Values were experimentally determined, except where referenced.

Table 4.2 Summary table showing diffusion coefficient, saturated solubility and apparent density (ρ_{app}) of components investigated in simple layered studies

COMPONENT INVESTIGATED	DIFFUSION COEFFICIENT (D) (cm ² /min x 10 ⁴)	SATURATED SOLUBILITY (C _s) (g/cm ³)	(ρ_{app}) (g/cm ³)
Salicylic acid in 0.1 N HCl	6.792 ⁺	2.58 ⁺	1.394
Benzoic acid in 0.1 N HCl	7.416 ⁺	4.55 ⁺	1.304
Theophylline monohydrate in 0.01N HCl	5.300	12.49	1.442
Adipic Acid in 0.01N HCl	5.670	44.02	1.290
Succinic Acid in 0.01N HCl	5.534 [*]	113.57	1.496

⁺ (Ramtoola, 1988.) ^{*} (Healy, 1995.)

Table 4.3 Summary table of predicted k values for components investigated, calculated from intrinsic properties (Method 2)

COMPONENT INVESTIGATED	RATE TYPE	PREDICTED k (x10 ⁴ cm/min)
Salicylic acid in 0.1 N HCl	k_{drug}	8.88
Benzoic acid in 0.1 N HCl	k_{excip}	4.28
Theophylline monohydrate in 0.01N HCl	k_{drug}	15.8
Adipic Acid in 0.01N HCl	k_{excip}	65.9
Succinic Acid in 0.01N HCl	k_{excip}	143.0

4.4.3 Initial modelling results of dissolution from layered systems

Dissolution profiles were calculated using the k values. The k values determined by either Method 1 or 2 as described above were used to calculate the changing surface area (Equation 4.13), which in turn can be used to calculate the dissolution rate (Equation 4.14) and the amount of drug released. The resulting predicted profiles are shown below.

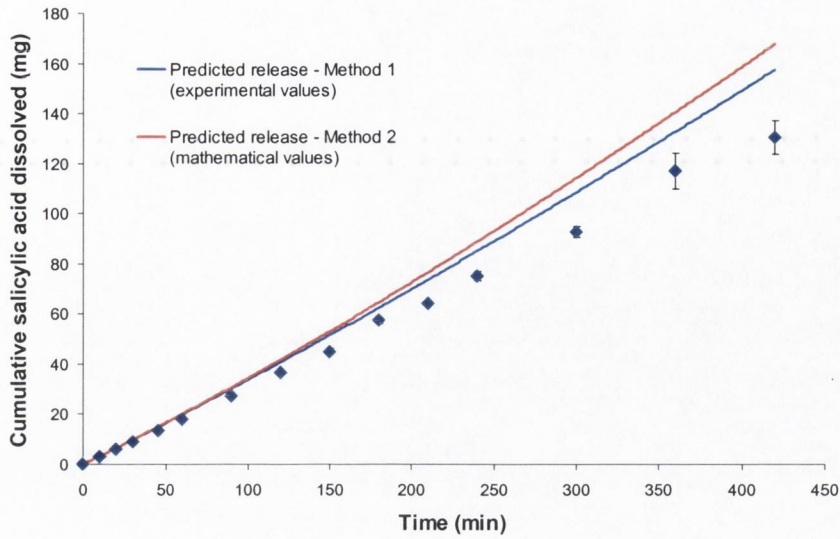


Figure 4.5 Comparison of dissolution profiles of salicylic acid, with modelled profiles using both method 1 and method 2, from benzoic acid/salicylic acid three-layered compacts (BA/SA/BA), 500mg per layer, in 0.1N HCl.

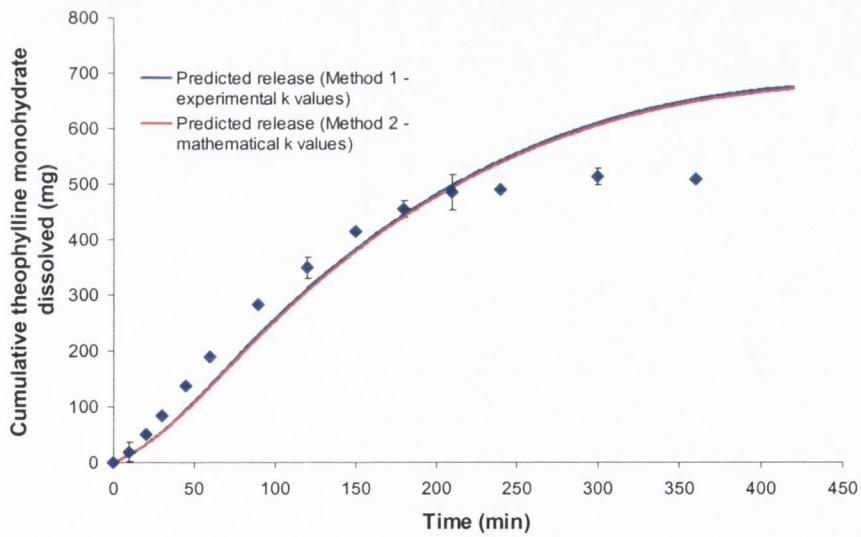


Figure 4.6 Comparison of dissolution profiles of theophylline monohydrate, with a modelled profile using method 1 and method 2, from theophylline monohydrate/succinic acid compacts (SuA/Thmh/SuA), 500mg per layer, in 0.01N HCl.

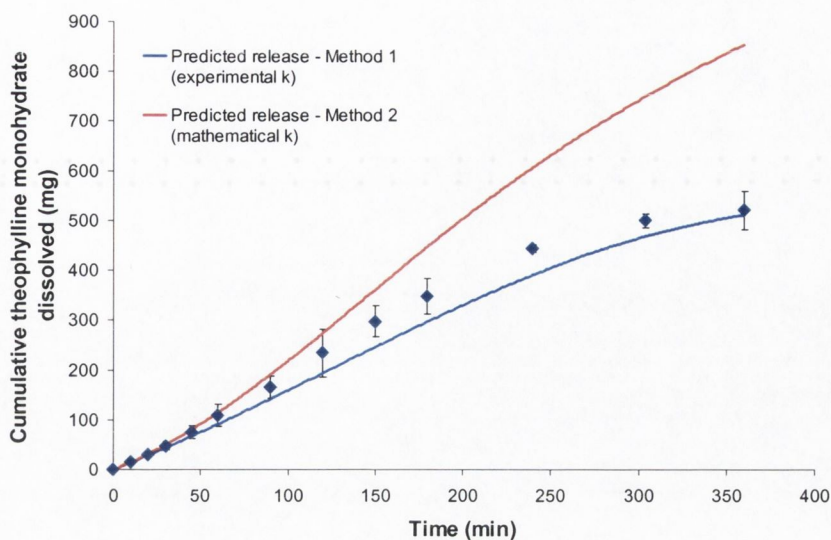


Figure 4.7 Comparison of dissolution profiles of theophylline monohydrate, with modeled profiles using both method 1 and method 2, from theophylline monohydrate/adipic acid compacts (AA/Thmh/AA), 500mg per layer, in 0.01N HCl.

The model predicts a sigmoidal release pattern. The general shape of the dissolution profiles has been matched by the predicted release patterns. In all cases the predicted release was above the actual release at later time points. Possible reasons to account for this positive deviation are as follows:

Firstly, the model does not account for a change in the thickness of the drug layer over time (even when the excipient has completely dissolved), thus the overall calculated area of drug available for dissolution is higher than the actual area, leading to increased predicted release rates. Secondly, the release rates were calculated using an overall diffusion boundary layer thickness, although previous studies have shown that minor location changes of compacts could lead to large differences in the calculated hydrodynamic boundary layer (section 3.1). It is possible that geometrical changes of these simple layered drug delivery systems can lead to changes in the apparent diffusion boundary thickness outside the various surfaces of the drug layer, with time.

4.5 DYNOCHEM SIMULATIONS OF DISSOLUTION FROM SIMPLE LAYERED SYSTEMS

A solution to the shortfalls of the initial modelling approach came in the form of access to a dynamic chemical engineering package, 'Dynochem'. Although the package is normally used in the kinetic modelling of chemical reactions between solid, liquid or gas phases in chemical reactors, the program was modified to allow simulation of mass-transfer from the simple layered systems, between the solid phases of the drug or excipient layers to the liquid phase of the dissolution medium. The Dynochem package allows the introduction of user defined equations, which facilitated the use of the program to simulate drug dissolution from the cylindrical simple layered systems. The application of the program in modelling dissolution from the simple layered systems was based on the introduction of fundamental geometrical and mass transfer equations, outlined in the following sections.

4.5.1 *Visual process scheme*

The Dynochem program recommends the simplification of the modelling problem to a visual scheme outlining the various phases, inputs and outputs, and mass transfer kinetics between the various phases. As there are only three phases involved in the current problem, the visual process scheme is quite simple and is outlined in Figure 4.8.

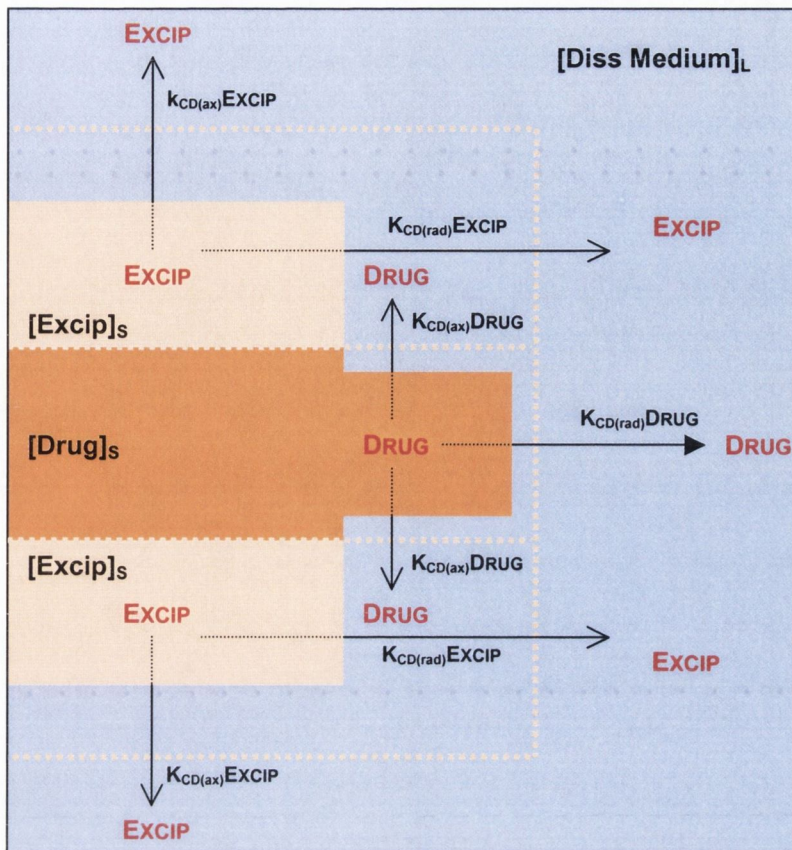


Figure 4.8 Dynochem process scheme for the dissolution of drug from a simple layered delivery systems consisting of a cylindrical layer of drug between two layers of soluble acid excipient dissolving into the dissolution medium. $K_{CD(rad)}DRUG$ and $K_{CD(ax)}DRUG$ are the overall mass transfer coefficients of drug between the surface of the drug layer and the dissolution medium in the radial and axial directions respectively. $K_{CD(rad)}EXCIP$ and $K_{CD(ax)}EXCIP$ are the overall mass transfer coefficients of excipient between the surface of the excipient layer and the dissolution medium in the radial and axial directions respectively. Note- right side only of visual process scheme shown for clarity.

The conversion of the visual process scheme to mass transfer equations depends on the definition of the individual surfaces from which the relevant mass transfer is occurring. A visual representation of the individual surfaces from where mass transfer occurs during the dissolution process is indicated in Figure 4.9.

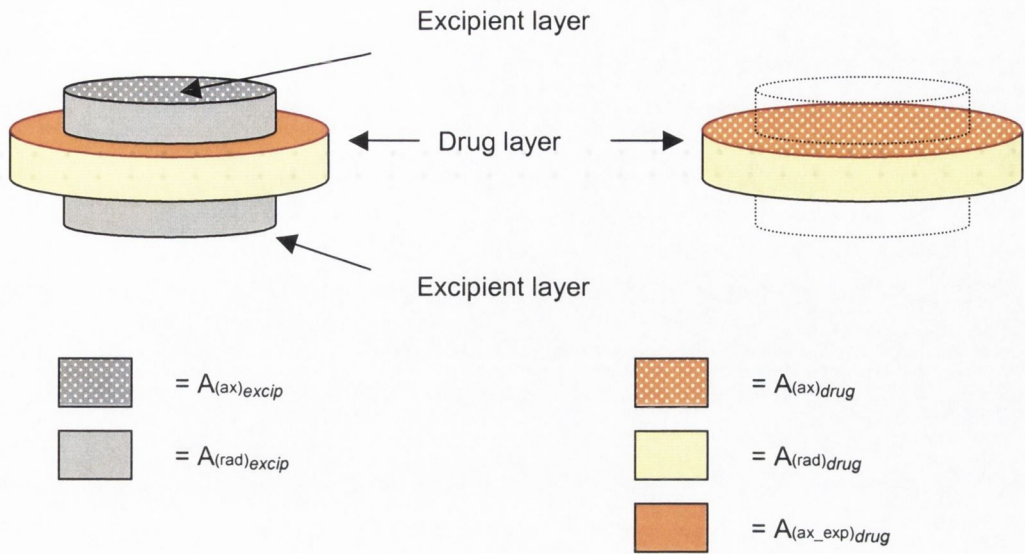


Figure 4.9 Visual representation of the individual surfaces from where mass transfer occurs during the dissolution process. $A_{(ax)excip}$ is the total cross-sectional area of the excipient layers exposed in the axial direction, $A_{(rad)excip}$ is the total area of the excipient layers exposed in the radial direction, $A_{(ax)drug}$ is the total cross-sectional area of the drug layer in the axial direction (including the area covered by the excipient layers), $A_{(rad)drug}$ is the total area of the drug layer exposed in the radial direction and $A_{(ax_exp)drug}$ is the axial surface area of the drug layer exposed to the dissolution medium (due to the dissolution of the excipient layers in the radial direction).

4.5.2 Process calculations

The process sheet of this model is concerned with defining the equations to determine geometrical parameters of the drug and excipient layers with time and consequently, using the mass transfer coefficients and calculated surface area for the various area components involved in mass transfer, to quantify the amount of drug (and excipient) in both the solid and liquid phases with time. All calculations are updated iteratively by Dynochem with time according to the mass transfer changes, which ultimately relate back to the geometric calculations. The geometric and mass transfer calculations that are important for the current model are outlined in the following section.

4.5.2.1 Geometrical calculations

$$h_{drug} = \sqrt[3]{\frac{AR_{drug}^2 \times V_{drug}}{\pi}} \quad \text{Equation 4.21}$$

$$d_{drug} = \sqrt[3]{\frac{8 \times V_{drug}}{\pi \times AR_{drug}}} \quad \text{Equation 4.22}$$

$$AR_{drug} = \frac{A_{(rad)_{drug}}}{A_{(ax)_{drug}}} \quad \text{Equation 4.23}$$

$$A_{(ax)_{drug}} = \frac{\pi \times d_{drug}^2}{2} \quad \text{Equation 4.24}$$

$$A_{(rad)_{drug}} = \pi \times d_{drug} \times h_{drug} \quad \text{Equation 4.25}$$

where h_{drug} is the height of the drug layer with time, d_{drug} is the diameter of the drug layer with time, V_{drug} is the volume of the drug layer, AR_{drug} is aspect ratio of the drug layer, $A_{(ax)_{drug}}$ is the total axial cross-sectional area of the drug layer with time as shown in Figure 4.9, $A_{(rad)_{drug}}$ is the total radial area of the drug layer, as shown in Figure 4.9. The above set of equations was repeated for the excipient layers. However, for the excipient layers, the geometry of the two layers was treated as a single cylinder of height equivalent the sum of the heights of the two individual layers, as mass transfer did not occur from these layers at axial interface between the drug and excipient layers. The complete set of process sheet calculations for this model are included in Appendix 11.

4.5.2.2 Mass transfer calculations

$$A_{(ax_exp)_{drug}} = A_{(ax)_{drug}} - A_{(ax)_{excip}} \quad \text{Equation 4.26}$$

$$TSA_{exp_{drug}} = A_{(ax_exp)_{drug}} + A_{(rad)_{drug}} \quad \text{Equation 4.27}$$

$$a_{drug} = \frac{TSA_{exp_{drug}}}{volume_{drug}} \quad \text{Equation 4.28}$$

$$f^{(ax)}_{drug} = \frac{A(ax_exp)_{drug}}{TSA_{exp\ drug}} \quad \text{Equation 4.29}$$

$$f^{(rad)}_{drug} = \frac{A(rad)_{drug}}{TSA_{exp\ drug}} \quad \text{Equation 4.30}$$

$$K_{C(ax)}_{drug} = \frac{D_{drug}}{h(ax)} \quad \text{Equation 4.31}$$

$$K_{C(rad)}_{drug} = \frac{D_{drug}}{h(rad)} \quad \text{Equation 4.32}$$

$$K_{CD(ax)}_{drug} = \frac{K_{D(ax)}_{drug} \times K_{C(ax)}_{drug}}{K_{D(ax)}_{drug} + \frac{K_{C(ax)}_{drug}}{S_{cd\ drug}}} \quad \text{Equation 4.33}$$

$$K_{CD(rad)}_{drug} = \frac{K_{D(rad)}_{drug} \times K_{C(rad)}_{drug}}{K_{D(rad)}_{drug} + \frac{K_{C(rad)}_{drug}}{S_{cd\ drug}}} \quad \text{Equation 4.34}$$

$$Drug_{liquid} = \int_0^t V_{drug} \times (K_{CD(ax)}_{drug} + K_{CD(rad)}_{drug}) \times \left(\frac{\rho'_{drug}}{S_{cd\ drug}} - C_{liquid\ drug} \right) dt$$

Equation 4.35

where $A(ax_exp)_{drug}$ is the area exposed of the drug layer in the axial direction, $TSA_{exp\ drug}$ is the total amount of surface area of the drug layer exposed to the dissolution medium, $h(ax)$ is the apparent diffusion layer thickness in the axial direction, $h(rad)$ is the apparent diffusion layer thickness in the radial direction, a_{drug} is the total specific interfacial surface area of the drug layer exposed to the dissolution medium, $f^{(ax)}_{drug}$ is the fraction of the total surface area of the drug layer exposed in the axial direction, $f^{(rad)}_{drug}$ is the fraction of the total surface area of the drug layer exposed in the radial direction, $K_{C(ax)}_{drug}$ and $K_{C(rad)}_{drug}$ are the mass transfer coefficients of the drug into the continuous phase (liquid) from the interface in the axial and radial directions, respectively. $K_{D(ax)}_{drug}$ and $K_{D(rad)}_{drug}$ are the mass transfer coefficient of the drug into the disperse (solid) phase from the interface in the axial direction and radial directions, respectively (negligible in this model), $K_{CD(ax)}_{drug}$ and $K_{CD(rad)}_{drug}$ are the

overall mass transfer coefficients in the axial and radial directions of the drug from the disperse phase to the continuous (liquid) phase, $S_{cd_{drug}}$ is the partition coefficient of the drug between the disperse phase and the continuous phase as defined by Equation 1.41, ρ'_{drug} is the apparent density of the drug layer (based on geometrical measurements), and $C_{liquid_{drug}}$ is the concentration of drug in the liquid at time t .

The above set of equations was repeated for the excipient layers (' $excip$ '), all equations being identical, except for the following equations:

$$TSA_{exp_{excip}} = A_{(ax)_{excip}} + A_{(rad)_{excip}} \quad \text{Equation 4.36}$$

As stated previously, the two excipient layers were treated as a single cylinder of height equivalent to the sum of the individual heights, therefore $A_{(ax)_{excip}}$ and $A_{(rad)_{excip}}$ represents the sum of the appropriate areas of the two layers. The complete set of process sheet calculations for this model are included in Appendix 11.

The current model provided a method of simulating drug dissolution from the simple layered compacts based on physicochemical parameters of the individual layers, including the solubility both the drug and excipient layers in the dissolution medium, the diffusion coefficient of the drug and excipient in the dissolution medium, the diameter of the drug and excipient layers and the initial heights and weights of the drug and excipient layers. The simulation model uses these inputs to calculate the volumes and apparent densities of the drug and excipient layers. The mass transfer coefficients are calculated based on the experimentally calculated magnitude of the apparent diffusion boundary layer (Section 3.1). As dissolution in this model is solely dissolution controlled, the value of the *apparent* diffusion layer thickness, h , in equation 4.32 can have effect on the resulting predicted release rates. The value of h in the radial direction for both the drug and excipient layers was that of system E (section 3.1.3). The value of h for the excipient in the axial direction was mean of that calculated for the upper and lower planar surfaces (systems H and I). The values of h for the drug in the axial and radial direction was that calculated by Healy (1995) for the complete surface of uncoated compacts of dimensions similar to the individual layers of the layered compacts (i.e. 60×10^{-4} cm).

4.5.3 Simulation of dissolution from benzoic acid/ salicylic acid compacts in 0.1N HCl

4.5.3.1 Three layered system (salicylic acid between two benzoic acid layers)

The initial application of the Dynochem layered drug delivery systems model was applied to simulate dissolution from the three layered system (BA/SA/BA) in 0.1N HCl. The scenario sheet parameters that were required to simulate dissolution of the drug (salicylic acid) are included in Table 4.4, while those of the excipient layer (benzoic acid) are included in Table 4.5.

Table 4.4 Dynochem scenario sheet design parameters for salicylic acid layer (drug, 500mg) to allow simulation of dissolution from a triple layered compact of benzoic acid and salicylic acid (BA/SA/BA) in 0.1N HCl. $Sc_{d_{drug}}$ = partition coefficient of the drug between the disperse phase and the continuous phase, h_{init} = initial height of the salicylic acid layer, ρ'_{drug} = initial amount of drug present per initial unit volume of matrix layer, D_{drug} = experimentally calculated diffusion coefficient of the drug in the dissolution medium, $Kc(ax)_{drug}$ and $Kc(rad)_{drug}$ are the mass transfer coefficient of the drug into the continuous phase (liquid) from the interface in the axial and radial directions, respectively.

$Sc_{d_{drug}}$	h_{init} (mm)	ρ'_{drug} (kg/m ³)	D_{drug} (x 10 ⁹ m ² /s)	$Kc(ax)_{drug}$ (x 10 ⁵ m/s)	$Kc(rad)_{drug}$ (x 10 ⁵ m/s)
504	2.75	1370	1.132	1.88	1.88

Table 4.5 Dynochem scenario sheet design parameters for benzoic acid layers (excipient, 500mg per layer) to allow simulation of dissolution from a triple layered compact of benzoic acid and salicylic acid (BA/SA/BA) in 0.1N HCl. $Sc_{d_{excip}}$ = partition coefficient of the excipient between the disperse phase and the continuous phase, h_{layer1} = initial height of the first acid excipient layer, h_{layer2} = initial height of the second acid excipient layer, ρ'_{excip} = initial amount of excipient present per initial unit volume of excipient layers, D_{excip} = experimentally calculated diffusion coefficient of the excipient in the dissolution medium, $Kc(ax)_{excip}$ and $Kc(rad)_{excip}$ are the mass transfer coefficient of the excipient into the continuous phase (liquid) from the interface in the axial and radial directions, respectively.

$Sc_{d_{excip}}$	h_{layer1} (mm)	h_{layer2} (mm)	ρ'_{excip} (kg/m ³)	D_{excip} (x 10 ⁹ m ² /s)	$Kc(ax)_{excip}$ (x 10 ⁵ m/s)	$Kc(rad)_{excip}$ (x 10 ⁵ m/s)
504	2.40	3.35	1300	1.243	1.17	2.08

The resulting simulations of dissolution from this system are shown in Figure 4.10, while the simulation of surface area changes during dissolution are shown in Figure 4.11.

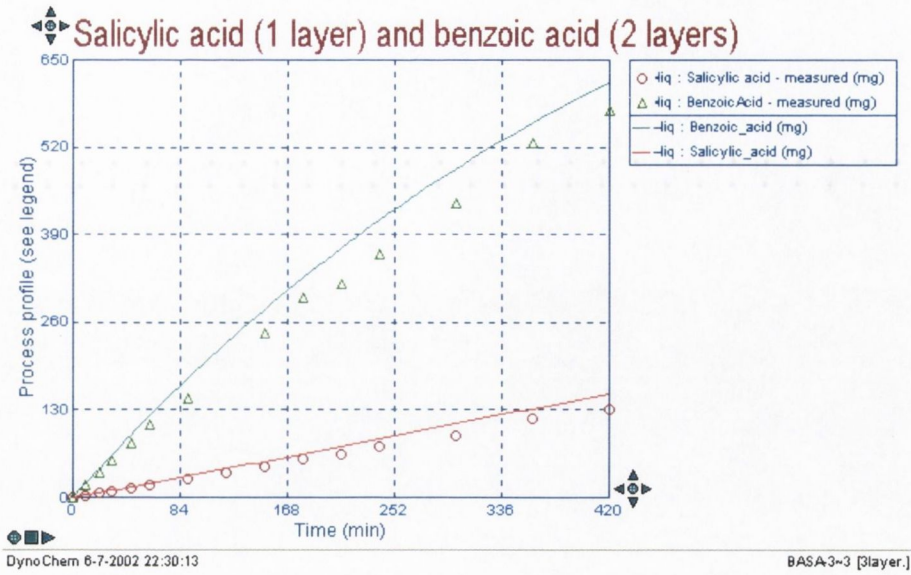


Figure 4.10 Dynochem generated simulation of dissolution from a layered compact consisting of a layer of salicylic acid (500 mg) between two layers of benzoic acid (500mg) in 0.1N HCl. The continuous lines are simulations of dissolution of benzoic acid (excipient, green line) and salicylic acid (drug, red line).

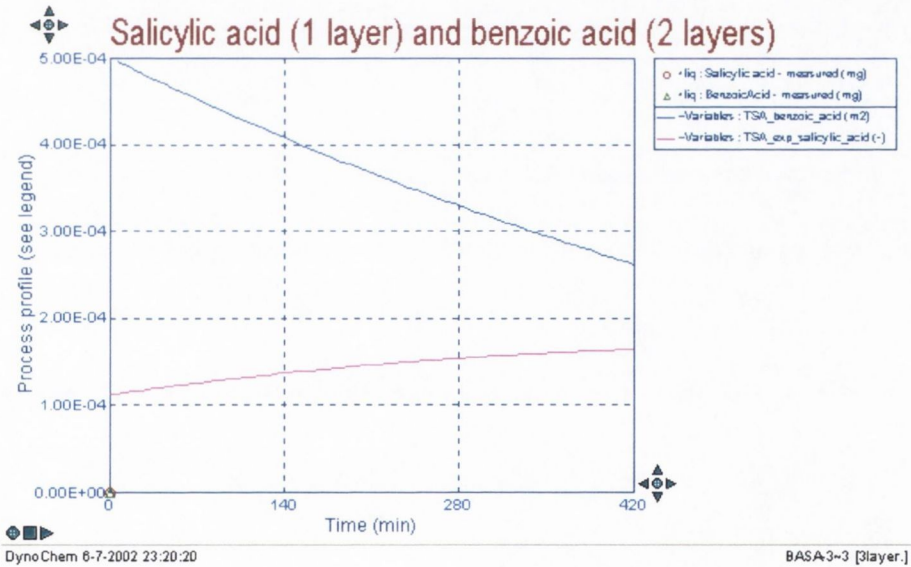


Figure 4.11 Dynochem generated simulation of surface area changes during dissolution from a layered compact consisting of a layer of salicylic acid (500 mg) between two layers of benzoic acid (500mg) in 0.1N HCl. 'TSA_benzoic_acid' is the total surface area exposed of both benzoic acid layers (blue line), 'TSA_exp_salicylic_acid' is the total surface area exposed of the central salicylic acid layer (pink line).

The general shape of the dissolution profiles in Figure 4.10 closely matched the shape of the experimental dissolution profile, for both benzoic acid and salicylic acid.

Quantitatively, the simulated dissolution profiles were higher than experimental, for both benzoic acid and salicylic acid. The model predicts a linear release profile for the salicylic acid component, over the time course studied. Figure 4.11 indicates that the total surface area exposed of the central drug layer (salicylic acid) remains practically constant over seven hours, while that of the benzoic acid component is decreasing with time. As only approximately 25% salicylic acid had dissolved in 7 hours, the dissolution profiles and surface area changes were extrapolated out to full dissolution and are indicated by Figure 4.12 and Figure 4.13. The predicted dissolution profile for salicylic acid remains practically linear for approximately 80% dissolution. The controlling effect of the more soluble benzoic acid layers on the surface area of the central salicylic acid is evident in Figure 4.13.

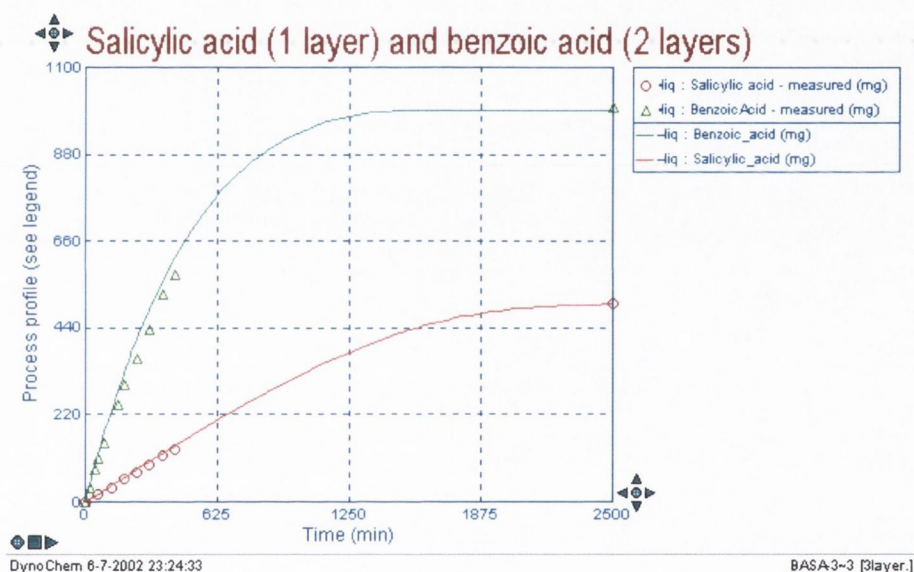


Figure 4.12 Dynochem generated simulation of dissolution (until completion) from a layered compact consisting of a layer of salicylic acid (500 mg) between two layers of benzoic acid (500mg) in 0.1N HCl. The continuous lines are simulations of dissolution of benzoic acid and salicylic acid based on experimentally calculated diffusion coefficients and apparent diffusion boundary layer thickness.

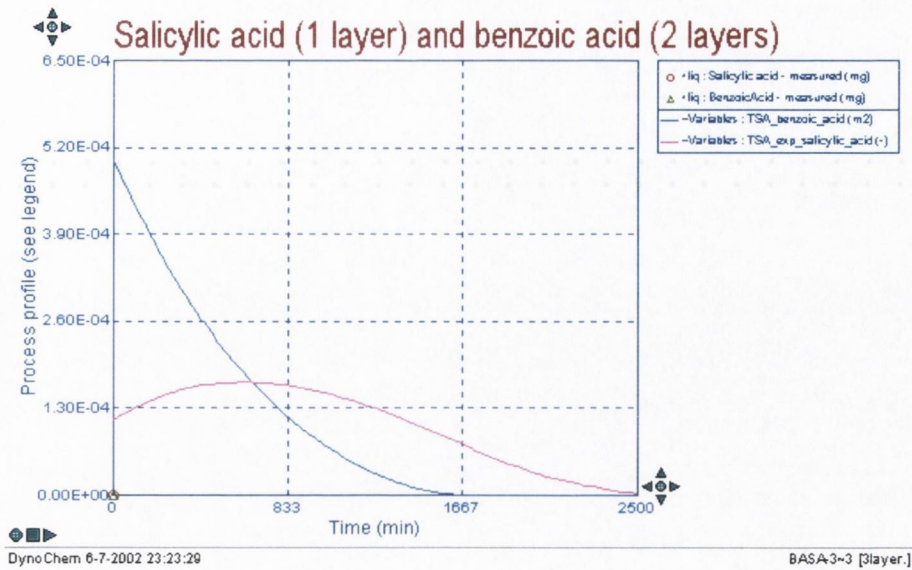


Figure 4.13 Dynochem generated simulation of surface area changes until complete dissolution from a layered compact consisting of a layer of salicylic acid (500 mg) between two layers of benzoic acid (500mg) in 0.1N HCl. 'TSA_benzoic_acid' (blue line) is the total surface area exposed of both benzoic acid layers, 'TSA_exp_salicylic_acid' (pink line) is the total surface area exposed of the central salicylic acid layer.

4.5.4 Simulation of dissolution from theophylline monohydrate/ succinic acid compacts in 0.01N HCl

The scenario sheet parameters that were required to simulate dissolution of the drug (theophylline monohydrate) are included in Table 4.6, while those of the excipient layer (succinic acid) are included in Table 4.7.

Table 4.6 *Dynochem scenario sheet design parameters for theophylline monohydrate layer (drug, 500mg) to allow simulation of dissolution from a triple layered compact of theophylline monohydrate (Thmh) and succinic acid (SuA), (SuA/Thmh/SuA) in 0.01N HCl. Sc_{drug} = partition coefficient of the drug between the disperse phase and the continuous phase, h_{init} = initial height of the salicylic acid layer, ρ'_{drug} = initial amount of drug present per initial unit volume of matrix layer, D_{drug} = experimentally calculated diffusion coefficient of the drug in the dissolution medium, $Kc_{(ax)drug}$ and $Kc_{(rad)drug}$ are the mass transfer coefficient of the drug into the continuous phase (liquid) from the interface in the axial and radial directions, respectively.*

Sc_{drug}	h_{init} (mm)	ρ'_{drug} (kg/m ³)	D_{drug} (x 10 ¹⁰ m ² /s)	$Kc_{(ax)drug}$ (x10 ⁶ m/s)	$Kc_{(rad)drug}$ (x10 ⁶ m/s)
115.5	2.497	1508	9.22	15.4	15.4

Table 4.7 Dynochem scenario sheet design parameters for succinic acid layer (excipient, 500mg per layer) to allow simulation of dissolution from a triple layered compact of theophylline monohydrate (Thmh) and succinic acid (SuA), (SuA/Thmh/SuA) in 0.01N HCl. Sc_{drug} = partition coefficient of the drug between the disperse phase and the continuous phase, h_{init} = initial height of the salicylic acid layer, ρ'_{drug} = initial amount of drug present per initial unit volume of matrix layer, D_{drug} = experimentally calculated diffusion coefficient of the drug in the dissolution medium, $Kc_{(ax)excip}$ and $Kc_{(rad)excip}$ are the mass transfer coefficient of the drug into the continuous phase (liquid) from the interface in the axial and radial directions, respectively.

Sc_{dexcip}	h_{layer1} (mm)	h_{layer2} (mm)	ρ'_{excip} (kg/m ³)	D_{excip} (x 10 ¹⁰ m ² /s)	$Kc_{(ax)excip}$ (x10 ⁶ m/s)	$Kc_{(rad)excip}$ (x10 ⁶ m/s)
13.3	2.09	2.89	1496	8.83	8.31	14.7

The resulting simulation of dissolution from this system is shown in Figure 4.14, while the simulation of surface area changes during dissolution are shown in Figure 4.15.

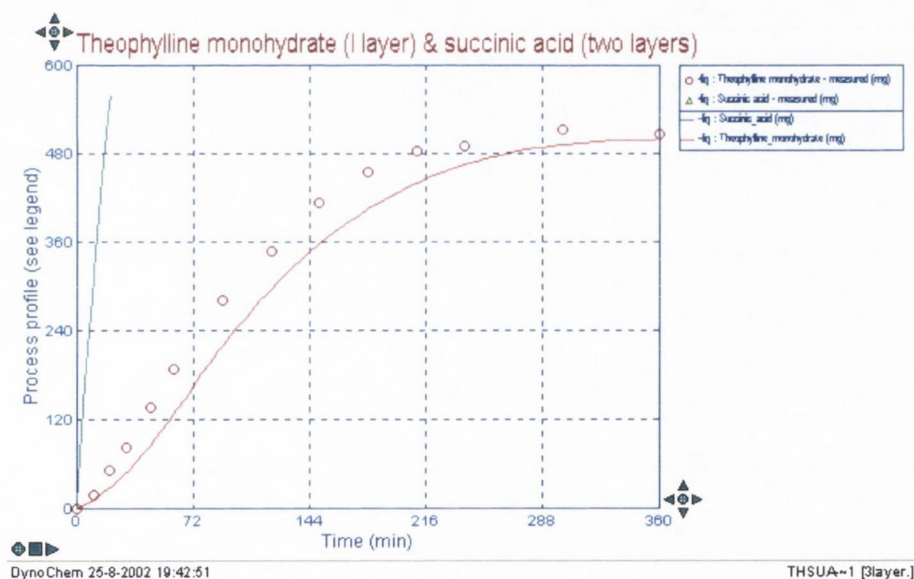


Figure 4.14 Dynochem generated simulation of dissolution from a layered compact consisting of a layer of theophylline monohydrate (500 mg) between two layers of succinic acid (500mg) in 0.01N HCl. The continuous line is a simulation of dissolution of theophylline monohydrate based on experimentally calculated diffusion coefficients and apparent diffusion boundary layer thickness.

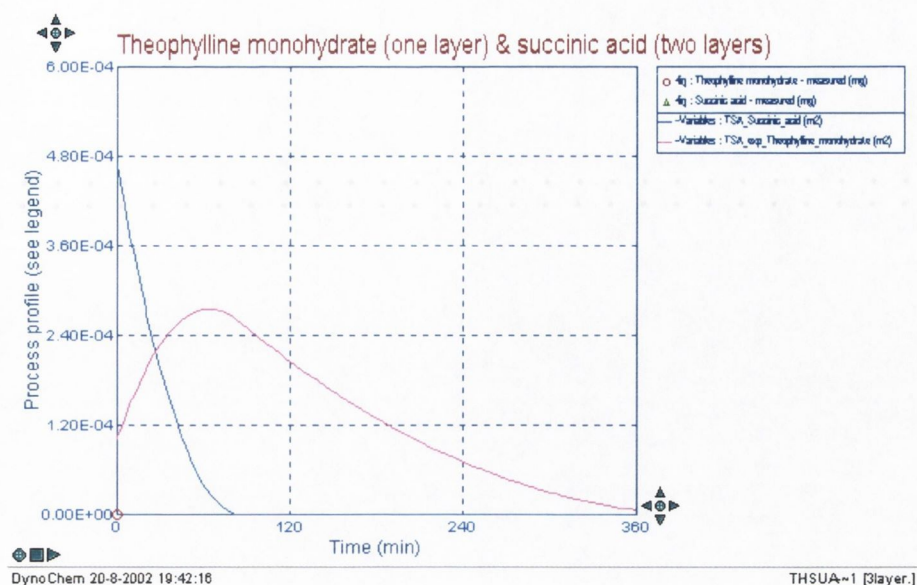


Figure 4.15 Dynochem generated simulation of surface area changes during dissolution from a layered compact consisting of a layer of theophylline monohydrate (500 mg) between two layers of succinic acid (500mg) in 0.01N HCl. 'TSA_succinic_acid' (blue line) is the total surface area exposed of both succinic acid layers, 'TSA_exp_Theophylline_monohydrate' (pink line) is the total surface area exposed of the central theophylline monohydrate layer.

The shape of the dissolution profile in Figure 4.14 closely resembled the experimental dissolution profile and there was close quantitative agreement between the experimental and simulated data. Quantitatively, the simulated dissolution profiles were higher than experimental, for both benzoic acid and salicylic acid. The simulated surface area changes predict an increasing surface area of the drug layer exposed for the first hour, after which time, the succinic acid had completely dissolved. The peak in the simulated surface area plot corresponds to the inflexion point in the dissolution plot, as dissolution rates of the central drug layer were decreasing after this time.

4.5.5 Simulation of dissolution from theophylline monohydrate/ adipic acid compacts in 0.01N HCl

The scenario sheet parameters that were required to simulate dissolution of the drug (theophylline monohydrate) are included in Table 4.8, while those of the excipient layer (benzoic acid) are included in Table 4.9.

Table 4.8 Dynochem scenario sheet design parameters for theophylline monohydrate layer (drug, 500mg) to allow simulation of dissolution from a triple layered compact of theophylline monohydrate (Thmh) and adipic acid (AdA), (AdA/Thmh/AdA) in 0.01N HCl. Sc_{drug} = partition coefficient of the drug between the disperse phase and the continuous phase, h_{init} = initial height of the salicylic acid layer, ρ'_{drug} = initial amount of drug present per initial unit volume of matrix layer, D_{drug} = experimentally calculated diffusion coefficient of the drug in the dissolution medium, $Kc_{(ax)drug}$ and $Kc_{(rad)drug}$ are the mass transfer coefficient of the drug into the continuous phase (liquid) from the interface in the axial and radial directions, respectively.

Sc_{drug}	h_{init} (mm)	ρ'_{drug} (kg/m ³)	D_{drug} (x 10 ¹⁰ m ² /s)	$Kc_{(ax)drug}$ (x10 ⁶ m/s)	$Kc_{(rad)drug}$ (x10 ⁶ m/s)
105.1	2.84	1313	9.22	15.4	15.4

Table 4.9 Dynochem scenario sheet design parameters for adipic acid layer (excipient, 500mg) to allow simulation of dissolution from a triple layered compact of theophylline monohydrate (Thmh) and adipic acid (AdA), (AdA/Thmh/AdA) in 0.01N HCl. Sc_{excip} = partition coefficient of the drug between the disperse phase and the continuous phase, h_{init} = initial height of the salicylic acid layer, ρ'_{excip} = initial amount of drug present per initial unit volume of matrix layer, D_{excip} = experimentally calculated diffusion coefficient of the drug in the dissolution medium, $Kc_{(ax)excip}$ and $Kc_{(rad)excip}$ are the mass transfer coefficient of the drug into the continuous phase (liquid) from the interface in the axial and radial directions, respectively.

Sc_{excip}	h_{layer1} (mm)	h_{layer2} (mm)	ρ'_{excip} (kg/m ³)	D_{excip} (x 10 ¹⁰ m ² /s)	$Kc_{(ax)excip}$ (x10 ⁶ m/s)	$Kc_{(rad)excip}$ (x10 ⁶ m/s)
29.2	2.92	2.86	1289	9.45	8.89	15.7

The resulting simulation of dissolution from this system is shown in Figure 4.16, while the simulation of surface area changes during dissolution are shown in Figure 4.17.

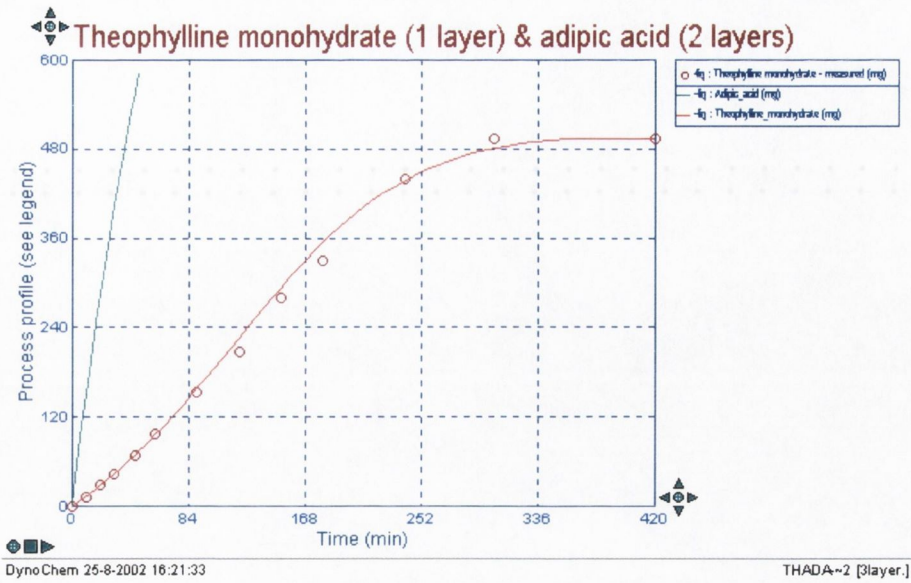


Figure 4.16 Dynochem generated simulation of dissolution from a layered compact consisting of a layer of theophylline monohydrate (500 mg) between two layers of adipic acid (500mg) in 0.01N HCl. The continuous line is a simulation of dissolution of theophylline monohydrate based on experimentally calculated diffusion coefficients and apparent diffusion boundary layer thickness.

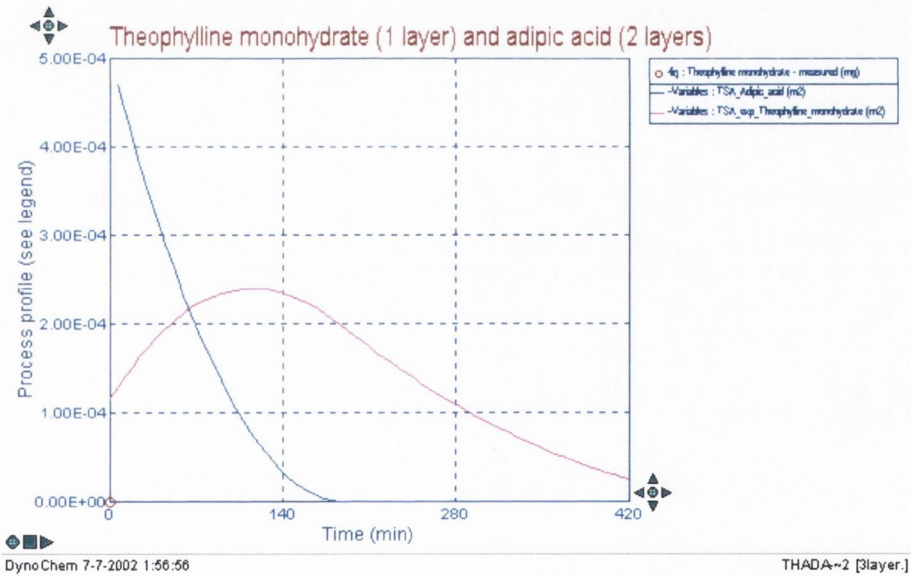


Figure 4.17 Dynochem generated simulation of surface area changes during dissolution from a layered compact consisting of a layer of theophylline monohydrate (500 mg) between two layers of adipic acid (500mg) in 0.01N HCl. 'TSA_adipid_acid' (blue line) is the total surface area exposed of both adipic acid layers, 'TSA_exp_Theophylline_monohydrate' (pink line) is the total surface area exposed of the central theophylline monohydrate layer.

The simulated dissolution profile in Figure 4.17 was in very close agreement with the experimental data. In this case, the surface area changes predict an increase in surface area of the drug layer exposed, caused by the dissolution of the adipic acid layers.

The maximum surface area of the drug layer is exposed after two hours, the point at which the adipic acid layers have completely dissolved. After this time, the surface area exposed of the drug layer decreases, resulting in the decreasing dissolution rates of the theophylline monohydrate layer after this time.

4.6 CONCLUSIONS

This section of work examined the possibility of controlling the surface area changes during the dissolution of drug from a layered drug/soluble-excipient system, to achieve a zero order type release profile. Initial studies involving benzoic acid/salicylic acid three layered systems, showed that zero order release was possible, at least for a certain amount of time. Sigmoidal shaped release profiles were seen when theophylline monohydrate was used as the model drug, between two layers of soluble acid excipient, dissolving in a medium 0.01N HCl. Release rates increased at earlier times, due to the increase in surface area of the drug layer exposed with time caused by the faster dissolution of the acid excipient layers and the resulting exposure of new surface area of the central drug layer. Following complete dissolution of the excipient layers, the release rate of the drug decreased resulting in the downward curvature of the dissolution profiles.

A mathematical model was derived to predict the release rate over time, based on the change in exposed surface area available for dissolution. The model involved the calculation of the rate of decrease of the diameter of the individual drug and excipient layers over time. Two methods were proposed to measure this rate; one based on direct experimental measurement, while the second was derived from intrinsic properties of the drug or excipients. The resulting predicted release profiles resembled the actual release profiles in shape, for both methods. Better fit to actual data was seen at earlier time points, explained in terms of the assumptions of the model, which did not account for a change in dimension of the drug layer in the axial direction, hence leading to over-predictions of exposed surface area of the drug layer at later times.

A second method to more accurately predict drug dissolution from these systems involved the application of a dynamic chemical engineering simulation package,

Dynochem. Application of the program involved the use of geometrical and mass transfer equations, based on assumptions of geometrical uniformity during the dissolution process, and using the hydrodynamic calculations from the earlier single layer studies. The resulting predicted dissolution profiles were in closer agreement with experimental data, than the initial modelling method.

Therefore, it is possible to control the surface area of drug available with time for dissolution from these simple layered compacts, and to predict the surface area changes (and hence dissolution rate of drug), based on the physicochemical properties of the drug and excipient layers.

Chapter 5

Dissolution from layered matrix compacts

5.1 INTRODUCTION

It has been shown in the previous section that various release profiles were achievable using simple layered systems consisting of a central drug layer between soluble acid excipient layers. However, a feature of this type of 'simple layered' system was that most release profiles were sigmoidal in nature, i.e. release rates increased at earlier time points, while release rates decreased at later times. Although release rates approached linear kinetics for a portion of time between the earlier and later time points, an increased period of linear release kinetics was desirable.

This section examines the possibility of controlling drug release from the middle layer of a layered matrix drug delivery system and the possibility of altering the release from Higuchi 'square root of time' type kinetics (matrix alone) to zero order kinetics, by the inclusion of soluble outer layers.

5.2 FEASIBILITY STUDIES ON LAYERED MATRIX SYSTEMS

5.2.1 *Initial studies*

Initial studies in this area focused on the effect of inclusion of polymer with drug to the central core layer and on the ability of the addition of acid excipient layers to shift the kinetics of release from square root of time shaped profiles to zero order release. The matrix former used in these initial studies was ethylcellulose 10FP (fine particle size). This is a new grade of ethylcellulose polymer marketed for use in the direct compression of non-swelling non-erodible monolithic matrix compacts, with a mean particle size distribution of $\sim 10 \mu\text{m}$ (Pollock and Sheskey, 2001). The polymer was screened using a $250 \mu\text{m}$ sieve to break up any aggregated material as described in section 2.7.

5.2.2 Three layered ethylcellulose and theophylline monohydrate drug core with fumaric acid outer layers

The powder mixes for the central matrix layers were produced in the relevant mix ratios of drug to polymer as described in section 2.8. The layered systems were formed by direct compression as described in section 2.10.3. Dissolution studies were carried out in a medium of 0.01N HCl as described in section 2.11. Two levels of theophylline: ethylcellulose were initially studied (1:1 and 2:1). The average dissolution profiles for theophylline monohydrate from the three-layered compacts containing the drug core of 500 mg of theophylline monohydrate: ethylcellulose (1:1 and 2:1) with a layer of 500 mg fumaric acid on each of the planar surfaces of drug-matrix core are shown in Figure 5.1. Dissolution results from an uncoated matrix containing theophylline monohydrate:ethylcellulose 10FP (2:1) is included for comparison.

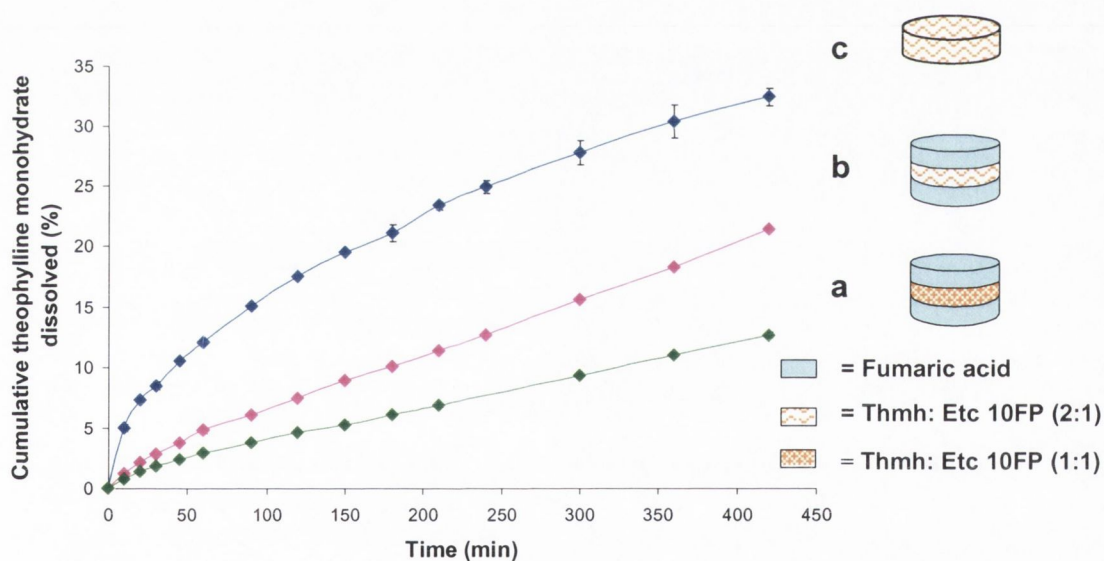


Figure 5.1 Dissolution profile of cumulative % theophylline monohydrate dissolved versus time in 0.01N HCl from initial feasibility studies on triple layered matrix systems; a) = matrix core of 500 mg (theophylline monohydrate: ethylcellulose 10FP, 1:1) with a layer of fumaric acid (500 mg) on each planar surface, b) = matrix core of 500 mg (theophylline monohydrate: ethylcellulose 10FP, 2:1), with a layer of fumaric acid (500 mg) on each planar surface, c) = matrix layer only of 500mg (theophylline monohydrate: ethylcellulose 10FP, 2:1), included for comparison. Error bars indicate standard deviations.

Complete dissolution of the fumaric acid layers occurred between six and seven hours. It is evident from Figure 5.1 that the addition of two layers of fumaric acid has shifted the shape of the release profile to a more zero order shaped release profile

(linear fit r^2 for the layered systems > 0.993). However, the rate of release from the systems was quite slow, with only 21% released from the faster releasing system after 7 hours and 13% released from the slower releasing system. It was thought that the reason for this observation was two-fold. Firstly, the low particle size range of the polymer would lead to the formation of a matrix system of a high tortuosity and secondly because this uncontrolled particle size polymeric material contained particles down to fine particulate matter. The presence of the fine particulate matter would therefore hinder the entrance of the dissolution medium to the porous network, by closing off the porous framework between larger particle size polymer particles.

5.3 CONTROLLED POLYMER PARTICLE SIZE

Due to the low release rates seen with the polymer of low particle size in the feasibility studies, future work focused on the conventional grades of ethylcellulose, i.e. ethylcellulose 'Std' grades, in controlled particle size fractions. An observation with some of the feasibility studies was the tendency of some of the layered matrix compacts to separate, either on ejection following compression, or during the dissolution test. For this reason, PVP was included at the level of 5% in the central layer of all layered matrix systems, which prevented the separation of layers in subsequent studies. PVP was shown to not significantly affect the intrinsic dissolution rate of theophylline monohydrate (Appendix 4).

A more comprehensive examination of the possible factors affecting release from a layered matrix compact was undertaken.

5.3.1 *Experimental design*

The parameters that were examined in the study of factors affecting release of drug from layered matrix compacts are outlined in the following section.

5.3.1.1 **Outer layer solubility**

In some cases, authors have reported attaining pseudo zero-order release from non-swelling non-erodible compact systems, without the inclusion of outer layers (Gurny et al., 1982). Such behaviour was attributed to the saturation of drug in the dissolution medium-filled pores of the matrix, at which point the dissolution rate

becomes slower than the rate of diffusion and determines the release kinetics of the process. In an effort to control the effect of surface area exposed at earlier times only (before this region of 'pseudo' zero order release from the uncoated matrix), a second acid excipient of higher solubility was studied. Adipic acid, was shown to dissolve from the surface of the simple layered systems within the first 120 minutes under similar dissolution conditions and was examined as the second acid excipient in the outer layers. The second acid excipient examined was fumaric acid, the solubility of which is lower than adipic acid, but higher than that of benzoic acid.

5.3.1.2 Particle size of polymer

Another factor reported to have an effect on release from these matrix systems is the particle size of the polymer (Dabbagh et al., 1996, Potter et al., 1990, Pollock and Sheskey, 2001). Therefore, two particle size fractions of ethylcellulose were examined; a large particle size fraction (250-355 μm) and a small particle size fraction (106-180 μm).

5.3.1.3 Polymer fraction

Three fractions of polymer were examined, the ratios of polymer:drug being 3:1, 1:1 and 1:3. The complete series of experiments examined is outlined graphically in Figure 5.2.

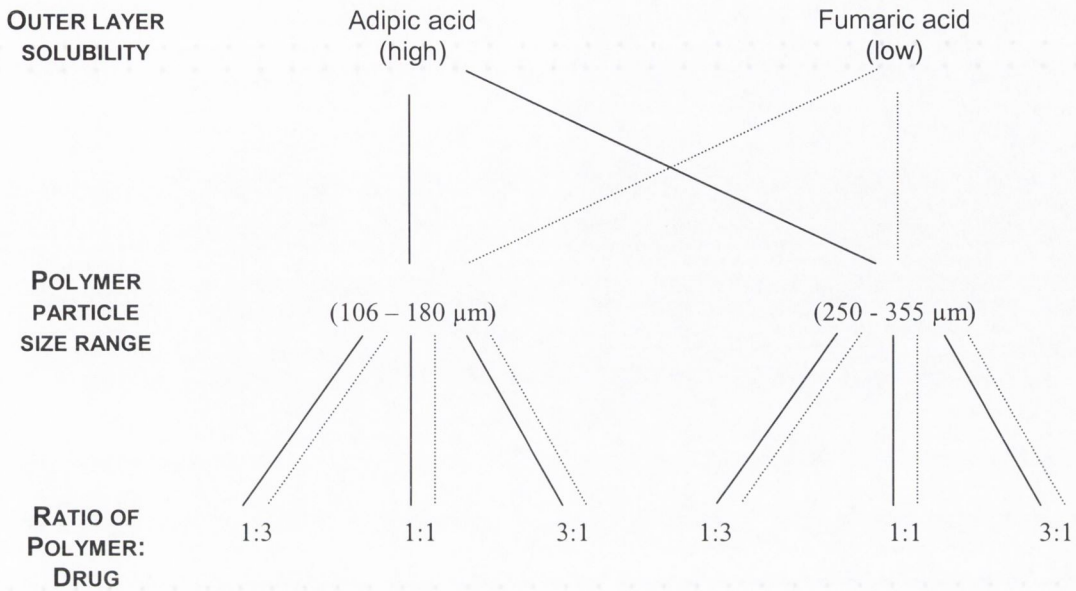


Figure 5.2 Graphical summary of experimental design used to examine the factors affecting release from the layered matrix compacts.

5.3.2 Single layer matrix compacts

To allow a comprehensive examination of the above effects on drug dissolution from layered matrix compacts, the above series of experiments were also examined as matrix compacts only (without the inclusion of the acid excipient layers). Dissolution studies were carried out in a medium of de-aerated 0.01N HCl as described in section 2.11.

5.3.2.1 Large particle size polymer

The dissolution profiles for matrix compacts composed of ethylcellulose 10cP in the particle size range of 250-355 μm and theophylline monohydrate (with 5% PVP) in three weight fractions, dissolving into 0.01N HCl are shown in Figure 5.3.

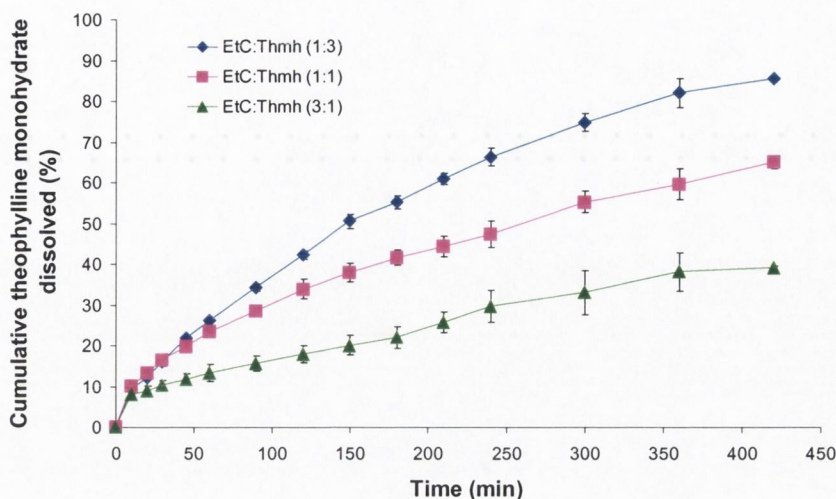


Figure 5.3 Dissolution profiles of theophylline monohydrate from matrix compacts composed of ethylcellulose 10cP in the particle size range 250-355 μm for three weight ratios of polymer to drug. Error bars indicate standard deviations (Etc = ethylcellulose 10cP, Thmh = theophylline monohydrate).

5.3.2.1.1 Effect of polymer level

A graded increase in release rate was observed from the matrix compacts composed of large particle size polymer as the proportion of polymer in the matrix decreased. Release approaching 85% drug loading was achieved for the compacts containing the ratio of Polymer:Drug (P:D) of 1:3 after 7 hours, while the amount released from the ratio of P:D (1:1) after 7 hours was only 65%. Conversely, the highest ratio of P:D (3:1) released only 40% drug during the same time period. An examination of the mechanism of drug release from the above compacts was performed by fitting the dissolution profiles to Equation 1.29, the Peppas equation (for up to 60% release). Application of the Peppas equation above 60% drug release is not strictly valid for pure Fickian drug release (Ritger and Peppas, 1987).

The resulting fits to Equation 1.29 are shown graphically in Figure 5.4, while the resulting fitted parameters are included in Table 5.1.

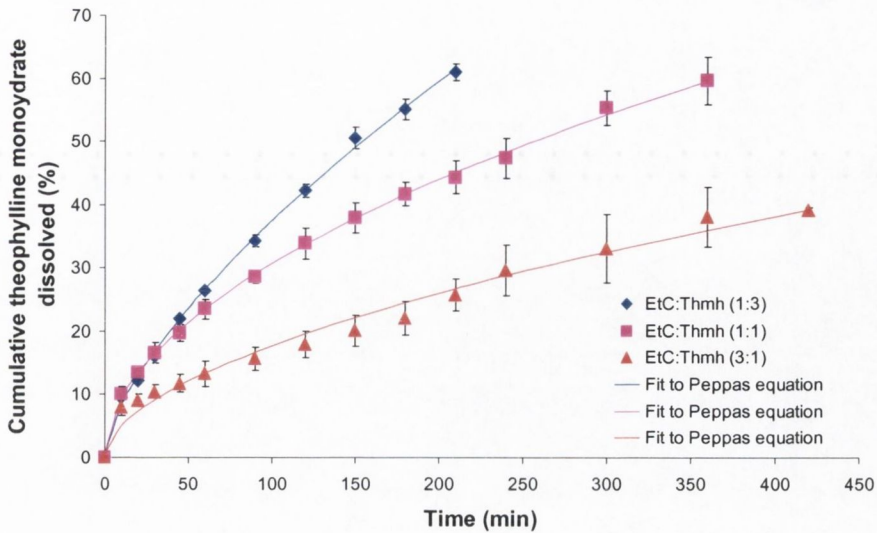


Figure 5.4 Dissolution profiles and the resulting fits to the Peppas equation for theophylline monohydrate dissolving from matrix compacts composed of ethylcellulose 10cP in the particle size range 250-355 μm , for three weight ratios of polymer to drug. Error bars indicate standard deviations (Etc = ethylcellulose 10cP, Thmh = theophylline monohydrate). Continuous lines represent the best fit to the Peppas equation.

Table 5.1 Table of parameters resulting from the fit of the Peppas equation to dissolution profiles for up to 60% dissolution of theophylline monohydrate from matrix compacts composed of ethylcellulose 10 cP in the particle size range 250-355 μm for three weight ratios of polymer to drug.

RATIO OF POLYMER:DRUG	k ($\times 10^2$)	n	MODEL SELECTION CRITERION (MSC)	COEFFICIENT OF DETERMINATION
1:3	1.7	0.67	6.23	0.999
1:1	2.8	0.52	6.67	0.999
3:1	1.4	0.55	3.73	0.982

The high values for the model selection criterion and the coefficient of determination confirm that the fits of the dissolution profiles of the above matrix compacts to the Peppas equation are quite good. For the ratios of Polymer to Drug (P:D) of 3:1 and 1:1, the release mechanism approximates that of Fickian release ($n \approx 0.5$), while the mechanism of release from the ratio 1:3 is an anomalous (non-Fickian) transport, which lies between the region of true Fickian transport ($n=0.5$) and zero-order release ($n=1$) (Ritger and Peppas 1987). This is not surprising, as the dimensions of the compact containing P:D in the ratio 1:3 decreased following dissolution, indicating that some erosion of the polymeric component of the matrix had occurred during the

dissolution process, resulting in a shift of the kinetics of drug release away from pure diffusional controlled release.

5.3.2.2 Small particle size polymer

The dissolution profiles for matrix compacts composed of ethylcellulose 10cP in the particle size range of 106-180 μm and theophylline monohydrate (with 5% PVP) in three weight fractions, dissolving into 0.01N HCl are shown in Figure 5.5, while the resulting parameters after fitting the dissolution profiles to the Peppas equation (Equation 1.29) are included in Table 5.2.

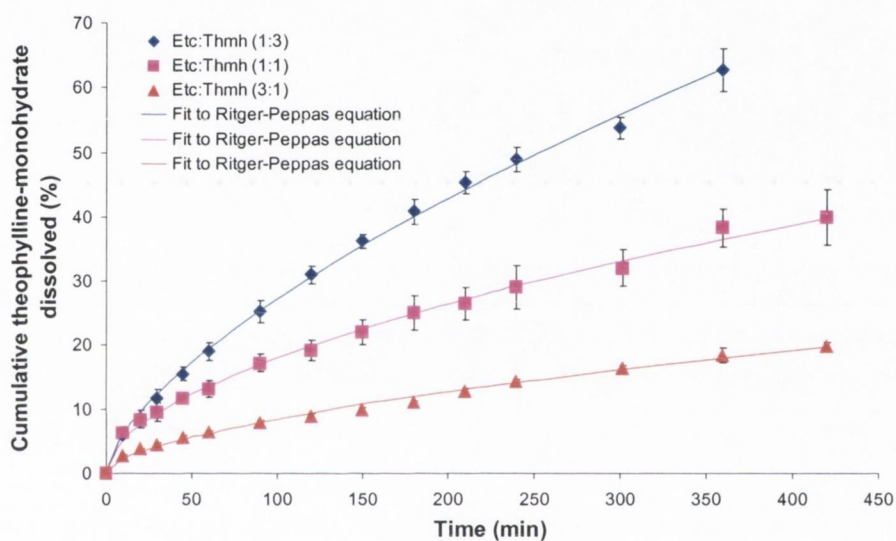


Figure 5.5 Dissolution profiles and the resulting fits to the Peppas equation for theophylline monohydrate dissolving from matrix compacts composed of theophylline monohydrate and ethylcellulose 10cP in the particle size range 106-180 μm , for three weight ratios of polymer to drug. Error bars indicate standard deviations (Etc = ethylcellulose 10cP, Thmh = theophylline monohydrate). Continuous lines represent the best fit to the Peppas equation.

Table 5.2 Table of parameters resulting from the fit of the Peppas equation to dissolution profiles for up to 60% dissolution of theophylline monohydrate from matrix compacts composed of ethylcellulose 10 cP in the particle size range 106-180 μm for three weight ratios of polymer to drug.

RATIO OF POLYMER:DRUG	k ($\times 10^2$)	n	MODEL SELECTION CRITERION (MSC)	COEFFICIENT OF DETERMINATION
1:3	1.3	0.66	6.05	0.998
1:1	1.4	0.55	5.15	0.996
3:1	0.6	0.59	4.85	0.994

5.3.2.2.1 Effect of polymer level

An increase in release rate was also observed from the matrix compacts composed of small particle size polymer as the proportion of polymer in the matrix decreased. Release approaching over 80% drug loading was not achieved for any of the matrix compacts with this lower particle size range of excipient. Again, the high values for the model selection criterion and the coefficient of determination confirm that the fits of the dissolution profiles for the above matrix compacts to Equation 1.29 are quite good. Similar to the large particle size polymer, for the ratio of Polymer to Drug (P:D) of 3:1 and 1:1, the release mechanism approximates that of Fickian release ($n \approx 0.5$), while the mechanism of release from the ratio 1:3 is approaching a more anomalous (non-Fickian) transport, as the value of n lies between the region of true Fickian transport ($n=0.5$) and zero-order release ($n=1$) (Ritger and Peppas, 1987). Again, the dimensions of the compact containing P:D in the ratio 1:3 decreased following dissolution, indicating that some erosion of the polymeric component of the matrix had occurred during the dissolution process, which would account for the deviation from true Fickian diffusion.

5.3.2.3 Effect of particle size

Decreased release rates were observed for the uncoated matrix compacts consisting of the smaller fraction of ethylcellulose used, for all levels ratios of P:D examined. This feature can be attributed to an increase in tortuosity experienced by the diffusing drug in the porous network composed of the smaller particle size fraction of polymer (Potter et al., 1990).

5.3.3 Triple layer matrix compacts

5.3.3.1 Adipic acid in outer layers

Layered matrix compacts containing adipic acid in the outer layers were prepared as described in section 2.10.3. PVP was included at the level of 5% in the central layer of all compacts to aid adhesion between the layers. Dissolution studies were carried out in a medium of de-aerated 0.01N HCl, results being the average of dissolution from three compacts.

5.3.3.1.1 Large particle size polymer fraction

The dissolution profiles for matrix compacts composed of a central matrix layer of ethylcellulose 10cP in the particle size range of 250-355 μm and theophylline monohydrate (with 5% PVP) in three weight fractions (500 mg), between two layers of fumaric acid (500 mg) dissolving into 0.01N HCl are shown in Figure 5.6. As deviation from simple Fickian drug release is expected due to the inclusion of the soluble acid excipient layers, dissolution profiles from the layered matrix systems were fitted to the Peppas equation (Equation 1.29) for the full extent of drug release, with the resulting best-fit profiles indicated by solid lines in Figure 5.6.

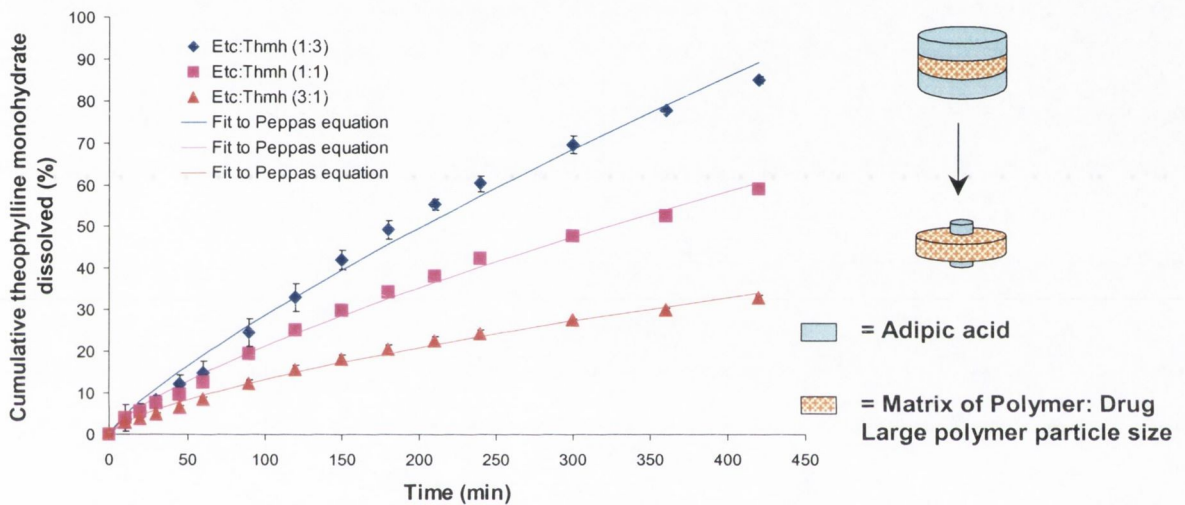


Figure 5.6 Dissolution profiles of theophylline monohydrate from triple layered matrix compacts containing a matrix layer of theophylline monohydrate and ethylcellulose 10cP in the particle size range 250-355 μm in three weight ratios of polymer to drug (500 mg), between two layers of adipic acid (500 mg). Error bars indicate standard deviations (Etc = ethylcellulose 10cP, Thmh = theophylline monohydrate). Continuous lines represent the best fit to the Peppas equation.

The adipic acid layers had completely dissolved between 90 minutes and 120 minutes. The addition of the adipic acid layers onto the central matrix layer shifted the shape of the dissolution profile from a Higuchi square root of time profile, to a more sigmoidal shape, characterised by increasing release rates for the first two hours followed by a decrease in release rate after the adipic layers had completely dissolved. As described earlier, the resulting dissolution profile is a result of two competing processes, the increase in diffusional path-length in the central matrix layer caused by dissolution of drug with time and the increase in surface area of the matrix layer exposed with time. In this case, the dominant factor on the release rate in the first two hours is the

increasing surface area effect of the acid excipient, which has had a more positive effect on drug release than the inhibitory effect of the increase in the diffusional path-length during this time. After the adipic acid has completely dissolved, the diffusional path-length effect results in a decreasing release rate. The dissolution parameters resulting from a fit of the data to the Peppas equation (Equation 1.29) are included in Table 5.3.

Table 5.3 *Table of parameters resulting from the fit to the Peppas equation of dissolution profiles of theophylline monohydrate from layered matrix compacts composed of a central matrix layer of ethylcellulose 10 cP in the particle size range 250-355 μm for three weight ratios of polymer to drug (500 mg), between two acid excipient layers of adipic acid (500 mg).*

RATIO OF POLYMER:DRUG	k ($\times 10^3$)	n	MODEL SELECTION CRITERION (MSC)	COEFFICIENT OF DETERMINATION
1:3	7.3	0.80	4.41	0.997
1:1	7.4	0.73	4.91	0.998
3:1	6.3	0.66	4.80	0.998

Therefore the addition of the adipic acid layers to the matrix layer has had the effect of shifting the kinetics of overall drug release from pure Fickian to anomalous (non-Fickian) transport (Ritger and Peppas, 1985), as described by the shift of exponent, n , of the Peppas equation towards 1 for the lower ratios of polymer to drug.

5.3.3.1.2 *Small particle size polymer fraction*

The dissolution profiles for matrix compacts composed of a central matrix layer ethylcellulose 10cP in the particle size range of 106-180 μm and theophylline monohydrate (with 5% PVP) in three weight fractions (500 mg), between two layers of adipic acid (500 mg) dissolving into 0.01N HCl are shown in Figure 5.7. The dissolution profiles were fitted to the Peppas equation (Equation 1.29) for the full extent of drug release.

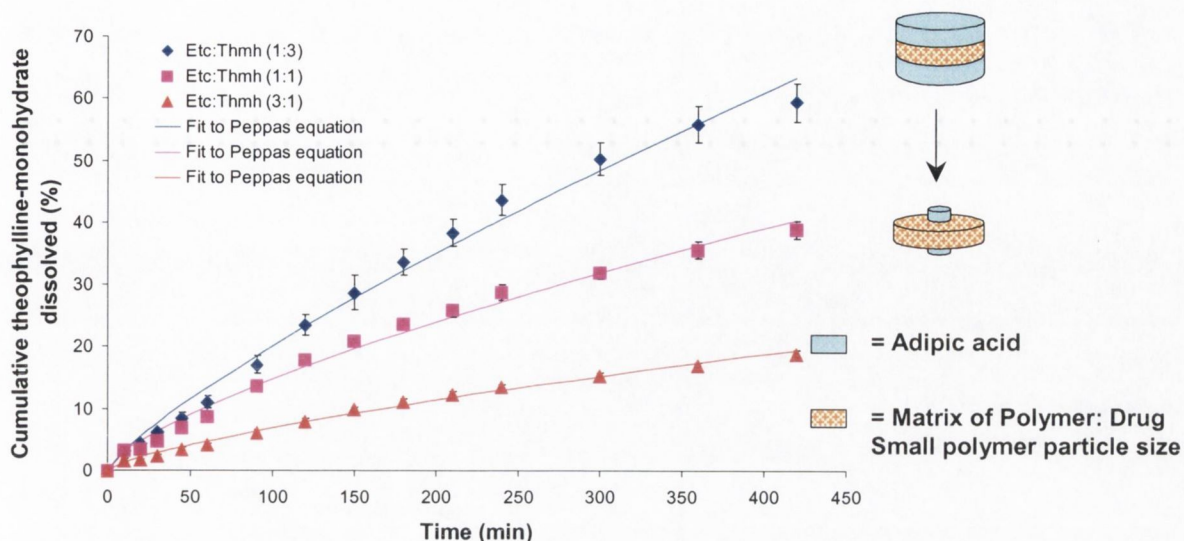


Figure 5.7 Dissolution profiles of theophylline monohydrate from triple layered matrix compacts containing a matrix layer of theophylline monohydrate and ethylcellulose 10cP in the particle size range 106-180 μm in three weight ratios of polymer to drug (500 mg), between two layers of adipic acid (500 mg). Error bars indicate standard deviations (Etc = ethylcellulose 10cP, Thmh = theophylline monohydrate). Continuous lines represent the best fit to the Peppas equation.

As before, the adipic acid layers had completely dissolved between 90 minutes and 120 minutes. The addition of the adipic acid layers onto the matrix core again shifted the kinetics from a Fickian type profile to a more sigmoidal shape, with increasing release rates at the early stages of dissolution (as previously discussed), followed by decreasing release rates at later times, as the dissolution process becomes solely controlled by Fickian diffusion at later times. The dissolution parameters resulting from a fit of the data to the Peppas equation (Equation 1.29) are included in Table 5.4.

Table 5.4 Table of parameters resulting from the fit of the Peppas equation to dissolution profiles of theophylline monohydrate from layered matrix compacts composed of a central matrix layer of theophylline monohydrate and ethylcellulose 10 cP in the particle size range 106-180 μm for three weight ratios of polymer to drug (500 mg), between two acid excipient layers of adipic acid (500 mg).

RATIO OF POLYMER:DRUG	k ($\times 10^3$)	n	MODEL SELECTION CRITERION (MSC)	COEFFICIENT OF DETERMINATION
1:3	5.2	0.80	4.46	0.991
1:1	6.0	0.70	4.50	0.991
3:1	2.6	0.71	4.90	0.994

In the case of drug release from layered matrix compact containing the 'small' particle size fraction of polymer, the drug release kinetics were between Fickian and zero-order release for all ratios of polymer:drug, all profiles exhibiting a sigmoidal shape dissolution profile. Again the most promising system with potential for attaining zero order release was the system containing the lowest fraction of polymer. However, drug release did not reach 80% for any of the systems containing the smaller particle size fraction of the polymer (106-180 μm).

5.3.3.2 Fumaric acid in outer layers

Layered matrix compacts containing fumaric acid in the outer layers were prepared as described in section 2.10.3. PVP was again included at the level of 5% in the central layer of all compacts to aid adhesion between the layers. Dissolution studies were carried out in 0.01N HCl as described in section 2.11.

5.3.3.2.1 Large particle size polymer fraction

The dissolution profiles for matrix compacts composed of a central matrix layer ethylcellulose 10cP in the particle size range of 250-355 μm and theophylline monohydrate (with 5% PVP) in three weight fractions (500 mg), between two layers of fumaric acid (500 mg) dissolving into 0.01N HCl are shown in Figure 5.8. The dissolution profiles were fitted to the Peppas equation (Equation 1.29) for the full extent of drug release.

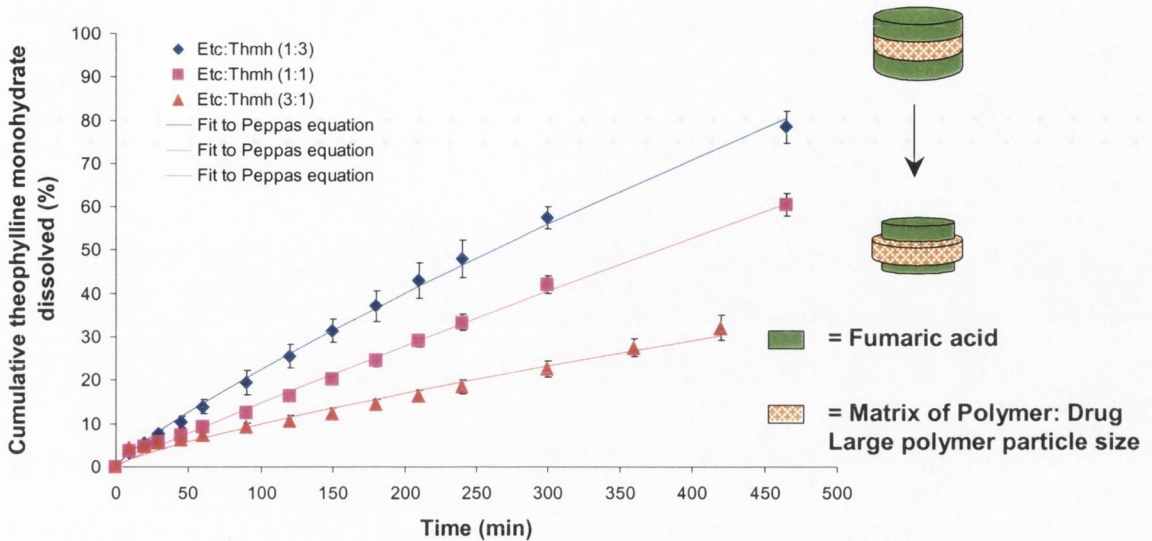


Figure 5.8 Dissolution profiles of theophylline monohydrate from triple layered matrix compacts containing a matrix layer of theophylline monohydrate and ethylcellulose 10cP in the particle size range 250–355 μm in three weight ratios of polymer to drug (500 mg), between two layers of fumaric acid (500 mg). Error bars indicate standard deviations (Etc = ethylcellulose 10cP, Thmh = theophylline monohydrate). Continuous lines represent the best fit to the Peppas equation.

In this case the acid excipient layers (fumaric acid) had not dissolved until between 6 and 7 hours, which resulted in a significant shift of the kinetics of release from pure Fickian release for the uncoated matrix compacts, or from the sigmoidal type release seen for the adipic acid layered compacts, towards a more zero-order release profile, for all three weight ratios investigated. Therefore, the mechanisms of the increasing diffusional path-length of drug with time and the increasing surface area of the matrix layer with time compete to effectively compensate each other for a longer time course than the adipic acid layered compacts, resulting in a more zero-order shaped dissolution profile. The dissolution parameters resulting from a fit of the data to the Peppas equation (Equation 1.29) are included in Table 5.5.

Table 5.5 Table of parameters resulting from the fit of the Peppas equation to dissolution profiles of theophylline monohydrate from layered matrix compacts composed of a central matrix layer of ethylcellulose 10 cP in the particle size range 250-355 μm for three weight ratios of polymer to drug (500 mg), between two acid excipient layers of fumaric acid (500 mg).

RATIO OF POLYMER:DRUG	k ($\times 10^3$)	n	MODEL SELECTION CRITERION (MSC)	COEFFICIENT OF DETERMINATION
1:3	5.7	0.83	5.865	0.998
1:1	2.5	0.92	5.412	0.997
3:1	2.8	0.78	3.540	0.978

The values of n in Table 5.5 suggest that the layers of fumaric acid have shifted the kinetics of drug release close to zero order release for the full time course of dissolution studied, particularly for the ratios of P:D of 1:3 and 1:1. An examination of the value of r^2 from a simple linear regression analysis, revealed that r^2 was greater than 0.978 for all three dissolution profiles, from time zero to seven hours (Table 5.6). In fact the deviation from a higher value of n for the highest ratio of P:D can be attributed to a slight burst release of drug after initial dissolution. Consequently, the r^2 of a linear regression analysis of the data from the first sampling time point to final dissolution sample time revealed that r^2 was equal to or greater than 0.997 for all three dissolution profiles, further confirming that drug release for all three systems is approaching zero order. The effect of excluding the zero time point in such a linear regression analysis is indicated by the resulting r^2 value shown in Table 5.6.

Table 5.6 Table of parameters resulting from the linear regression analysis of the dissolution profiles of layered matrix compacts composed of a central matrix layer of ethylcellulose 10 cP in the particle size range 250-355 μm for three weight ratios of polymer to drug (500 mg) between two acid excipient layers of fumaric acid (500 mg), indicating the effect of excluding the zero time point in the analysis. 'Final point' = 420 or 465 minutes.

RATIO OF POLYMER: DRUG	r^2 OF LINEAR REGRESSION ANALYSIS OF DISSOLUTION PROFILE	
	From 0 min. to final point.	From 15 min. to final point.
1:3	0.988	0.998
1:1	0.997	0.997
3:1	0.978	0.998

The difference in r^2 of the linear regression analysis when the zero time point is excluded would indicate that there is a slight burst release of drug from the systems at the start of the dissolution process. Following this point, the dissolution rate approximates zero order release for the full time course of dissolution studied.

5.3.3.2.2 Small particle size fraction

The dissolution profiles for matrix compacts composed of a central matrix layer of ethylcellulose 10cP in the particle size range of 106-180 μm and theophylline monohydrate (with 5% PVP) in three weight fractions (500 mg), between two layers of fumaric acid (500 mg) dissolving into 0.01N HCl are shown in Figure 5.9.

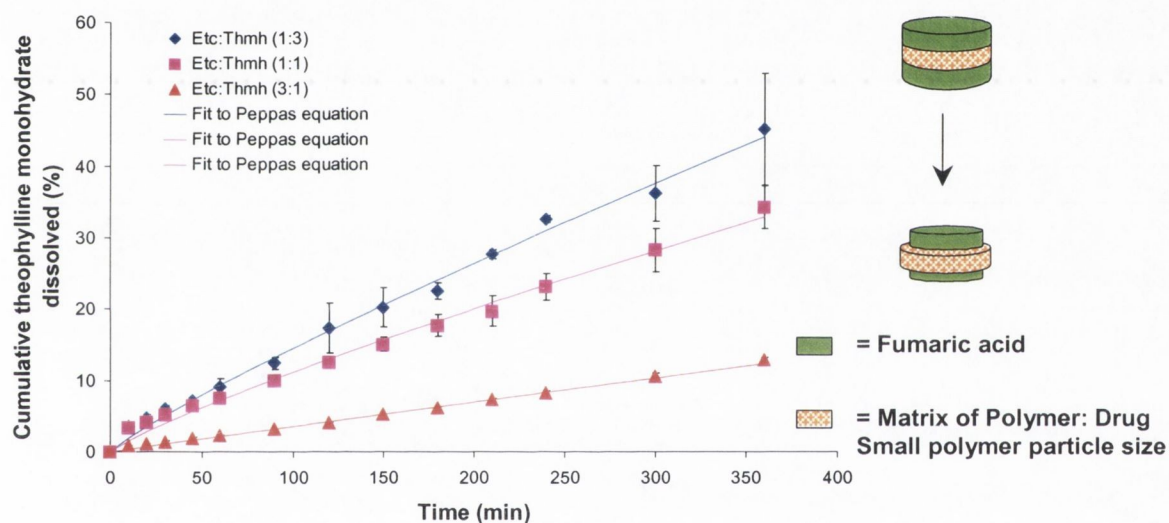


Figure 5.9 Dissolution profiles of theophylline monohydrate from triple layered matrix compacts containing a matrix layer of theophylline monohydrate and ethylcellulose 10cP in the particle size range 106-180 μm in three weight ratios of polymer to drug (500 mg), between two layers of fumaric acid (500 mg). Error bars indicate standard deviations (Etc = ethylcellulose; Thmh = theophylline monohydrate). Continuous lines represent the best fit to the Peppas equation.

The dissolution profile results were fitted to the Peppas Equation (Equation 1.29), with the resulting fitted parameters included in Table 5.7.

Table 5.7 Table of parameters resulting from the fit of the Peppas equation to dissolution profiles of theophylline monohydrate from layered matrix compacts composed of a central matrix layer of ethylcellulose 10 cP in the particle size range 106-180 μm for three weight ratios of polymer to drug (500 mg), between two acid excipient layers of fumaric acid (500 mg).

RATIO OF POLYMER: DRUG	k ($\times 10^3$)	n	MODEL SELECTION CRITERION (MSC)	COEFFICIENT OF DETERMINATION
1:3	2.61	0.87	4.925	0.998
1:1	2.29	0.84	4.505	0.997
3:1	0.44	0.96	4.896	0.998

Similar to the effect seen with the 'large' particle size of polymer, the inclusion of the fumaric acid layers has shifted the kinetics of dissolution close to zero order for the three concentrations of polymer in the layered matrix compacts. In an effort to examine how linear the release profiles were, r^2 of a linear regression analysis of the data was performed, the results of which are shown in Table 5.8.

Table 5.8 Table of parameters resulting from the linear regression analysis of the dissolution profiles of layered matrix compacts composed of a central matrix layer of ethylcellulose 10 cP in the particle size range 106-180 μm for three weight ratios of polymer to drug (500 mg) between two acid excipient layers of fumaric acid (500 mg), indicating the effect of excluding the zero time point in the analysis.

RATIO OF POLYMER:DRUG	r^2 OF LINEAR REGRESSION ANALYSIS OF DISSOLUTION PROFILE	
	From 0 min. to final point	From 15 min. to 360 min.
1:3	0.995	0.996
1:1	0.996	0.999
3:1	0.997	0.997

Again, the improvement in the linearity of the dissolution profiles on exclusion of the zero time point from the analysis would indicate that there is a slight burst release from these systems, followed by a period of zero order release for the full time course of dissolution studied.

5.4 PREDICTING DRUG RELEASE FROM LAYERED MATRIX SYSTEMS

In earlier work, it was possible to predict the rate of drug dissolution from the simple layered systems, based on the intrinsic properties of the drug and excipients used, the geometry of the system and the geometrical changes occurring over time due to

dissolution of the soluble outer layers. In an effort to further predict dissolution rates from the more complicated layered matrix systems, using such an approach, it was necessary to first examine and predict drug release from a single surface of matrix compacts.

5.4.1 Percolation studies

In recent years percolation theory has become a powerful tool in predicting dissolution kinetics of soluble drugs from inert solid matrices (see Introduction, section 1.3.2.). Percolation studies were performed in the present work to determine apparent bulk diffusion coefficients of drug through the inert solid matrix at a series of concentrations. This would allow prediction of dissolution from the complete surface of a matrix and eventually would aid in the prediction of drug dissolution from layered matrix systems.

A series of matrix compacts containing ethylcellulose 10 cP (particle size range 250-355 μm): theophylline monohydrate with polymer concentrations ranging between 20% and 70% were prepared (section 2.10.2) to allow determination of the percolation threshold for these systems. Dissolution studies (from the top planar surface only) were carried out in 0.01N. The dissolution profiles from the top planar surface of these single layer matrix compacts are shown in Figure 5.10.

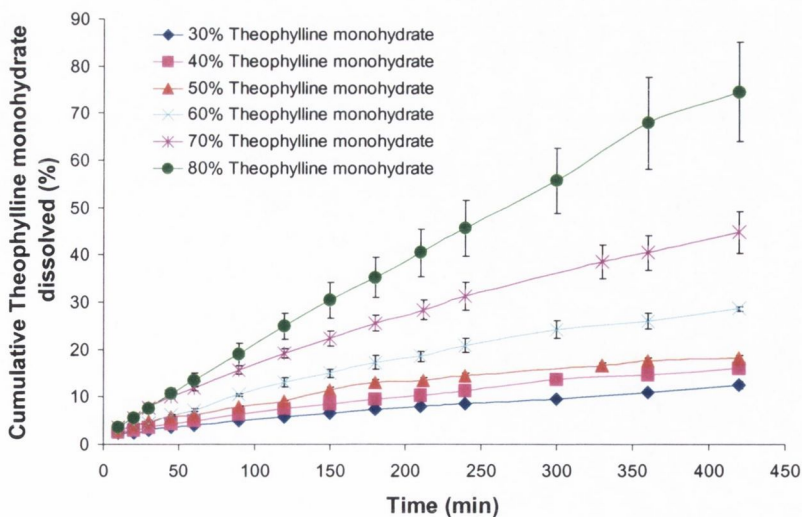


Figure 5.10 Dissolution profiles of theophylline monohydrate from the top surface only of matrix compacts composed of a series of ratios of theophylline and ethylcellulose 10cP (in the particle size range 250-355 μm). Error bars indicate standard deviations.

The approach proposed by Bonny and Leuenberger (1991) used in the determination of the upper and lower percolation thresholds, p_{c1} and p_{c2} , is outlined in section 1.3.2.4. A Higuchi plot of the percolation study data (according to Equation 1.35, i.e. $Q(t)$ versus $t^{1/2}$) is shown in Figure 5.11.

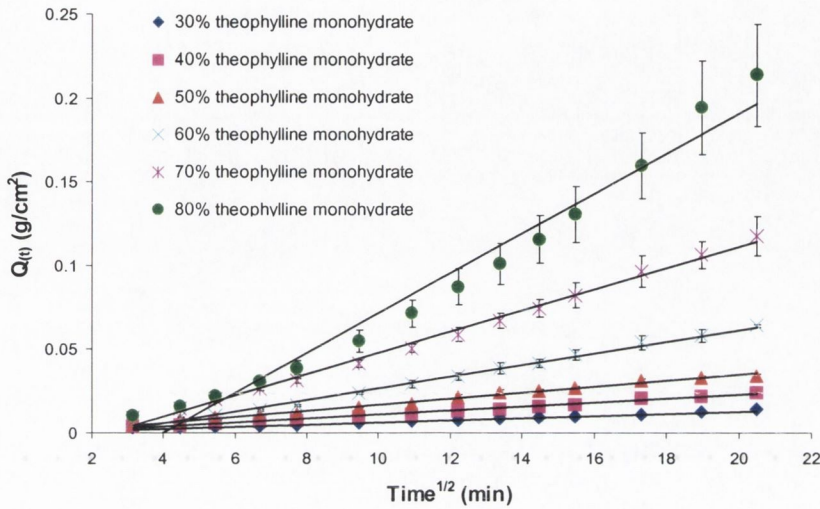


Figure 5.11 Higuchi plot of cumulative amount of theophylline monohydrate dissolved per unit surface area, $Q(t)$, versus square root of time, $t^{1/2}$, from the top surface of matrix compacts composed of a series of ratios of theophylline and ethylcellulose (in the particle size range 250-355 μm). Straight lines represent the best fits of linear regression analyses of the data. Error bars indicate standard deviations.

5.4.1.1.1 Upper percolation threshold determination

The best simple linear regression fit of the Higuchi plot for the percolation dissolutions allowed calculation of a and b according to Equation 1.35, the results of which are outlined in Table 5.9. Similarly, a plot of $Q(t)$ versus t allowed calculation of a^I and b^I using the best non linear least squares regression fit according to Equation 1.36, the results of which are also included in Table 5.9.

Table 5.9 Table of evaluated dissolution parameters from percolation studies of dissolution of theophylline monohydrate from a single surface of matrix compacts containing various levels of theophylline monohydrate and ethylcellulose 10cP (particle size fraction 250-355 μm) fitted to Equation 1.35 and 1.36, respectively. b = slope in $\text{g cm}^{-2} \text{min}^{-1/2}$. CD = coefficient of determination.

% Drug	$Q_{(t)} = a + b.t^{1/2}$		$Q_{(t)} = a' + b'.t^n$		
	b ($\times 10^3$)	CD	b^1 ($\times 10^3$)	n	CD
30	0.64	0.9970	0.32	0.610	0.9914
40	1.17	0.9973	0.55	0.621	0.9952
50	1.76	0.9981	1.49	0.526	0.9942
60	3.33	0.9954	1.28	0.653	0.9991
70	6.02	0.9955	2.04	0.674	0.9994
80	11.9	0.9980	0.94	0.899	0.9997

Application of the method of Bonny and Leuenberger (1991) to the above data would indicate the upper percolation threshold, p_{c2} , to be in the region between 50% and 60% drug content, as there is a change in the coefficient of determination value of a linear regression to the square root of time kinetics equation (Equation 1.35) and also a change in the n exponent of regression fits to Equation 1.36.

5.4.1.1.2 Lower percolation threshold determination

Evaluation of the lower percolation threshold p_{c1} involves calculation of the tablet property β , as described by Equation 1.37. The values for b were determined in the previous section, however, calculation of the porosity factor, ϵ , is necessary for each matrix formulation. The porosity factor, ϵ , represents the volume fraction of soluble drug in the system, plus any natural porosity present initially in the compact following compaction. Therefore, calculation of the porosity for each system requires knowledge of the true (skeletal) density of the soluble drug and the insoluble matrix forming polymer, together with the dimensions of the compacted matrix (Bonny and Leuenberger, 1991). If the true (skeletal) densities of ethylcellulose and theophylline monohydrate can be represented by ρ_{et} and ρ_{th} , respectively, and the mass of each component in the matrix is represented by W_{et} and W_{th} , then the true volume of the matrix, V_t , can be calculated as shown in Equation 5.1.

$$V_t = \left(\frac{W_{th}}{\rho_{th}} + \frac{W_{et}}{\rho_{et}} \right) \quad \text{Equation 5.1}$$

The apparent volume of a cylindrical compact, V_{tot} , corresponds to $\pi \cdot x^2 \cdot h/4$, where h and x correspond to the height and diameter of the compact, respectively. Knowledge of V_{tot} and V_t can then lead to calculation of the initial porosity following compaction of the matrix, ϵ_o , as described by Equation 5.2.

$$\epsilon_o = \frac{V_{tot} - V_t}{V_{tot}} \quad \text{Equation 5.2}$$

The results of helium pycnometry determinations on ethylcellulose 10cP and theophylline monohydrate are summarised in Table 5.10, while the subsequent determination of matrix porosities are included in Table 5.11.

Table 5.10 Table of helium pycnometry measurements performed to calculate the true (skeletal) densities of theophylline monohydrate and ethylcellulose 10cP.

COMPONENT	TRUE DENSITY* (x 10 ³ g cm ⁻³)
Ethylcellulose 10cP	1145.8 ± 1.1
Theophylline monohydrate	1466.0 ± 5.7

* Average value ± S.D. (n = 3)

Table 5.11 Table of parameters involved in the determination of the initial porosities of matrix compacts used in percolation studies.

% DRUG	DIAMETER (mm)	HEIGHT* (mm)	V_{tot} (cm ³)*	V_t (cm ³)	ϵ_o	ϵ
30	13	0.320	0.4247	0.4078	0.0399	0.2808
40	13	0.310	0.4115	0.3982	0.0321	0.3637
50	13	0.305	0.4048	0.3887	0.0398	0.4610
60	13	0.300	0.3982	0.3791	0.0477	0.5615
70	13	0.290	0.3849	0.3697	0.0397	0.6599
80	13	0.275	0.3650	0.3601	0.0140	0.7609

* Average values (n = 3)

Calculation of the tablet (total) porosity, ϵ , thus allowed determination of the tablet property, β , via Equation 1.37, as outlined in Table 5.12.

Table 5.12 Table of parameters involved in the calculation of the tablet property, β .

% DRUG	A (g/cm ³)	ϵ	C_s (g/cm ³)	β (g ^{1/2} .cm ^{-1/2} .s ^{-1/2} x10 ³)				
30	0.353	0.341	0.0125	1.00				
40	0.486	0.417	0.0125	1.24				
50	0.618	0.506	0.0125	1.46				
60	0.753	0.598	0.0125	2.33				
70	0.909	0.722	0.0125 </tr <tr> <td>80</td> <td>1.096</td> <td>0.804</td> <td>0.0125</td> <td>5.45</td> </tr>	80	1.096	0.804	0.0125	5.45
80	1.096	0.804	0.0125	5.45				

For estimating ϵ_c , the critical porosity corresponding to p_{cl} , β is plotted versus porosity, ϵ . Linear regression is employed on the linear region of the plot to determine the intercept with the X-axis, where $\epsilon = \epsilon_c$. The resulting linear regression plot is shown in Figure 5.12.

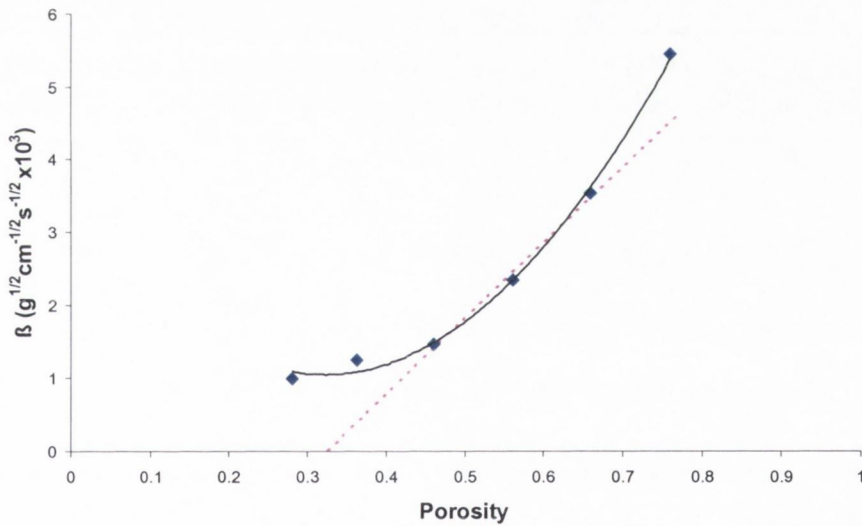


Figure 5.12 Plot of the tablet property β versus the total porosity ϵ . The dashed line is the regression line for the linear region of the plot (50% to 70%).

The linear regression leads to an estimated $\epsilon_c = 0.326$. This critical porosity corresponds to a theophylline monohydrate content of 35%. Also, a plot of drug loading versus porosity (ϵ) was linear with r^2 of 0.999. Drug loading was therefore used in place of ϵ in later matrix studies.

5.4.1.1.3 Relevance of percolation results

Therefore, percolation theory predicts that, for the current system, the drug begins to form an interconnecting network at approximately 35% drug loading in the matrix. Below 35% drug loading, incomplete release of drug from the matrix is predicted. Between 35% drug loading and the upper percolation threshold, drug release will occur by diffusion (Fickian release). After the upper percolation threshold (50-60% drug loading), the polymer will begin to exist as isolated pockets and the system will no longer remain as an intact matrix during dissolution. Therefore, erosion of the polymer particles will occur, leading to non-Fickian release of drug from the matrix.

5.4.2 Dynochem simulations

As the Dynochem program produced good simulations of drug dissolution from single and multiple layered drug-excipient compacts (Chapter 4), based on simple geometric assumptions, the program was adapted to attempt to simulate drug dissolution profiles from the more complex inert matrix systems.

In the case of dissolution from a matrix compact, the leached porous region of the matrix grows at the expense of the drug/polymer region, due to the dissolution and release of drug from the matrix. The porous structure in the dissolution medium-filled porous zone is due to both the dissolution of the solute and the inherent porosity. The boundary that interfaces the dissolution medium-filled porous zone and the undissolved drug/polymer matrix is moving with time, resulting in a 'moving boundary' phenomenon. Focusing on drug release from the top surface of a cylindrical matrix compact, the process is represented graphically in Figure 5.13.

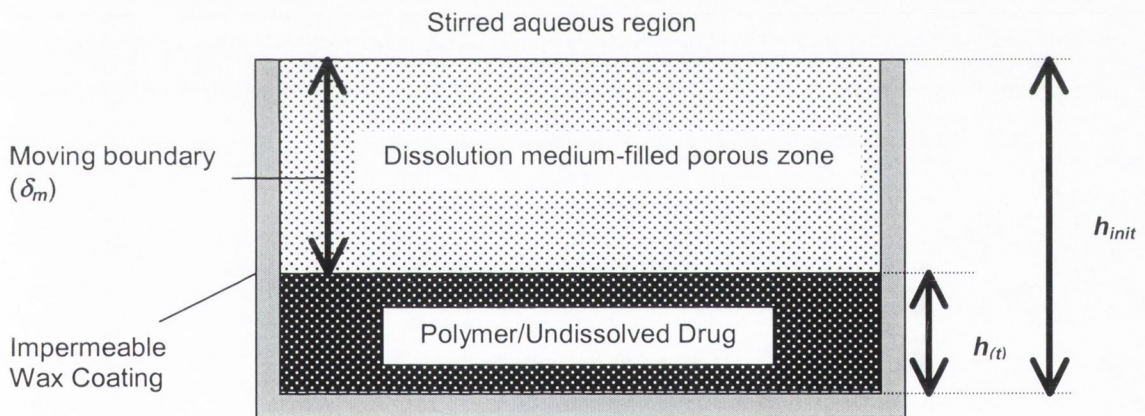


Figure 5.13 Schematic two-dimensional diagram of pseudo-steady state diffusion problem for the dissolution of soluble drug from an inert insoluble matrix compact releasing from the top surface only, showing the development of a moving boundary, of thickness δ_m (modified from Harstedt and Wright, 1990).

5.4.2.1 Dissolution from the top surface of a matrix compact

5.4.2.1.1 Process scheme

The approach used in the Dynochem program was to allow the drug to diffuse through the moving boundary (of thickness δ) with an apparent diffusion coefficient, D_{app} , similar to that described by Equation 1.32. This 'apparent' diffusion coefficient

differs from the diffusion coefficient in the permeating fluid (D_{aq}) due to the porosity and tortuosity effects, introduced by the inter-granular openings in the dissolution medium-filled porous zone. The process scheme defining the main components contributing to mass transfer in the model is indicated in Figure 5.14.

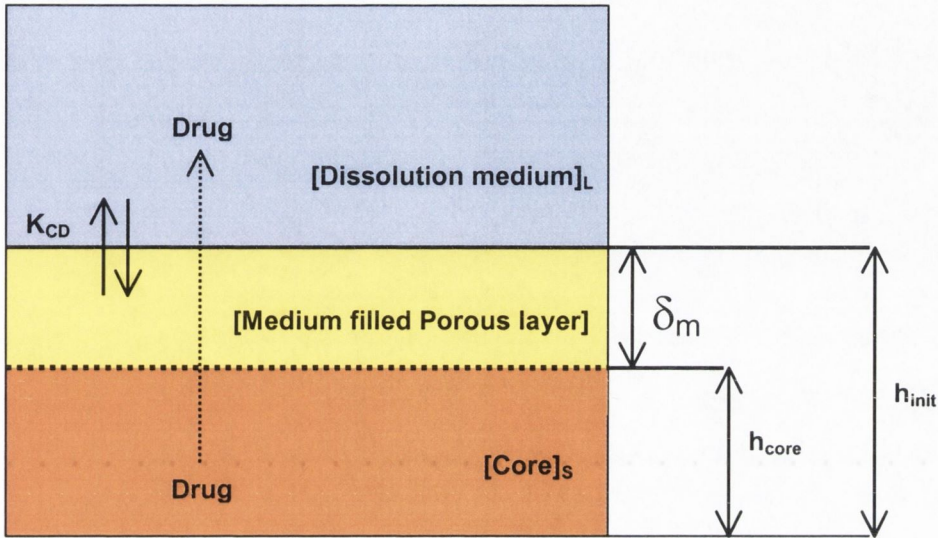


Figure 5.14 Dynochem process scheme for the dissolution of soluble drug from an inert insoluble matrix compact releasing from the top surface, indicating the diffusion of drug through the dissolution medium-filled porous layer and the development of a moving boundary of thickness, δ_m . The model assumes that the drug undergoes Fickian diffusion through the porous layer with an apparent diffusion coefficient D_{app} , the rate of transfer is proportional to both the difference between the bulk and interfacial concentration and to the interfacial area. K_{CD} is the overall mass transfer coefficient of drug between the medium-filled porous layer and the dissolution medium, h_{core} is the height of the polymer/undissolved drug core and h_{init} is the total height of the compact before dissolution.

The model therefore assumes that the only resistance to mass transfer occurs in the porous layer.

5.4.2.1.2 Process calculations

The geometric and mass transfer calculations that are specific to the current model are summarised in the following section.

$$d_{core} = d_{init_{core}} \quad \text{Equation 5.3}$$

$$h_{core} = \frac{V_{core} \times 4}{\pi \times d_{core}^2} \quad \text{Equation 5.4}$$

$$A_{(ax)_{core}} = \frac{\pi \times d_{core}^2}{2} \quad \text{Equation 5.5}$$

$$A_{(rad)_{core}} = \pi \times d_{core} \times h_{core} \quad \text{Equation 5.6}$$

$$AR_{core} = \frac{A_{(rad)_{core}}}{A_{(ax)_{core}}} \quad \text{Equation 5.7}$$

$$TSA_{exp_{core}} = \frac{A_{(ax)_{core}}}{2} \quad \text{Equation 5.8}$$

$$a = \frac{TSA_{exp_{core}}}{V_{core}} \quad \text{Equation 5.9}$$

where d_{core} is the diameter of the polymer/undissolved drug matrix core with time, $d_{init_{core}}$ is the initial diameter of the polymer/undissolved drug matrix core, h_{core} is the height of the polymer/undissolved drug matrix core, V_{core} is the volume of the polymer/undissolved drug matrix core, $A_{(ax)_{core}}$ is the total axial area of polymer/undissolved drug matrix core, $A_{(rad)_{core}}$ is the total radial area of the polymer/undissolved drug matrix core, AR_{core} is the aspect ratio of the polymer/undissolved drug matrix core, $TSA_{exp_{core}}$ is the total surface area exposed to the dissolution medium of the polymer/undissolved drug matrix core and a is the total specific interfacial surface area exposed.

The mass transfer calculations were as follows:

$$\delta_m = h_{init_{core}} - h_{core} \quad \text{Equation 5.10}$$

$$K_{C(ax)} = \frac{D_{app}}{\delta_m} \quad \text{Equation 5.11}$$

$$K_{CD(ax)} = \frac{K_{D(ax)} \times K_{C(ax)}}{K_{D(ax)} + \frac{K_{C(ax)}}{S_{cd}}} \quad \text{Equation 5.12}$$

$$Drug_{liquid} = \int_0^t V_{core} \times K_{CD(ax)} \times a \times \left(\frac{C_{drug_{core}}}{S_{cd}} - C_{drug_{liquid}} \right) dt \quad \text{Equation 5.13}$$

where δ_m is the thickness of the dissolution medium-filled porous layer (in the axial direction), $h_{init_{core}}$ is the initial height of the polymer/undissolved drug matrix core, h_{core} is the height of the polymer/undissolved drug matrix core with time, D_{app} is the apparent diffusion coefficient of the drug in the dissolution medium-filled porous region, $K_{C(ax)}$ is the mass transfer coefficient of the drug in the axial direction from the continuous phase (liquid) to the interface, $K_{D(ax)ax}$ is the mass transfer coefficient of the drug in the axial direction from the interface to the disperse (solid) phase (negligible in this model), $K_{CD(ax)}$ is the overall mass transfer coefficient in the axial direction, $C_{drug_{core}}$ is the concentration of drug in the polymer/undissolved drug matrix core at time t , $C_{drug_{liquid}}$ is the concentration of drug in the liquid at time t and S_{cd} is the partition coefficient of the drug between the disperse phase and the continuous phase defined by Equation 1.41 (Dynochem user manual, 2000).

5.4.2.1.3 Modelling of dissolution from the top surface of a matrix compact (30% drug)

The application of the Dynochem program to modelling drug dissolution from the top planar surface of an inert matrix is initially demonstrated for a drug concentration of 30% theophylline monohydrate. The parameters that were necessary to run the program for this system are included in Table 5.13, while the resulting Dynochem generated fit of drug dissolution is shown in Figure 5.15. The apparent diffusion coefficient of the drug D_{app} is allowed to 'float' in the scenario sheet to achieve the best visual fit of all data points of the experimentally determined dissolution profile (Dynochem user manual, version 1.0.3, PFD, 2000).

Table 5.13 Dynochem design parameters for the dissolution of theophylline monohydrate from the top planar surface of a matrix compact consisting of 30% theophylline monohydrate with ethylcellulose 10cP in the particle size range 250-355 μm . S_{cd} = partition coefficient of the drug between the disperse phase and the continuous phase, d_{init} is the initial diameter of the matrix core, h_{init} is the initial height of the drug core, V_{init} is the initial (apparent) volume of the matrix core, $Drug_{init}$ is the initial weight of drug in the matrix, $C_{drug_{core}}$ is the total amount of drug present in the matrix per unit volume and D_{app} is the apparent diffusion coefficient of the drug through the porous layer.

S_{cd}	d_{init} (mm)	h_{init} (mm)	V_{init} ($\text{m}^3 \times 10^7$)	$Drug_{init}$ (mg)	$C_{drug_{core}}$ (mol/m^3)	D_{app}^* ($\times 10^6 \text{ cm}^2/\text{s}$)
29.4	13	3.2	4.25	149.9	1961.1	0.735

*Resulting from best fit of model to data

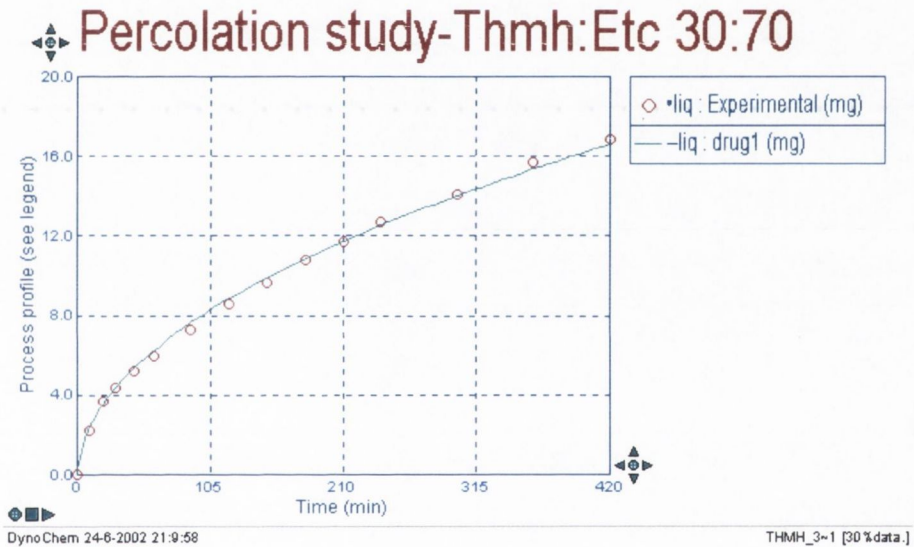


Figure 5.15 Dynochem generated fit of drug dissolution from the top planar surface of a matrix compact consisting of 30% theophylline monohydrate with ethylcellulose 10cP in the particle size range 250-355 μm . The continuous line is the fit generated from parameters as in Table 5.13.

As the model is based on a moving boundary theory, the height of the drug containing core is plotted in Figure 5.16, while the thickness of the dissolution medium filled porous layer, δ , was examined and is plotted in Figure 5.17.

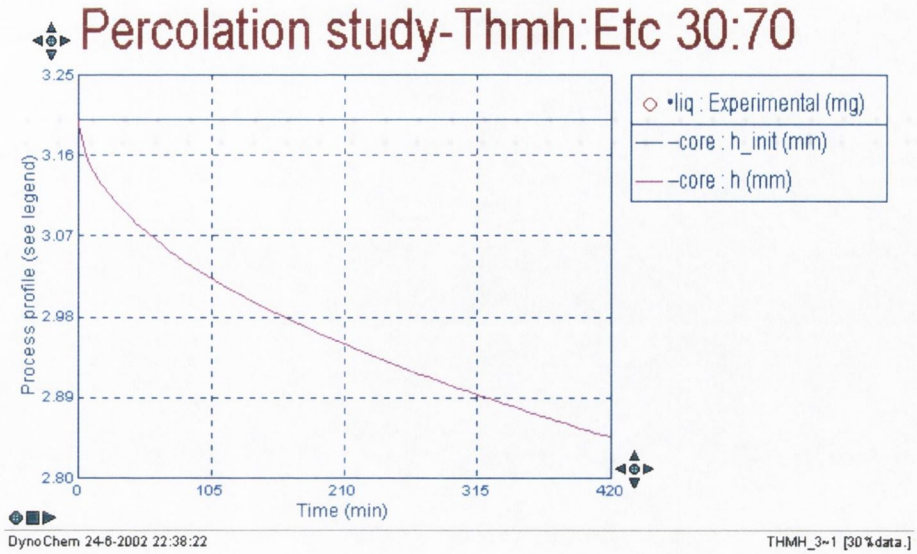


Figure 5.16 Dynochem generated simulation of the change in the height of polymer/undissolved drug matrix core with time during drug dissolution from the top planar surface of a matrix compact consisting of 30% theophylline monohydrate with ethylcellulose 10cP in the particle size range 250-355 μm .

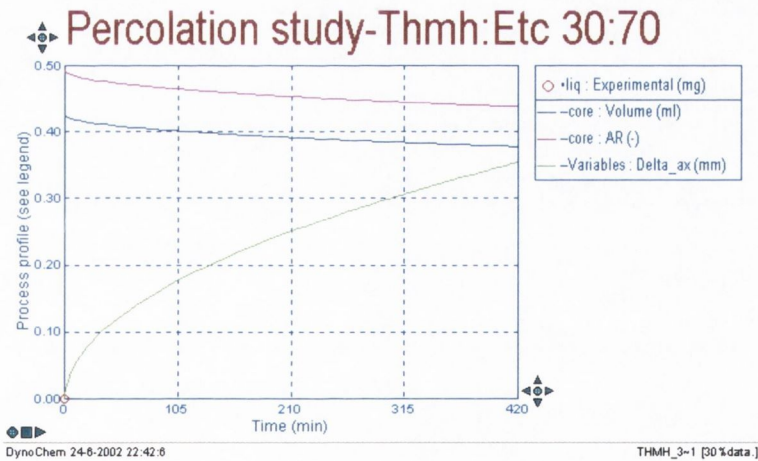


Figure 5.17 Dynochem generated simulation of the geometrical changes in the volume and aspect ratio of the polymer/undissolved drug matrix core with time (blue line) and of the thickness of the porous dissolution medium filled layer, i.e. δ_m (green line) during drug dissolution from the top planar surface of a matrix compact consisting of 30% theophylline monohydrate with ethylcellulose 10cP in the particle size range 250-355 μm .

5.4.2.1.4 Modelling of dissolution from the top surface of all percolation matrix experiments

Similarly, the above model was applied to all experimental data generated in the percolation study for matrix compacts containing theophylline monohydrate in the range of 30% to 80% with ethylcellulose 10cP. The parameters necessary to run the simulations and the resulting fitted values for D_{app} are included in Figure 5.18.

Table 5.14 Dynochem scenario sheet design parameters for the dissolution of theophylline monohydrate from the top planar surface of matrix compacts consisting of theophylline monohydrate between 30% and 80% with ethylcellulose 10cP in the particle size range 250-355 μ m. S_{cd} = partition coefficient of the drug between the disperse phase and the continuous phase, d_{init} is the initial diameter of the matrix core, h_{init} is the initial height of the drug core, V_{init} is the initial (apparent) volume of the matrix core, $Drug_{init}$ is the initial weight of drug in the matrix, $C_{drug_{core}}$ = initial amount of drug present per initial unit volume of matrix layer and D_{app} is the apparent diffusion coefficient of the drug through the porous dissolution medium-filled region.

% Thmh	S_{cd} -	d_{init} (mm)	h_{init} ⁺ (mm)	V_{init} ⁺ (x 10 ⁷ m ³)	$Drug_{init}$ (mg)	$C_{drug_{core}}$ (kg/m ³)	D_{app} [*] (x 10 ⁶ cm ² /s)
30	29.4	13	3.20	4.247	150	353.0	0.735
40	40.6	13	3.08	4.088	200	487.1	1.76
50	51.7	13	3.05	4.048	250	620.0	3.29
60	62.4	13	3.00	3.982	300	748.4	7.20
70	72.8	13	3.00	3.982	350	873.9	19.5
80	86.4	13	2.77	3.677	400	1087.9	38.5

*Resulting from best fit of model to the data

+ Average values (n = 3)

The corresponding Dynochem simulations for drug dissolution from the top surface of the matrix compacts used in the percolation studies with theophylline monohydrate levels between 30% and 80% are included in Figure 5.18.

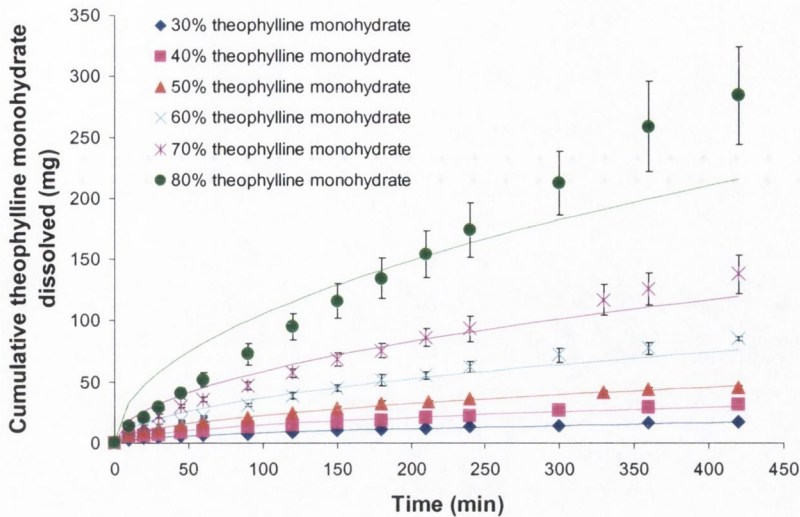


Figure 5.18 Dynochem generated fits of drug dissolution from the top planar surface of matrix compacts consisting of between 30% and 80% theophylline monohydrate with ethylcellulose 10cP in the particle size range 250-355 μm . The continuous line represents the best fit of D_{app} to each data set. Error bars indicate standard deviations.

The Dynochem moving boundary model based on diffusion predicts dissolution profiles that match the experimental model quite well for theophylline monohydrate levels of between 30% and 50%. After this point, there is some deviation, which increases with increasing levels of drug. Therefore, the data can be represented by pure Fickian diffusion for drug levels between 30% and 50%, but the data cannot be modelled by simple diffusion after this point.

According to the scaling law of Equation 1.33 (with an exponent of 2 for a three dimensional lattice), a plot of $D_{app}^{1/2}$ versus ϵ is linear in nature (Stauffer and Aharony, 1992). As drug loading was interchangeable with ϵ in this study (section 5.4.1.1.2), a plot of $D_{app}^{1/2}$ versus % drug for the present fitted data is shown in Figure 5.19.

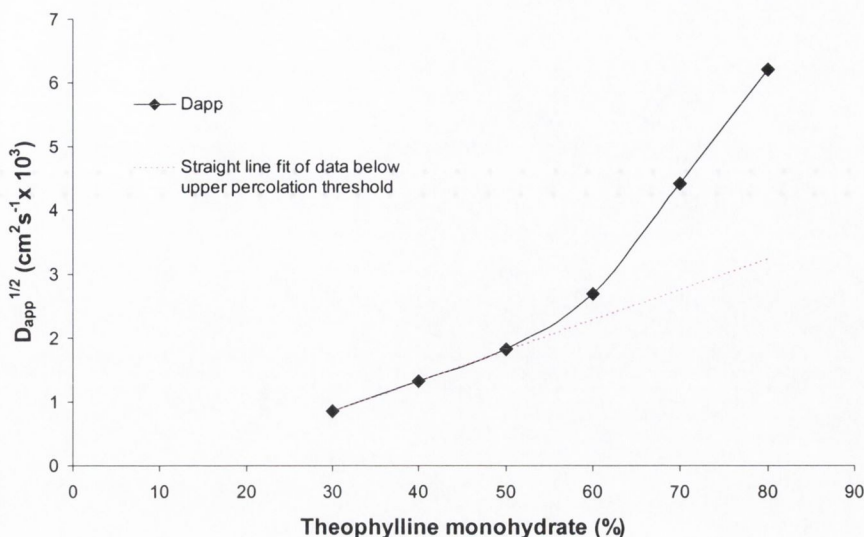


Figure 5.19 Plot of Dynochem fitted $D_{app}^{1/2}$ versus % drug loading for drug dissolution from the top planar surface of matrix compacts consisting of between 30% and 80% theophylline monohydrate with ethylcellulose 10cP in the particle size range 250-355 μm .

There is deviation from the expected linear region when the % of theophylline monohydrate is greater than 50%, further evidence that the mechanism controlling dissolution after this point is not solely diffusion based. It is speculated that between 50% and 60% drug levels, the drug reaches its percolation threshold and that this leads to the development of isolated cluster of polymer throughout the matrix. This prevents the polymer substance from completely percolating the matrix and results in shedding of the polymeric component during the dissolution process.

5.4.2.2 Dissolution including polymer erosion from the top surface of matrix (above upper percolation threshold)

In an effort to further predict dissolution from the matrix systems with higher drug loadings, the previous model was adapted to include the effect of polymer erosion from the outside of the porous dissolution-medium filled layer.

5.4.2.2.1 Process scheme

The earlier model was modified to include the effect of the postulated drug erosion for compacts containing greater than 50% theophylline monohydrate (above the upper percolation threshold, p_{c2}). The process scheme for the newer model is shown in Figure 5.20.

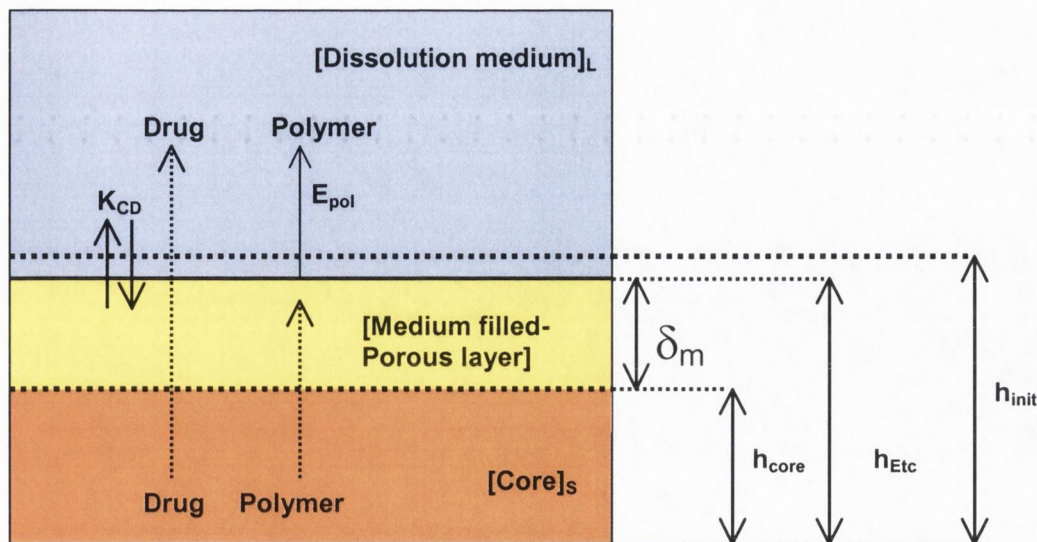


Figure 5.20 Dynochem process scheme for the dissolution of soluble drug from an inert insoluble matrix compact releasing from the top surface, indicating the diffusion of drug through the dissolution medium-filled porous layer, the development of a moving boundary, δ_m and the erosion of polymer from the outside of the medium-filled porous layer when the drug is present at levels greater than the upper percolation threshold. K_{CD} is the overall mass transfer coefficient of drug between the medium-filled porous layer and the liquid, E_{pol} is the ‘erosion’ rate of polymer from the outside of the medium-filled porous layer, h_{core} is the height of the polymer/undissolved drug core and h_{init} is the total height of the compact before dissolution and h_{Etc} is the height from the outside of the medium-filled porous layer (ethylcellulose) to the base of the compact.

Again, the model assumes that the only resistance to mass transfer occurs in the porous medium-filled layer.

5.4.2.2.2 Process calculations

The previous model was adapted to allow the polymer at the outside of the dissolution medium-filled porous layer to ‘erode’ at a certain rate per unit surface area exposed. Effectively, this adapted model focuses on two solid phases, the first calculating the geometry of the polymer/undissolved drug core (‘core’), while the second focuses on the geometry of the medium-filled porous layer (‘Etc’).

The geometric calculations for the polymer/undissolved drug core were identical to the process sheet calculations described in section 5.4.2.1.2. This series of equations was also repeated for the new phase (‘Etc’), that representing the volume defined by the polymer remaining in the matrix, i.e., the volume represented by the height from the outside of the dissolution medium-filled porous layer (ethylcellulose) to the base

of the compact. The geometry of the drug ‘core’ layer is based on the mass of drug remaining and calculating the height of this phase with time, based on the initial weight of drug per total volume. The geometry of the ‘Etc’ layer is based on the mass of polymer remaining (after being allowed to erode at a certain rate per area exposed) and calculating the height of this phase with time, based on the initial weight of ethylcellulose per total volume.

The mass transfer of drug calculations were also carried out as described in 5.4.2.1.2. A series of equations were also added to allow the ‘erosion’ of polymer from the outer surface of the dissolution medium-filled porous layer as follows:

$$a_{Etc} = \frac{TSA_{exp\ Etc}}{Volume_{Etc}} \quad \text{Equation 5.14}$$

$$E_{rate} = E_{pol} \times V_{Etc} \times a_{Etc} \quad \text{Equation 5.15}$$

$$Polymer_{liquid} = \int_0^t E_{rate} \cdot dt \quad \text{Equation 5.16}$$

where a_{Etc} is the specific interfacial area at the outside of the dissolution medium-filled porous layer (after accounting for the erosion of polymer), E_{pol} is the erosion rate of polymer from the outside of the medium-filled porous layer per unit area per unit time, E_{rate} is the total erosion rate of polymer from the outside of the medium-filled porous layer per unit time, and $Polymer_{liquid}$ is the total amount of polymer eroded into the dissolution medium at time t . The complete set of process sheet calculations for the model which included the erosion of polymer are included in Appendix 12.

5.4.2.2.3 Modelling of dissolution including erosion of polymer from the top surface of a matrix compact (60% drug)

Results of the modelling of drug dissolution from the top planar surface of an inert matrix including the erosion of polymer is initially demonstrated for a drug concentration of 60% theophylline monohydrate. The parameters of the scenario sheet used to model the system are included in Table 5.15, while the modelled dissolution profile is included in Figure 5.21.

Table 5.15 Dynochem scenario sheet design parameters for modelling dissolution of theophylline monohydrate from the top planar surface of a matrix compact consisting of 60% theophylline monohydrate with ethylcellulose 10cP in the particle size range 250-355 μm , including the erosion of polymer from the medium-filled porous layer. S_{cd} = partition coefficient of the drug between the disperse phase and the continuous phase, d_{init} = initial diameter of the matrix core, h_{init} = initial height of the drug core, Drug_{init} = initial mass of drug in the compact, ρ'_{drug} = initial amount of drug present per initial unit volume of matrix layer, ρ'_{Etc} = initial amount of ethylcellulose present per initial unit volume of matrix layer, D_{app} = the apparent diffusion coefficient of the drug through the porous layer and E_{pol} = erosion rate of polymer from the surface of the dissolution medium-filled porous layer.

S_{cd}	d_{init} (mm)	h_{init} (mm)	Drug_{init} (mg)	ρ'_{drug} kg/m^3	ρ'_{Etc} kg/m^3	D_{app}^* ($\text{cm}^2/\text{s} \times 10^6$)	E_{pol}^* ($\text{mg m}^{-2} \text{s}^{-1}$)
62.4	13	3.00	300	748.4	507.3	4.80	10.5

*Resulting from best fit of model to the data

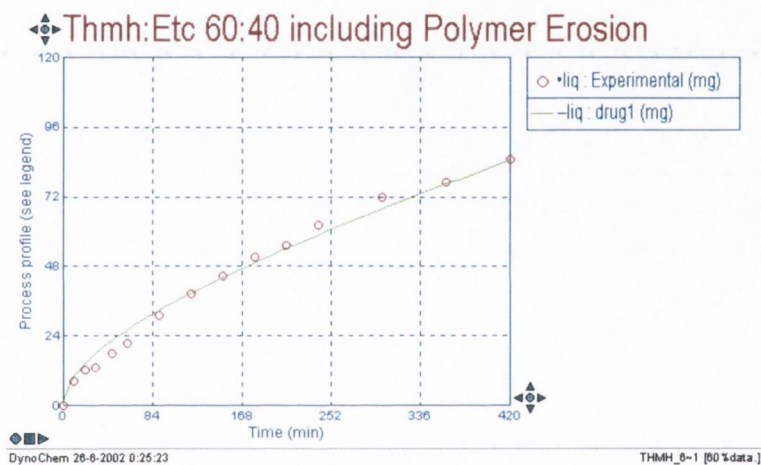


Figure 5.21 Dynochem generated fit of drug dissolution from the top planar surface of a matrix compact consisting of 60% theophylline monohydrate with ethylcellulose 10cP in the particle size range 250-355 μm , including polymer 'erosion' from the outside of the dissolution medium-filled porous region. The continuous line is the fit generated from parameters as in Table 5.15.

The predicted changes in the volume of the undissolved drug-polymer core and changes in the thickness of the medium-filled porous layer are included in Figure 5.22.

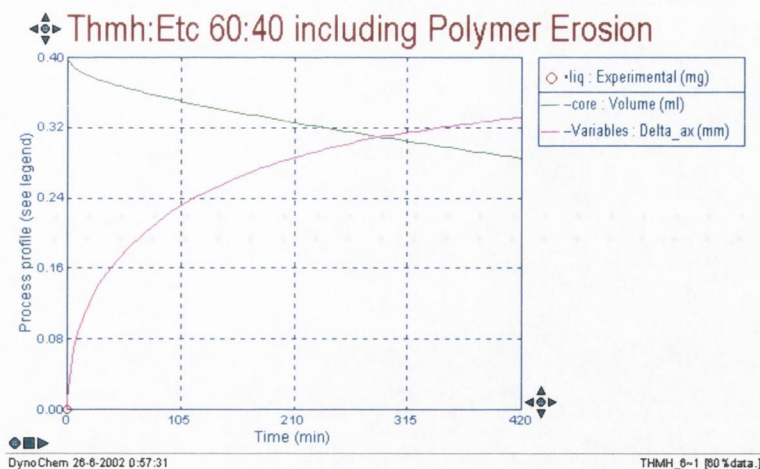


Figure 5.22 Dynochem generated simulation of the changes in the volume of the undissolved drug-polymer core (green line) and of the thickness of the porous dissolution medium-filled layer, δ_m (pink line) during drug dissolution from the top planar surface of a matrix compact consisting of 60% theophylline monohydrate with ethylcellulose 10cP in the particle size range 250-355 μm , with the inclusion of polymer erosion from the dissolution medium-filled porous layer in the model.

5.4.2.2.4 Modelling of dissolution including polymer erosion from top surfaces of matrix compacts above the upper percolation threshold

The model including the polymer erosion was applied to the experimental data of the percolation study for matrix compacts containing theophylline monohydrate in the range of 60% to 80% with ethylcellulose 10cP. The parameters necessary to run the simulations and the resulting fitted values for D_{app} and E_{pol} are included in Table 5.16.

Table 5.16 Dynochem scenario sheet design parameters for modelling dissolution of theophylline monohydrate from the top planar surface of a matrix compact consisting of 60% theophylline monohydrate with ethylcellulose 10cP in the particle size range 250-355 μm , including the erosion of polymer from the medium-filled porous layer. S_{cd} = partition coefficient of the drug between the disperse phase and the continuous phase, d_{init} = initial diameter of the matrix core, h_{init} = initial height of the drug core, $Drug_{init}$ = initial mass of drug in the compact, ρ'_{drug} = initial amount of drug present per initial unit volume of matrix layer, ρ'_{Etc} = initial amount of ethylcellulose present per initial unit volume of matrix layer, D_{app} = the apparent diffusion coefficient of the drug through the porous layer and E_{pol} = erosion rate of polymer from the surface of the medium-filled porous layer.

% Drug	S_{cd}	d_{init} (mm)	h_{init} (mm)	$Drug_{init}$ (mg)	ρ'_{drug} kg/m^3	ρ'_{Etc} kg/m^3	D_{app}^* ($\text{cm}^2/\text{s} \times 10^6$)	E_{pol}^* ($\text{mg m}^{-2} \text{s}^{-1}$)
60	62.4	13	3.00	300	748.4	507.3	4.80	10.5
70	72.8	13	3.00	350	904.1	395.0	6.50	15.0
80	86.4	13	2.77	400	1036.3	272.0	7.50	20.0

*Resulting from the best fit of model to the data

The corresponding Dynochem simulations for drug dissolution from the top surface of the matrix compacts used in the percolation studies, including the erosion of polymer from the upper planar surface, with theophylline monohydrate levels between 60% and 80% are included in Figure 5.23, while the corresponding magnitudes of height of the relevant dissolution medium-filled porous layers (δ_m) are included in Figure 5.24.

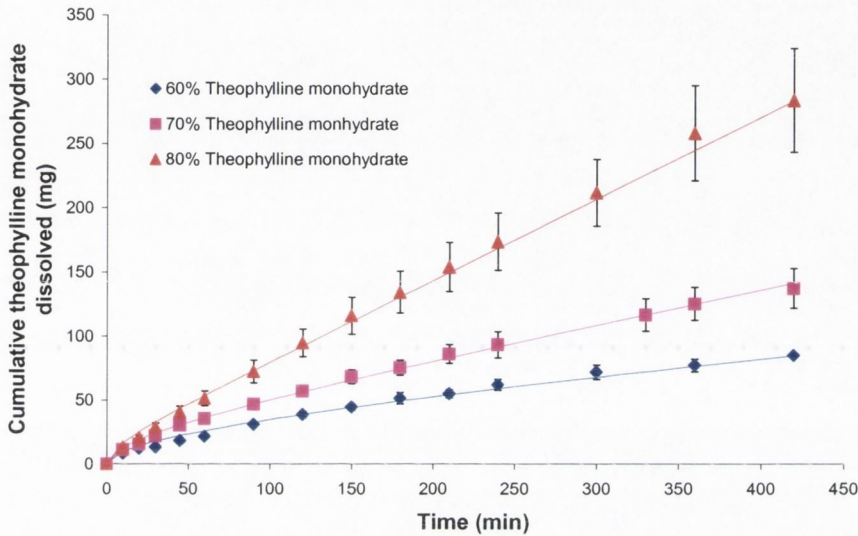


Figure 5.23 Dynochem generated fits of drug dissolution from the top planar surface of a matrix compact consisting of between 60% and 80% theophylline monohydrate with ethylcellulose 10cP in the particle size range 250-355 μm , for the model including erosion of polymer from the outside of the dissolution medium-filled porous layer. The continuous lines represent the best fit of D_{app} and E_{pol} to each data set. Error bars indicate standard deviations.

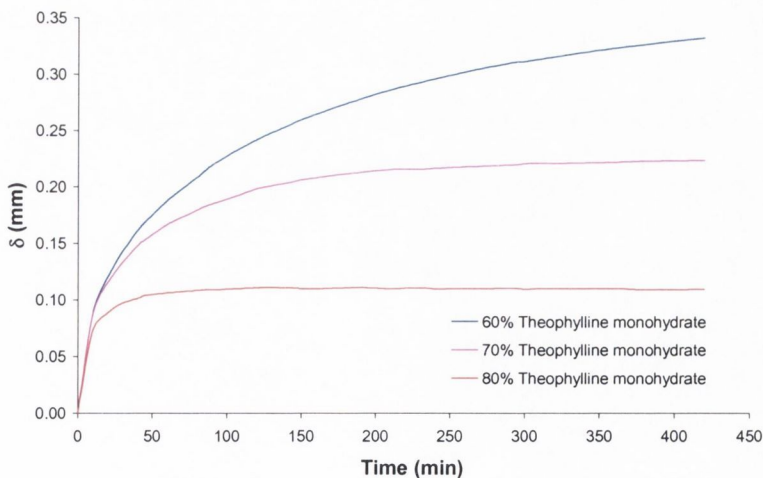


Figure 5.24 Dynochem simulated plots of the height of the of the dissolution-medium filled porous layer (δ_m) of matrix compacts undergoing drug dissolution from the top planar surface consisting of between 60% and 80% theophylline monohydrate with ethylcellulose 10cP in the particle size range 250-355 μm , for the model including erosion of polymer from the outside of the medium-filled porous layer.

A plot of $D_{app}^{1/2}$ versus % drug loading was again generated for all levels of theophylline monohydrate, the values below 50% based on the simple dissolution model, values above 50% based on the dissolution and polymer erosion model, as shown in Figure 5.25.

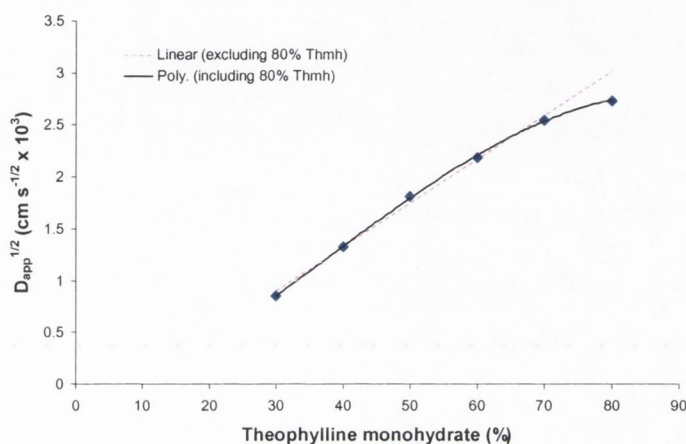


Figure 5.25 Plot of Dynochem fitted $D_{app}^{1/2}$ versus % theophylline monohydrate for drug dissolution from the top planar surface of matrix compacts consisting of between 30% and 80% theophylline monohydrate with ethylcellulose 10cP in the particle size range 250-355 μm . Values below the upper percolation threshold are based on the simple drug diffusion model; values above the upper percolation threshold are based on the drug diffusion and polymer erosion model.

The data in Figure 5.25 were represented by a linear fit for 30% to 70% theophylline monohydrate ($r^2 = 0.995$), however, the full data set, including 80% theophylline monohydrate, was best represented by a polynomial fit. A plot of E_{pol} versus % theophylline monohydrate, above the percolation threshold, is shown in Figure 5.26.

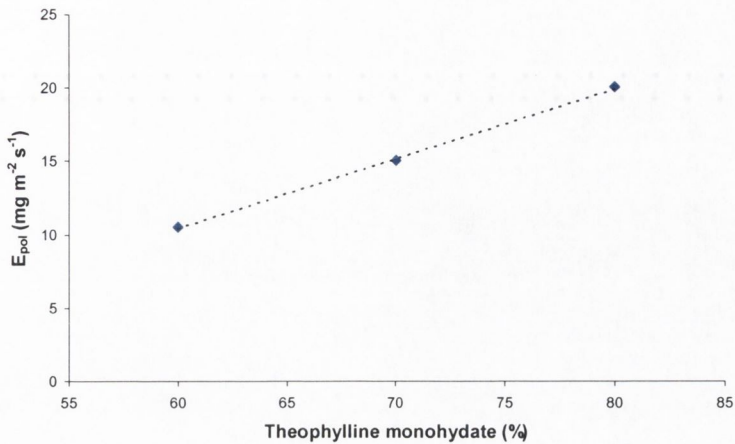


Figure 5.26 Plot of Dynochem fitted E_{pol} versus % theophylline monohydrate for drug dissolution from the top planar surface of matrix compacts consisting of between 60% and 80% theophylline monohydrate with ethylcellulose 10cP in the particle size range 250-355 μm .

The best fit trendlines to the data in Figure 5.25 and Figure 5.26 will be used in the next section to predict drug dissolution from the complete surface of uncoated matrix compacts.

5.4.2.3 Dissolution including polymer erosion from the complete surface of matrix compacts

5.4.2.3.1 Process scheme

The process scheme used to model dissolution from the complete surface of uncoated matrix compacts was identical to that shown in Figure 5.20. However, in this case, the mass transfer of drug (and erosion of polymer, if applicable) occurred from the complete surface of the cylindrical compact. For this reason, a number of modifications were made to the geometrical calculations.

5.4.2.3.2 Process calculations

The major modifications that were made to the geometrical calculations of the process sheet calculations, to allow a change in the dimensions of both the diameter and the height of the compacts, are outlined as follows:

$$AR_{core} = \frac{A_{o(rad)core}}{A_{o(ax)core}} \quad \text{Equation 5.17}$$

$$h_{core} = \frac{AR_{core}^2 \times V_{core}}{\pi} \quad \text{Equation 5.18}$$

$$d_{core} = \frac{8 \times V_{core}}{\pi \times AR_{core}} \quad \text{Equation 5.19}$$

All terms are as previous described, with ‘ax’ referring to the terms in the axial direction, ‘rad’ referring to the terms in the radial direction. $A_{o(ax)core}$ is the initial area of the core in the axial direction and $A_{o(rad)core}$ is the initial area of the core in the radial direction. Similar changes were also made to the geometrical calculations of the ethylcellulose phase, all ‘core’ terms being altered for ‘Etc’.

The modifications that were made to the process sheet calculations, to allow mass transfer from the complete surface of the compact to be modelled, are as follows:

$$TSA_{exp\ Etc} = A_{(ax)\ Etc} + A_{(rad)\ Etc} \quad \text{Equation 5.20}$$

$$a = \frac{TSA_{exp\ Etc}}{V_{Etc}} \quad \text{Equation 5.21}$$

$$\delta_{(ax)} = \frac{h_{Etc} - h_{core}}{2} \quad \text{Equation 5.22}$$

$$\delta_{(rad)} = \frac{d_{Etc} - d_{core}}{2} \quad \text{Equation 5.23}$$

$$f_{(ax)} = \frac{A_{(ax)\ Etc}}{TSA_{exp\ Etc}} \quad \text{Equation 5.24}$$

$$f_{(rad)} = \frac{A_{(rad)\ Etc}}{TSA_{exp\ Etc}} \quad \text{Equation 5.25}$$

$$K_{C(ax)} = \frac{f_{ax} \times D_{app}}{\delta_{ax}} \quad \text{Equation 5.26}$$

$$K_{C(rad)} = \frac{f_{rad} \times D_{app}}{\delta_{rad}} \quad \text{Equation 5.27}$$

$$K_{CD(ax)} = \frac{K_{D(ax)} \times K_{C(ax)}}{K_{D(ax)} + \frac{K_{C(ax)}}{S_{cd}}} \quad \text{Equation 5.28}$$

$$K_{CD(rad)} = \frac{K_{D(rad)} \times K_{C(rad)}}{K_{D(rad)} + \frac{K_{C(rad)}}{S_{cd}}} \quad \text{Equation 5.29}$$

$$Drug_{liquid} = \int_0^t V_{core} \times (K_{CD_{ax}} + K_{CD_{rad}}) \times a_2 \times \left(\frac{C_{core}}{S_{cd}} - C_{liquid} \right) dt \quad \text{Equation 5.30}$$

All terms are as previous described, with 'ax' referring to the axial direction, 'rad' referring to the radial direction. The complete process sheet calculations are included in Appendix 13.

5.4.2.4 Simulated dissolution profiles from the complete surface of matrix compacts

For the complete surface simulations of drug release, the apparent diffusion coefficient of the drug D_{app} and the erosion rate constant of the polymer, E_{pol} were taken from fitted values predicted by the trendlines fitted to the data for the single surface calculations, as shown in Figure 5.25 and Figure 5.26.

The dissolution studies involving release from the complete surface of the matrix were performed before the development of the Dynochem model (section 5.3.3). As these experiments contained differing ratios of drug:polymer to those performed in the percolation studies, a direct simulation of drug release from the complete surface, based on the previously calculated model parameters from the single surface Dynochem model was not directly possible. For this reason, matrix compacts of the same composition as those in the percolation study, were analysed for drug release from the complete surface, the first containing a drug level below the upper percolation threshold (30% drug), the second containing a drug level above the upper percolation threshold (70%). Simulations of dissolution from the complete surface were then based on the corresponding fitted parameters from the percolation study.

5.4.2.4.1 Below the upper percolation threshold (30% drug)

The model simulating drug dissolution from the complete surface of a matrix was applied to predict drug dissolution from a compact containing 30% theophylline monohydrate, based on the design parameters from the percolation experiment of the same composition as shown in Table 5.14 (with $E_{pol} = 0$). The resulting simulated data as shown in Figure 5.27.

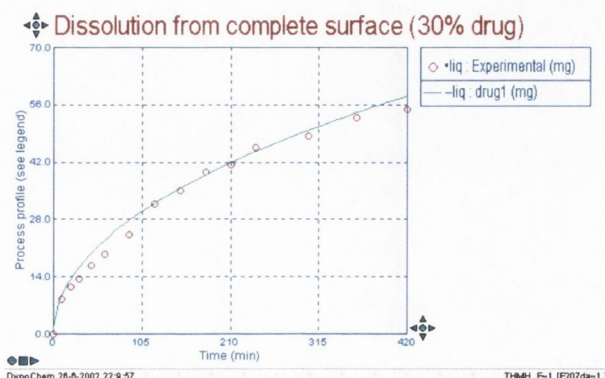


Figure 5.27 Dynochem generated SIMULATION of drug dissolution from the complete surface of a matrix compact consisting of 30% theophylline monohydrate and ethylcellulose 10cP in the particle size range 250-355 μm . The continuous line is a simulation using D_{app} calculated from the best fit of dissolution data from the top planar surface of a compact of similar composition.

5.4.2.4.2 Above the upper percolation threshold (70% drug)

Similarly, the complete surface model was applied to predict drug dissolution from a compact containing 70% theophylline monohydrate, based on the design parameters from the percolation experiment of the same composition as shown in Table 5.16. The resulting simulated data being included in Figure 5.28.

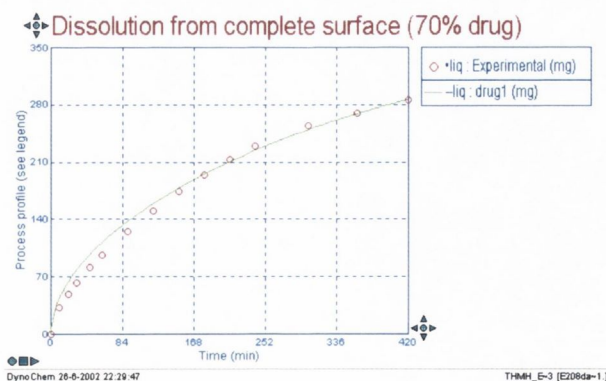


Figure 5.28 Dynochem generated SIMULATION of drug dissolution from the complete surface of a matrix compact consisting of 70% theophylline monohydrate and ethylcellulose 10cP in the particle size range 250-355 μm . The continuous line is a simulation using D_{app} and E_{pol} calculated from the best fit of dissolution data from the top planar surface of a compact of similar composition.

5.4.2.4.3 Simulations of drug release from matrix cores used in layered matrix studies

The matrix cores of the layered matrix systems previously studied contained theophylline monohydrate at different composition levels to those studied in the matrix percolation experiments. These matrix cores also contained PVP at the level of 5%, to permit comparison with the layered matrix experiments. To allow simulation of drug release from the central matrix cores only (experiments without the acid excipient layers), the design parameters D_{app} and E_{pol} were predicted from the fitted trendlines in Figure 5.25 and Figure 5.26 at the corresponding percentage of (drug + PVP) of the simulated experiment (the density of the 5% PVP is assumed to be equal to that of theophylline monohydrate). The resulting predicted parameters are included in Table 5.17, with the simulated data shown in Figure 5.29.

Table 5.17 Dynochem scenario sheet design parameters for simulating dissolution of theophylline monohydrate from complete surface matrix compacts consisting of theophylline monohydrate with ethylcellulose 10cP in the particle size range 250-355 μ m and 5% PVP. ϵ = the total porosity of the matrix, S_{cd} = partition coefficient of the drug between the disperse phase and the continuous phase, d_{init} = initial diameter of the matrix core, h_{init} = initial height of the drug core, $Drug_{init}$ = initial mass of drug in the compact, ρ'_{drug} = initial amount of drug present per initial unit volume of matrix layer, ρ'_{Etc} = initial amount of ethylcellulose present per initial unit volume of matrix layer, D_{app} = the apparent diffusion coefficient of the drug through the porous layer and E_{pol} = erosion rate of polymer from the surface of the medium-filled porous layer.

Thmh:Etc	ϵ	S_{cd} -	h_{init} (mm)	$Drug_{init}$ (mg)	ρ'_{drug} kg/m ³	ρ'_{Etc} kg/m ³	D_{app} [*] (cm ² /s x 10 ⁶)	E_{pol} [*] (mg m ⁻² s ⁻¹)
1:3	0.374	24.9	3.3	118.8	271.1	n/a	0.66	0
1:1	0.579	48.1	3.1	237.5	577.2	577.2	3.65	6.75
3:1	0.770	72.2	3.1	356.25	865.8	288.6	6.2	17.9

*Resulting from data fitted from single surface experiments

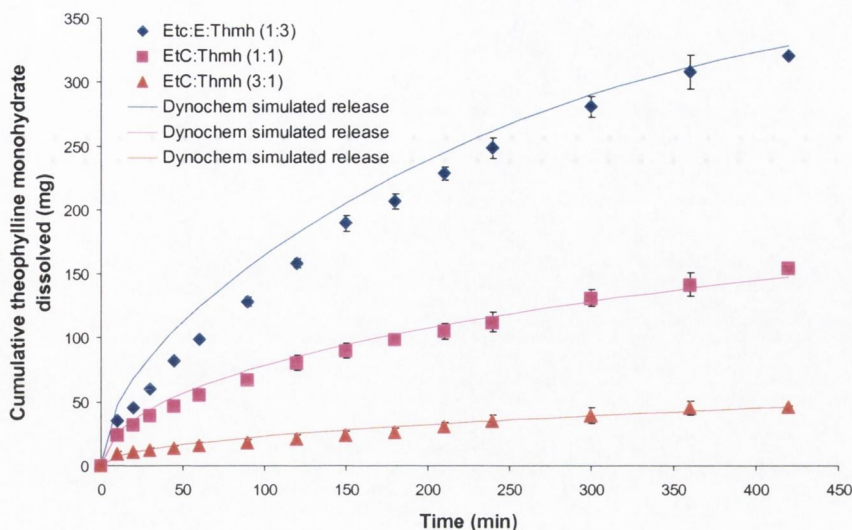


Figure 5.29 Dynochem generated SIMULATION of drug dissolution from the complete surface of matrix compact consisting of compacts composed of theophylline monohydrate ethylcellulose (with 5% PVP), from three weight ratios of polymer to drug. Error bars indicate standard deviations (Etc = ethylcellulose 10cP, particle size range 250-355 μm ; Thmh = theophylline monohydrate). The continuous lines are simulations using D_{app} and E_{pol} calculated from interpolations based on the best fit of dissolution data from the top planar surface only of matrix compacts.

5.4.2.5 Dissolution from layered matrix compacts

The final application of the modelling program involved development of the model for drug dissolution from a simple matrix compact, to modelling drug dissolution from the more complex systems consisting of a matrix core between two acid excipient layers.

5.4.2.5.1 Process scheme

The previous scheme to model dissolution from the complete surface of matrix compacts, (including polymer erosion above the percolation threshold) was finally combined with the scheme to model dissolution from layered compacts, to ultimately predict drug release from the more complex layered systems containing a drug-matrix central core layer, as illustrated in Figure 5.30.

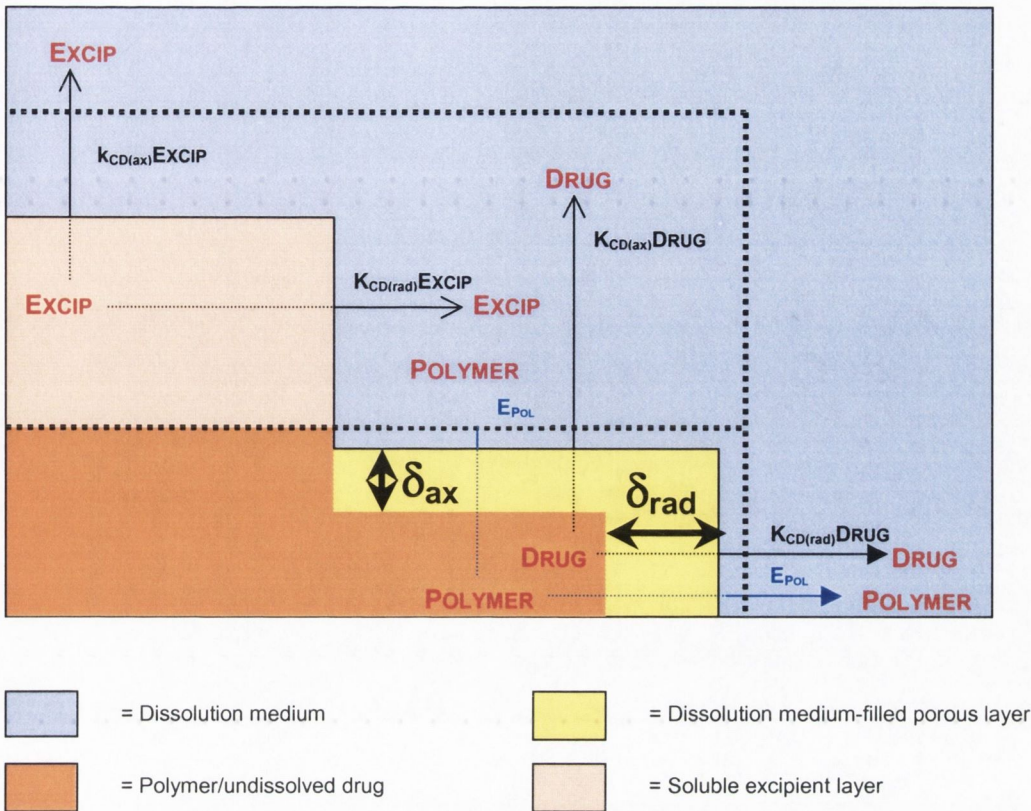


Figure 5.30 Dynochem process scheme for the dissolution of soluble drug from an inert insoluble matrix core layer between two acid excipient layers (symmetrical quarter of complete 2 dimensional process illustrated) indicating the development of newly exposed area in the axial direction of the matrix layer, due to the dissolution of the acid excipient layer in the radial direction. $k_{CD}DRUG(ax \text{ or } rad)$ is the mass transfer coefficient of the drug between the dissolution medium-filled porous layer and the liquid in the axial or radial directions, E_{POL} is the 'erosion' rate of polymer from the outside of the dissolution medium-filled porous layer, $k_{CD}EXCIP(ax \text{ or } rad)$ is the mass transfer coefficient of the excipient between the excipient layer and the liquid in the axial or radial direction. $\delta(ax \text{ or } rad)$ is the thickness of the porous polymer network in the axial or radial directions.

5.4.2.5.2 Process calculations

The process sheet calculations for the final model resulted from a combination of the drug release equations from the complete surface area of the matrix (including polymer erosion, if appropriate) with the effect of the addition of a soluble acid excipient on the planar surfaces of the compact.

Apart from the geometrical equations for the polymer containing core, a similar set of equations were included for the excipient layer. The geometrical equations for the dimensions of the drug-polymer core and the acid excipient layers were identical to those previously described in 5.4.2.3.2 and section 5.4.2.4, except for the modifications which allow linkage between the two models as follows.

$$A_{(ax_exp)Etc} = A_{(ax)Etc} - A_{(ax)Excip} \quad \text{Equation 5.31}$$

$$TSA_{exp Etc} = A_{(ax_exp)Etc} + A_{(rad)Etc} \quad \text{Equation 5.32}$$

$$a = \frac{TSA_{exp Etc}}{V_{Etc}} \quad \text{Equation 5.33}$$

where $A_{(ax_exp)Etc}$ is the axial area exposed to the dissolution medium of the matrix, $A_{(ax)Etc}$ is the complete area of the matrix in the axial direction, $A_{(ax)Excip}$ is the complete surface area of the excipient in the axial direction (i.e. the interfacial area between the excipient and the matrix), $TSA_{(exp)Etc}$ is the complete surface area of the matrix exposed, $A_{(rad)Etc}$ is the complete radial area of the matrix layer, a is the interfacial surface area per unit volume and V_{Etc} is the volume of the matrix (including the developing dissolution medium-filled region).

The major modifications that were made to the process sheet calculations to allow mass transfer from the complete surface of the compact were as follows:

$$f_{(ax)} = \frac{A_{(ax_exp)Etc}}{TSA_{exp Etc}} \quad \text{Equation 5.34}$$

$$f_{(rad)} = \frac{A_{(rad)Etc}}{TSA_{exp Etc}} \quad \text{Equation 5.35}$$

$$Drug_{liquid} = \int_0^t V_{Etc} \times (K_{CD(ax)} + K_{CD(rad)}) \times a_{Etc} \times \left(\frac{C_{core}}{S_{cd}} - C_{drug_{liquid}} \right) dt \quad \text{Equation 5.36}$$

where V_{Etc} is the volume of the matrix (taking into account the erosion of the polymer).

5.4.2.6 Simulated dissolution profiles from layered matrix compacts

5.4.2.6.1 Adipic acid as outer layer excipient

Dynochem simulations were performed for matrix compacts composed of a central matrix layer of ethylcellulose 10cP in the particle size range of 250-355 μm and theophylline monohydrate (with 5% PVP) in three weight fractions (500 mg),

surrounded by two layers of adipic acid (500 mg) dissolving into 0.01N HCl using the final Dynochem dissolution model. The parameters used to simulate dissolution from the central layer were those used in Table 5.17, while the parameters used to simulate the changes in the adipic acid layers are summarised Table 5.18.

Table 5.18 *Dynochem scenario sheet design parameters for adipic acid excipient layers to allow simulation of dissolution of theophylline monohydrate from matrix compacts consisting of theophylline monohydrate with ethylcellulose 10cP in the particle size range 250-355 μ m and 5% PVP with a layer of adipic acid (500mg) on each planar surface of the matrix. Thmh = theophylline monohydrate, Etc = Ethylcellulose 10cP, $S_{cd(excip)}$ = partition coefficient of the drug between the disperse phase and the continuous phase, $h_{init(layer\ 1)}$ = initial height of the lower acid excipient layer, $h_{init(layer\ 2)}$ = initial height of the upper acid excipient layer, ρ_{excip} = initial 'apparent' density of the acid excipient layers, $K_{CDax(excip)}$ = overall mass transfer coefficient of the excipient layers in the axial direction, $K_{CDrad(excip)}$ = overall mass transfer coefficient of the excipient layers in the radial direction.*

Thmh:Etc	$S_{cd(excip)}$	$h_{init(layer\ 1)}$	$h_{init(layer\ 2)}$	ρ_{excip} kg/m ³	$K_{CDax(excip)}$ (m/s x 10 ⁶)	$K_{CDrad(excip)}$ (m/s)
1:3	29.3	2.86	3.10	1260	8.89	15.7
1:1	29.3	3.02	2.79	1289	8.89	15.7
3:1	29.3	2.79	5.81	1286	8.89	15.7

The simulated dissolution profiles for drug release from matrix compacts consisting of theophylline monohydrate with ethylcellulose 10cP in the particle size range 250-355 μ m and 5% PVP with a layer of adipic acid (500mg) on each planar surface of the matrix, for three ratios of polymer to drug are shown in Figure 5.31.

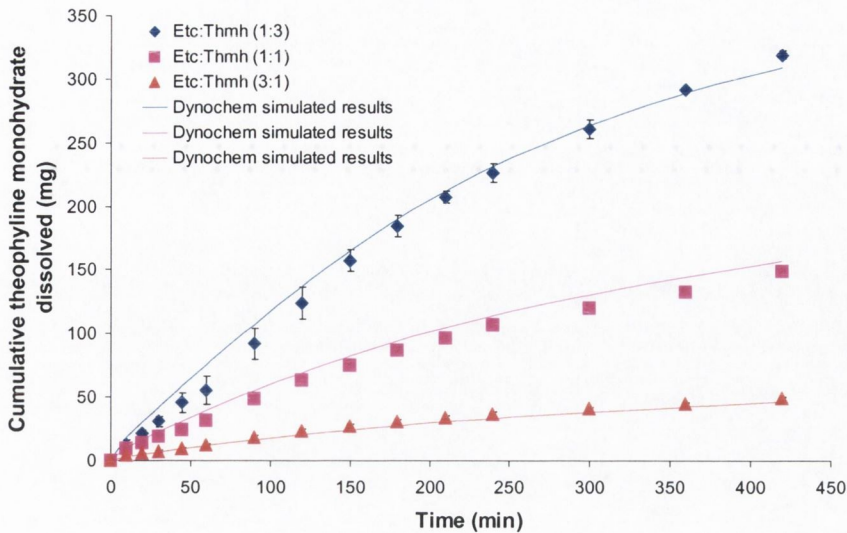


Figure 5.31 Dynochem generated SIMULATION of drug dissolution from compacts consisting of theophylline monohydrate with ethylcellulose 10cP in the particle size range 250-355 μm and 5% PVP with a layer of adipic acid (500mg) on each planar surface of the matrix, for three ratios of polymer to drug. Error bars indicate standard deviations (Etc = ethylcellulose 10cP, particle size range 250-355 μm ; Thmh = theophylline monohydrate). The continuous lines are simulations using D_{app} and E_{pol} for the matrix layer calculated from interpolations based on the best fit of dissolution data from the top planar surface only of matrix compacts and on the experimentally determined solubility and diffusion coefficients of theophylline monohydrate and adipic acid.

The general shapes of the predicted profiles in Figure 5.31 are very similar to the experimentally determined dissolution profiles. However, the sigmoidal inflection seen in the experimental data between 90 minutes and 120 minutes is not as sharply predicted by the simulated data. The reason for this observation is due to the method Dynochem uses to update the geometry of the drug-containing core. The mass of drug in the core is updated according to mass transfer rates, which in turn are related back to volumes via the initial core drug density. However, the geometry of the core layer is calculated assuming that the initial aspect ratio of the core layer is maintained during dissolution. An artefact of this assumption is that the model will predict that the thickness of the porous layer, δ_m , in the newly exposed axial area at the drug-excipient interface is of a greater magnitude than would be expected. Therefore the increase in dissolution rate seen experimentally during the dissolution of acid excipient layer is not as sharply predicted by the Dynochem model.

A slight positive deviation from the experimental dissolution profiles was obvious for the ratios of P:D of 1:3 and 1:1 at earlier time points.

5.4.2.6.2 Fumaric acid as outer layer excipient

Similarly, Dynochem simulations were performed for matrix compacts composed of a central matrix layer of ethylcellulose 10cP in the particle size range of 250-355 μm and theophylline monohydrate (with 5% PVP) in three weight fractions (500 mg), surrounded by two layers of fumaric acid (500 mg) dissolving into 0.01N HCl using the final Dynochem dissolution model. The parameters used to simulate dissolution from the central layer were those in Table 5.17, while the parameters used to simulate the changes in the adipic acid layers are summarised Table 5.19.

Table 5.19 *Dynochem scenario sheet design parameters for fumaric acid excipient layers to allow simulation of dissolution of theophylline monohydrate from matrix compacts consisting of theophylline monohydrate with ethylcellulose 10cP in the particle size range 250-355 μm and 5% PVP with a layer of fumaric acid (500mg) on each planar surface of the matrix. Thmh = theophylline monohydrate, Etc = Ethylcellulose 10cP, $S_{cd(\text{excip})}$ = partition coefficient of the drug between the disperse phase and the continuous phase, $h_{\text{init}(\text{layer } 1)}$ = initial height of the lower acid excipient layer, $h_{\text{init}(\text{layer } 2)}$ = initial height of the upper acid excipient layer, ρ_{excip} = initial 'apparent' density of the acid excipient layers, $k_{\text{ax}(\text{excip})}$ = overall mass transfer coefficient of the excipient layers in the axial direction, $k_{\text{rad}(\text{excip})}$ = overall mass transfer coefficient of the excipient layers in the radial direction.*

Thmh:Etc	$S_{cd(\text{excip})}$	$h_{\text{init}(\text{layer } 1)}$	$h_{\text{init}(\text{layer } 2)}$	ρ_{excip} kg/m ³	$K_{CD(\text{ax})\text{excip}}$ (m/s x 10 ⁶)	$K_{CD(\text{rad})\text{excip}}$ (m/s)
1:3	160.1	2.86	3.10	1264	12.5	22.1
1:1	200.8	2.15	2.60	1586	12.5	22.1
3:1	191.6	2.24	2.74	1512	12.5	22.1

The simulated dissolution profiles for drug release from matrix compacts consisting of theophylline monohydrate with ethylcellulose 10cP in the particle size range 250-355 μm and 5% PVP with a layer of fumaric acid (500mg) on each planar surface of the matrix, for three ratios of polymer to drug are shown in Figure 5.32.

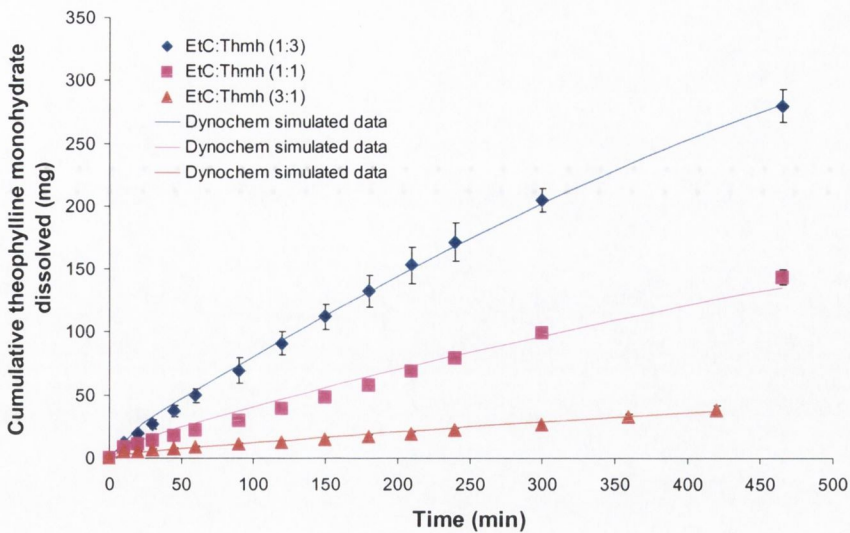


Figure 5.32 Dynochem generated SIMULATION of drug dissolution from compacts consisting of theophylline monohydrate with ethylcellulose 10cP in the particle size range 250-355 μm and 5% PVP with a layer of fumaric acid (500mg) on each planar surface of the matrix, for three ratios of polymer to drug. Error bars indicate standard deviations (Etc = ethylcellulose 10cP, particle size range 250-355 μm ; Thmh = theophylline monohydrate). The continuous lines are simulations using D_{app} and E_{pol} for the matrix layer calculated from interpolations based on the best fit of dissolution data from the top planar surface only of matrix compacts and on the experimentally determined solubility and diffusion coefficients of theophylline monohydrate and fumaric acid.

Again, the general shapes of the predicted profiles in Figure 5.32 are very similar to the experimentally determined dissolution profiles, the linearity of the experimental data being closely predicted by the simulated data for the three ratios of P:D.

5.5 CONCLUSIONS

The particle size of the polymer was shown to have a significant effect on the release rate of drug from both the single layer and multi-layered matrix compacts, with faster dissolution rates from the larger particle size fraction of polymer. As the concentration of polymer in the matrix was increased, there was a decrease in the resulting release rate of drug from the matrix for a large and small particle size fraction of polymer from both the single layer and multi-layered matrix compacts. Drug release kinetics from the uncoated matrix systems were Fickian in nature for the higher concentrations of polymer, with some deviation towards anomalous (non-Fickian) release for the lower concentrations of polymer.

The effect of the addition of layers of adipic acid to the matrix cores was to shift the release kinetics to a more sigmoidal shape, with increasing release rates at earlier times, due to the dissolution of the soluble adipic layers and exposure of new surface area of the matrix layer at the planar interface, and by decreasing release rates at later times, following complete dissolution of the adipic acid layers. The addition of the less soluble fumaric acid to the matrix cores was to shift the drug release kinetics to a more zero order type release profile, as the fumaric acid layers had a controlling effect on the surface area exposed of the matrix core until approximately 6 hours, after which time the fumaric acid had completely dissolved. The effect of the fumaric acid layers was evident in a shift of the exponent, n , from a fit of the data to the Peppas equation towards 1 indicating that drug release was approaching zero order, for all polymer concentrations studied.

Release from the top surface of matrix compacts allowed calculation of the percolation thresholds. The lower percolation threshold was calculated to be at 35% drug loading, while the upper percolation threshold was calculated to be between 50% and 60% drug loading.

A series of models were developed to eventually simulate drug dissolution from layered matrix compacts. This involved a progressive application of the program to model drug dissolution from single surface matrix compacts, from the complete surface of matrix compacts, and finally from matrix compacts between soluble acid excipient layers. The calculations involved modelling the diffusion of the drug through the developing porous region of the matrix, which grows at the expense of the drug/polymer region as the drug diffuses out through the system. The thickness of this moving boundary region was modelled according to the rate of drug diffusion, which was initially determined by fitting the data from a single surface to the moving boundary model to determine the magnitude of the apparent diffusion coefficient for each percolation experiment. The percolation data was well matched by the modelled data for drug concentrations between 30% and 50%, based on a diffusion only model. Good fit to data was obtained for systems above the upper percolation by developing a model to account for the speculated erosion of the polymer.

The model was expanded to simulate dissolution from the complete surface of inert matrix compacts, using the apparent diffusion coefficients of drug through the matrix and polymer erosion (for systems above the percolation thresholds) that were obtained from the best fit to the single surface data.

The final amalgamated model for drug dissolution from the complete surface of a matrix compact with the effect of the addition of layers of soluble acid excipient onto the matrix core produced simulated dissolution profiles, which agreed well with the experimental data for a series of polymer concentrations in the matrix core and for acid excipient layers of relative low and high solubilities.

6.1 INTRODUCTION

Drug release rate from conventional dosage forms generally declines with time. This is caused by a decrease in surface area and/or increase in diffusional pathway of the drug over time. This work focused on the possibility of controlling the surface area changes of a drug layer positioned between two layers of soluble acid excipient, to achieve controlled release of drug.

While triple layered matrix compacts have been previously described (Deasy et al., 1993; Conte et al., 1993, 1994a, 1994b; Yang and Fassihi, 1997b; Conte and Maggi 1998; Chidambaram et al., 1998), initial investigations of the current work examined dissolution from less complex layered systems consisting of drug and soluble excipient layers (the drug and excipient forming single component layers), to investigate the possibility of controlling the surface area of the drug layer exposed with time and to determine the effect of changing surface area, over time, on dissolution. In an effort to adequately model drug dissolution from such systems, dissolution rates were examined from individual surfaces of single component compacts in the paddle dissolution apparatus. It became apparent that uniform hydrodynamics were not present on the various surfaces of the compacts, thus complicating the modelling of drug dissolution. This observation prompted further evaluation of the hydrodynamics in the paddle dissolution apparatus. A virtual computational fluid dynamics (CFD) model of the apparatus was built up, which was initially validated against published laser Doppler velocimetry measurements in the apparatus (Bocanegra et al., 1990). Further evaluation of the CFD model allowed mass transfer prediction from single component compacts, based on physico-chemical and hydrodynamic principles.

Subsequent studies focussed on dissolution from multi-layered drug delivery systems, on the inclusion of a drug-containing inert non-swellable matrix layer and on the development of a simulation model to predict drug dissolution from such systems, based on intrinsic properties of the drug and excipient layers, the geometry of the system and on the dissolution behaviour from the individual surfaces.

Chapter 6

General Discussion

6.2 HYDRODYNAMICS AND DISSOLUTION FROM SINGLE COMPONENT COMPACTS

While the paddle dissolution apparatus is the most widely used dissolution method, despite its simple design, its hydrodynamics are complex and not well understood (Bocanegra, 1988). A number of reports in the literature have suggested that there is considerable variability, unpredictability and randomness in dissolution profiles using the USP paddle dissolution apparatus, even for dissolution apparatus calibrator tablets (Cox et al., 1983; Gray and Hubert, 1994; Achanta et al., 1995; McCormick, 1995, Qureshi and McGilveray, 1995; Qureshi and McGilveray, 1999). Dissolution of most drugs is diffusion controlled (Carstensen, 1972) and, consequently, the mass transfer of such drugs in a stirred vessel is dependant on fluid flow, i.e. forced convection (Grijseels, 1981). Alterations in hydrodynamics in the USP paddle dissolution apparatus, may therefore significantly affect drug dissolution and the dissolution rates may change depending on the location of the dissolving substance in the dissolution vessel.

6.2.1 *Dissolution rates from different surfaces/ positions of compacts*

The initial objective of the present work was to experimentally estimate the apparent diffusion boundary layer thickness and dissolution rate constant (parameters reflective of the hydrodynamics of the systems) for single component compacts, at different surfaces and positions in the paddle dissolution apparatus. Initial studies involving dissolution from the complete surface of compacts revealed that uniform hydrodynamic conditions were not present on all parts of the curved surface. To facilitate modelling using more uniform hydrodynamic conditions, compacts were raised above the region where a groove had been previously observed, using a moulded portion of 3 mm high paraffin wax. Studies on drug release from the curved surface of various compacts revealed that highest release per unit surface area occurred with compacts of height 1.5 mm, sitting at the base of the vessel. There was a statistically higher dissolution rate from various surfaces of compacts of height 8.5 mm, which were situated at the base of the vessel compared with similar compacts raised up by 3 mm from the base of the vessel. It was postulated that turbulent flow caused by a change in fluid velocity from an inward radial velocity to an axial velocity component at the base of the vessel was responsible for the increased

dissolution rate from compacts situated within this region. This effect was also obvious from compacts of 1.5 mm height releasing from the top surface when located within 3 mm of the base of the vessel compared to compacts releasing from the top surface above this region.

6.2.2 Hydrodynamics in the paddle dissolution apparatus at 50 rpm

While the calculation of apparent diffusion layer thickness provided insight into the fluid dynamics on the surface of a drug compact, it was desirable to relate these findings to actual measurements of bulk fluid dynamics in the vessel, in an effort to determine if variable hydrodynamics in the apparatus were responsible for the differences in dissolution fluxes from the various surfaces. Experimental measurements of fluid velocities in the USP paddle dissolution apparatus have been previously undertaken (Bocanegra et al., 1990; Diebold, 2000), however laser Doppler measurements have led to results for single points in space only. Bulk fluid flow between these points has been speculated based on the results obtained. The application of CFD to determine the hydrodynamics throughout the vessel of the USP paddle dissolution apparatus provides a novel approach to examine this problem. A CFD approach has been previously applied to examine fluid flow in the vessel, providing results which were in reasonable qualitative agreement with experimentally determined laser velocimetry results. However, the CFD results were consistently quantitatively lower than the measured velocities (Kosiol, 2000). A re-examination of the approach by Kosiol in the present work revealed that, apart from a large quantitative discrepancy, the approach was at its limit of refinement, making it impossible to generate results at higher than 50 rpm. A good correlation between experimental and computational fluid velocities in the apparatus was necessary as a validation of the computational method. A newer approach was undertaken with a more rigorous treatment of the pre-processor to produce a structured grid of the wireframe of the USP paddle apparatus. Subsequent alteration of the post-processor set-up led to CFD-predicted results, which were in close agreement, both qualitatively and quantitatively, with all published laser velocimetry measurements in the USP vessel at 50 rpm (Bocanegra et al., 1990). A comparison between the laser Doppler fluid velocity measurements and the CFD generated velocities, for each component of the velocity (axial, tangential and radial) at three different planes in the vessel is presented in Figure 6.1, Figure 6.2 and Figure 6.3. Error bars in the laser Doppler

data were obtained by personal communication (Bocanegra, 2002), as previously published data did not include an indication of the experimental error (Bocanegra et al, 1990).

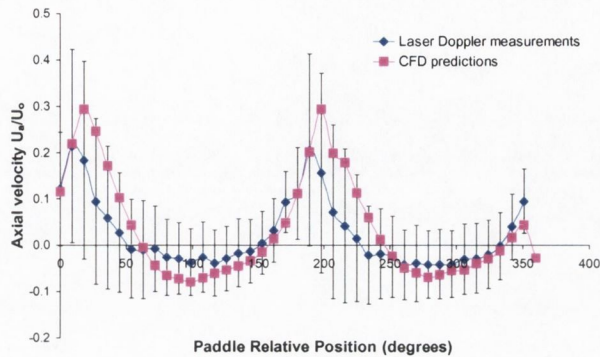


Figure 6.1 Comparison between laser Doppler fluid flow measurements and CFD predictions of *axial* velocities on a plane at $Z=-0.066$ for a radius $R=0.762$ (as per Bocanegra et al., 1990). Error bars are the standard deviations of the laser Doppler measurements (Bocanegra, 2002).

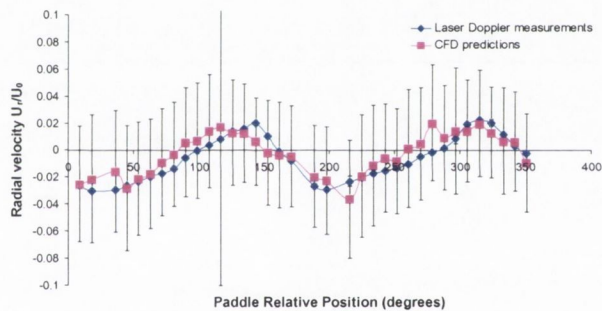


Figure 6.2 Comparison between laser Doppler fluid flow measurements and CFD predictions of *radial* velocities on a plane at $Z=-0.461$ for a radius $R=0.427$ (as per Bocanegra et al., 1990). Error bars are the standard deviations of the laser Doppler measurements (Bocanegra, 2002).

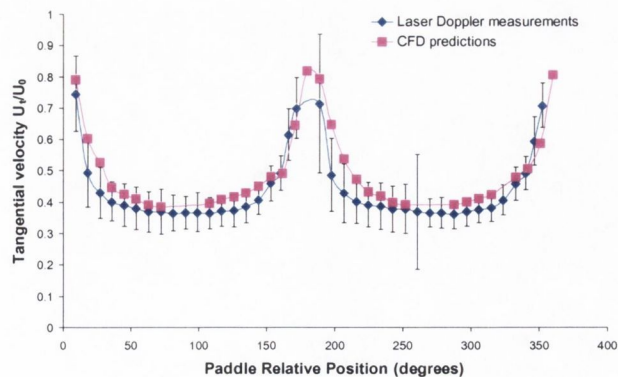


Figure 6.3 Comparison between laser Doppler fluid flow measurements and CFD predictions of *tangential* velocities on a plane at $Z=-0.197$ for a radius $R=0.594$ (as per Bocanegra et al., 1990). Error bars are the standard deviations of the laser Doppler measurements (Bocanegra, 2002).

Therefore, all CFD generated fluid velocities were in close agreement with the laser Doppler measurements. A linear regression analysis of laser Doppler measurements versus CFD predicted velocities (at the same paddle relative position) for the above three data sets yielded correlation coefficients of 0.77, 0.76 and 0.93 respectively. More importantly, all CFD predicted velocities were within the quantitative region defined by \pm one standard deviation of the laser Doppler experimental data. This close correlation between the two data sets has therefore validated that CFD can be applied to accurately predict hydrodynamics in the paddle dissolution apparatus.

Analysis of the behaviour of the fluid on vertical mid-planes through the vessel provided further insight into the flow behaviours that lead to fluid re-circulation throughout the vessel. These secondary flow patterns were in agreement with those previously speculated (Bocanegra et al., 1990; Beckett et al., 1996). The most predominant component of velocity throughout the vessel was the tangential component, although the axial and radial components were quite high in the region of the paddle impeller. Velocity vectors at 90° to the paddle impeller revealed a region of high eddy flow at the same horizontal level as the paddle tip, which was initially speculated to be a hindrance to mixing between the two regions. Examination of fluid flow behaviour below the level of the paddle revealed a region with a high inward radial velocity component, immediately inside the wall of the hemispherical base, from a region below the impeller to a region near the base of the hemisphere. However, centrally, at the very base of the hemisphere, a region of low fluid velocity magnitude was evident. Directly outside this region, the magnitude of fluid velocity was considerably higher (three to four times change in velocity over a distance of approximately 8-10 mm). In fact, the fluid at the very base of the vessel has negligible fluid velocity towards the centre of the base for a region of diameter approximately 10-15 mm. This region extended upwards towards the bottom of the paddle.

It is conceivable that drug delivery systems, which are mobile during the dissolution test (e.g. solid particulate systems or disintegration of solid delivery systems) could repeatedly move between these regions of low and high fluid velocities and could

therefore be a contributable factor to the variable dissolution results previously reported (Qureshi et al., 1995; Qureshi et al., 1999, Achanta et al., 1995).

Path-lines of fluid mixing were examined from this central region at the base of the vessel for the duration of 1 minute at 50 rpm. After approximately 5 seconds, the resulting initial axial path-lines converged with the fluid in the region swept out by the paddle and subsequent fluid flow was predominantly tangential in nature, with some axial and radial flow, which facilitated the ultimate mixing throughout the vessel. Although it had appeared that fluid behaviour at the level of the paddle resulted in two regions of mixing, the path-lines did not reveal a region of poor mixing between the upper cylindrical and lower hemi-spherical volumes.

6.2.3 Effect of different paddle rotation speeds

Other impeller speeds of 25, 100 and 150 rpm were also studied and their effect on the resulting hydrodynamics in the vessel examined. Axial and tangential velocities were compared at the various rpm for two different locations in the vessel. The maximum velocity magnitude for each position at different rpm was seen to increase linearly with respect to paddle rpm. Therefore, the model predicted laminar flow in the vessel for paddle rotation speeds of up to 150 rpm, consistent with laser Doppler measurements carried out at various rpm in the vessel (Diebold et al., 2001).

The effect of paddle rotation speed on the time required to achieve complete mixing in the vessel was examined by tracking the path-lines of massless particles with time. Considerable differences in the resulting flow patterns at 5 seconds were observed, for paddle rotations speeds between 25 and 150 rpm. Although complete mixing was achievable for each paddle rotation speed examined, the approximate time required to achieve complete mixing varied between 2-5 seconds at 150 rpm, to 40-60 seconds at 25 rpm.

6.2.4 Effect of the addition of a cylindrical compact

The effect of the addition of a compact at the base of the vessel was then simulated, in an effort to gain further insight into the reasons for the varied experimental

dissolution rates, which had been observed from the various surfaces and location of the compact. The presence of the compact complicated the fluid flow at the base of the vessel. A region of high fluid shear was noticeable towards the base of the compact. It appeared that the positioning of the experimental compacts on a wax pedestal of 3mm height would have the desired effect of raising the compacts above this region of complicated fluid flow.

A strict mathematical examination of the evolution of hydrodynamic boundary layers outside the surfaces of the compact, necessary for an approach to mass transfer, called for the definition of a region of very high grid refinement in an 'envelope' volume immediately outside the surface of the compact, to allow the development of highly refined boundary layers in this region. Examination of the resulting fluid velocity vectors in the envelope volume region displayed the definition of a region of increasing velocity extending from the surface into the bulk fluid flow (hydrodynamic boundary layer). A more rigorous treatment of the resulting velocities above the top surface revealed that the fluid in this region was undergoing solid body rotation with a gradually increasing tangential velocity (constant angular velocity) from the surface into the bulk, a feature which had been previously speculated by laser Doppler velocimetry results (Bocanegra et al., 1990). Bulk fluid flow was attained after approximately 1 mm., which was taken to be the magnitude of the hydrodynamic boundary layer in this region. An examination of fluid flow behaviour outside the curved surface revealed that the fluid flow in this region was more complex than fluid flow above the upper surface. The parabolic rotational velocity boundary layer outside the curved surface extended for approximately 1.25 mm, while the dimension of the axial velocity boundary layer outside this surface was also approximately 1.25 mm. Closer examination of the velocity boundary layers outside the curved surface of the compact revealed that there were large peaks in the shear rates for a region within approximately 3 mm from the base of the compact, consistent with the grooving effect, which had been previously seen on the surface of compacts following dissolution.

6.2.5 Mass transfer predictions from a single component compact

A mass transfer prediction was made from the top planar surface of the compact using an empirical relationship derived by Khoury et al. (1988) for a stationary disc in a fluid undergoing 'solid-body rotation'. Fluid above the compact was shown to undergo solid-body rotation. The dissolution rate predicted from the CFD generated angular velocities above the top planar surface of the compact was in close agreement with the corresponding experimentally determined result (CFD predicted dissolution rate was 10% higher than the experimentally measured rate).

A semi analytical solution of the diffusion convection equation based on fluid shear rates in the concentration boundary layer, applied to a cylindrical geometry, was developed to predict mass transfer rates from the curved surface of a compact sitting at the base of the vessel. This approach was based on the examination of fluid shear rates in the axial direction in the diffusion boundary layer immediately outside the curved surface. The predicted mass transfer rate using this equation was 25% higher than the experimentally calculated dissolution rate. The deviation was explained in terms of the shortcomings of the assumptions of the model. Firstly, the model assumed that fluid flow was parallel to the surface only, which was shown to be not valid in the present case and secondly, the assumption that the cylinder was infinitely long was not valid for the cylindrical compacts studied.

6.3 SIMPLE LAYERED DRUG COMPACTS

This section of work examined the possibility of controlling the surface area changes during dissolution of drug from a layered drug/soluble-excipient system, to achieve a zero order type release profile.

The concept of a drug delivery systems consisting of more than one layer has been examined by previous investigators (Deasy et al., 1993; Conte et al., 1993, 1994a, 1994b; Yang and Fassihi, 1997a; Conte and Maggi, 1998). Most systems examined have involved the application, during tableting, of compressed barrier layers on one or both planar surfaces of a hydrophilic matrix containing the active ingredient. Linear (zero order) and quasi linear release kinetics have been achieved from such systems through various geometrical and compositional modifications of the layered

monolithic matrices. Little attention has been focused on the development of models to predict drug release from such systems, nor has there been an attempt to control dissolution rate from the central drug layer via a control of the change in its surface area available during dissolution.

According to the equation of Nernst and Brunner, 1904 (Equation 1.4), drug dissolution is directly proportional to the surface area of drug available for dissolution. Therefore, a zero-order type release profile is predicted, should the surface area of drug remain constant, for a simple one component system, dissolving by convective diffusion. The initial feasibility studies in attempting to control the drug surface area during dissolution involved dissolution from simple cylindrical compacts of drug and soluble excipient, the drug and excipient comprising single component layers. If the excipient dissolved at a faster rate than the drug, this would result in an increase in the planar surface area of the drug exposed to the dissolution medium, at what was the original drug-excipient layer interface. It should be theoretically possible to compensate for the decreasing release rate of drug from the central layer, with the increase in surface area exposed in the axial direction. In the present work, it was desirable to develop a model to predict the effect of such factors as physicochemical properties of the drug and excipient layers and the geometry of the system on the resulting dissolution kinetics from the simple layered systems.

Initial feasibility studies involving a benzoic acid/ salicylic acid three layered system dissolving in 0.01N HCl, showed that zero order release was possible, at least for a certain period of time. Sigmoidal shaped release profiles were seen when theophylline monohydrate was used as the model drug, between two layers of soluble acid excipient, dissolving in 0.01N HCl. Faster dissolution rates at early times were seen when succinic acid was used as the acid excipient, compared to adipic acid.

6.3.1 Initial modelling of dissolution from simple multi-layered compacts

A mathematical model was derived to predict the release rate over time based on the physicochemical and geometrical properties of the drug and excipient layers, dissolution rates being calculated from the rate of change of the diameters in each layer and the subsequent change in exposed surface area available for dissolution.

The model involves the calculation of the rate of decrease of the diameter of the layers over time. Two methods were proposed to measure this rate; one based on direct experimental measurement of dissolution of the relevant component, while the second was derived from intrinsic properties of the drug or excipients. Both methods involved the use of the apparent diffusion boundary layer values for the complete surface calculated from earlier studies on single layer compacts in the dissolution apparatus. The resulting predicted release profiles resembled the actual release profiles in shape, for both methods. There was close agreement between the two methods for most systems. Better fit to actual data was seen at earlier time points. Possible reasons for this positive deviation involved the shortcomings of the simple model to completely predict the surface area and geometrical changes of the drug layer with time. Firstly, the model did not account for a change in the thickness of the drug layer over time (even when the excipient had completely dissolved), thus the overall calculated area of drug available for dissolution was higher than the actual area, leading to increased predicted release rates. Secondly, the release rates were calculated using an overall diffusion boundary layer thickness, although previous studies had shown that minor location changes of compacts could lead to large differences in the calculated hydrodynamic boundary layer. It is possible that geometrical changes of these simple layered drug delivery systems during dissolution can lead to changes with time in the apparent diffusion boundary thickness outside the various surfaces of the drug layer.

6.3.2 *Dynochem modelling of dissolution from simple layered DDS*

A second method to more accurately predict drug dissolution from these systems involved the application of a dynamic chemical engineering simulation package, Dynochem. Application of the program involved the use of geometrical and mass transfer equations, based on assumptions of geometrical uniformity during the dissolution process, and using the hydrodynamic calculations from individual surfaces from the earlier single layer studies. The program provided a tool for examining the effect of various parameters, including altering the geometry of the system or the solubility of the excipient layers, on the surface area changes with time of individual layers. Thus, the model ultimately allowed predictions of dissolution rates from such layered systems, based on the intrinsic properties of the individual components. The

resulting predicted dissolution profiles resembled the experimental data, both quantitatively and qualitatively for most systems studied.

A comparison of the models to predict mass transfer from such simple layered DDS is shown in Figure 6.4 for a system containing theophylline monohydrate between two layers of adipic acid, dissolving into 0.01N HCl.

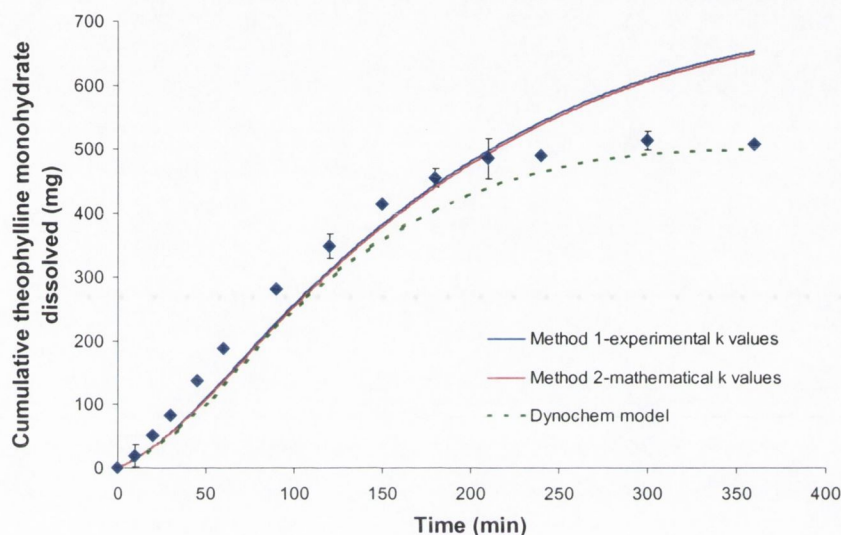


Figure 6.4 Comparison of modelling methods for drug release from a simple layered drug delivery system consisting of theophylline monohydrate between two layers of adipic acid, dissolving in 0.01N HCl (500 mg in each layer).

Although all methods predicted similar release rates at earlier times, the initial simple modelling methods (methods 1 and 2) over-predicted the drug release for later times. The mass transfer in the Dynochem model accounts for dissolution from all exposed faces and ultimately, the geometrical changes with time are based on the mass remaining in the layer and its initial density. The mass transfer calculations in the Dynochem model were also calculated individually for the axial and radial directions based on the apparent diffusion layer thickness results previously calculated for the axial and radial surfaces of compacts of similar dimensions. Correspondingly, the shortcomings of the initial simple modelling methods have been improved upon by the Dynochem model, which produced dissolution profiles that closely matched the experimental profiles, both qualitatively and quantitatively. The application of the model in predicting drug dissolution from the simple layered drug compacts, depended on the assumptions of the persistence of cylindrical geometry during the

dissolution process. Although such an assumption may not be physically true for the full time scale of the dissolution process, the application of the assumption to the model provided modelled dissolution profiles, which matched the shape of experimentally determined dissolution profiles quite well.

As drug release from these systems is fundamentally controlled by simple dissolution from the various surfaces, slight changes in the apparent diffusion boundary layer thickness should impact significantly on the mass transfer rates. It is possible that such changes occur during dissolution from such systems, as the geometry of the systems changes markedly during dissolution, thus complicating the modelling process.

6.4 LAYERED MATRIX COMPACTS

The concept of controlling the surface area exposed for dissolution was then applied to the case of a central cylindrical drug containing inert non-swellable matrix core. It was hoped that such an application could slow the release rate of drug to rates lower than was seen in the simple layered systems, and to possibly shift the shape of drug release profiles from a sigmoidal to a more zero-order dissolution rate. It was thought that the increase in the surface area of the matrix layer in the axial direction, caused by the dissolution of the soluble acid excipient layers with time, could compensate for the increase in the diffusional path-length in the matrix layer with time.

Initial feasibility studies focused on the utilisation of a fine particle size grade of ethylcellulose (10FP) using an uncontrolled particle size fraction of the polymer. The initial studies focused on drug release from a matrix core, examining the effect of varying the polymeric concentration in the drug-polymer core and the effect of the addition of fumaric acid to the planar surfaces of the core. The polymer concentration had a significant effect on drug release and the addition of the soluble acid excipient layers had the desired effect of shifting the kinetics of drug release to a more zero order release profile. However, the total amount of drug released after 7 hours was in the region of only 20%. It was speculated that the low particle size polymer component, coupled with its uncontrolled particle size, led to a porous network of insoluble polymer, which was of very low permeability to the dissolution medium. It

was postulated that the development of a porous network of sufficient permeability for the dissolution medium and the dissolved drug was hindered by the presence of polymer material of very low particle sizes. In an effort to allow drug release of a sufficient rate from the matrix core, later experiments focused on controlling the polymer particle size, using the more commonly used ethylcellulose grade, 10cP Std.

With the aim of monitoring the factors controlling the drug release rate and kinetics from the layered matrix systems, a series of experiments were performed, varying the polymer particle size range, the solubility of the acid excipient layers, and the concentration of polymer in the drug-matrix core. To determine the effect of the acid excipient layers on drug release, the experiments were also carried out as matrix compacts only, without the acid excipient layers.

The particle size of the polymer was shown to have a significant effect on the release rate of drug from the uncoated matrix compacts. This observation was in agreement with previous studies and was attributed to the increased penetration of water into the matrices when coarser particle size fractions of polymer were used (Ford et al., 1996). Traditional modelling from such systems would ascribe this behaviour to the decrease in tortuosity exhibited by the matrix formed by the larger size fraction of polymer (Potter et al., 1990).

As the concentration of polymer in the matrix was increased, there was a decrease in the resulting release rate of drug from the matrix for both particle size fractions of polymer examined. This was attributed to a decrease in porosity and increase in tortuosity of the matrix systems containing increasing amounts of polymer (Dabbagh et al., 1996).

Drug release kinetics from the uncoated matrix systems were Fickian in nature for the higher concentrations of polymer, with some deviation towards anomalous (non-Fickian) release for the lower concentrations of polymer. It was postulated that this effect was due to erosion of the polymeric component of the matrix at the lower concentrations of polymer examined.

6.4.1 Effect of outer layer solubility

The effect of the addition of layers of adipic acid to the planar surfaces of matrix cores was to shift the release kinetics to a more sigmoidal shape, with increasing release rates at earlier times, due to the dissolution of the soluble adipic layers and exposure of new surface area of the matrix layer at the planar interface, and decreasing release rates at later times, following complete dissolution of the adipic acid layers. The effect of the addition of the less soluble fumaric acid to the matrix cores was to shift the drug release kinetics to a more zero order type release profile, as the fumaric acid layers had a controlling effect on the surface area exposed of the matrix core until approximately 6 hours, after which time the fumaric acid had completely dissolved. The effect of the fumaric acid layers was evident in a shift of the exponent, n , from a fit of the data to the equation of Peppas, towards 1, indicating that the drug release was approaching zero order, for all polymer concentrations studied.

A comparison of the effect of the inclusion of such layers on the central matrix layer, and of the effect of the solubility of these layers on the resulting dissolution profile is shown in Figure 6.5 for the 'large' polymer particle size fraction, while the effect on the 'small' polymer particle size fraction is shown in Figure 6.6, for one concentration level of polymer in both cases.

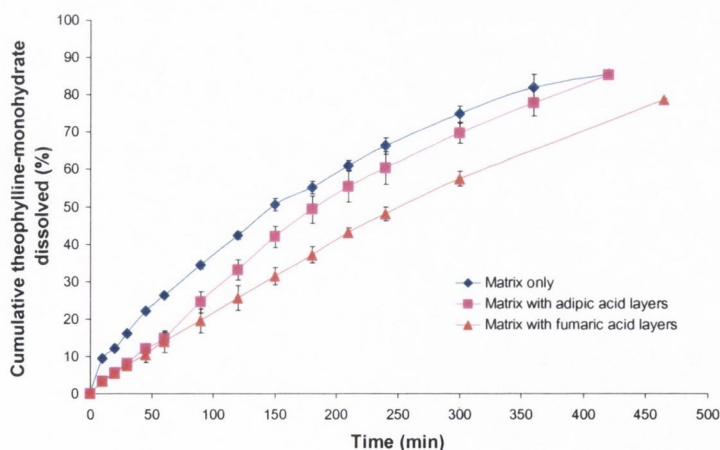


Figure 6.5 Dissolution profiles of theophylline monohydrate from matrix compacts containing theophylline monohydrate (Thmh): ethylcellulose (EtC) in the particle size range 250-355 μm in the ratio EtC: Thmh 1:3, showing the effect of the addition of layers of soluble acid excipient (500 mg) on each planar surface of the matrix (adipic acid or fumaric acid). Error bars indicate standard deviation.

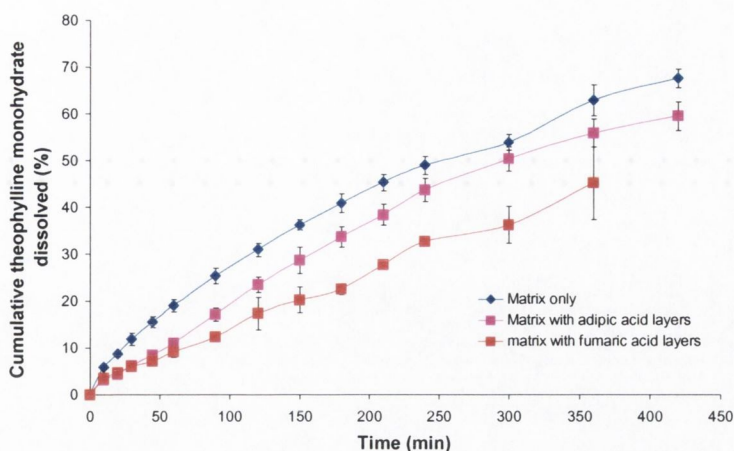


Figure 6.6 Dissolution profiles of theophylline monohydrate from matrix compacts containing theophylline monohydrate (Thmh): ethylcellulose (EtC) in the particle size range 106-180 μm in the ratio EtC: Thmh 1:3, showing the effect of the addition of layers of soluble acid excipient (500 mg) on each planar surface of the matrix (adipic acid or fumaric acid). Error bars indicate standard deviation.

The effect of the inclusion of the soluble acid excipient layers on the central matrix layer was similar for both the 'small' and 'large' polymer particle size fractions. The dissolution profiles for the adipic acid layers were sigmoidal in shape with increasing dissolution rates at earlier times, until approximately 2 hours (when the adipic acid layers had completely dissolved), and followed by decreasing dissolution rates after this time. After 6 hours, the total amount of drug released was only marginally lower than that of the uncoated matrix layer. The dissolution profiles from the systems containing fumaric acid were characterised by a more linear release profile, with dissolution rates remaining practically constant for the first five to six hours, after which time the fumaric acid had completely dissolved (explained earlier). Similar characteristics were observed for the other concentrations of polymer in the matrix layers.

6.4.2 Effect of particle size of polymer

A comparison of the effect of the particle size and fraction of polymer on the dissolution profiles from the three ratios of ethylcellulose:theophylline monohydrate from layered systems containing adipic acid in the outer layers is shown in Figure 6.7.

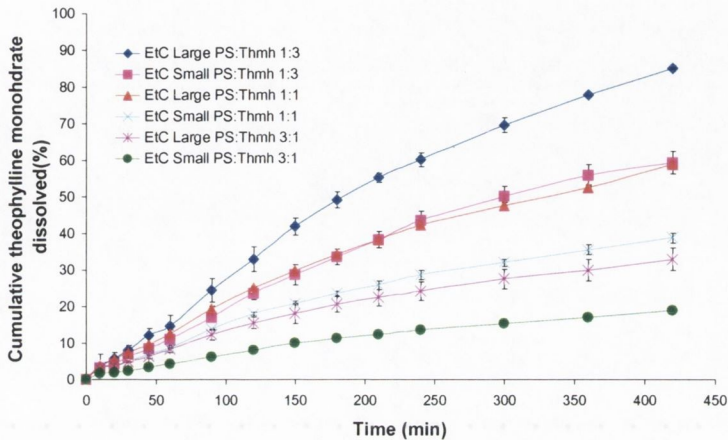


Figure 6.7 Dissolution profiles of theophylline monohydrate from layered matrix compacts containing a central matrix of ethylcellulose: theophylline monohydrate in three ratios of polymer: drug (500mg), between two layers (500 mg) of adipic acid. (EtC = Ethylcellulose 10cP, Thmh = theophylline monohydrate, Large PS = 250-355 μm , Small PS = 106-180 μm). Error bars indicate standard deviation.

A sigmoidal type release profile was shown by each system in Figure 6.7. Similar to the uncoated matrix compacts, increased dissolution rates were seen for the larger particle size fractions compared to the lower particle size fractions of polymer, for all concentrations of polymer examined. A similar comparison of the effect of the particle size fraction on the dissolution profiles from the three ratios of ethylcellulose: theophylline monohydrate from layered systems containing fumaric acid in the outer layers is shown in Figure 6.8.

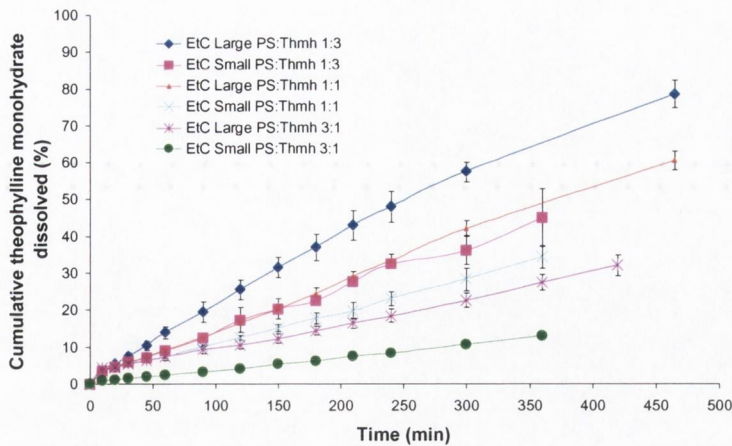


Figure 6.8 Dissolution profiles of theophylline monohydrate from layered matrix compacts containing a central matrix of ethylcellulose:theophylline monohydrate in three ratios of polymer: drug (500mg), between two layers (500 mg) of fumaric acid. (EtC = Ethylcellulose 10cP, Thmh = theophylline monohydrate, Large PS = 250-355 μm , Small PS = 106-180 μm). Error bars indicate standard deviation.

A more linear type release profile was observed for all layered systems containing fumaric acid in the outer layers, compared to the layered systems containing adipic acid in the outer layers. Again, release rates were higher from the large particle size fraction of polymer for all ratios of polymer:drug. This was caused by the decreased tortuosity in the systems containing the large particle size fraction of the polymer in both the single layer and multi-layered compacts.

6.4.3 Percolation studies

A series of percolation studies were performed to determine the percolation thresholds of the polymeric material and theophylline monohydrate in matrix compacts consisting of the large particle size fraction of the polymer. Such experiments involved quantifying drug release per unit surface area from the circular upper face of matrix compacts containing theophylline monohydrate from 30% to 80% with ethylcellulose 10cP, the matrix having been made impervious to drug release from all other parts of the surface. Determination of the upper percolation threshold, i.e. the fraction of drug in the matrix, above which point the polymer will exist as isolated pockets of polymer, involved examination of deviations of release kinetics from pure Fickian release. An examination of the residuals of a fit of the data to simple Fickian release revealed that the upper percolation threshold was in the region between 50% and 60% theophylline monohydrate. This low value of p_{c2} can be explained by the

correlated percolation model as previously described by Caraballo (1996), where the very large difference between particle size of the polymer and drug substance requires a large volume of the polymer material to allow its complete percolation through the matrix. Determination of the lower percolation threshold, p_{cl} , i.e. the fraction of drug at which point the drug completely spans the volume as an interconnected network, below which the drug will exist as isolated pockets of drug, involved the application of the method of Bonny and Leuenberger (1991). The method involved the calculation of b , i.e. calculation of the slope of the release rate per surface area versus $t^{1/2}$ and the subsequent calculation of the tablet property, β , as described by Bonny and Leuenberger (1991). A plot of β versus the matrix porosity, ε , allowed the determination of the lower percolation threshold, as the porosity at which the asymptote of the plot of β versus ε crosses the X-axis. Application of this method determined the lower percolation for these systems to be 0.326, corresponding to a theophylline monohydrate concentration of 35%. The percolation study revealed that the lower fraction of drug examined in the present work was below the level of the lower percolation threshold. However, the ratio of polymer to drug (1:1) was in the region of the upper percolation threshold (all systems also containing 5% PVP). The lowest ratio of polymer to drug examined (1:3) was above the upper percolation threshold, thus explaining the observed erosion of the polymeric material during dissolution and the deviation from Fickian release behaviour, as the polymeric material was unable to percolate completely to maintain the matrix structure during the dissolution process.

6.4.4 Simulation of dissolution from layered matrix compacts

The Dynochem simulation program was then utilised to attempt to model drug dissolution from the more complicated drug delivery systems consisting of a drug-matrix cylindrical core between two layers of soluble acid excipient. The utilisation of the program to ultimately model drug dissolution from the layered matrix systems involved a progressive application of the program to model drug dissolution, from single surface matrix compacts, from the complete surface of matrix compacts, and finally from matrix compacts between soluble acid excipient layers. The definition of equations of geometry and mass transfer in the process scheme for drug dissolution from the top surface of single layered matrix compacts involved modelling the

diffusion of the drug through the developing leached porous region of the matrix, which grows at the expense of the drug/ polymer region as the drug diffuses out through the system. The thickness of this moving boundary region was modelled according to the rate of drug diffusion, which was initially determined by fitting the data to the moving boundary model to determine the magnitude of the apparent diffusion coefficient for each percolation experiment.

Using this approach, the percolation data was well matched by the modelled data for drug concentrations between 30% and 50%. Above this level there was some deviation between the model and the experimental data, which was also evident by a deviation from linearity in a plot of the fitted apparent diffusion coefficient versus porosity. It was speculated that above this level, the drug was present at levels above the upper percolation threshold, preventing the polymeric material from percolating the matrix and resulting in the polymer 'eroding' from the surface of the matrix over time. To apply this theory to the current moving boundary model (above 50% drug), the polymer was allowed to 'erode' at a certain rate per time per unit surface area of the matrix exposed.

The data above the percolation threshold was then modelled according to the modified moving boundary model, the erosion of polymer from the outside of the medium-filled porous polymer region and the apparent diffusivity of the drug through the region being calculated from best fits to the data. The resulting model yielded a good fit to the data for all dissolution points for drug levels of higher than 50% theophylline monohydrate. The resulting apparent diffusivities for all levels of drug investigated and the apparent erosion rate of polymer for greater than 50% drug were fit to a linear regression plot and a polynomial plot respectively.

Alteration of the geometrical and mass-transfer calculations of the process sheet allowed the model to be applied to simulate dissolution from the complete surface of uncoated matrix compacts. In this case, dissolution profiles were simulated from the values of the apparent diffusivity of the drug and erosion rate of polymer (above the percolation threshold). The resulting simulated dissolution profiles were in close agreement with the experimental data for both polymer levels at exactly the same concentration as previously studied and also for other polymer levels, the resulting

apparent drug diffusivity and polymer erosion rates in this case being determined by interpolation from the single surface fits.

The final application of Dynochem was to amalgamate the model for drug dissolution from the complete surface of a matrix compact with the effect of the addition of layers of soluble acid excipient onto the matrix core. The final layered matrix model produced simulated dissolution profiles, which agreed well with the experimental data for a series of polymer concentrations in the matrix core and for acid excipient layers of relatively low and high solubilities. Simulated dissolution and experimentally determined dissolution profiles from an uncoated matrix of ethylcellulose 10cP:theophylline monohydrate 1:1 and from the corresponding layered matrix compacts with adipic acid and fumaric acid in the outer layers, dissolving into 0.01N HCl are shown in Figure 6.9.

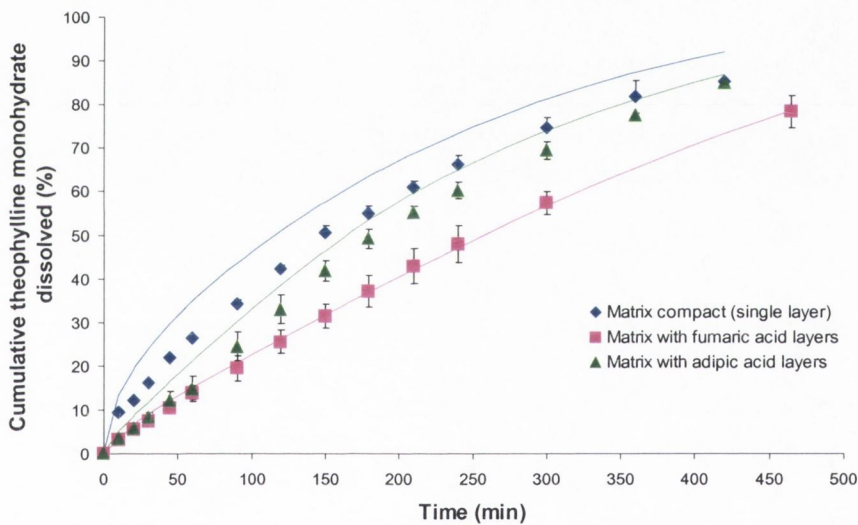


Figure 6.9 Dynochem generated simulations (continuous lines) of dissolution from a matrix compact containing theophylline monohydrate (Thmh): ethylcellulose (EtC) in the particle size range 250-355 μm in the ratio EtC:Thmh 1:3 and for the corresponding layered matrix compacts with adipic acid and fumaric acid.

Although predicted release from the uncoated matrix was slightly higher than experimental in Figure 6.9, predicted release from other drug loadings closely matched the experimental data. The completed model provided a set-up, which could predict drug dissolution from complex layered matrix systems, based on intrinsic properties of the drug layer, the acid excipient layers (solubility, diffusivity etc.) and the geometry of the system.

6.5 CONCLUSIONS

- Dissolution studies from the complete surface of large single component compacts in the paddle dissolution apparatus revealed that uniform hydrodynamic conditions were not present on all parts of the surface, with statistically higher dissolution rates from compacts situated at the base of the vessel compared with similar compacts raised up 3 mm from the base of the vessel.
- A virtual fluid flow model of the paddle dissolution apparatus was developed using computational fluid dynamics technology. The final structured grid approach provided fluid flow predictions at 50 rpm, which were in very close quantitative agreement with published laser Doppler measurements of hydrodynamics in the apparatus.
- Rapid changes in velocity over a small region towards the base of the vessel were speculated to be responsible for variable dissolution rates previously reported in the apparatus. However, simulated path-lines of fluid mixing did not lead to the development of two separate regions of fluid mixing above and below the paddle, as had previously been speculated. Although simulations of paddle speeds from 25 to 150 rpm did predict changes in the time to reach complete mixing, no essential changes to the relative fluid flow patterns in the vessel were observed.
- Shear rates of velocity components within the velocity boundary layer outside the curved surface of compact at the base of the vessel were substantially higher for a region within approximately 3 mm from the base of the vessel. Mass transfer predictions from the planar and curved surface of compacts were in reasonable agreement with experimentally determined values, with closer agreement to experimental values from the top planar surface than from the curved planar surface.
- Dissolution profiles from simple triple layered cylindrical compacts of drug (salicylic acid or theophylline monohydrate) and soluble excipients were sigmoidal in shape, with increasing dissolution rates until complete dissolution of the excipient layers followed by decreasing dissolution rates of the drug layer.

- Two initial simple models were developed to predict dissolution rates from the drug layer, based on the changes of diameter of the drug and excipient layers; an experimentally calculated rate of change of diameter, and a rate mathematically predicted from intrinsic properties of the component. Both methods over-predicted dissolution rates at later times.
- A dynamic simulation model was also developed using geometrical and mass transfer equations from individual surfaces, based on assumptions of geometrical uniformity during the dissolution process, and using experimentally determined dimensions of the apparent diffusion layer outside the individual surfaces (calculated from the earlier single layer studies). The resulting predicted dissolution profiles were an improvement on the initial models and resembled the experimental data, both quantitatively and qualitatively for most systems studied.
- The addition of cylindrical layers of soluble acid excipients to both planar surfaces of a central drug-containing matrix layer resulted in a shift of release kinetics from Higuchi square root type release towards zero order release profiles. Particle size of polymer, solubility of the acid excipient and polymer fraction affected the resulting release profiles from such systems.
- A model was also developed to predict drug release from the layered matrix compacts via a progressive application of the dynamic simulation program to model drug dissolution from single surface matrix compacts, from the complete surface of matrix compacts, and finally from matrix compacts between soluble acid excipient layers. The final layered matrix dissolution model produced simulated dissolution profiles, which agreed both qualitatively and quantitatively with the experimental data for a series of polymer concentrations in the matrix core and for acid excipient layers of relative low and high solubilities.

6.6 FUTURE WORK

6.6.1 *CFD model of the dissolution apparatus*

In the present work, the study into the cause of variable dissolution rates from individual surfaces of large single component compacts in the vessel of the paddle dissolution apparatus led to the development of a virtual fluid flow model of the USP apparatus. As the method has now been validated against laser Doppler

measurements of fluid flow at 50 rpm, it is possible with the current set-up to examine the effect of any number of parameters on the hydrodynamics or mixing properties within the apparatus. Possible parameters to examine include:

- *Dosage form effects* – Alteration of the size, shape or position of the dosage form in the paddle dissolution apparatus can be modelled and the resulting change in hydrodynamic conditions may further establish possible reasons for observed variability in the test.
- *Particulate systems* - It is possible to track the flow of particles using the Fluent package. Dissolution rates can be calculated from the particulate systems based on the relative velocities of the particles and the surrounding fluid (Diebold, 2000).
- *Altered vessel dimensions* - Some modifications of the USP paddle dissolution test apparatus have previously been advocated to improve on the variable hydrodynamics of the apparatus. One modification includes the use of the ‘peak vessel’ (Beckett, 1996), while another alteration of the apparatus involves the placement of a 2 cm wide metal strip immediately inside the vessel wall (Qureshi and Shabnam, 2001). Both methods attempt to attain more uniform hydrodynamic conditions, the effect of which could be easily modelled by the CFD model. It is also possible that a change in the volume of the dissolution medium itself could result in altered hydrodynamics and mixing in the vessel.
- *Paddle dimensions and set-up* – The examination of a paddle with altered dimensions or with an angle of pitch may facilitate quicker mixing in the vessel. The examination of tilt in the paddle could also be examined as a possible source of variable dissolution rates in the apparatus.
- *Altered viscosity* – The effect of altering the viscosity of the medium was not examined in the current work.
- *Effect of compact geometry on hydrodynamics* – It is likely that the changes induced by the dissolution of the excipient layers with time, resulted in altered hydrodynamic rate around the dissolving layered compacts, thus complicating mass transfer predictions in the present work. Simulation of fluid flow around

the geometry of a dissolving layered compact may help to determine if this is the case.

- *Basket method* –The geometry of the basket method could readily be examined using CFD.

The frequent failure to obtain an appropriate *in vivo*-*in vitro* correlations (IVIVC) is in part due to our incomplete understanding/quantification of the complex physicochemical hydrodynamic relationships involved (Young, Devane & Butler, 1997). The virtual model of the dissolution apparatus could prove a useful tool in the examination of the hydrodynamic relations in IVIVC.

6.6.2 Model of drug dissolution from layered compacts

Experimental determination of the apparent diffusion layer at the heights of the individual layers may lead to better mass transfer predictions, particularly with regard to the simple layered compacts. If a closer correlation between the CFD generated velocities and mass transfer can be attained and validated against experimentally determined dissolution rates, it should be possible to link the predicted mass transfer rates from the CFD for the various surfaces to the Dynochem model. Ultimately, it may be possible to model dissolution from two-component mixed systems to look at the effect of pore development and the resulting surface area changes at the particulate level.

Although various dissolution rates approaching zero order were achieved from the ‘proof of concept’ layered matrix compacts, more complex systems would be required to be developed to eventually allow *in-vivo* use. The current model is based on the geometrical assumption that the aspect ratio of the individual layers is maintained during dissolution. This assumption is valid in the present case, where the ratio of height/diameter is close to 1. However, a more complicated model accounting for an altering aspect ratio with time is necessary to allow accurate modelling of systems with the dimensions of normal tablets. Altered dimensions of the compacts could be simulated using the Dynochem model to attain a system which both delivers drug at the desired rate and whose dimensions are acceptable for *in-vivo* use.

The final Dynochem model could be used as a pre-formulation tool to predict dissolution profiles from layered matrix systems, based on physicochemical properties, thus decreasing the time spent on initial dissolution feasibility studies.

REFERENCES

- Achanta, A.S., Gray, V.A., Cecil, T.L., Grady L.T., Evaluation of the performance of prednisone and salicylic acid calibrators. *Drug Dev. Ind. Pharm.*, 21 (1995) 1171-1182.
- Ballard E. and Nelson E., Absorption of implanted solid drug. *J. Pharm. Sci.*, 51 (1962) 915-923.
- Banaker, U.V., *Pharmaceutical Dissolution Testing*, Drugs and the Pharmaceutical Sciences, Volume 49, Marcel Dekker Inc, New York, 1992, Chapters 3 and 5, pp.53-105, 133-187.
- Bartels, C., Breuer, M., Wechsler, K. and Durst, F., Computational fluid dynamics applications on parallel-vector computers: computations of stirred vessel flows. *Computers & Fluids*, 31 (2002) 69-97.
- Beckett, A.N., Quach, T.T., Kurs, G.S., Improved hydrodynamics for USP apparatus 2. *Dissolut. Technol.*, 3 (1996) 7-10.
- Bettini, R., Acerbi, D., Caponetti, G., Musa, R., Magi, N., Colombo, P., Cocconi, D., Santi, P., Catellani, P.L., and Ventura, P., Influence of layer position on in vitro and in vivo release of levodopa methyl ester and carbidopa from three-layer matrix tablets. *Eur. J. Pharm. Biopharm.*, 52 (2002) 227-232.
- Bisaillon, S., and Tawashi, R., Influence of fluid motion in dissolution-rate determinations. *J. Pharm. Sci.*, 60 (1971) 1874-1877.
- Bocanegra, L.M., *A two phase flow experimental study of the united states pharmacopeia paddle method dissolution test apparatus*, Ph.D. Dissertation, West Virginia University, 1988.
- Bocanegra, L.M., Morris, G.J., Jurewicz, J.T. and Mauger, J.W., Fluid and particle laser doppler velocity measurements and mass transfer predictions for the USP paddle method dissolution apparatus. *Drug. Dev. Ind. Pharm.*, 16 (1990) 1441-1464.

- Bocanegra, L.M., Personal communication, (2002).
- Bödewadt, V.T., Die Drehströmung über festem Grunde. *Z. Angew. Math.*, 20 (1940) p241.
- Bonny, J.D. and Leuenberger, H., Matrix type controlled release systems: I. Effect of percolation on drug dissolution kinetics. *Pharm. Acta. Helv.*, 66 (1991) 160-164.
- British Pharmacopoeia*, Volume II, Her Majesty's Stationery Office. London, 2001.
- Brunner, E., Reaktionsgeschwindigkeit in heterogenen systemen. *Z. Phys. Chem.* 47 (1904) 56-102.
- Caraballo, I., Fernández-Arévalo, M., Holgado, M.A. and Rabasco, A.M., Percolation theory: application to the study of the release behaviour from inert matrix systems. *Int. J. Pharm.*, 96 (1993) 175-181.
- Caraballo, I., Millán, M., and Rabasco, A.M., Relationship between drug percolation threshold and particle size in matrix tablets. *Pharm. Res.*, 13 (1996) 387-390.
- Caraballo, I., Holgado, M.A., Fernández-Arévalo, Millán, M. and Rabasco, A.M., Application of percolation theory to characterize the release behaviour of carteolol matrix systems. *Drug Dev. Ind. Pharm.*, 23 (1997) 1-8.
- Carstensen, J.T., *Theory of Pharmaceutical Systems, Volume I.*, Academic Press Inc., London, 1972, Chapter 4, pp.238-241.
- CFD-Online*: CFD Resources Online Version 2.1.29, Larson, J., 2002.
<http://www.cfd-online.com>
- Chidambaram, N., Porter, W., Flood, K., and Qiu, Y., Formulation and characterization of new layered diffusional matrices for zero-order sustained release. *J. Control. Rel.*, 52 (1998) 149-158.

- Cobby, J., Mayersohn, M., and Walker, G.C., Influence of shape factors on kinetics of drug release from matrix tablets I: Theoretical. *J. Pharm. Sci.*, 63 (5) (1974), 725-732.
- Cobby, J., Mathematical Models for the Release of Drugs from Matrix Tablets, *J Biomed. Mat. Res.*, 12 (1978) 627-634.
- Cohen, J.L., Hubert, B.B., Leeson, L.J., Rhodes, C.T., Robinson, J.R., Roseman, T.J. and Shefter, E., The development of the USP dissolution and drug release standards. *Pharm. Res.* 7 (1990) 983-987.
- Cohen, J.L., *Theophylline monohydrate*, in *Analytical profiles of drug substances*, Florey ,K. (Ed.), Academic press, San Diego, 1990, pp. 466-493.
- Colton, C.K., and Smith, K.A., Mass transfer to a rotating fluid: Part 1. Transport from a stationary disk to a fluid in Bödewadt Flow. *AIChE*, 18 (1972a) 949-958.
- Colton, C.K., and Smith, K.A., Mass transfer to a rotating fluid: Part 2. Transport from the base of an agitated cylindrical tank. *AIChE*, 18 (1972b) 958-967.
- Conte, U., Maggi, L., Colombo, P. and La Manna, A, Multi-layered hydrophilic matrices as constant release devices (GeomatrixTM Systems). *J. Control. Rel.*, 26 (1993) 39-47.
- Conte, U., Maggi, L., and La Manna, A., Compressed barrier layers for constant drug release from swellable matrix tablets. *S.T.P. Pharma. Sciences*, 4 (1994a) 107-113.
- Conte, U., Maggi, L., Torre, M.L., Giunechedi, P., and La Manna, A., Modulation of the release profile of multi-layer tablets using polymeric barriers. *Proceedings of the 13th Pharmaceutical Technology Conference*, Strasbourg, France, April (1994b), Volume 1, pp.53-64.

- Conte, U. and Maggi, L., Multi-layer tablets as drug delivery devices. *Pharm. Tech. Europe*, February 1998, 18-25.
- Corrigan, O.I. and Timoney, R.F., The influence of polyvinylpyrrolidone on the dissolution properties of hydroflumethiazide. *J. Pharm. Pharmacol.*, 27 (1975) 759-764.
- Cox, D.C., Wells, C.E., Furnam, W.B., Savage, T.S. and King, A.C., Systematic error associated with apparatus 2 of the USP dissolution test II: Effects of deviations in vessel curvature from that of a sphere. *J. Pharm. Sci.*, 71 (1982) 395-399.
- Dabbagh, M.A., Ford, J.L., Rubinstein, M.H. and Hogan, J.E., Effects of polymer particle size, compaction pressure and hydrophilic polymers on drug release from matrices containing ethylcellulose. *Int. J. Pharm.*, 140 (1996) 85-95.
- Dakkuri, A., and Shah, A.C., Dissolution methodology. *Pharmaceutical Technology*, 1982 (6) 28-46.
- Deasy, P.B., Brophy, M.R., Ecanow, B., and Joy., M.M., Effect of ethylcellulose grade and sealant treatments on the production and in vitro release of microencapsulated sodium salicylate. *J. Pharm. Pharmacol.*, 32 (1980) 15-20.
- Deasy, P.B., Finan, M.P., Klatt, P.R., and Hornykiewytsh, T., Design and evaluation of a biodegradable implant for improved delivery of oestradiol-17 β to steers. *Int. J. Pharm.*, 89 (1993) 251-259.
- Desai, S.J., Simonelli, A.P., and Higuchi, W.I., Investigation of factors influencing release of solid drug dispersed in inert matrices. *J. Pharm. Sci.*, 54 (1965) 1459-1464.
- Desai, S.J., Singh, P., Simonelli, A.P., and Higuchi, W.I., Investigation of factors influencing release of solid drug dispersed in inert matrices III. *J. Pharm. Sci.*, 55 (1966a) 1230-1234.

- Desai, S.J., Singh, P., Simonelli, A.P., and Higuchi, W.I., Investigation of Factors Influencing Release of Solid Drug Dispersed in Inert Matrices IV. *J. Pharm. Sci.*, 55 (1966b) 1235-1239.
- Diebold, S.M, *Hydrodynamik and Lösungsgeschwindigkeit*, Ph.D. Thesis, Wolfgang Goethe-Universität, Frankfurt, Germany, 2000.
- Diebold, S.M. and Dressman, J.B., Hydrodynamik kompendialer Lösungsgeschwindigkeits-Testapparaturen. *Pharm. Ind.*, 63 (2001) 94-104.
- Dow Chemical Brochure* (Form No. 192-1172-1291 AMS). ETHOCEL Premium Ethylcellulose in Pharmaceutical Applications.
- Dynochem User Manual, Version 1.0.3.*, Performance Fluid Dynamics (PFD), 2000, pp77-78.
- European Pharmacopoeia*, 4th Edition, European Pharmacopoeial Secretariat, Strasbourg, France (2002)
- Fessi, H., Marty, J.P., Puisieux, F. and Carstensen, J.P., The Higuchi square root equation applied to matrices with high content of soluble drug substance. *Int. J. Pharm.*, 1 (1978) 265-274.
- Fluent5 User's Guide Volumes 1-4*, edited by Fluent Incorporated, 10 Cavendish Court, Canterra Resource Park, NH 03766, USA, (1998).
- Ford, J.L., Mitchell, K., Rowe, P., Armstrong, D.J., Elliot P.N.C., Rostron, C. and Hogan, J.E., Mathematical modelling of drug release from hydroxyprpylmethylcellulose matrices: Effect of temperature. *Int. J. Pharm.*, 71 (1991) 95-104.
- Franzini, J.B. and Finnemore, E.J., *Fluid mechanics with engineering applications*, WCB/ McGraw Hill, Ninth Ed., 1997, Chapters 2 and 6, pp.13-45, 187-239.

- Gray, V.A. and Hubert, B.B., Calibration of dissolution apparatus 1 and 2 – What to do when equipment fails. *Pharmacop. Forum*, 20 (1994) 8571-8573.
- Gambit Modelling Guide*, edited by Fluent Incorporated, 10 Cavendish Court, Canterra Resource Park, NH 03766, USA, (1998).
- Grijseels, H., Crommelin, D.J.A. and de Blaey, C.J., Hydrodynamic approach to dissolution rate. *Pharm. Weekblad. Sci. Ed.*, 3 (1981) 129-144.
- Gurny, R., Doelker, E. and Peppas, N.A., Modelling of sustained release water-soluble drugs from porous, hydrophobic polymers. *Biomaterials*, 3 (1982) 27-32.
- Harstedt, J.E. and Wright, J.L., Diffusion in porous material above the percolation threshold. *Pharm. Res.*, 7 (1990) 893-901.
- Healy, A.M., *Investigations of the dissolution mechanisms of acidic drug-excipient compacts*, Ph.D. Thesis, University of Dublin (1995).
- Healy, A.M. and Corrigan, O.I., The influence of excipient particle size, solubility and acid strength on the dissolution of an acidic drug from two-component compacts. *Int. J. Pharm.*, 143 (1996) 211-221.
- Higuchi, T., Rate of release of medicaments from ointment bases containing drugs in suspension. *J. Pharm. Sci.*, 50 (1961) 874-875.
- Higuchi, T., Mechanism of sustained-action medication (Theoretical analysis of rate of release of solid drugs dispersed in solid matrices). *J. Pharm. Sci.*, 52 (1963) 1145-1149.
- Khoury, N., Mauger, J.W., and Howard, S., Dissolution rate studies from a stationary disk/ rotating fluid system. *Pharm. Res.*, 5 (1988) 495-500.
- Kosiol, C., *A flow model for the USP Paddle Dissolution Apparatus*, M.Sc. Thesis, University of Dublin (2000).

- Kumar, V. and Banker, G.S., Chemically modified cellulosic polymers. *Drug Dev. Ind. Pharm.*, 19 (1993) 1-31.
- Ledwidge, M.T., *The effects of pH, crystalline phase and salt formation on the solubility of ionisable drugs*, Ph.D. Thesis, University of Dublin (1997).
- Leuenberger, H., Rohera, B.D., and Haas, C., Percolation theory – a novel approach to solid dosage form design. *Int. J. Pharm.*, 38 (1987) 109–115.
- Leuenberger, H., Leu, R. and Bonny, J.D., Application of percolation theory and fractal geometry to tablet compaction. *Drug Dev. Ind. Pharm.*, 18 (1992) 723-766.
- Leuenberger, H and Leu, R., Formation of a tablet: A site and bond percolation phenomenon. *J. Pharm. Sci.*, 81 (1992) 976-982.
- Levich, V.A., *Physicochemical Hydrodynamics*, Prentice-Hall Inc., Englewood Cliffs, N.J., U.S.A., 1962, Chapter 2, pp.39-184.
- McCormick, T.J., Industry perspective on dissolution apparatus calibration. *Dissolut. Technol.*, 2 (1995) 12-15.
- Millán, M., Caraballo, I. and Rabasco, A.M., The role of the drug/excipient particle size ratio in the percolation model for tablets. *Pharm. Res.*, 15 (1998) 216-220.
- Mooney, K.G., Mintun, M.A., Himmelstein, K.J. and Stella, V.J., Dissolution kinetics of carboxylic acids I: Effect of pH under unbuffered conditions. *J. Pharm. Sci.*, 70 (1981) 13-22.
- Muller L.M., DynoChem - Detailed case study: Scale-Up of a 4-phase hydrogenator. IChemE Symposium Series, 1996 No5, Paper 1.4.

- Narisawa, S., Yoshino, H., Hirakawa, Y. and Noda, K., Porosity-controlled film formation in the spraying process and its solute permeability. *Int. J. Pharm.*, 104 (1994) 95–106.
- Neervannan, S., Reinert, J.D., Stella, V.J. and Southard, M.Z., A numerical convective-diffusion model for dissolution of neutral compounds under laminar flow conditions. *Int. J. Pharm.*, 96 (1993) 167-174.
- Nelson, K.G. and Shah, A.C., Convective diffusion model for a transport-controlled dissolution rate process. *J. Pharm. Sci.*, 64 (1975) 610-614.
- Nernst, W., Theorie der reaktionsgeschwindigkeit in heterogenen systemen. *Z. Phys. Chem.*, 47 (1904) 52-55.
- Noyes, A.A. and Whitney, W., The rate of solution of substances in their own solutions. *J. Am. Chem. Soc.*, 19 (1897) 930-936.
- Owen, A.J., *The Diode-Array Advantage in UV/Visible Spectroscopy*, Hewlett-Packard Co., Federal Republic of Germany, 1988, Chapters 6 and 7, pp.22-39.
- Pedrosa, S.M.C.P. and Nunhez, J.R., The behaviour of stirred vessels with anchor type impellers. *Computers and Chem. Eng.*, 24 (2000) 1745-1751.
- Peppas, N.A., Analysis of Fickian and Non-Fickian Drug Release from Polymers. *Pharm. Acta. Helv.*, 60 (1985) 110-111.
- PhRMA, The USP dissolution calibrator tablet collaborative study – An overview of the fourth quarter 1994 process. *Pharmacopeil Forum* 23, 4198-4237.
- Pollock, D.K. and Sheskey, P.J., Evaluation of FP Polymers for use in controlled-release matrix drug delivery, *The Dow Chemical Company*, 1997.
- Pollock, D.K., Sheskey, P.J., Micronized ethylcellulose: opportunities in direct-compression controlled-release tablets. *Pharm. Tech. Asia*, 4 (2001) 7-11.

- Porter, S.C., Controlled-release film coatings based on ethylcellulose. *Drug Dev. Ind. Pharm.*, 15 (1989) 1495–1989.
- Potter, A., Proudfoot, S.G., Banks, M. and Aulton, M.E., Factors affecting dissolution-controlled drug release from a compacted dry powder mix. *Proceedings of the 6th International Congress on Particle Technology*, Kyoto, 19-22 September 1990, pp.1-8.
- Public final report of Esprit HPCN PST Activity, PSUDO, Parallel Simulation of drUg Release cOde*, 2001, Hitachi Dublin Laboratory (HDL), Elan Corporation plc., ICeTACT, Department of Mathematics, Trinity College Dublin and Department of Pharmaceutics and Pharmaceutical Technology, Trinity College Dublin.
- Qureshi, S.A. and McGilveray, I.J., A critical assessment of the USP dissolution apparatus suitability test criteria. *Drug Dev. Ind. Pharm.*, 21 (1995) 905-912.
- Qureshi, S.A. and McGilveray, I.J., Typical variability in drug dissolution testing: study with USP and FDA calibrator tablets and a marketed drug (glibenclamide) product. *Eur. J. Pharm. Sci.*, 7 (1999) 249-258.
- Qureshi, S.A. and Shabnam, J., Cause of high variability in drug dissolution testing and its impact on setting tolerances. *Eur. J. Pharm. Sci.*, 12 (2001) 271-276.
- Ramtoola, Z., *Dissolution mechanism of drug and excipient mixtures in reactive media*, Ph.D. Thesis, University of Dublin, 1988.
- Rekhi, G.S. and Jambhekar, S.S., Ethylcellulose – A Polymer Review. *Drug Dev. Ind. Pharm.*, 21 (1995) 61-77.
- Ritger, P.L. and Peppas, N.A., A simple equation for description of solute release I. Fickian and non-Fickian release from non-swellable devices in the form of slabs, spheres, cylinders or discs. *J. Control. Rel.*, 5 (1987) 23-36.

- Scale Up and Post Approval Changes (SUPAC) - Guidance for Industry. Immediate Release Solid Oral Dosage Forms*, Center for Drug Evaluation and Research (CDER) November, 1995, Section VII, p 23.
- Schlichting, H., *Boundary Layer Theory, 4th Edition.*, McGraw Hill, New York, 1975, Chapter XI, pp.225-230.
- Schwarzenbach, R., High-performance liquid chromatography of carboxylic acids. *J. Chromatogr.*, 231 (1982) 339-358.
- Scientist Handbook*, Micromath Scientific Software, Utah, U.S.A., 1995.
- Shah, S.A. and Nelson, K.G., Evaluation of a convective diffusion drug dissolution rate model. *J. Pharm. Sci.*, 64 (1975) 1518-1520.
- Singh, P., Desai, S.J., Simonelli, A.P., and Higuchi, W.I., Release Rates of Solid Drug Mixtures in Inert Matrices I. *J. Pharm. Sci.*, 56 (1967) 1542-1547.
- Smith, K.A. and Colton, C.K., Mass transfer to a rotating fluid: Part I. Transport from a stationary disk to a fluid in Bödewadt flow. *AICHE*, 18 (5) (1972a) 949-958.
- Smith, K.A. and Colton, C.K., Mass transfer to a rotating fluid: Part II. Transport from the base of an agitated cylindrical tank. *AICHE*, 18 (5) (1972b) 958-967.
- Soriano, M.C., Caraballo, I., Millán, M., Piñero, R.T., Melgoza, L.M. and Rabasco, A.M., Influence of two different types of excipient on drug percolation threshold. *Int. J. Pharm.*, 174 (1998) 63-69.
- Stauffer, D. and Aharony, A., *Introduction to Percolation Theory, 2nd Edition.*, Taylor and Francis, London, 1992, Chapters 1 and 2, pp.1-56, Chapter 6, pp.115-136.

- Upadrashta, S.M., Katikaneni, P.R., Hileman, G.A. and Keshary, P.R., Direct compression controlled release tablets using ethylcellulose matrices. *Drug Dev. Ind. Pharm.*, 19 (1993) 449-460.
- USP 24, *The United States Pharmacopeia*, United States Pharmacopeial Convention Inc., Rockville, MD, 2000, pp.1941-1943.
- Visawanth, D.S. and Natarajan, G. *Data Book on the Viscosity of Liquids*, Hemisphere Publishing Corporation, U.S.A., 1989, Chapters 3 and 4, pp.41-45, 714-715.
- Wells, J.L., *Pharmaceutical Preformulation. The Physicochemical Properties of Drug Substances*, Ellis Horwood Ltd., Chichester, England, 1988, Chapter 2, pp.21-28.
- Withey, R.J., and Bowker, A.J., Agitation of the solvent in tablet dissolution studies- a flow visualisation technique. *J. Pharm. Pharmacol.*, 24 (1972) 345-351.
- Yang, L. and Fassihi, R., Examination of drug solubility, polymer types, hydrodynamics and loading dose on drug release behaviour from a triple-layer asymmetric configuration delivery system. *Int. J. Pharm.*, 155 (1997a) 219-229.
- Yang, L. and Fassihi, R., Modulation of diclofenac release from a totally soluble controlled release drug delivery system. *J. Control. Rel.*, 44 (1997b) 135-140.
- Young D., Devane, J.G. and Butler, J., *In vitro-in vivo correlations*, Plenum Press, New York, 1997, Chapters 2 and 6, pp.17-30, 289-295.

APPENDICES

APPENDIX 1

Navier-Stokes equations in a cylindrical co-ordinate system**The continuity equation:**

$$A) \quad \frac{\partial u_r}{\partial r} + \frac{u_r}{r} + \frac{1}{r} \frac{\partial u_\phi}{\partial \phi} + \frac{\partial u_z}{\partial z} = 0,$$

The Navier-Stokes equations:

$$B) \quad \rho \left(\frac{\partial u_r}{\partial t} + u_r \frac{\partial u_r}{\partial r} + \frac{u_\phi}{r} \frac{\partial u_r}{\partial \phi} + u_z \frac{\partial u_r}{\partial z} - \frac{u_\phi^2}{r} \right) = -\frac{\partial P}{\partial r} \\ + \eta \left(\frac{\partial^2 u_r}{\partial r^2} + \frac{1}{r} \frac{\partial u_r}{\partial r} - \frac{u_r}{r^2} + \frac{1}{r^2} \frac{\partial^2 u_r}{\partial \phi^2} + \frac{\partial^2 u_r}{\partial z^2} - \frac{2}{r^2} \frac{\partial u_\phi}{\partial \phi} \right) + F_r$$

$$C) \quad \rho \left(\frac{\partial u_\phi}{\partial t} + u_r \frac{\partial u_\phi}{\partial r} + \frac{u_r u_\phi}{r} + \frac{u_\phi}{r} \frac{\partial u_\phi}{\partial \phi} + u_z \frac{\partial u_\phi}{\partial z} \right) = -\frac{1}{r} \frac{\partial P}{\partial \phi} \\ + \eta \left(\frac{\partial^2 u_\phi}{\partial r^2} + \frac{1}{r} \frac{\partial u_\phi}{\partial r} - \frac{u_\phi}{r^2} + \frac{1}{r^2} \frac{\partial^2 u_\phi}{\partial \phi^2} + \frac{\partial^2 u_\phi}{\partial z^2} + \frac{2}{r^2} \frac{\partial u_r}{\partial \phi} \right) + F_\phi$$

$$D) \quad \rho \left(\frac{\partial u_z}{\partial t} + u_r \frac{\partial u_z}{\partial r} + \frac{u_\phi}{r} \frac{\partial u_z}{\partial \phi} + u_z \frac{\partial u_z}{\partial z} \right) \\ = -\frac{\partial P}{\partial z} + \eta \left(\frac{\partial^2 u_z}{\partial r^2} + \frac{1}{r} \frac{\partial u_z}{\partial r} + \frac{1}{r^2} \frac{\partial^2 u_z}{\partial \phi^2} + \frac{\partial^2 u_z}{\partial z^2} \right) + F_z.$$

The components of the velocity vector are give by $u = (u_r, u_\phi, u_z)$ where u_r is the radial component of velocity, u_ϕ is the tangential (or circumferential) component of velocity u_z is the axial component of velocity, r is distance in the radial direction, ϕ is distance in the tangential direction, z is distance in the axial direction. P is pressure, η is the dynamic viscosity and ρ is the density of the fluid. F_r , F_ϕ and F_z are functions of position.

APPENDIX 2

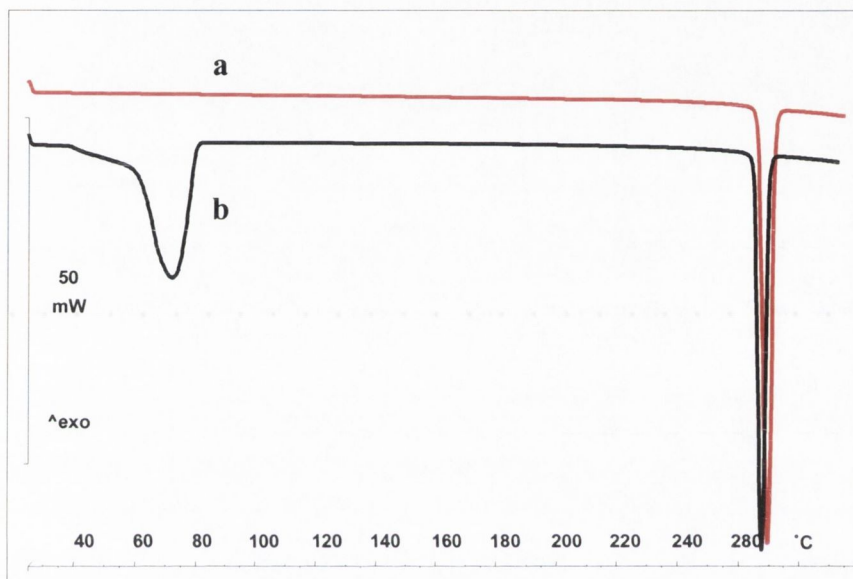
Characterisation of theophylline monohydrate after formation from the anhydrous starting material**Differential Scanning Calorimetry (DSC)**

Figure 1 DSC trace of anhydrous theophylline (a) and theophylline monohydrate after formation from the anhydrous starting material (b).

Thermogravimetric analysis (TGA)

The TG scan of theophylline monohydrate showed an increase in weight loss over the range 35-80°C, relative to the anhydrous starting material. The inflexion in the trace corresponded to a weight loss of 8.31 ± 0.13 % w/w. The theoretical water content of the monohydrate form of theophylline is 9.09 % w/w.

X-Ray Diffraction (XRD)

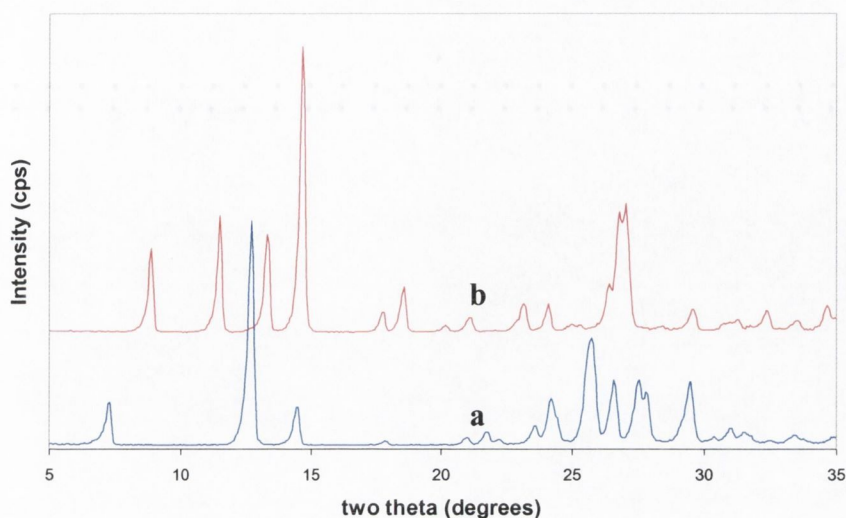
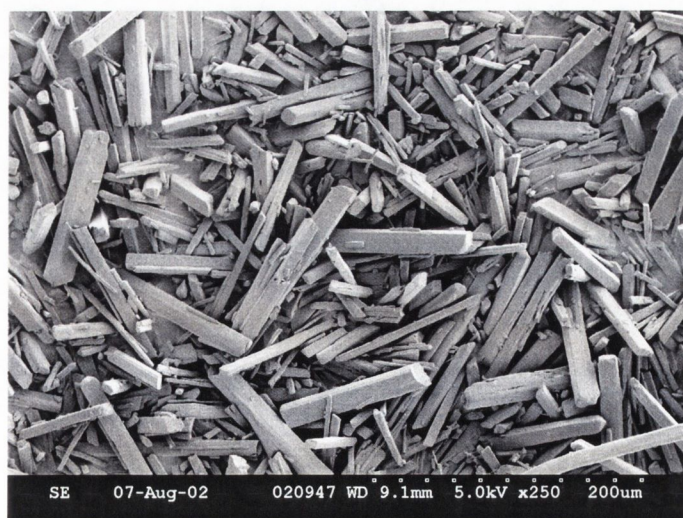


Figure 2 XRD traces of (a) anhydrous theophylline and (b) theophylline monohydrate after formation from the anhydrous starting material. The strong lines at ~ 9 , 11.5 , and 19 degrees 2θ are characteristic of theophylline monohydrate in trace b) above (Ledwidge, 1997).

Karl Fisher titration

The monohydrate product was found to contain 8.75 ± 0.14 % w/w water ($n=3$). The theoretical water content of the monohydrate form of theophylline is 9.09 % w/w.

Scanning Electron Microscopy



The SEM image of the theophylline monohydrate (after formation from the anhydrous starting material).

APPENDIX 3**Calibration curves used to determine the concentration of substances in solution.****UV calibration curves****(1) Benzoic acid in 0.1N HCl**

Analytical wavelength: 274

Reference wavelength: 400

Absorbance = (0.0753*Concentration [mg/100ml]) – 0.0003

 $r^2 = 0.9989$ **(2) Salicylic acid in 0.1N HCl**

Analytical wavelength: 230

Reference wavelength: 400

Absorbance = (0.8426* Concentration [mg/100ml]) + 0.11

 $r^2 = 0.9995$ **(3) Theophylline monohydrate in 0.01N HCl**

Analytical wavelength: 272

Reference wavelength: 400

Absorbance = (0.5022* Concentration [mg/100ml]) + 0.0015

 $r^2 = 0.9998$ **(4) Adipic acid in 0.01N HCl**

Analytical wavelength range: 204-206

Reference wavelength range: 350-400

Absorbance = (0.0066* Concentration [mg/100ml]) + 0.0051

 $r^2 = 0.9994$

HPLC calibration curves**(1) Theophylline monohydrate in 0.01N HCl**

Column: Waters Spherisorb S5 ODS2 4.6 x 125 mm

$\lambda = 280$ nm

Mobile phase: 7% v/v acetonitrile in aqueous buffer of 0.136% w/v sodium acetate trihydrate and 0.5% w/v glacial acetic acid at 1.0 ml/min.

Peak area = (331.76*Concentration [mg/ 100 ml]) + 0.2982

$r^2 = 1.0000$

(2) Succinic acid in 0.01N HCl

Column: Spherisorb S5 C8 5 μ m, 4.6 mm x 250 mm

$\lambda = 202$ nm

Mobile phase: Methanol:1% phosphoric acid, 50:50 at 1.0 ml/min.

Peak area = (0.059* Concentration [mg/ 100 ml]) – 0.0241

$r^2 = 0.9991$

(2) Fumaric acid in 0.01N HCl

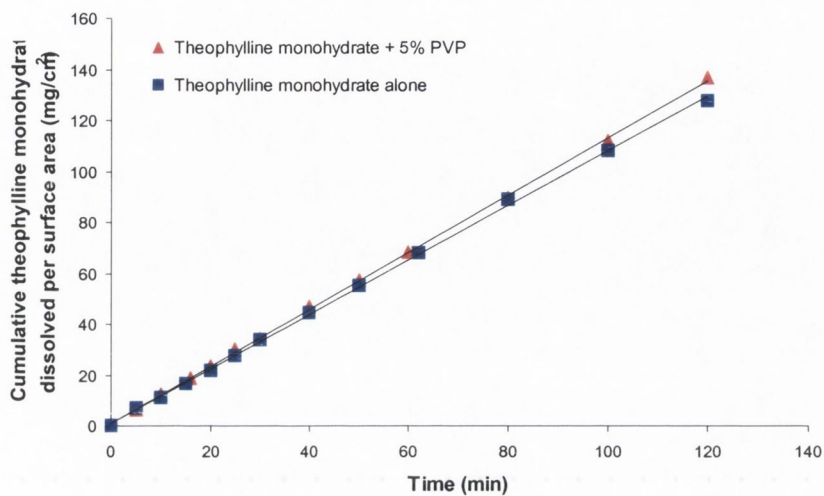
Column: Spherisorb S5 C8 5 μ m, 4.6 mm x 250 mm

$\lambda = 202$ nm

Mobile phase: Methanol: 1% phosphoric acid, 50:50 at 1.0 ml/min.

Peak area = (10.715* Concentration [mg/ 100 ml]) – 0.9181

APPENDIX 4

Intrinsic dissolution rate of theophylline monohydrate (\pm 5% PVP)

Graph of dissolution from constant surface area (1.33 cm²) of discs containing theophylline monohydrate only or theophylline monohydrate with 5% PVP (n=3). There was no statistical difference between the slopes of both plots ($p = 0.43$).

APPENDIX 5

Gambit Journal File 1

Journal file generated for the build up and meshing of the paddle dissolution apparatus in the Gambit CFD pre-processor program using an unstructured grid approach

```

/ Journal File for GAMBIT 1.3.0
volume create height 0.004 radius1 0.0415 radius3 0.0415 offset 0
0.002 0 \
  yaxis frustum
volume create width 0.1 depth 0.01 height 0.05 offset 0.05 0.005
0.025 brick
volume move "volume.2" offset -0.05 0 -0.0358
volume intersect volumes "volume.1" "volume.2" keeporiginals
volume delete "volume.1" lowertopology
volume move "volume.2" offset 0 0 0.019
volume subtract "volume.3" volumes "volume.2"
volume move "volume.3" offset 0 0 0.0358
volume create width 0.1 depth 0.01 height 0.05 offset 0.05 0.005
0.025 brick
volume move "volume.4" offset 0.03725 0 0
volume subtract "volume.3" volumes "volume.4" keptool
volume move "volume.4" offset -0.1745 0 0
volume subtract "volume.3" volumes "volume.4"
volume create height 0.08 radius1 0.004875 radius3 0.004875 offset 0
0 0.04 \
  zaxis frustum
volume move "volume.3" offset 0 -0.002 0
volume unite volumes "volume.4" "volume.3"
volume create "vessel" height 0.0755 radius1 0.051 radius3 0.051
offset 0 0 \
  0.03775 zaxis frustum
volume move "vessel" offset 0 0 0.051
volume create radius 0.051 sphere
volume move "volume.6" offset 0 0 0.051
volume unite volumes "vessel" "volume.6"
volume create "mrfvolume" height 0.06 radius1 0.0451 radius3 0.0451
offset 0 \
  0 0.03 zaxis frustum
volume move "mrfvolume" offset 0 0 0.0451
volume create radius 0.0451 sphere
volume move "volume.7" offset 0 0 0.0451
volume unite volumes "mrfvolume" "volume.7"
volume move "mrfvolume" offset 0 0 0.015
volume move "volume.4" offset 0 0 0.025
volume create "tablet" height 0.0115 radius1 0.0065 radius3 0.0065
offset 0 0 \
  0.00575 zaxis frustum
volume subtract "vessel" volumes "mrfvolume"
volume create "mrfvolume" stitch "face.57" "face.59" "face.61" real
volume subtract "mrfvolume" volumes "volume.4"
volume create "stirrer" stitch "face.38" "face.46" "face.48"
"face.40" \

```



```

"face.21" "face.51" "face.39" "face.47" "face.35" "face.50"
"face.45" \
"face.49" "face.43" real
volume subtract "vessel" volumes "tablet"
face create "bottom of tablet" wireframe "edge.103" real
volume create "tablet" stitch "face.62" "face.64" "bottom of tablet"
real
solver select "FLUENT 5"
physics create "vesselwall" btype "WALL" face "face.52" "face.54"
"face.56"
physics create "mrfwall" btype "WALL" face "face.57" "face.59"
"face.61"
physics create "tabletwall" btype "WALL" face "face.62" "face.64" \
"bottom of tablet"
physics create "stirrerwall" btype "WALL" face "face.38" "face.46"
"face.48" \
"face.40" "face.21" "face.51" "face.39" "face.47" "face.35"
"face.50" \
"face.45" "face.49" "face.43"
physics create "vesselfluid" ctype "FLUID" volume "vessel"
physics create "mrfvolfluid" ctype "FLUID" volume "mrfvolume"
physics create "stirrer" ctype "SOLID" volume "stirrer"
physics create "tablet" ctype "SOLID" volume "tablet"
/ Mesh the stirrer faces
face mesh "face.38" "face.46" "face.48" "face.40" "face.21" "face.51"
\
"face.39" "face.47" "face.35" "face.50" "face.45" "face.49"
"face.43" \
triangle intervals 10
/ Mesh the tablet faces
face mesh "face.62" "face.64" "bottom of tablet" triangle intervals
20
/ Mesh the vessel faces
face mesh "face.52" "face.54" "face.56" triangle intervals 120
/ Mesh the mrfvolume faces
face mesh "face.57" "face.59" "face.61" triangle intervals 120
volume mesh "vessel" tetrahedral size 1
volume mesh "mrfvolume" tetrahedral size 1
volume mesh "stirrer" tetrahedral size 1
volume mesh "tablet" tetrahedral size 1

```

APPENDIX 6

Gambit Journal File 2

Journal file generated for the build up and meshing of the paddle dissolution apparatus in the Gambit CFD pre-processor program using a structured grid approach

```

/ Journal File for GAMBIT 1.3.0
vertex create "centre pt of vess sphere" coordinates 0 0 0
vertex create coordinates 0.03725 0 0
vertex create coordinates 0.051 0 0
vertex create coordinates 0 0 -0.026
vertex create coordinates 0 0 -0.051
vertex create coordinates 0.021 0 -0.026
vertex create coordinates 0.03725 0 -0.008494
vertex create coordinates 0 0 -0.007
vertex create coordinates 0.004875 0 -0.007
vertex create coordinates 0.03725 0 -0.007
vertex create coordinates 0.004875 0 0
vertex create coordinates 0.004875 0 -0.026
vertex create "ctr pt of paddle curve" coordinates 0 0 0.0098
edge create "vessel curve" center2points "centre pt of vess sphere" \
  "vertex.5" "vertex.3" minarc arc
vertex delete "vertex.7"
vertex create coordinates 0.0415 0 0.0098
vertex delete "vertex.10"
vertex delete "vertex.6"
vertex create coordinates 0 0 -0.0415
vertex delete "vertex.15"
vertex create coordinates 0 0 -0.0317
edge create "paddle curve" center2points "ctr pt of paddle curve" "vertex.15" \
  "vertex.14" minarc arc
vertex create coordinates 0.03725 0 -0.026
edge create straight "vertex.2" "vertex.16"
vertex create edgeints "paddle curve" "edge.3" real
vertex create coordinates 0.051 0 -0.007
edge create straight "vertex.9" "vertex.18"
vertex create edgeints "edge.4" "edge.3" real
edge delete "edge.4"
edge delete "edge.3"
vertex delete "vertex.18"
vertex delete "vertex.16"
vertex create coordinates 0.03725 0 -0.026
edge create straight "vertex.12" "vertex.20"
vertex create edgeints "paddle curve" "edge.3" real
edge delete "edge.3"
vertex delete "vertex.20"
edge delete "paddle curve"
edge create center2points "ctr pt of paddle curve" "vertex.21" "vertex.17" \
  minarc arc
vertex delete "vertex.15" "vertex.14"
edge create straight "vertex.4" "vertex.12"
edge create straight "vertex.12" "vertex.21"
edge create straight "centre pt of vess sphere" "vertex.11"
edge create straight "vertex.11" "vertex.2"
edge create straight "vertex.2" "vertex.3"
edge create straight "vertex.17" "vertex.2"
edge create straight "centre pt of vess sphere" "vertex.5"
edge create straight "vertex.11" "vertex.12"
vertex delete "ctr pt of paddle curve"
edge delete "edge.9"
edge create straight "centre pt of vess sphere" "vertex.4"
edge create straight "vertex.4" "vertex.5"
face create "rotate inner face" wireframe "edge.5" "edge.6" "edge.8" "edge.2" \
  "edge.4" "edge.3" "edge.11" real
face create "rotateouter face" wireframe "edge.4" "edge.3" "edge.12" \
  "vessel curve" "edge.7" "edge.8" "edge.2" real
face create revolve "vessel curve" "edge.2" "edge.3" "edge.4" "edge.5" \
  "edge.6" "edge.7" "edge.8" "edge.10" dangle -90 vector 0 0 -1 origin 0 0 0
face create wireframe "edge.19" "edge.22" "edge.17" "edge.33" "edge.30" \
  "edge.14" "edge.12" real
face create wireframe "edge.19" "edge.11" "edge.24" "edge.36" real
face create wireframe "edge.11" "edge.10" "edge.5" "edge.3" real
volume create "stirrer_shaft_bottom" stitch "face.14" "face.7" "face.13" \
  "face.5" "face.11" real
face create wireframe "edge.10" "edge.6" "edge.8" "edge.2" "edge.4" real
face create wireframe "edge.36" "edge.22" "edge.17" "edge.33" "edge.27" real
volume create "inner_voll" stitch "face.11" "face.6" "face.15" "face.4" \
  "face.10" "face.8" "face.16" real
volume create "outer_volume" stitch "rotateouter face" "face.3" "face.9" \
  "face.4" "face.12" "face.5" "face.10" "face.6" real
volume create width 0.051 depth 0.051 height 0.008494 offset 0.0255 0.0255 \
  0.004247 brick
volume move "volume.4" offset 0 0 -0.008494

```



```

volume intersect volumes "volume.4" "inner_voll" keeporiginals
volume delete "volume.4" lowertopology
volume subtract "inner_voll" volumes "volume.5" keeptool
face connect "face.25" "face.47" real
face connect "face.41" "face.38" real
face connect "face.46" "face.35" real
edge connect "edge.33" "edge.89" real
volume create width 0.051 depth 0.002 height 0.051 offset 0.0255 0.001 0.0255 brick
volume move "volume.8" offset 0 0 -0.051
volume intersect volumes "volume.5" "volume.8" keeporiginals
volume intersect volumes "volume.8" "inner_voll" keeporiginals
volume move "volume.8" offset 0 0 -0.007
volume intersect volumes "volume.9" "volume.8" keeporiginals
volume delete "volume.8" lowertopology
volume subtract "volume.9" volumes "volume.11" keeptool
volume subtract "volume.5" volumes "volume.9" keeptool
volume subtract "volume.5" volumes "volume.11" keeptool
volume subtract "volume.13" volumes "volume.10" keeptool
volume modify "volume.9" label "vol_above_wing"
volume modify "volume.10" label "wing_lower"
volume modify "volume.11" label "wing_upper"
volume modify "volume.13" label "inside_vol_lower"
volume modify "volume.14" label "outside_vol"
volume modify "volume.15" label "inside_vol_upper"
volume modify "volume.16" label "shaft_lower"
volume unite volumes "inside_vol_upper" "wing_upper" "vol_above_wing" \
  keeporiginals
volume subtract "volume.17" volumes "wing_upper" keeptool
volume subtract "volume.17" volumes "vol_above_wing" keeptool
face connect "face.152" "face.122" real
face connect "face.152" "face.122" real
volume delete "inside_vol_upper"
face connect "face.152" "face.122" real
volume create stitch "face.36" "face.37" "face.122" "face.123" "face.114" \
  "face.65" "face.96" real
face delete "face.152" lowertopology
volume delete "volume.17" lowertopology
volume modify "volume.18" label "inside_vol_upper"
face delete "face.109" lowertopology
face connect "face.54" "face.46" real
face connect "face.112" "face.97" real
face connect "face.88" "face.74" real
face connect "face.90" "face.98" real
face connect "face.82" "face.130" real
face connect "face.80" "face.4" real
face connect "face.124" "face.85" real
face connect "face.81" "face.6" real
face connect "face.11" "face.75" real
face connect "face.115" "face.104" real
volume mesh "inside_vol_lower" cooper source "face.16" "face.82" intervals 16
volume mesh "inside_vol_upper" map intervals 6
volume mesh "vol_above_wing" map intervals 2
face mesh "face.81" map intervals 2
face mesh "face.80" map intervals 2
face mesh "face.124" map intervals 2
face mesh "face.5" "face.7" triprimitive
volume mesh "outside_vol" cooper source "face.5" "face.3" "face.81" \
  "face.133" "face.114" "face.80" "face.115" "face.131" "face.124" intervals \
  16
solver select "FLUENT 5"
physics create "Vessel Wall" btype "WALL" face "face.3" "face.9" "face.36" \
  "face.66"
window modify 1 AND 2 AND 3 AND 4 invisible mesh
physics create "Stirrer Wall" btype "WALL" face "face.7" "face.122" \
  "face.133" "face.124" "face.80" "face.96" "face.90" "face.54" "face.81"
physics create "Stirrer interior" btype "INTERIOR" face "face.83" "face.88" \
  "face.14" "face.13" "face.11" "face.112" "face.89"
physics create "Fluid interior" btype "WALL" face "face.12" \
  "rotateouter face" "face.16" "face.37" "face.105"
window modify 1 AND 2 AND 3 AND 4 visible mesh
volume delete "vol_above_wing" "wing_lower" "wing_upper" "inside_vol_lower" \
  "outside_vol" "shaft_lower" "inside_vol_upper" lowertopology onlymesh
face copy "face.83" "face.89" "face.105" "rotateouter face" "face.3" "face.5" \
  "face.7" "face.9" "face.11" "face.12" "face.13" "face.14" "face.16" \
  "face.36" "face.37" "face.54" "face.65" "face.66" "face.80" "face.81" \
  "face.82" "face.88" "face.90" "face.96" "face.112" "face.114" "face.115" \
  "face.122" "face.123" "face.124" "face.124" "face.131" "face.132" "face.133" to \
  "face.134" "face.135" "face.136" "face.137" "face.138" "face.139" \
  "face.140" "face.141" "face.142" "face.143" "face.144" "face.145" \
  "face.146" "face.147" "face.148" "face.149" "face.150" "face.151" \
  "face.152" "face.153" "face.154" "face.155" "face.156" "face.157" \
  "face.158" "face.159" "face.160" "face.161" "face.162" "face.163" \
  "face.164" "face.165" "face.166"
face reflect "face.134" "face.135" "face.136" "face.137" "face.138" \
  "face.139" "face.140" "face.141" "face.142" "face.143" "face.144" \
  "face.145" "face.146" "face.147" "face.148" "face.149" "face.150" \
  "face.151" "face.152" "face.153" "face.154" "face.155" "face.156" \
  "face.157" "face.158" "face.159" "face.160" "face.161" "face.162" \
  "face.163" "face.164" "face.165" "face.166" vector 3.12285e-18 0.051 0 \
  origin 0 0 0
face connect "face.145" "face.14" real
face connect "face.105" "face.136" real
face connect "face.89" "face.135" real
face connect "face.83" "face.134" real
face connect "rotateouter face" "face.137" real
volume create "shaft_lower_2" stitch "face.139" "face.144" "face.145" \
  "face.161" "face.165" "face.142" "face.158" "face.149" "face.140" real
volume create "Vol_above_wing_2" stitch "face.151" "face.150" "face.105" \
  "face.149" "face.156" "face.160" real
volume create "wing_upper_2" stitch "face.155" "face.157" "face.156" \
  "face.89" "face.163" "face.158" real
volume create "sing_lower_2" stitch "face.83" "face.155" "face.154" \

```

```

"face.152" "face.153" "face.142" real
volume create "inner_vol_lower" stitch "face.166" "face.146" "face.165" \
"face.154" "face.162" "face.164" real
volume create "inner_vol_upper_2" stitch "face.159" "face.147" "face.162" \
"face.148" "face.161" "face.150" "face.157" real
volume create "outer_vol_2" stitch "face.141" "face.159" "face.161" \
"face.163" "face.138" "rotateouter face" "face.164" "face.143" "face.152" \
"face.153" "face.139" "face.166" real
face copy "face.83" "face.89" "face.105" "rotateouter face" "face.3" "face.5" \
"face.7" "face.9" "face.11" "face.12" "face.13" "face.16" "face.36" \
"face.37" "face.54" "face.65" "face.65" "face.66" "face.80" "face.81" "face.82" \
"face.88" "face.90" "face.96" "face.112" "face.114" "face.115" "face.122" \
"face.123" "face.124" "face.131" "face.132" "face.133" "face.131" \
"face.139" "face.140" "face.141" "face.142" "face.143" "face.14" \
"face.145" "face.146" "face.147" "face.147" "face.148" "face.149" "face.15" \
"face.151" "face.152" "face.153" "face.154" "face.155" "face.15" \
"face.157" "face.158" "face.159" "face.160" "face.161" "face.16" \
"face.163" "face.164" "face.165" "face.166" to "face.167" "face.168" \
"face.169" "face.170" "face.171" "face.172" "face.173" "face.17" \
"face.175" "face.176" "face.177" "face.178" "face.179" "face.18" \
"face.181" "face.182" "face.183" "face.184" "face.185" "face.18" \
"face.187" "face.188" "face.189" "face.190" "face.191" "face.19" \
"face.193" "face.194" "face.195" "face.196" "face.197" "face.19" \
"face.199" "face.200" "face.201" "face.202" "face.203" "face.20" \
"face.205" "face.206" "face.207" "face.208" "face.209" "face.21" \
"face.211" "face.212" "face.213" "face.214" "face.215" "face.21" \
"face.217" "face.218" "face.219" "face.220" "face.221" "face.22" \
"face.223" "face.224" "face.225" "face.226" "face.227" \
face reflect "face.167" "face.168" "face.169" "face.170" "face.17" \
"face.172" "face.173" "face.174" "face.175" "face.176" "face.17" \
"face.178" "face.179" "face.180" "face.181" "face.182" "face.18" \
"face.184" "face.185" "face.186" "face.187" "face.188" "face.18" \
"face.190" "face.191" "face.192" "face.193" "face.194" "face.19" \
"face.196" "face.197" "face.198" "face.199" "face.200" "face.20" \
"face.202" "face.203" "face.204" "face.205" "face.206" "face.20" \
"face.208" "face.209" "face.210" "face.211" "face.212" "face.21" \
"face.214" "face.215" "face.216" "face.217" "face.218" "face.21" \
"face.220" "face.221" "face.222" "face.223" "face.224" "face.22" \
"face.226" "face.227" vector 0.051 -6.2457e-18 0 origin 0 0 0
face connect "face.16" "face.178" real
face connect "face.12" "face.176" real
face connect "face.177" "face.13" real
face connect "face.209" "face.148" real
face connect "face.146" "face.207" real
face connect "face.143" "face.204" real
face connect "face.205" "face.144" real
volume create "Vol_above_wing_2" stitch "face.212" "face.211" "face.221" \
"face.217" "face.169" "face.210" real
volume modify "volume.26" label "Vol }above_wing_3"
volume create "Wing_upper" stitch "face.217" "face.224" "face.216" "face.168" \
"face.218" "face.219" real
volume modify "Wing_upper" label "wing_upper"
volume modify "volume.27" label "Wing_upper_3"
volume create "Wing_lower_3" stitch "face.215" "face.216" "face.167" \
"face.213" "face.214" "face.203" real
volume create "inner_vol_lower" stitch "face.225" "face.227" "face.215" \
"face.226" "face.146" "face.223" real
volume modify "volume.29" label "Inner_vol_lower_3"
volume modify "Vol }above_wing_3" label "Vol_above_wing_3"
volume create "Inner_vol_upper_3" stitch "face.223" "face.209" "face.220" \
"face.208" "face.211" "face.218" "face.222" real
volume create "outer_vol_3" stitch "face.221" "face.220" "face.224" \
"face.225" "face.213" "face.214" "face.227" "face.200" "face.19" \
"face.170" "face.143" "face.202" real
volume create "Vol_above_stirrer_4" stitch "face.183" "face.182" "face.188" \
"face.169" "face.192" "face.181" real
volume create "wing_top_4" stitch "face.188" "face.195" "face.187" "face.189" \
"face.168" "face.190" real
volume create "Wing_lower" stitch "face.187" "face.184" "face.167" "face.186" \
"face.185" "face.175" real
volume modify "Wing_lower" label "Wing_lower_4"
volume create "inner_vol_upper_4" stitch "face.191" "face.179" "face.194" \
"face.37" "face.189" "face.182" "face.193" real
volume create "inner_vol_lower_4" stitch "face.196" "face.198" "face.16" \
"face.186" "face.194" "face.197" real
volume create "outer_vol_4" stitch "face.174" "face.192" "face.184" \
"face.195" "face.191" "face.196" "face.185" "face.172" "face.12" "face.198" \
"face.171" "face.170" real
undo begingroup
vertex create coordinates 0 0 0.0755
undo endgroup
vertex delete "vertex.35"
physics delete "Fluid interior" btype
physics delete "Stirrer interior" btype
physics create "Stirrer wall" btype "WALL" face "face.163" "face.157" \
"face.156" "face.154" "face.152" "face.153" "face.81" "face.82" "face.80" \
"face.124" "face.96" "face.90" "face.132" "face.122" "face.54" "face.149" \
"face.172" "face.5" "face.165" "face.197" "face.193" "face.173" "face.186" \
"face.189" "face.188" "face.224" "face.195" "face.213" "face.184" \
"face.185" "face.214" "face.218" "face.217" "face.226" "face.215" \
"face.222" "face.201" "face.200" "face.139" "face.140" "face.7"
physics create "Vessel Wall" btype "WALL" face "face.3" "face.9" "face.36" \
"face.66" "face.171" "face.174" "face.179" "face.212" "face.183" "face.199" \
"face.202" "face.208" "face.138" "face.141" "face.147" "face.151"
physics delete "new_Vessel Wall" btype
volume create "stirrer_shaft_3" stitch "face.222" "face.201" "face.205" \
"face.206" "face.219" "face.210" "face.226" "face.203" "face.200" real
volume create "stirrer_shaft_4" stitch "face.193" "face.173" "face.177" \
"face.206" "face.181" "face.190" "face.175" "face.172" "face.197" real
physics create "Stirrer" ctype "SOLID" volume "shaft_lower" "shaft_lower_2" \
"stirrer_shaft_3" "stirrer_shaft_4" "wing_lower" "wing_upper" \
"wing_upper_2" "sing_lower_2" "Wing_upper_3" "Wing_lower_3" "wing_top_4" \

```



```

"Wing_lower_4"
physics create "Vessel_fluid" ctype "FLUID" volume "vol_above_wing" \
"inside_vol_lower" "outside_vol" "inside_vol_upper" "Vol_above_wing_2" \
"inner_vol_lower" "inner_vol_upper_2" "outer_vol_2" "Vol_above_wing_3" \
"inner_vol_lower_3" "inner_vol_upper_3" "outer_vol_3" "Vol_above_stirrer_4" \
"inner_vol_upper_4" "inner_vol_lower_4" "outer_vol_4" \
edge picklink "edge.391" "edge.223" "edge.181" "edge.340" "edge.404" \
"edge.265" "edge.324" "edge.164" "edge.372" "edge.267" "edge.246" \
"edge.416" "edge.239" "edge.413" "edge.185" "edge.415" "edge.169" \
"edge.368"
edge mesh "edge.368" "edge.169" "edge.415" "edge.185" "edge.413" "edge.239" \
"edge.416" "edge.246" "edge.267" "edge.372" "edge.164" "edge.324" \
"edge.265" "edge.404" "edge.340" "edge.181" "edge.223" "edge.391" \
successive ratio 1 intervals 3
edge picklink "edge.309"
edge mesh "edge.309" successive ratio 1 intervals 8
edge picklink "edge.377"
edge mesh "edge.377" successive ratio 1 intervals 18
edge picklink "edge.688"
edge mesh "edge.688" successive ratio 1 intervals 18
edge picklink "edge.311" "edge.569"
edge mesh "edge.569" "edge.311" successive ratio 1 intervals 8
edge picklink "edge.420"
edge mesh "edge.420" successive ratio 1 intervals 38
window matrix 1 entries 0.9986874461174 -0.007694563828409 0.0506381355226 \
0.001076618558727 -0.04715602472425 0.2477908283472 0.9676652550697 \
0.0211363825947 -0.01999342627823 -0.9687831401825 0.2471027374268 \
-0.003027009777725 -0.08586810529232 0.1902461051941 -0.08255008608103 \
0.07756884396076 -0.1387193799019 0.1387193799019
edge picklink "edge.378"
edge mesh "edge.378" successive ratio 1 intervals 22
edge picklink "edge.401"
edge mesh "edge.401" successive ratio 1 intervals 10
undo begingroup
edge delete "edge.309" keepsettings onlymesh
edge mesh "edge.309" successive ratio 1 intervals 9
edge delete "edge.169" "edge.368" "edge.391" "edge.223" "edge.181" "edge.340" \
"edge.404" "edge.265" "edge.324" "edge.164" "edge.372" "edge.267" \
"edge.246" "edge.416" "edge.239" "edge.413" "edge.185" "edge.415" \
keepsettings onlymesh
edge mesh "edge.169" "edge.368" "edge.391" "edge.223" "edge.181" "edge.340" \
"edge.404" "edge.265" "edge.324" "edge.164" "edge.372" "edge.267" \
"edge.246" "edge.416" "edge.239" "edge.413" "edge.185" "edge.415" \
successive ratio 1 intervals 2
edge delete "edge.309" keepsettings onlymesh
edge mesh "edge.309" successive ratio 1 intervals 8
undo endgroup
face mesh "face.139" triprimitive
face mesh "face.166" pave
face mesh "face.153" map
face mesh "face.152" map
face mesh "face.163" "face.160" map
face mesh "face.164" map
face delete "face.159" lowertopology onlymesh
face mesh "face.159" map
face mesh "face.80" "face.124" map
face mesh "face.115" map
edge delete "edge.446" keepsettings onlymesh
edge picklink "edge.446"
edge mesh "edge.446" successive ratio 1 intervals 16
volume mesh "Outer_vol_2" submap
edge mesh "edge.705" "edge.696" successive ratio 1 intervals 8
volume mesh "wing_lower_2" map
window modify 1 AND 2 AND 3 AND 4 invisible mesh
volume delete "wing_upper_2" lowertopology onlymesh
volume mesh "wing_upper_2" map
volume delete "Vol_above_wing_2" lowertopology onlymesh
volume mesh "Vol_above_wing_2" map
volume mesh "inner_vol_lower" cooper source "face.162" "face.166"
volume mesh "inner_vol_upper_2" cooper source "face.147" "face.162"
window modify 1 AND 2 AND 3 AND 4 visible mesh
volume delete "wing_upper_2" "wing_lower_2" lowertopology onlymesh
face mesh "face.81" map
face mesh "face.90" map
face mesh "face.96" map
volume mesh "vol_above_wing" map
undo begingroup
edge delete "edge.22" keepsettings onlymesh
edge picklink "edge.22"
edge mesh "edge.22" successive ratio 1 intervals 18
edge delete "edge.284" keepsettings onlymesh
edge picklink "edge.284"
edge mesh "edge.284" successive ratio 1 intervals 38
edge delete "edge.283" keepsettings onlymesh
edge picklink "edge.283"
edge mesh "edge.283" successive ratio 1 intervals 8
edge delete "edge.451" "edge.454" keepsettings onlymesh
edge picklink "edge.454" "edge.451"
edge mesh "edge.451" "edge.454" successive ratio 1 intervals 8
edge delete "edge.559" "edge.570" keepsettings onlymesh
edge picklink "edge.570" "edge.559"
edge mesh "edge.559" "edge.570" successive ratio 1 intervals 8
edge delete "edge.514" "edge.686" keepsettings onlymesh
edge picklink "edge.686" "edge.514"
edge mesh "edge.514" "edge.686" successive ratio 1 intervals 18
edge delete "edge.557" "edge.679" keepsettings onlymesh
edge picklink "edge.679" "edge.557"
edge mesh "edge.557" "edge.679" successive ratio 1 intervals 38
face mesh "face.5" triprimitive
edge delete "edge.174" keepsettings onlymesh
edge picklink "edge.174"
edge mesh "edge.174" successive ratio 1 intervals 22

```

```

edge delete "edge.513" "edge.639" keepsettings onlymesh
edge picklink "edge.639" "edge.513"
edge mesh "edge.513" "edge.639" successive ratio1 1 intervals 22
volume mesh "inside_vol_upper" cooper source "face.36" "face.123"
face mesh "face.9" map
face delete "face.12" onlymesh
face modify "face.12" map
face summarize "face.141"
face mesh "face.172" triprimitive
face mesh "face.198" pave
window modify 1 AND 2 AND 3 AND 4 visible mesh
window modify 1 AND 2 AND 3 AND 4 invisible mesh
face mesh "face.185" map
edge delete "edge.504" keepsettings onlymesh
edge picklink "edge.504"
edge mesh "edge.504" successive ratio1 1 intervals 22
face mesh "face.184" map
edge delete "edge.553" "edge.522" "edge.661" "edge.657" keepsettings onlymesh
edge picklink "edge.657" "edge.661" "edge.522" "edge.553"
edge mesh "edge.553" "edge.522" "edge.661" "edge.657" successive ratio1 1 \
intervals 2
edge delete "edge.496" "edge.620" keepsettings onlymesh
edge picklink "edge.620" "edge.496"
edge mesh "edge.496" "edge.620" successive ratio1 1 intervals 18
undo endgroup
face mesh "face.195" "face.224" map
face mesh "face.188" "face.217" map
face mesh "face.182" map
face mesh "face.189" map
face mesh "face.218" map
edge delete "edge.341" "edge.443" keepsettings onlymesh
edge picklink "edge.443" "edge.341"
edge mesh "edge.341" "edge.443" successive ratio1 1 intervals 10
volume mesh "Vol_above_wing_3" "Vol_above_stirrer_4" map
face mesh "face.213" "face.214" map
volume mesh "inner_vol_lower_4" cooper source "face.194" "face.198"
volume mesh "inner_vol_upper_4" cooper source "face.194" "face.179"
edge delete "edge.694" "edge.711" keepsettings onlymesh
window modify 1 AND 2 AND 3 AND 4 visible mesh
volume mesh "inner_vol_lower_4" cooper source "face.198" "face.194"
volume mesh "inner_vol_upper_4" cooper
face mesh "face.253" triprimitive
face mesh "face.254" map
face mesh "face.174" map
volume mesh "Outer_vol_4" cooper source "face.253" "face.198" "face.172" \
"face.255" "face.191" "face.196" "face.185" "face.184" "face.195" \
"face.192"
volume mesh "Outer_vol_4" cooper source "face.253" "face.198" "face.172" \
"face.255" "face.191" "face.196" "face.185" "face.184" "face.195" \
"face.192"
volume mesh "Outer_vol_4" cooper source "face.253" "face.198" "face.172" \
"face.255" "face.191" "face.196" "face.185" "face.184" "face.195" \
"face.192"
volume mesh "Outer_vol_4" cooper source "face.253" "face.198" "face.172" \
"face.255" "face.191" "face.196" "face.185" "face.184" "face.195" \
"face.192"
volume mesh "Outer_vol_4" cooper source "face.253" "face.198" "face.172" \
"face.255" "face.191" "face.196" "face.185" "face.184" "face.195" \
"face.192"
face mesh "face.227" pave
volume mesh "Inner_vol_lower_3" cooper source "face.227" "face.223"
volume mesh "Inner_vol_upper_3" cooper source "face.223" "face.208"
vertex delete "vertex.8"
vertex delete "vertex.9" "vertex.239"
vertex delete "vertex.19"
face delete "face.174" lowertopology onlymesh
face delete "face.9" lowertopology onlymesh
volume delete "inside_vol_upper" lowertopology onlymesh
face mesh "face.200" triprimitive
volume mesh "Vol_above_wing_2" map
volume mesh "vol_above_wing" map
face delete "face.81" lowertopology onlymesh
face mesh "face.152" "face.153" map
face mesh "face.81" map
face mesh "face.163" map
face mesh "face.133" pave
face mesh "face.96" map
volume mesh "inside_vol_lower" cooper source "face.133" "face.123"
volume mesh "inside_vol_upper" cooper source "face.36" "face.123"
window modify 1 AND 2 AND 3 AND 4 noshade
default set "GRAPHICS.GENERAL.CONNECTIVITY_BASED_COLORING" numeric 0
default set "GRAPHICS.GENERAL.CONNECTIVITY_BASED_COLORING" numeric 1
default set "GRAPHICS.GENERAL.CONNECTIVITY_BASED_COLORING" numeric 0
default set "GRAPHICS.GENERAL.CONNECTIVITY_BASED_COLORING" numeric 1
default set "GRAPHICS.GENERAL.CONNECTIVITY_BASED_COLORING" numeric 1
edge delete "edge.265" lowertopology onlymesh
edge delete "edge.446" lowertopology onlymesh
undo begingroup
edge delete "edge.444" keepsettings onlymesh
edge picklink "edge.444"
edge mesh "edge.444" successive ratio1 1 intervals 30
undo endgroup
undo begingroup
edge delete "edge.446" keepsettings onlymesh
edge mesh "edge.446" successive ratio1 1 intervals 30
undo endgroup
face mesh "face.170" submap
face mesh "face.143" map
face mesh "face.202" map

```



```

volume mesh "outer_vol_3" cooper source "face.199" "face.227" "face.200" \
"face.214" "face.224" "face.221" "face.225" "face.213" "face.220"
face mesh "face.141" map
face mesh "rotateouter face" map
volume mesh "outer_vol_2" cooper source "face.139" "face.166" "face.138" \
"face.153" "face.152" "face.163" "face.164" "face.159" "face.160"
face mesh "face.9" map
face mesh "face.12" submap
volume mesh "outside_vol" cooper source "face.5" "face.3" "face.133" \
"face.131" "face.81" "face.114" "face.80" "face.115" "face.124"
face mesh "face.174" map
volume mesh "outer_vol_4" cooper source "face.198" "face.172" "face.171" \
"face.185" "face.191" "face.192" "face.196" "face.184" "face.195"
vertex create coordinates 0 0 0.0755
edge create straight "vertex.347" "vertex.577"
volume create translate "face.9" "face.36" "face.66" "face.141" "face.147" \
"face.151" "face.7" "face.140" "face.202" "face.208" "face.212" "face.201" \
"face.174" "face.179" "face.173" onedge "edge.689"
blayer create first 0.0003 growth 1.3 total 0.0018561 rows 4 transition 1 \
trows 0
blayer attach "b_layer.1" face "face.229" edge "edge.695"
blayer create first 0.0003 growth 1.3 total 0.0018561 rows 4 transition 1 \
trows 0
blayer attach "b_layer.2" face "face.289" edge "edge.797"
blayer create first 0.0003 growth 1.3 total 0.0018561 rows 4 transition 1 \
trows 0
blayer attach "b_layer.3" face "face.237" edge "edge.706"
blayer create first 0.0003 growth 1.3 total 0.0018561 rows 4 transition 1 \
trows 0
blayer attach "b_layer.4" face "face.288" edge "edge.796"
blayer create first 0.0003 growth 1.3 total 0.0018561 rows 4 transition 1 \
trows 0
blayer attach "b_layer.5" face "face.286" edge "edge.791"
blayer create first 0.0003 growth 1.3 total 0.0018561 rows 4 transition 1 \
trows 0
blayer attach "b_layer.6" face "face.283" edge "edge.788"
blayer create first 0.0003 growth 1.3 total 0.0018561 rows 4 transition 1 \
trows 0
blayer attach "b_layer.7" face "face.285" edge "edge.790"
blayer create first 0.0003 growth 1.3 total 0.0018561 rows 4 transition 1 \
trows 0
blayer attach "b_layer.8" face "face.267" edge "edge.759"
blayer create first 0.0003 growth 1.3 total 0.0018561 rows 4 transition 1 \
trows 0
blayer attach "b_layer.9" face "face.293" edge "edge.804"
blayer create first 0.0003 growth 1.3 total 0.0018561 rows 4 transition 1 \
trows 0
blayer attach "b_layer.10" face "face.277" edge "edge.775"
blayer create first 0.0003 growth 1.3 total 0.0018561 rows 4 transition 1 \
trows 0
blayer attach "b_layer.11" face "face.273" edge "edge.768"
blayer create first 0.0003 growth 1.3 total 0.0018561 rows 4 transition 1 \
trows 0
blayer attach "b_layer.12" face "face.276" edge "edge.774"
blayer create first 0.0003 growth 1.3 total 0.0018561 rows 4 transition 1 \
trows 0
blayer attach "b_layer.13" face "face.270" edge "edge.765"
blayer create first 0.0003 growth 1.3 total 0.0018561 rows 4 transition 1 \
trows 0
blayer attach "b_layer.14" face "face.266" edge "edge.758"
blayer create first 0.0003 growth 1.3 total 0.0018561 rows 4 transition 1 \
trows 0
blayer attach "b_layer.15" face "face.265" edge "edge.757"
blayer create first 0.0003 growth 1.3 total 0.0018561 rows 4 transition 1 \
trows 0
blayer attach "b_layer.16" face "face.268" edge "edge.760"
blayer create first 0.0003 growth 1.3 total 0.0018561 rows 4 transition 1 \
trows 0
blayer attach "b_layer.17" face "face.252" edge "edge.731"
blayer create first 0.0003 growth 1.3 total 0.0018561 rows 4 transition 1 \
trows 0
blayer attach "b_layer.18" face "face.244" edge "edge.720"
blayer create first 0.0003 growth 1.3 total 0.0018561 rows 4 transition 1 \
trows 0
blayer attach "b_layer.19" face "face.251" edge "edge.730"
blayer create first 0.0003 growth 1.3 total 0.0018561 rows 4 transition 1 \
trows 0
blayer attach "b_layer.20" face "face.248" edge "edge.724"
blayer create first 0.0003 growth 1.3 total 0.0018561 rows 4 transition 1 \
trows 0
blayer attach "b_layer.21" face "face.245" edge "edge.721"
blayer create first 0.0003 growth 1.3 total 0.0018561 rows 4 transition 1 \
trows 0
blayer attach "b_layer.22" face "face.257" edge "edge.739"
blayer create first 0.0003 growth 1.3 total 0.0018561 rows 4 transition 1 \
trows 0
blayer attach "b_layer.23" face "face.241" edge "edge.713"
blayer create first 0.0003 growth 1.3 total 0.0018561 rows 4 transition 1 \
trows 0
blayer attach "b_layer.24" face "face.250" edge "edge.729"
blayer create first 0.0003 growth 1.3 total 0.0018561 rows 4 transition 1 \
trows 0
blayer attach "b_layer.25" face "face.242" edge "edge.714"
blayer create first 0.0003 growth 1.3 total 0.0018561 rows 4 transition 1 \
trows 0
blayer attach "b_layer.26" face "face.235" edge "edge.704"
blayer create first 0.0003 growth 1.3 total 0.0018561 rows 4 transition 1 \
trows 0
blayer attach "b_layer.27" face "face.238" edge "edge.707"
blayer create first 0.0003 growth 1.3 total 0.0018561 rows 4 transition 1 \
trows 0
blayer attach "b_layer.28" face "face.247" "face.231" edge "edge.723" \

```

```

"edge.697"
blayer create first 0.0003 growth 1.3 total 0.0018561 rows 4 transition 1 \
trows 0
blayer attach "b_layer.29" face "face.232" edge "edge.698"
blayer create first 0.0003 growth 1.3 total 0.0018561 rows 4 transition 1 \
trows 0
blayer attach "b_layer.30" face "face.230" edge "edge.696"
blayer create first 0.0003 growth 1.3 total 0.0018561 rows 4 transition 1 \
trows 0
blayer attach "b_layer.31" face "face.233" edge "edge.699"
volume mesh "volume.42" map intervals 40
blayer modify "b_layer.1" growth 1.5 total 0.00395625 rows 5
blayer attach "b_layer.1" face "face.229" edge "edge.695"
graphics resume
blayer modify "b_layer.1" growth 1.5 total 0.0024375
blayer attach "b_layer.1" face "face.229" edge "edge.695"
blayer modify "b_layer.1" growth 1.7 total 0.0031509
blayer attach "b_layer.1" face "face.229" edge "edge.695"
blayer modify "b_layer.6" growth 1.7 total 0.0031509
blayer attach "b_layer.6" face "face.283" edge "edge.788"
blayer modify "b_layer.5" growth 1.7 total 0.0031509
blayer attach "b_layer.5" face "face.286" edge "edge.791"
blayer modify "b_layer.3" growth 1.7 total 0.0031509
blayer attach "b_layer.3" face "face.237" edge "edge.706"
blayer modify "b_layer.4" growth 1.7 total 0.0031509
blayer attach "b_layer.4" face "face.288" edge "edge.796"
blayer modify "b_layer.8" growth 1.7 total 0.0031509
blayer attach "b_layer.8" face "face.267" edge "edge.759"
blayer modify "b_layer.16" growth 1.7 total 0.0031509
blayer attach "b_layer.16" face "face.268" edge "edge.760"
blayer modify "b_layer.7" growth 1.7 total 0.0031509
blayer attach "b_layer.7" face "face.285" edge "edge.790"
blayer modify "b_layer.10" growth 1.7 total 0.0031509
blayer attach "b_layer.10" face "face.277" edge "edge.775"
blayer modify "b_layer.14" growth 1.7 total 0.0031509
blayer attach "b_layer.14" face "face.266" edge "edge.758"
blayer modify "b_layer.13" growth 1.7 total 0.0031509
blayer attach "b_layer.13" face "face.270" edge "edge.765"
blayer modify "b_layer.15" growth 1.7 total 0.0031509
blayer attach "b_layer.15" face "face.265" edge "edge.757"
blayer modify "b_layer.9" growth 1.7 total 0.0031509
blayer attach "b_layer.9" face "face.293" edge "edge.804"
blayer modify "b_layer.12" growth 1.7 total 0.0031509
blayer attach "b_layer.12" face "face.276" edge "edge.774"
blayer modify "b_layer.9" growth 1.7 total 0.0031509
blayer attach "b_layer.9" face "face.293" edge "edge.804"
blayer modify "b_layer.11" growth 1.7 total 0.0031509
blayer attach "b_layer.11" face "face.273" edge "edge.768"
blayer modify "b_layer.17" growth 1.7 total 0.0031509
blayer attach "b_layer.17" face "face.252" edge "edge.731"
blayer modify "b_layer.19" growth 1.7 total 0.0031509
blayer attach "b_layer.19" face "face.251" edge "edge.730"
blayer modify "b_layer.22" growth 1.7 total 0.0031509
blayer attach "b_layer.22" face "face.257" edge "edge.739"
blayer modify "b_layer.24" growth 1.7 total 0.0031509
blayer attach "b_layer.24" face "face.250" edge "edge.729"
blayer modify "b_layer.25" growth 1.7 total 0.0031509
blayer attach "b_layer.25" face "face.242" edge "edge.714"
blayer modify "b_layer.23" growth 1.7 total 0.0031509
blayer attach "b_layer.23" face "face.241" edge "edge.713"
blayer modify "b_layer.26" growth 1.7 total 0.0031509
blayer attach "b_layer.26" face "face.235" edge "edge.704"
blayer modify "b_layer.27" growth 1.7 total 0.0031509
blayer attach "b_layer.27" face "face.238" edge "edge.707"
blayer modify "b_layer.2" growth 1.7 total 0.0031509
blayer attach "b_layer.2" face "face.289" edge "edge.797"
blayer modify "b_layer.18" growth 1.7 total 0.0031509
blayer attach "b_layer.18" face "face.244" edge "edge.720"
blayer modify "b_layer.20" growth 1.7 total 0.0031509
blayer attach "b_layer.20" face "face.248" edge "edge.724"
blayer modify "b_layer.21" growth 1.7 total 0.0031509
blayer attach "b_layer.21" face "face.245" edge "edge.721"
blayer modify "b_layer.29" growth 1.7 total 0.0031509
blayer attach "b_layer.29" face "face.232" edge "edge.698"
graphics resume
graphics pause
blayer modify "b_layer.28" growth 1.7 total 0.0031509
blayer attach "b_layer.28" face "face.247" "face.231" edge "edge.723" \
"edge.697"
blayer create first 0.0003 growth 1.3 total 0.0018561 rows 4 transition 1 \
trows 0
blayer attach "b_layer.30" face "face.230" edge "edge.696"
blayer create first 0.0003 growth 1.7 total 0.0031509 rows 4 transition 1 \
trows 0
blayer attach "b_layer.30" face "face.230" edge "edge.696"
blayer create first 0.0003 growth 1.7 total 0.0031509 rows 4 transition 1 \
trows 0
blayer attach "b_layer.31" face "face.233" edge "edge.699"
volume mesh "volume.45" "volume.42" map intervals 40
volume mesh "volume.50" map intervals 40
window modify 1 AND 2 AND 3 AND 4 invisible mesh
face create wireframe "edge.775" "edge.804" "edge.796" "edge.790" real
volume create stitch "face.288" "face.183" "face.285" "face.293" "face.277" \
"face.294" real
window modify 1 AND 2 AND 3 AND 4 visible mesh
volume mesh "volume.55" map
volume mesh "volume.41" cooper source "face.36" "face.234"
volume mesh "volume.40" map
volume mesh "volume.53" cooper source "face.179" "face.287"
volume mesh "volume.52" map
volume mesh "volume.48" "volume.49" cooper
volume mesh "volume.44" cooper source "face.249" "face.147"

```



```

volume mesh "volume.43" map
physics modify "Vessel Wall" btype face "face.3" "face.138" "face.199" \
"face.171" "face.233" "face.245" "face.268" "face.283" "face.263" \
"face.269" "face.274" "face.243" "face.249" "face.253" "face.228" \
"face.234" "face.239" "face.281" "face.287" "face.294"
window modify 1 AND 2 AND 3 AND 4 invisible mesh
physics delete "Stirrer_wall" btype
physics modify "Stirrer Wall" btype face "face.122" "face.132" "face.124" \
"face.80" "face.96" "face.90" "face.54" "face.81" "face.5" "face.153" \
"face.154" "face.152" "face.163" "face.157" "face.149" "face.156" \
"face.139" "face.165" "face.161" "face.200" "face.226" "face.222" \
"face.214" "face.215" "face.218" "face.210" "face.217" "face.213" \
"face.224" "face.185" "face.184" "face.195" "face.188" "face.186" \
"face.189" "face.181" "face.172" "face.197" "face.193" "face.293" \
"face.289" "face.238" "face.241" "face.257" "face.251"
physics modify "Stirrer Wall" btype face "face.81" "face.122" "face.132" \
"face.124" "face.80" "face.96" "face.90" "face.54" "face.5" "face.153" \
"face.154" "face.152" "face.163" "face.157" "face.149" "face.156" \
"face.139" "face.165" "face.161" "face.200" "face.226" "face.222" \
"face.214" "face.215" "face.218" "face.210" "face.217" "face.213" \
"face.224" "face.185" "face.184" "face.195" "face.188" "face.186" \
"face.189" "face.181" "face.172" "face.197" "face.193" "face.293" \
"face.289" "face.238" "face.241" "face.257" "face.251" "face.261" \
"face.258" "face.290" "face.278" "face.273" "face.276"
physics modify "Stirrer Wall" btype face "face.81" "face.122" "face.132" \
"face.124" "face.80" "face.96" "face.90" "face.54" "face.5" "face.153" \
"face.154" "face.152" "face.163" "face.157" "face.149" "face.156" \
"face.139" "face.165" "face.161" "face.200" "face.226" "face.222" \
"face.214" "face.215" "face.218" "face.210" "face.217" "face.213" \
"face.224" "face.185" "face.184" "face.195" "face.188" "face.186" \
"face.189" "face.181" "face.172" "face.197" "face.193" "face.293" \
"face.289" "face.238" "face.241" "face.257" "face.251" "face.261" \
"face.258" "face.290" "face.278" "face.273" "face.276" "face.82"
window modify 1 AND 2 AND 3 AND 4 visible mesh
volume delete "volume.43" "volume.40" "volume.52" "volume.48" onlymesh
face delete "face.228" "face.243" "face.232" "face.229" "face.281" "face.263" \
"face.267" "face.245" "face.233" "face.283" "face.268" lowertopology onlymesh
volume delete "outside_vol" "outer_vol_3" "outer_vol_4" "outer_vol_2" onlymesh
face delete "rotateouter face" "face.232" "face.141" "face.9" "face.143" \
"face.202" "face.244" "face.268" "face.245" onlymesh
face delete "face.3" onlymesh
face delete "face.9" "face.141" lowertopology onlymesh
face delete "face.9" "face.3" "face.138" lowertopology onlymesh
face delete "face.199" lowertopology onlymesh
face delete "face.171" lowertopology onlymesh
face delete "face.171" lowertopology onlymesh
face delete "face.171" "face.283" "face.174" lowertopology onlymesh
face delete "face.170" lowertopology onlymesh
face delete "face.12" lowertopology onlymesh
blayer create first 0.0002 growth 1.5 total 0.001625 rows 4 transition 1 \
trows 0
blayer attach "b_layer.32" face "face.12" edge "edge.14"
blayer create first 0.0002 growth 1.5 total 0.001625 rows 4 transition 1 \
trows 0
blayer attach "b_layer.33" face "face.174" edge "edge.449"
blayer create first 0.0002 growth 1.5 total 0.001625 rows 4 transition 1 \
trows 0
blayer attach "b_layer.34" face "face.170" edge "edge.450"
blayer create first 0.0002 growth 1.5 total 0.001625 rows 4 transition 1 \
trows 0
blayer attach "b_layer.35" face "face.202" edge "edge.568"
blayer create first 0.0002 growth 1.5 total 0.001625 rows 4 transition 1 \
trows 0
blayer attach "b_layer.36" face "face.143" edge "edge.566"
blayer create first 0.0002 growth 1.5 total 0.001625 rows 4 transition 1 \
trows 0
blayer attach "b_layer.37" face "face.141" edge "edge.306"
blayer create first 0.0002 growth 1.5 total 0.001625 rows 4 transition 1 \
trows 0
blayer attach "b_layer.38" face "rotateouter face" edge "edge.307"
blayer create first 0.0002 growth 1.5 total 0.001625 rows 4 transition 1 \
trows 0
blayer attach "b_layer.39" face "face.9" edge "edge.13"
edge picklink "edge.30"
edge mesh "edge.30" successive ratio 1 intervals 22
face mesh "face.174" map size 1
volume mesh "outer_vol_4" cooper source "face.198" "face.196" "face.172" \
"face.185" "face.184" "face.195" "face.171" "face.191" "face.192" size 1
volume mesh "outer_vol_3" cooper source "face.227" "face.225" "face.200" \
"face.214" "face.213" "face.199" "face.220" "face.224" "face.221" size 1
volume mesh "outer_vol_2" cooper source "face.152" "face.163" "face.153" \
"face.164" "face.139" "face.166" "face.159" "face.160" "face.138" size 1
volume mesh "outside_vol" cooper source "face.124" "face.114" "face.80" \
"face.115" "face.131" "face.81" "face.5" "face.3" "face.133" size 1
window modify 1 AND 2 AND 3 AND 4 invisible mesh
blayer create first 0.0002 growth 1.5 total 0.001625 rows 4 transition 1 \
trows 0
blayer attach "b_layer.40" face "face.243" edge "edge.721"
blayer create first 0.0002 growth 1.5 total 0.001625 rows 4 transition 1 \
trows 0
blayer attach "b_layer.41" face "face.228" edge "edge.699"
blayer create first 0.0002 growth 1.5 total 0.001625 rows 4 transition 1 \
trows 0
blayer attach "b_layer.42" face "face.281" edge "edge.788"
blayer create first 0.0002 growth 1.5 total 0.001625 rows 4 transition 1 \
trows 0
blayer attach "b_layer.43" face "face.263" edge "edge.760"
undo endgroupvolume mesh "volume.41" cooper source "face.36" "face.234" size 40
volume mesh "volume.40" map
volume mesh "volume.52" map
window modify 1 AND 2 AND 3 AND 4 visible mesh
edge delete "edge.716" lowertopology onlymesh

```

```
edge delete "edge.720" lowertopology onlimesh
volume mesh "volume.48" map
volume mesh "volume.43" map
window modify 1 AND 2 AND 3 AND 4 invisible mesh
physics modify "Stirrer" ctype volume "shaft_lower" "shaft_lower_2" \
  "stirrer_shaft_3" "stirrer_shaft_4" "wing_lower" "wing_upper" \
  "wing_upper_2" "sing_lower_2" "Wing_upper_3" "Wing_lower_3" "wing_top_4" \
  "Wing_lower_4" "volume.46" "volume.54" "volume.51" "volume.47"
physics modify "Vessel_fluid" ctype volume "vol_above_wing" \
  "inside_vol_lower" "outside_vol" "inside_vol_upper" "Vol_above_wing_2" \
  "inner_vol_lower" "inner_vol_upper_2" "outer_vol_2" "Vol_above_wing_3" \
  "Inner_vol_lower_3" "Inner_vol_upper_3" "outer_vol_3" "Vol_above_stirrer_4" \
  "inner_vol_upper_4" "inner_vol_lower_4" "outer_vol_4" "volume.41" \
  "volume.42" "volume.40" "volume.53" "volume.55" "volume.52" "volume.50" \
  "volume.49" "volume.48" "volume.45" "volume.44" "volume.43"
solver select "FLUENT 5"
export uns "new_no_compact_bndry.msh"
```

APPENDIX 7

Unix code 1

Unix journal file to allow Fluent program to run iterations in parallel in background mode

Filename: run.jou

```
rcd unstructured_grid.cas
(iterate 500)
wd unstructured_grid_500.dat
(iterate 500)
wcd unstructured_grid_1000.dat
```

The code is initiated to run Fluent in parallel by typing the following command on the Fluent processor system:

```
FLUENT 3ddp -t4 -p -g < run.jou > & log_output
```

Once initiated, the 3-dimensional solver of Fluent is run using double precision in background mode. The file 'unstructured_grid' is run for 500 iterations and the results are saved as 'unstructured_grid_500.cas'. After a further 500 iterations, the resulting case and data files are saved as 'unstructured_grid_1000.cas' and 'unstructured_grid_2000.dat', respectively. (Note - If the default convergence criteria are met before this time, the data is saved automatically).

APPENDIX 8

Unix code 2

Unix journal file to allow Fluent program to run iterations in parallel via the Loadleveler queue system on the IBM SP system

Filename: fluent_parallel.cmd

```

#@ group          = tsphe
#@ job_name       = unstructured_grid
#@ class         = medium
#@ min_processors = 9
#@ max_processors = 9
#@ notify_user    = mccarthl@tcd.ie
#@ executable     = /usr/support/Fluent.Inc/bin/fluent
#@ initialdir    = /tcdhomea/tsphe/mccarthl/USP_NO_COMPACT
#@ arguments     = 3ddp -p -t9 -g
#@ requirements   = ( Memory >= 512 )
#@ wall_clock_limit = 16:00:00
#
# -----
#
#@ job_type       = parallel
#@ network.MPI    = css0,shared,US
#@ input          = run.jou
#@ output         = $(job_name).$(jobid).out
#@ error          = $(job_name).$(jobid).err
#@ environment    = COPY_ALL;\
                  FLUENT_INC=/usr/support/Fluent.Inc;
#@ notification   = complete
#@ queue
#

```

The code is initiated to enter the Loadleveler queue by typing the following command on the IBM SP Fluent processor system:

```
llsubmit no_compact.cmd
```

Once initiated, the system is informed to run the filename 'run.jou' as previously described in Appendix 7, after entering into the Loadleveler queue system.

APPENDIX 9

Unix code 3

Program to read velocity co-ordinates from a virtual cylindrical geometry at various distances outside the curved surface of a cylindrical compact in the paddle dissolution apparatus and to determine the average velocity for various heights within the virtual cylinder

The program (CYLINDERS) was written in C code by Dr. Geoff Bradley, Trinity Centre for High Performance Computing, Trinity College Dublin.

```

#include <stdio.h>
#include <math.h>
int main(int argc, char **argv) {
    int i,j,nodes;
    int strips = 0;
    int *zavs;
    double *x, *y, *z, *v;
    double rav = 0.0;
    double *zbits;
    double zmin = 0.0, zmax = 0.0, zextent = 0.0;
    double zmax_in = 0.0;
    char filename[128] = "0.025mm_axial";
    FILE *input_fp;
    input_fp = fopen(filename, "r");
    if ( input_fp == NULL ) {fprintf(stderr, "Error opening file %s
for reading.\n",filename);exit(2);}
    if ( fscanf(input_fp,"%*s %*s %d %*s",&nodes) != 1 )
    {fprintf(stderr, "Error reading in no. of nodes from file
%s",filename);exit(2);}
    printf("Nodes %d\n",nodes);

    /* Allocate memory to hold data for x, y, z, and v */
    if( (x = (double *)malloc(sizeof(double) * nodes)) == NULL ||
        (y = (double *)malloc(sizeof(double) * nodes)) == NULL ||
        (z = (double *)malloc(sizeof(double) * nodes)) == NULL ||
        (v = (double *)malloc(sizeof(double) * nodes)) == NULL )
        {fprintf(stderr, "Error allocating memory.\n");exit(2);}

    /* Readin X data */
    fscanf(input_fp, "%*s ");
    for(i=0;i<nodes;i++) {
        if ( fscanf(input_fp, "%lf ", &x[i]) != 1 )
            {fprintf(stderr,"Fatal error reading in element x[%d].
%f\n",i,x[i]);exit(2);}

    /* Readin Y data */
    fscanf(input_fp,"%*s %*s"); for(i=0;i<nodes;i++) {if (
    fscanf(input_fp, "%lf", &y[i]) != 1 ) {fprintf(stderr,"Fatal
error reading in element y[%d].\n",i);exit(2);}}

```

```

/* Readin Z data */
fscanf(input_fp,"%*s %*s");
for(i=0;i<nodes;i++) {if ( fscanf(input_fp, "%lf", &z[i]) != 1
) { fprintf(stderr,"Fatal error reading in element
z[%d].\n",i);exit(2);}}

/* Readin V data */
fscanf(input_fp,"%*s %*s");
for(i=0;i<nodes;i++) {if ( fscanf(input_fp, "%lf", &v[i]) != 1)
{fprintf(stderr,"Fatal error reading in element v[%d].\n",i);
exit(2);}}

/* Find the average radius of the cylinder */
for(i=0;i<nodes;i++)
{rav += Pow((x[i]*x[i]+y[i]*y[i]),0.5);}rav /= nodes;
printf("Radius of cylinder is %lf\n",rav);

/* Find the min and max z extent */
/* Set zmin and zmax */
zmin = z[0]; zmax = z[0];
for(i=1;i<nodes;i++) {
    if ( z[i] < zmin ) zmin = z[i];
    if ( z[i] > zmax ) zmax = z[i];}
printf("Zmin: %lf\tZmax: %lf\n",zmin,zmax);
printf("Enter the value of Zmax you wish to use ? ");
if (scanf("%lf",&zmax_in) != 1) {fprintf(stderr,"Error reading
in the value for zmax\n");exit(2);} else {if ( zmax_in > zmax
|| zmax_in < zmin ) {fprintf(stderr,"Error, zmax must be less
than %lf and more than %lf\n",zmax,zmin);exit(2);}zmax =
zmax_in;printf("Zmax modified to : %lf\n",zmax);}
zextent = zmax - zmin;

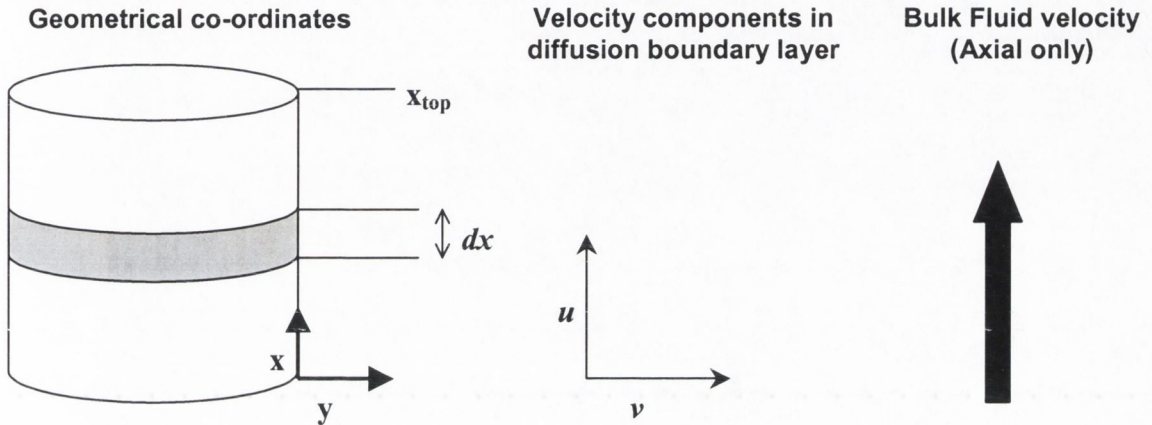
printf("How many cylindrical strips do you want to average over
? ");
if (scanf("%ld",&strips) != 1) {fprintf(stderr,"Error reading
in number of strips.\n");exit(2);}
printf("Averaging over %d strips.\n",strips);
if ( (zbits = (double *)malloc(sizeof(double) * strips)) ==
NULL) {fprintf(stderr,"Error allocating memory for zbits.\n");}
if ( (zavs = (int *)malloc(sizeof(int) * strips)) == NULL)
{fprintf(stderr,"Error allocating memory for zavs.\n");}

for(i=0;i<strips;i++) {zbits[i] = 0.0;zavs[i] = 0;
for(j=0;j<nodes;j++) {if ( (z[j] >= (zmin +
(zextent*i)/strips)) && (z[j] < (zmin +
(zextent*(i+1)/strips))) ) {zbits[i] += v[j];zavs[i] +=
1;}}zbits[i] /= zavs[i];printf("Zrange: %lf to %lf v
%lf\n", (zmin + (zextent*i)/strips), (zmin +
(zextent*(i+1)/strips)),zbits[i]);}return 0;

```


APPENDIX 10

Derivation of equation to determine mass transfer from curved surface of a cylinder



Mass flux (per unit surface area) from the curved surface of a cylinder in a fluid with bulk flow parallel to the surface in the axial direction only, as shown in the schematic above, can be defined as

$$D \left(\frac{dc}{dy} \right)_{y=0}$$

where D is the diffusion coefficient of the drug, c is the concentration of drug and y is the distance from the curved surface area. An area element of the curved surface can be defined as $2\pi a \cdot dx$, where a is the radius of the cylinder. Therefore the total flux of drug from the surface, R , can be defined as

$$R = 2\pi a \int_0^{x_{top}} D \left(\frac{dc}{dy} \right)_{y=0} dx \tag{Equation 1}$$

Therefore, it is necessary to determine $\frac{dc}{dy}$ in terms of x .

The convective diffusion equation in a diffusion boundary layer takes the form:

$$u \frac{dc}{dy} + v \frac{dc}{dy} = -D \frac{d^2c}{dy^2} \tag{Levich, 1962}$$

which is a partial differential equation for steady state diffusion in the diffusion boundary layer. Integration leads to the following:

$$\frac{d}{dx} \int_0^{\infty_{top}} u c dy = -D \left(\frac{dc}{dy} \right)_{y=0}$$

If we let $u = \alpha y$, where α is a function of the shear rate of velocity in the x direction at $y = 0$, then:

$$\frac{d}{dx} \int_0^{\infty_{top}} \alpha y c dy = -D \left(\frac{dc}{dy} \right)_{y=0}$$

A parabolic expression for the concentration in the hydrodynamic boundary layer can be defined as:

$$c = c_o e^{-y/\delta}$$

where δ is the thickness of the effective diffusion boundary layer and c_o is the concentration of drug at the solid surface. Therefore:

$$\frac{d}{dx} \int_0^{\infty} \alpha y c_o e^{-y/\delta} dy = D \frac{c_o}{\delta}$$

If we let $\eta = y/\delta$, then:

$$\frac{d}{dx} \left[\delta^2 \int_0^{\infty} \alpha \eta e^{-\eta} d\eta \right] = \frac{D}{\delta}$$

and

$$\frac{d}{dx} [\alpha \delta^2] = \frac{D}{\delta}$$

therefore:

$$\delta^3 \frac{d\alpha}{dx} + 2\alpha \delta^2 \frac{d\delta}{dx} = D$$

If we let $W = \delta^3$, then:

$$W \frac{d\alpha}{dx} + \frac{2}{3} \alpha \delta^2 \frac{dW}{dx} = D$$

and

$$W \frac{dW}{dx} + \frac{3}{2\alpha} \frac{d\alpha}{dx} W = \frac{3}{2\alpha} D$$

and

$$\alpha^{3/2} \frac{dW}{dx} + \frac{3}{2} \alpha^{1/2} \frac{d\alpha}{dx} W = \frac{3\alpha^{1/2}}{2} D$$

and

$$W\alpha^{3/2} = \frac{3}{2}D \left[\int \alpha^{1/2} dx \right]$$

therefore

$$W = \frac{3}{2}D \frac{1}{\alpha^{3/2}} \int \alpha^{1/2} dx$$

If we let

$$F(x) = \int \alpha^{1/2} dx$$

then

$$\delta = \left(\frac{3}{2} \right)^{1/3} D^{1/3} \frac{1}{\alpha^{1/2}} [F(x)]^{1/3}$$

which will allow determination of $\frac{dc}{dy}$ in terms in x, as :

$$\left(\frac{dc}{dy} \right)_{y=0} = \frac{c_o}{\delta}$$

Therefore, from Equation 1, the total flux of drug can be defined as:

$$\begin{aligned} R &= 2\pi a D c_o \int_0^{x_{top}} \frac{\left(\frac{2}{3} \right)^{1/3} D^{1/3} \alpha^{1/2}}{[F(x)]^{1/3}} \\ &= 2\pi a D^{2/3} c_o \left(\frac{2}{3} \right)^{1/3} \int_0^{x_{top}} \frac{dF}{[F(x)]^{1/3}} \\ &= 2\pi a D^{2/3} c_o \left(\frac{3}{2} \right)^{2/3} \int_0^{x_{top}} [F(x)]^{2/3} \end{aligned}$$

Therefore

$$R = 2\pi a c_o \left(\frac{3}{2} D F_o \right)^{2/3}$$

Where

$$F_o = \int_0^{x_{top}} \alpha^{1/2} dx$$

This expression allows determination of the mass transfer from the curved surface from intrinsic properties of the drug and the shear rates in the hydrodynamic layer immediately outside the compact.

APPENDIX 11

Dynochem process sheet example 1

Calculations involved in the prediction of mass transfer from a drug layer between two soluble acid excipient layers

PHASE	dr1	solid		
	pressure	1	bar	hide
	Temperature	37	C	hide
	CP	4200	J/kgK	hide
	Density	0	kg/m3	adjust
	Adipic_acid	0	g	vary
	d_init	0	m	hide
	h_layer1	0	m	hide
	h_layer2	0	m	hide
	h_init	0	m	hide
	v_init	0	ml	hide
	m_init	0	g	hide
	h	0	m	
	d	0	m	
	AR	0	-	vary
	Volume	0	ml	hide
dr2 = Thmh layer				
PHASE	dr2	solid		
	pressure	1	bar	hide
	Temperature	37	C	hide
	CP	4200	J/kgK	hide
	Density	0	kg/m3	adjust
	Theophylline_monohydrate	0	g	vary
	d_init	0	m	hide
	h_layer1	0	m	hide
	h_layer2	0	m	hide
	h_init	0	m	hide
	v_init	0	ml	hide
	m_init	0	g	hide
	h	0	m	
	d	0	m	
	AR	0	-	vary
	Volume	0	ml	hide
PHASE	liq	liquid		
	Density	1000	kg/m3	
	Adipic_acid	0	mg	vary
	Theophylline_monohydrate	0	mg	vary
				plot
				plot
Variables				
	dr1_kda	1000	1/s	
	dr1_Scd	0	-	adjust
	dr2_kda	1000	1/s	
	dr2_Scd	0	-	adjust
Define dynamic variables				
	Ao_ax_dr1	0	m2	hide
	Ao_rad_dr1	0	m2	hide
	c_dr1_mass	0	kg	hide
	c_dr1_v	0	m3	hide
	A_ax_dr1	0	m2	hide
	A_rad_dr1	0	m2	hide
	TSA_Adipic_acid	0	m2	
	f_ax_dr1	0	-	hide
	f_rad_dr1	0	-	hide
	a2_dr1	0	1/m	hide
	c_dr1_conc	0	mol/m3	hide
	dr1_kca_ax	0	1/s	
	dr1_kca_rad	0	1/s	hide
	dr1_kcda_ax	0	1/s	hide
	dr1_kcda_rad	0	1/s	hide
	dr1_k_ax	0	m/s	hide
	dr1_k_rad	0	m/s	hide
	Ao_ax_dr2	0	m2	hide
	Ao_rad_dr2	0	m2	hide
	c_dr2_mass	0	kg	hide
	c_dr2_v	0	m3	hide
	A_ax_dr2	0	m2	hide
	A_rad_dr2	0	m2	hide
	A_ax_exp_dr2	0	m2	
	TSA_dr2	0	m2	hide
	f_ax_exp_dr2	0	-	hide

TSA_exp_Theophylline_monohydrate	0	m2	
f_rad_dr2	0	-	hide
a2_dr2	0	1/m	hide
c_dr2_conc	0	mol/m3	hide
dr2_kca_ax	0	1/s	
dr2_kca_rad	0	1/s	hide
dr2_kcda_ax	0	1/s	hide
dr2_kcda_rad	0	1/s	hide
dr2_k_ax	0	m/s	hide
dr2_k_rad	0	m/s	hide
dr1_rel_rate	0	mg/s	
dr2_rel_rate	0	mg/s	

```

calculate |dr1
dr1.d:= dr1.d_init
dr1.h:= dr1.h_init

Ao_ax_dr1:= 3.1416/2*(dr1.d_init)^2
Ao_rad_dr1:= 3.1416*dr1.d_init*dr1.h_init

dr1.AR:= Ao_rad_dr1/Ao_ax_dr1

c_dr1_mass:= ((dr1.Adipic_acid*300))/1000
c_dr1_v:= c_dr1_mass/dr1.density
dr1.d:= (8/3.1416/dr1.AR*dr1.volume)^.3333
dr1.h:= (1/3.1416*(dr1.AR)^2*dr1.volume)^.3333
A_ax_dr1:= 3.1416/2*(dr1.d)^2
A_rad_dr1:= 3.1416*dr1.d*dr1.h
dr1.AR:= A_rad_dr1/A_ax_dr1
TSA_Adipic_acid:= A_ax_dr1+A_rad_dr1
f_ax_dr1:= A_ax_dr1/TSA_Adipic_acid
f_rad_dr1:= A_rad_dr1/TSA_Adipic_acid
a2_dr1:= TSA_Adipic_acid/dr1.volume
c_dr1_conc:= conc(dr1.Adipic_acid)
dr1_kca_ax:= f_ax_dr1*a2_dr1*dr1_k_ax
dr1_kca_rad:= f_rad_dr1*a2_dr1*dr1_k_rad
    
```

```

calculate |dr2
dr2.d:= dr2.d_init
dr2.h:= dr2.h_init
Ao_ax_dr2:= 3.1416/2*(dr2.d_init)^2
Ao_rad_dr2:= 3.1416*dr2.d_init*dr2.h_init
dr2.AR:= Ao_rad_dr2/Ao_ax_dr2
c_dr2_mass:= ((dr2.Theophylline_monohydrate*300))/1000
c_dr2_v:= c_dr2_mass/dr2.density
dr2.d:= (8/3.1416/dr2.AR*dr2.volume)^.3333
dr2.h:= (1/3.1416*(dr2.AR)^2*dr2.volume)^.3333
A_ax_dr2:= 3.1416/2*(dr2.d)^2
A_rad_dr2:= 3.1416*dr2.d*dr2.h
A_ax_exp_dr2:= 3.1416/2*(dr2.d)^2-(A_ax_dr1)
dr2.AR:= A_rad_dr2/A_ax_dr2
TSA_dr2:= A_ax_dr2+A_rad_dr2
f_ax_exp_dr2:= A_ax_exp_dr2/TSA_dr2
TSA_exp_Theophylline_monohydrate:= A_ax_exp_dr2+A_rad_dr2
f_rad_dr2:= A_rad_dr2/TSA_exp_Theophylline_monohydrate
a2_dr2:= TSA_exp_Theophylline_monohydrate/dr2.volume
c_dr2_conc:= conc(dr2.Theophylline_monohydrate)
dr2_kca_ax:= f_ax_exp_dr2*a2_dr2*dr2_k_ax
dr2_kca_rad:= f_rad_dr2*a2_dr2*dr2_k_rad
    
```

```

calculate | Mass exchange of Adipic_acid
dr1_kcda_ax:= (dr1_kda*dr1_kca_ax)/(dr1_kda+dr1_kca_ax/dr1_Scd)
dr1_kcda_rad:= (dr1_kda*dr1_kca_rad)/(dr1_kda+dr1_kca_rad/dr1_Scd)
dr1.Adipic_acid.dndt:= dr1.Adipic_acid -((dr1_kcda_ax+dr1_kcda_rad)*
.dndt
& dr1.volume*((c_dr1_conc/dr1_Scd)-conc(liq.Adipic_acid)))
liq.Adipic_acid.dndt:= liq.Adipic_acid. +((dr1_kcda_ax+dr1_kcda_rad)*
.dndt
& dr1.volume*((c_dr1_conc/dr1_Scd)-conc(liq.Adipic_acid)))
    
```

```

calculate | Mass exchange of Theophylline_monohydrate
dr2_kcda_ax:= (dr2_kda*dr2_kca_ax)/(dr2_kda+dr2_kca_ax/dr2_Scd)
dr2_kcda_rad:= (dr2_kda*dr2_kca_rad)/(dr2_kda+dr2_kca_rad/dr2_Scd)
dr2.Theophylline_monohydrate.dndt:= dr2.Theophyllin -((dr2_kcda_ax+dr2_kcda_rad)*
e_monohydrate
.dndt
& dr2.volume*((c_dr2_conc/dr2_Scd)-conc(liq.Theophylline_monohydrate)))
liq.Theophylline_monohydrate.dndt:= liq.Theophylline_monohydrate. +((dr2_kcda_ax+dr2_kcda_rad)*
.dndt
& dr2.volume*((c_dr2_conc/dr2_Scd)-conc(liq.Theophylline_monohydrate)))
    
```

APPENDIX 12

Dynochem process sheet example 2

Calculations involved in the prediction of mass transfer from the top surface of a matrix compact including the erosion of polymer

PHASE	core	solid		
	pressure	1	bar	hide
	Temperature	37	C	hide
	CP	4200	J/kgK	hide
	Density	0	kg/m3	
	drug1	0	mg	plot
	D_drug1_obs	0	m2/s	hide
	d_init	0	m	
	h_init	0	m	
	v_init	0	ml	
	m_init	0	g	
	h	0	mm	plot
	d	0	m	
	drug_conc_init	0	mol/m ³	hide
	drug1_init	0	g	
	AR	0	-	plot
	volume	0	ml	plot

PHASE	Etc	solid		
	pressure	1	bar	hide
	Temperature	37	C	hide
	CP	4200	J/kgK	hide
	Density	0	kg/m3	
	polymer	0	mg	plot
	d_init	0	mm	hide
	h_init	0	mm	hide
	v_init	0	ml	hide
	m_init	0	g	hide
	h	0	mm	plot
	d	0	mm	hide
	d_fraction	0	-	hide
	volume	0	m3	
	AR	0	-	hide

PHASE	liq	liquid		
	Density	1000	kg/m3	
	polymer	0	mg	plot
	water	0	mg	
	drug1	0	mg	plot

Variables				
	drug1_kca_rad	1000	1/s	
	E_constant	0	g/m2 s	
	drug1_kda	1000	1/s	
	drug1_Scd	0	-	hide
Define dynamic variables				
	Delta_ax	0	mm	plot
	Delta_rad	0	mm	hide
	A_ax	0	m2	hide
	A_rad	0	m2	hide
	f_ax	0	-	hide

f_rad	0	-	hide
TSA_exp	0	m3	hide
a2	0	1/m	
c_core_mass	0	g	
c_core_v	0	ml	
c_core_d	0	m	hide
c_core_h	0	m	hide
dead_vol_diss	0	ml	hide
drug1_kca_ax	0	1/s	
drug1_kca_rad	0	1/s	hide
drug1_kcda_ax	0	1/s	hide
drug1_kcda_rad	0	1/s	hide
Ao_ax	0	m2	hide
Ao_rad	0	m2	hide
ratio_ax	0	-	hide
ratio_rad	0	-	hide
gel_vol	0	m3	hide
Etc_a2	0	1/m	hide
Etc_Ao_ax	0	m2	hide
Etc_Ao_rad	0	m2	hide
Etc_A_ax	0	m2	hide
Etc_A_rad	0	m2	hide
Etc_TSA_exp	0	m3	hide
E_rate	0	g/s	hide

calculate

```

core.d:=          core.d_init
core.h:=          core.h_init
Ao_ax:=           3.1416/2*(core.d_init)^2
Ao_rad:=          3.1416*core.d_init*core.h_init
core.AR:=         Ao_rad/Ao_ax
core.h:=          4*core.volume/(3.1416*(core.d)^2)
A_ax:=            3.1416/2*(core.d)^2
A_rad:=           3.1416*core.d*core.h
core.AR:=         A_rad/A_ax
TSA_exp:=         A_ax/2
a2:=              TSA_exp/core.volume
Delta_ax:=        ABS((Etc.h-core.h))
drug1_kca_ax:=    a2*(core.D_drug1_obs)/Delta_ax
Etc.d:=           Etc.d_init
Etc.h:=           Etc.h_init
Etc_Ao_ax:=       3.1416/2*(Etc.d_init)^2
Etc_Ao_rad:=      3.1416*Etc.d_init*Etc.h_init
Etc.AR:=          Etc_Ao_rad/Etc_Ao_ax
Etc.h:=           4*Etc.volume/(3.1416*(Etc.d)^2)
Etc_A_ax:=        3.1416/2*(Etc.d)^2
Etc_A_rad:=       3.1416*Etc.d*Etc.h
Etc.AR:=          Etc_A_rad/Etc_A_ax
Etc_TSA_exp:=     Etc_A_ax/2
Etc_a2:=          Etc_TSA_exp/Etc.volume
    
```

calculate | Mass exchange of drug

```

drug1_kcda_ax:=   (drug1_kda*drug1_kca_ax)/(drug1_kda+drug1_kca_ax/drug1_Scd)
drug1_kcda_rad:= (drug1_kda*drug1_kca_rad)/(drug1_kda+drug1_kca_rad/drug1_Scd)
core.drug1.dndt:= core.drug1.dndt -((drug1_kcda_ax+drug1_kcda_rad)*
& core.volume*((core.drug_conc_init/drug1_Scd)-conc(liq.drug1)))
& liq.drug1.dndt:= liq.drug1.dndt +((drug1_kcda_ax+drug1_kcda_rad)*
& core.volume*((core.drug_conc_init/drug1_Scd)-conc(liq.drug1)))
    
```

calculate | Mass transfer of polymer (erosion)

```

E_rate:=          E_constant*(Etc.volume)*Etc_a2
Etc.polymer.dndt:= Etc.polymer.dndt -E_rate
Liq.polymer.dndt:= Liq.polymer.dndt +E_rate
    
```

APPENDIX 13

Dynochem process sheet example 3

Calculations involved in the prediction of mass transfer from a central drug-containing cylindrical matrix layer between two layers of soluble acid excipient

PHASE	core	solid			
	pressure	1	bar		hide
	Temperature	37	C		hide
	CP	4200	J/kgK		hide
	Density	0	kg/m3	adjust	
	drug1	0	mg	vary	hide
	D_drug1_obs	0	m2/s	adjust	hide
	d_init	0	m		hide
	h_init	0	m		hide
	v_init	0	ml		hide
	m_init	0	g		hide
	h	0	m		hide
	d	0	m		hide
	drug_conc_init	0	mol/m3		hide
	drug1_init	0	g		
	AR	0	-	vary	hide
	volume	0	ml		hide

PHASE	Etc	solid			
	pressure	1	bar		hide
	Temperature	37	C		hide
	CP	4200	J/kgK		hide
	Density	0	kg/m3	adjust	
	polymer	0	mg	vary	hide
	d_init	0	mm		hide
	h_init	0	mm		hide
	v_init	0	ml		hide
	m_init	0	g		hide
	h	0	mm		hide
	d	0	mm		hide
	d_fraction	0	-		hide
	AR	0	-	vary	hide

|dr2 = AdA

PHASE	dr2	solid			
	pressure	1	bar		hide
	Temperature	37	C		hide
	CP	4200	J/kgK		hide
	Density	0	kg/m3	adjust	
	Drug2	0	g	vary	
	d_init	0	m		hide
	h_layer1	0	m		hide
	h_layer2	0	m		hide
	h_init	0	m		hide
	v_init	0	ml		hide
	m_init	0	g		hide
	h	0	m		hide
	d	0	m		hide
	AR	0	-	vary	hide
	Volume	0	ml		hide

PHASE	liq	liquid			
-------	-----	--------	--	--	--

Density	1000	kg/m3		
polymer	0	mg	vary	plot
drug1	0	mg	vary	plot
water	0	mg	vary	hide
drug2	0	mg	vary	plot

Variables

drug1_kda	1000	1/s	adjust	
E_pol	0	g/m2 s	adjust	
dr2_kda	1000	1/s		
dr2_Scd	0	-	adjust	hide
drug1_Scd	0	-	adjust	hide

Define dynamic variables

drug_percent	0	-		hide
Delta_ax	0	mm		hide
Delta_rad	0	mm		hide
A_ax	0	m2		hide
A_rad	0	m2		hide
A_ax_exp	0	m2		hide
f_ax	0	-		hide
f_rad	0	-		hide
TSA_exp	0	m2		hide
a2	0	1/m		hide
c_core_mass	0	g		hide
c_core_v	0	ml		hide
E_rate	0	mol/s		hide
drug1_kca_ax	0	1/s		hide
drug1_kca_rad	0	1/s		hide
drug1_kcda_ax	0	1/s		hide
drug1_kcda_rad	0	1/s		hide
Ao_ax	0	m2		hide
Ao_rad	0	m2		hide
Etc_a2	0	1/m		hide
Etc_Ao_ax	0	m2		hide
Etc_Ao_rad	0	m2		hide
Etc_A_ax	0	m2		hide
Etc_A_rad	0	m2		plot
Etc_A_ax_exp	0	m2		plot
Etc_TSA_exp	0	m3		plot
a	0	-		hide
b	0	-		hide
drug1_rel_rate	0	mg/min		plot
dr2				
Ao_ax_dr2	0	m2		hide
Ao_rad_dr2	0	m2		hide
c_dr2_mass	0	kg		hide
c_dr2_v	0	m3		hide
A_ax_dr2	0	m2		hide
A_rad_dr2	0	m2		hide
A_ax_exp_dr2	0	m2		hide
TSA_dr2	0	m2		hide
f_ax_exp_dr2	0	-		hide
TSA_exp_dr2	0	-		hide
f_rad_dr2	0	-		hide
a2_dr2	0	1/m		hide
c_dr2_conc	0	mol/m3		hide
dr2_kca_ax	0	1/s		hide
dr2_kca_rad	0	1/s		hide
dr2_kcda_ax	0	1/s		hide
dr2_kcda_rad	0	1/s		hide
dr2_k_ax	0	m/s		hide
dr2_k_rad	0	m/s		hide

calculate

core.d:=	core.d_init
core.h:=	core.h_init
Ao_ax:=	3.1416/2*(core.d_init)^2
Ao_rad:=	3.1416*core.d_init*core.h_init
core.AR:=	Ao_rad/Ao_ax
c_core_mass:=	(core.drug1*180)/1000

Density	1000	kg/m3		
polymer	0	mg	vary	plot
drug1	0	mg	vary	plot
water	0	mg	vary	hide
drug2	0	mg	vary	plot

Variables

drug1_kda	1000	1/s	adjust	
E_pol	0	g/m2 s	adjust	
dr2_kda	1000	1/s		
dr2_Scd	0	-	adjust	hide
drug1_Scd	0	-	adjust	hide

Define dynamic variables

drug_percent	0	-		hide
Delta_ax	0	mm		hide
Delta_rad	0	mm		hide
A_ax	0	m2		hide
A_rad	0	m2		hide
A_ax_exp	0	m2		hide
f_ax	0	-		hide
f_rad	0	-		hide
TSA_exp	0	m2		hide
a2	0	1/m		hide
c_core_mass	0	g		hide
c_core_v	0	ml		hide
E_rate	0	mol/s		hide
drug1_kca_ax	0	1/s		hide
drug1_kca_rad	0	1/s		hide
drug1_kcda_ax	0	1/s		hide
drug1_kcda_rad	0	1/s		hide
Ao_ax	0	m2		hide
Ao_rad	0	m2		hide
Etc_a2	0	1/m		hide
Etc_Ao_ax	0	m2		hide
Etc_Ao_rad	0	m2		hide
Etc_A_ax	0	m2		hide
Etc_A_rad	0	m2		plot
Etc_A_ax_exp	0	m2		plot
Etc_TSA_exp	0	m3		plot
a	0	-		hide
b	0	-		hide
drug1_rel_rate	0	mg/min		plot
dr2				
Ao_ax_dr2	0	m2		hide
Ao_rad_dr2	0	m2		hide
c_dr2_mass	0	kg		hide
c_dr2_v	0	m3		hide
A_ax_dr2	0	m2		hide
A_rad_dr2	0	m2		hide
A_ax_exp_dr2	0	m2		
TSA_dr2	0	m2		hide
f_ax_exp_dr2	0	-		hide
TSA_exp_dr2	0	-		
f_rad_dr2	0	-		hide
a2_dr2	0	1/m		hide
c_dr2_conc	0	mol/m3		hide
dr2_kca_ax	0	1/s		hide
dr2_kca_rad	0	1/s		hide
dr2_kcda_ax	0	1/s		hide
dr2_kcda_rad	0	1/s		hide
dr2_k_ax	0	m/s		hide
dr2_k_rad	0	m/s		hide

calculate

core.d:=	core.d_init
core.h:=	core.h_init
Ao_ax:=	3.1416/2*(core.d_init)^2
Ao_rad:=	3.1416*core.d_init*core.h_init
core.AR:=	Ao_rad/Ao_ax
c_core_mass:=	(core.drug1*180)/1000


```

c_core_v:=      c_core_mass/core.density
core.d:=      (8/3.1416/Core.AR*c_core_v)^.3333
core.h:=      (1/3.1416*(core.AR)^2*c_core_v)^.3333
A_ax:=      3.1416/2*(core.d)^2
A_rad:=      3.1416*core.d*core.h
Delta_ax:=      ABS((Etc.h-core.h))/2
Delta_rad:=      ABS((Etc.d-core.d))/2
Etc.d:=      Etc.d_init
Etc.h:=      Etc.h_init
Etc_Ao_ax:=      3.1416/2*(Etc.d_init)^2
Etc_Ao_rad:=      3.1416*Etc.d_init*Etc.h_init
Etc.AR:=      Etc_Ao_rad/Etc_Ao_ax
Etc.d:=      (8/3.1416/Etc.AR*Etc.volume)^.3333
Etc.h:=      (1/3.1416*(Etc.AR)^2*Etc.volume)^.3333
Etc_A_ax:=      3.1416/2*(Etc.d)^2
Etc_A_rad:=      3.1416*Etc.d*Etc.h
Etc_A_ax_exp:=      Etc_A_ax-A_ax_dr2
Etc_TSA_exp:=      Etc_A_ax_exp+Etc_A_rad
Etc_a2:=      Etc_TSA_exp/Etc.volume
f_ax:=      Etc_A_ax_exp/Etc_TSA_exp
f_rad:=      Etc_A_rad/Etc_TSA_exp
drug1_kca_ax:=      f_ax*Etc_a2*(core.D_drug1_obs)/Delta_ax
drug1_kca_rad:=      f_rad*Etc_a2*(core.D_drug1_obs)/Delta_rad
|dr2
dr2.d:=      dr2.d_init
dr2.h:=      dr2.h_init
Ao_ax_dr2:=      3.1416/2*(dr2.d_init)^2
Ao_rad_dr2:=      3.1416*dr2.d_init*dr2.h_init
dr2.AR:=      Ao_rad_dr2/Ao_ax_dr2
c_dr2_mass:=      ((dr2.drug2*300))/1000
c_dr2_v:=      c_dr2_mass/dr2.density
dr2.d:=      (8/3.1416/dr2.AR*c_dr2_v)^.3333
dr2.h:=      (1/3.1416*(dr2.AR)^2*c_dr2_v)^.3333
A_ax_dr2:=      3.1416/2*(dr2.d)^2
A_rad_dr2:=      3.1416*dr2.d*dr2.h
A_ax_exp_dr2:=      3.1416/2*(dr2.d)^2
dr2.AR:=      A_rad_dr2/A_ax_dr2
TSA_dr2:=      A_ax_dr2+A_rad_dr2
f_ax_exp_dr2:=      A_ax_dr2/TSA_dr2
TSA_exp_dr2:=      A_ax_dr2+A_rad_dr2
f_rad_dr2:=      A_rad_dr2/TSA_dr2
a2_dr2:=      TSA_dr2/c_dr2_v
c_dr2_conc:=      conc(dr2.drug2)
dr2_kca_ax:=      f_ax_exp_dr2*a2_dr2*dr2_k_ax
dr2_kca_rad:=      f_rad_dr2*a2_dr2*dr2_k_rad
a:=      (drug1_kca_ax+drug1_kca_rad)
b:=      Etc.volume*((core.drug_conc_init/drug1_Scd)-conc(liq.drug1))
drug1_rel_rate:=      a*b

```

```

calculate | Mass exchange of drug
drug1_kcda_ax:=      (drug1_kda*drug1_kca_ax)/(drug1_kda+drug1_kca_ax/drug1_Scd)
drug1_kcda_rad:=      (drug1_kda*drug1_kca_rad)/(drug1_kda+drug1_kca_rad/drug1_Scd)
core.drug1.dndt:=      core.drug1.dndt      -((drug1_kcda_ax+drug1_kcda_rad)*
&      Etc.volume*((core.drug_conc_init/drug1_Scd)-conc(liq.drug1)))
liq.drug1.dndt:=      liq.drug1.dndt      +((drug1_kcda_ax+drug1_kcda_rad)*
&      Etc.volume*((core.drug_conc_init/drug1_Scd)-conc(liq.drug1)))

```

```

calculate | Mass exchange of drug2
dr2_kcda_ax:=      (dr2_kda*dr2_kca_ax)/(dr2_kda+dr2_kca_ax/dr2_Scd)
dr2_kcda_rad:=      (dr2_kda*dr2_kca_rad)/(dr2_kda+dr2_kca_rad/dr2_Scd)
dr2.drug2.dndt:=      dr2.drug2.dndt      -((dr2_kcda_ax+dr2_kcda_rad)*
&      dr2.volume*((c_dr2_conc/dr2_Scd)-conc(liq.drug2)))
liq.drug2.dndt:=      liq.drug2.dndt      +((dr2_kcda_ax+dr2_kcda_rad)*
&      dr2.volume*((c_dr2_conc/dr2_Scd)-conc(liq.drug2)))

```

```

calculate | Mass transfer of polymer (erosion)
E_rate:=      E_pol*(Etc.volume)*Etc_a2
Etc.polymer.dndt:=      Etc.polymer.dndt      -E_rate
Liq.polymer.dndt:=      Liq.polymer.dndt      +E_rate

```